PROPERTIES OF MAGNETIZED PLASMAS

by

Martin L.G. Oldfield

A thesis submitted for the degree of
Doctor of Philosophy at the
University of Oxford

Keble College
Oxford
July 1969

ABSTRACT

This D.Phil. thesis describes the experimental determination of the voltage reflection coefficient from a vacuum-plasma plane boundary in a coaxial transmission line with an axial magnetic field $\underset{\sim}{B}_l$ applied. A theoretical analysis of microwave propagation in the magnetized plasma filled coaxial line, using rotating coordinate techniques, is given, and computed solutions of the dispersion determinant agree well with the experimental results. Both experiment and theory were for conditions where the microwave- , plasma- , electron collision- , and electron cyclotron- frequencies are of the same order.

A 9 GHz coaxial microwave probe is mounted along the axis of a 44 mm diameter, hydrogen driven, dry Air filled, shock tube. Shock-ionised Air (M_s = 9 - 14 , T~4000°K, electron density = 10^{17} - 3 x 10^{19} /m³ initial pressure p_o = 1 - 10 Torr, electron collision frequency = 10^{10} - 10^{11}/s) fills the coaxial line and partially reflects a microwave signal.

Initially this probe, and a similar rectangular waveguide probe, was used with $\underset{\sim}{B}_l$ = 0 in order to calibrate the electron density and electron collision frequency behind the shock in terms of the shock tube parameters (p_o , M_s). By using two (7.5 & 9 GHz) microwave frequencies, it was shown that the assumed electron collision frequencies are substantially correct, and the experimental electron densities agreed well with the computed equilibrium electron densities.

Earlier experiments with surface saturated-ion-current electrostatic probes inset into a flat plate in the shock tube flow showed that the sheath-edge ion density is close to the free-stream equilibrium ion density. The apparent ionisation potential derived from electrostatic probe results decreased as p_o was reduced from 10 to 1 Torr.

CONTENTS

		Page
1	Introduction.	1
2	The shock tube as a plasma source.	
2.1	Introduction.	2
2.2	Advantages of shock tube as a plasma source.	2
2.3	Disadvantages of shock tube as a plasma source.	4
2.4	Details of shock tube.	6
2.5	The test gas :- Air.	12
3	The flat plate electrostatic probe.	
3.1	The electrostatic probe as a preliminary diagnostic.	21
3.2	Construction and use of flat plate electrostatic probe.	26
3.3	Shock tube test time.	31
3.4	Ion number density.	33

Page

4 Microwave reflection without magnetic field.

4.1 Introduction. 51

4.2 Analysis of reflection from plasma. 55

4.3 Construction and calibration of coaxial microwave probe. 65

4.4 Construction and calibration of rectangular waveguide probe. 77

4.5 Electron collision frequency. 79

4.6 Electron density : experimental results. 82

5 Microwave reflection with axial magnetic field applied.

5.1 Introduction. 94

5.2 Theory of microwave reflection from magnetized-plasma. 95

5.3 Construction and calibration of axial magnetic field solenoid. 109

5.4 Experimental results : magnetized plasma filled coaxial line. 112

5.5 Experimental results : magnetized plasma filled rectangular waveguide. 118

Page

6 Conclusion. 122

Appendices :

A Field theory of microwave propagation in a coaxial transmission line filled with anisotropic plasma.

A.1 Introduction. 124

A.2 The anisotropic dieletric tensor. 124

A.3 Propagation of TEM waves along the magnetic field in an unbounded uniform plasma. 128

A.4 Solution of Maxwell's equations for propagation of EM waves in anisotropic plasma in a waveguide. 131

A.5 Particular solution in longitudinally magnetized coaxial line. 135

A.6 Reflection from magnetized plasma in coaxial line. 142

B Rotating coordinates.

B.1 Definition. 146

B.2 Transformation of matrices. 147

B.3 Vector manipulations. 147

B.4 Differential vector operators. 148

B.5 Transformation of rotating coordinates to cylindrical coordinates. 149

Page

C Program for the computation of the reflection from a magnetized plasma filled coaxial line.

C.1 Introduction. 152

C.2 Program print out. 154

Reference list. 164

Acknowledgements. 171

UNITS

Standard SI units are used. The Torr (1mm Hg) is used as the pressure unit for shock tube initial pressure.

NOMENCLATURE

The following list gives the most common usage of the listed symbols:

$\underset{\sim}{B}$ Magnetic induction.

$\underset{\sim}{B}_1$ Applied d.c. magnetic field.

c Velocity of light in vacuo $= 2.99793 \times 10^8$ m/s.

$\bar{c}$ $= \sqrt{\frac{8kT}{\pi m}}$ = mean thermal velocity.

$\underset{\sim}{D}$ Electric displacement.

D_a Coefficient of ampibolar diffusion.

e $= 1.6021 \times 10^{-19}$ coulomb = electronic charge.

$\underset{\sim}{E}$ Electric field vector.

$\underset{\sim}{H}$ Magnetic field vector.

j $= \sqrt{-1}$

$\underset{\sim}{J}$ Current density.

J_n Bessel's function.

j_+ Ion current to probe.

k Boltzmann constant $= 1.3806 \times 10^{-23}$ Joule/ ^oK .

$k = k^r + j\,k^i$ Normalised plasma wave number.

k_o $= \omega\sqrt{\mu_o \varepsilon_o}$ = free space wave number.

k_{co} Waveguide cut - off wave number.

K_i Ion mobility.

ℓ Shock tube test length.

ℓ Left-hand rotating coordinate.

m_e Electron mass.

M_s Shock Mach number.

n Power law of microwave diode.

n_e Electron number density.

n_i Ion number density.

n_o Neutral number density.

p Pressure.

p_o Shock tube test gas initial pressure.

p_i, p_j, p_1, p_2 Transverse wave numbers.

r Right-hand rotating coordinate.

R_1 Inner radius of coaxial line.

R_2 Outer radius of coaxial line.

R_v Microwave voltage reflection coefficient.

R_p Microwave power reflection coefficient.

R_x Reflection coefficient in free space parallel to incident wave.

S Ambipolar Schmidt number.

S_e Ambipolar Schmidt number at boundary-layer edge.

T Neutral gas temperature.

T_e Electron temperature.

T_i Ion temperature.

V Voltage.

V_o Incident wave voltage.

V_i Ionisation potential.

V_d Diode output voltage.

$\underset{\sim}{V_m}$ microwave voltage.

VSWR Voltage standing wave ratio.

X_e $= \frac{n_e}{n_o}$ = electron mole fraction.

x distance from flat-plate leading edge to electrostatic probe.

Y_n Bessel's function.

Z Impedance of plasma filled coaxial line or waveguide.

Z_o Impedance of empty coaxial line or waveguide.

δ velocity boundary layer thickness.

δ_u 99% velocity layer boundary thickness.

ε_o $= 8.8542 \times 10^{-12}$ farad/m . Dielectric constant of free space.

ε Relative dielectric constant.

$\underset{\approx}{\varepsilon}$ Relative dielectric tensor of anisotropic plasma.

$\varepsilon_{11}, \varepsilon_{12}, \varepsilon_{33}$ Components of $\underset{\approx}{\varepsilon}$ in (x,y,z) frame.

$\varepsilon_\ell, \varepsilon_r, \varepsilon_{33}$ Components of $\underset{\approx}{\varepsilon}$ in (ℓ, r, z) frame.

θ Azimuthal coordinate.

λ microwave wavelength.

λ_d Debye shielding length $= \sqrt{\dfrac{\varepsilon_o k T_e}{n_e e^2}}$.

λ_e Electron mean free path.

λ_i Ion mean free path.

μ_o Free space permeability $= 4 \times 10^{-7}$ Henry/m .

μ Coefficient of viscosity.

ν Electron collision frequency for momentum transfer.

ρ Gas density behind shock.

ρ Charge density in Maxwell's equations.

ρ radial coordinate.

ρ_a Reference density at T = 300 ^{o}K, p = 1 atm., $= 1.2915$ kg/m^3.

ρ_e Gas density at edge of boundary layer.

τ Shock tube test time.

ω Microwave rotational frequency.

ω_p Plasma frequency $= \sqrt{\dfrac{n_e e^2}{m_e \varepsilon_o}}$.

ω_c Electron cyclotron frequency $= \dfrac{e B_1}{m_e}$.

ω_{co} Waveguide cut-off frequency.

1 INTRODUCTION.

The purpose of the work described in this thesis was to obtain experimental measurements of the effect of a d.c. magnetic field on the propagation of microwaves through a weakly ionised, collision dominated, thermal plasma. These measurements were to be obtained under conditions where the microwave - , plasma - , electron collision - and electron cyclotron - frequencies are of the same order. The results were then to be compared with theoretical predictions obtained from a solution of the electromagnetic equations in a homogeneous, anisotropic, magnetised plasma, with approximations and boundary conditions appropriate to those in the experiments.

The geometry chosen was that of reflection of 9 GHz microwaves from a plane interface with a uniform equilibrium plasma in a coaxial transmission line, with the magnetic field applied in the direction of propagation.

The plasma used was generated by a pressure-driven shock tube, using dry Air as the experimental gas.

As precise measurements of this type, in a magnetised plasma - filled coaxial line, have, to the author's knowledge, not previously been attempted, initial exploratory experiments were considered necessary, in order to understand the exact nature of the plasma under examination. Shock tube plasmas are by no means as well defined as one would like, and earlier experiments by Laird (1), using rectangular

waveguide in a shock tube, gave rise to certain anomalies. Consequently, to qualify the plasma generated by the shock tube, Laird's experiments were carefully repeated over a wider range of experimental parameters, and rectangular waveguide and coaxial line experiments were compared afresh.

For this reason, a large part of this thesis deals with the non magnetic field propagation case, and the calibration of the shock tube as a plasma source.

Only after this were experiments made with the magnetic field applied, both with the coaxial line and with the rectangular waveguide.

A fuller introduction and a literature survey are included at the beginning of each of the chapters, on the shock tube, the electrostatic probe, non - magnetic microwave reflection, and in the final chapter on magnetised plasma microwave reflection.

The highly complex, theoretical analysis of magnetised plasma propagation in a coaxial line, using rotating coordinate techniques, is presented in detail in Appendix A. The computer program necessary to obtain numerical values for the wave number, and reflection coefficient, in the magnetised plasma coaxial line is listed in Appendix C.

2. THE SHOCK TUBE AS A PLASMA SOURCE.

2.1 Introduction.

For plasma - microwave interaction experiments the shock tube is a convenient plasma source. The theory and practice of shock tubes are well described by Wright (2) and Glass & Hall (3): a long tube (the driver,or low pressure, section) , filled with the test gas, is separated from a shorter (driver) section by a diaphragm. The driver is filled with a driver gas at high pressure until the diaphragm ruptures and a shock front is driven at nearly uniform velocity down the tube by the expanding driver gas. On passing through the shock front the test gas is compressed adiabatically to a high temperature and undergoes slight thermal ionisation, as shown in Fig.1.

The time history of the shock front can be plotted on a distance - time plot (Fig.2).

2.2 Advantages of Shock Tube as a Plasma Source.

Compared with other plasma source the shock tube has the following advantages:-

(a). With suitable choice of operating conditions a nearly uniform plasma region at near thermal equilibrium is generated.

(b). From simple measurement of the shock speed (Mach No. M_s) and the test gas initial pressure (p_o), the major thermodynamic and gas - dynamic variables, including the

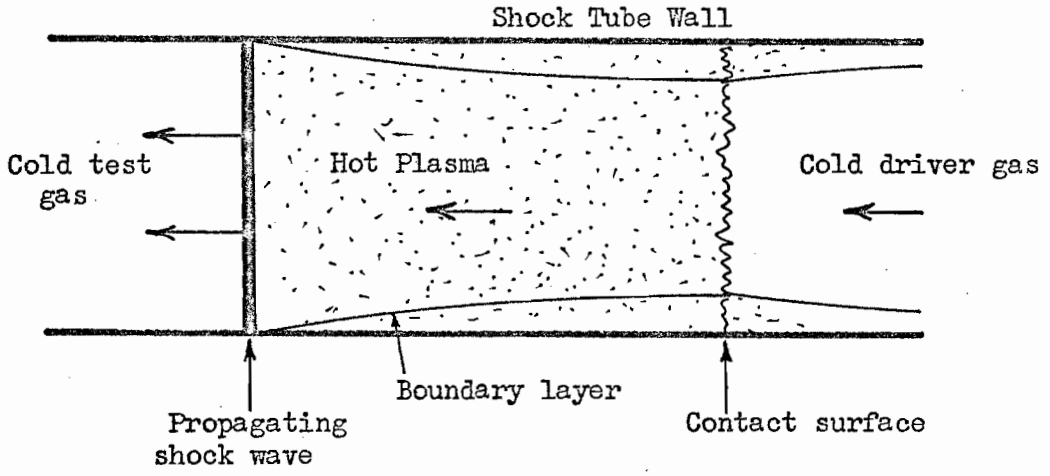


Fig. 1 Plasma behind incident shock.

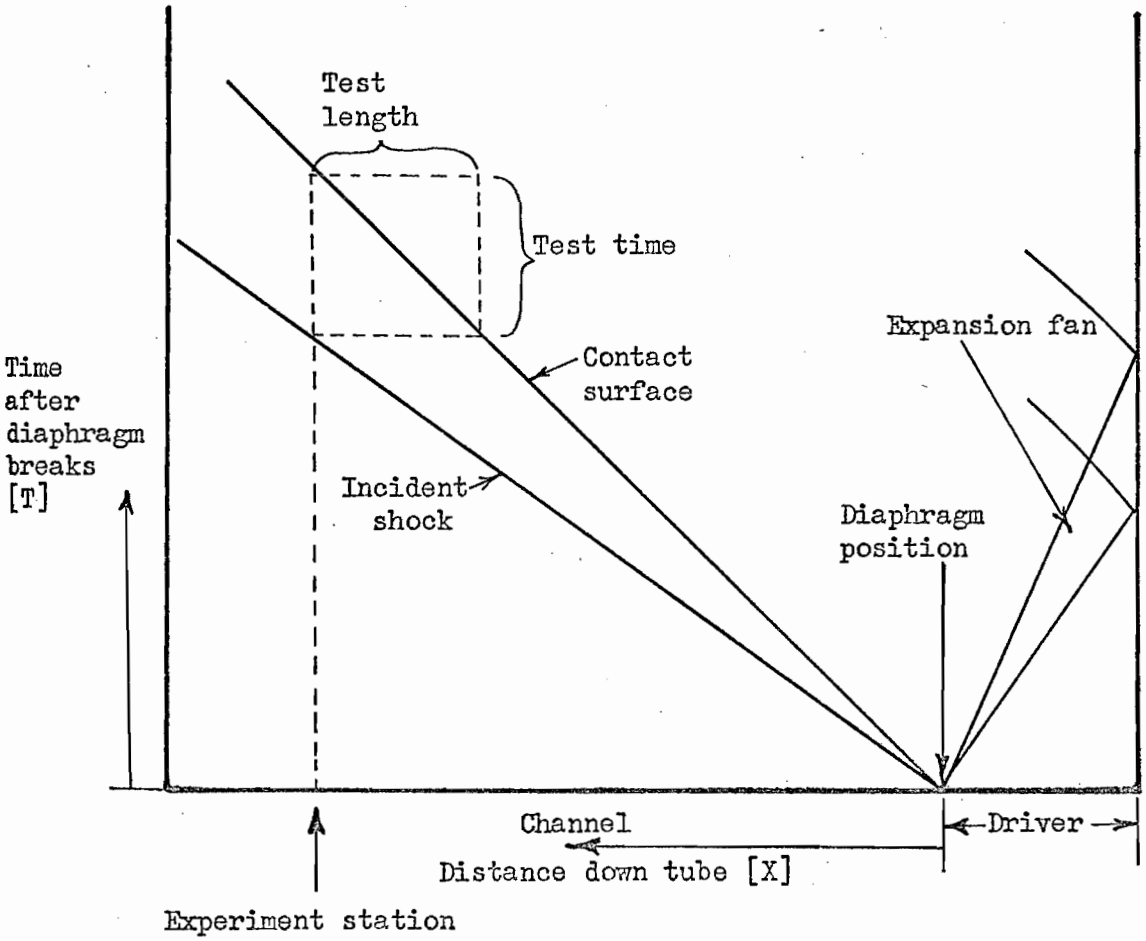


Fig.2 Shock tube X - T diagragm.

electron density, may be inferred. Tables and charts such as those of Feldman (4), Laird and Heron (5), and Lewis and Burgess (6), give the pressure, density, temperature, enthalpy and compressibility behind the incident shock, for imperfect air in equilibrium. Other transport properties, such as viscosity, are given for high temperature air by Hansen (7), and the equilibrium composition at high temperatures, from which electron and ion densities can be derived have been computed by Logan and Treanor (8) in 1957, and more recently by Hilsenrath and Klein (9).

(c). For Air as a test gas, Lin, Neal and Fyfe (10) and Lin and Teare (11) show that the distance required to reach 90% of the equilibrium electron density is approximately 50 times the mean free path in front of the shock. For an initial pressure of 1 Torr, the mean free path of approximately 5×10^{-5} m gives an ionisation distance of approximately 2.5×10^{-3} m. This is much less than the microwave wavelength (30 mm) used, and so the plasma can be considered uniform up to a sharp boundary at the shock front. Lin, Neal and Fyfe's (10) results have been more recently confirmed by Wilson (12).

(d). The test time (see Fig. 2), typically 30 μs, is short, and so the apparatus in the incident shock region remains at near room temperature for the duration of the experiment. For this reason collision-dominated dense plasmas can be generated without thermal damage to the apparatus.

2.3 Disadvantages of Shock Tube as a Plasma Source.

(a). The short test time available limits the information

obtained on each run, and experimental data curves must usually be obtained on a point per run basis. This contrasts with the long time necessary to vacuum-pump the tube after each run, and hence with the long turn-around time between runs.

(b). Boundary layers on the wall can influence the conditions behind the shock, and especially at low initial pressures they reduce the test time from the theoretical value. Mirels (13, 14, 15, 16) has analysed these effects for both laminar and turbulent boundary layers.

(c). To achieve thermal equilibrium, a thin shock transition region and a reasonable test time, ranges of p_o and M_s must be chosen which limit experiments to highly collisional, slightly ionised plasmas.

(d). For significant electron densities Mach Nos. of 9 - 12 must be used and this requires the use of Hydrogen as a driver gas. This is a safety hazard as the hot plasma would serve to ignite the Hydrogen after any structural failure.

(e). The plasma flow behind the shock is supersonic, and any apparatus mounted in the flow must be designed both to stand the aerodynamic forces involved and to minimise interference with the flow. The structural criterion is especially relevant in areas where shock reflection occurs, with resultant high pressures and temperatures (typically 5×10^6 N/m^2, 7500°K).

2.4 Details of Shock Tube.

(See Figs. 3, 4, 5). The shock tube used in the experiments to be described had originally been used without a dump tank by Woolgar (17) for spectroscopic work in Argon, and was known to be uncontaminated. Woolgar (17) gives a detailed description of the design of the tube, including the convergent section between the driver and low pressure section, and so only a brief description will be given here.

The shock tube was lengthened, a dump tank added to reduce the final pressure in the system after high speed runs, and the vacuum system was replumbed with larger diameter (25.4 mm)tubing and snap-action valves to improve ease of operation.

A 0.95 m long, removable section of shock tube, fabricated from EN58B non-magnetic stainless steel,was inserted in the experiment area between the main shock tube and the dump tank. This facilitated the mounting of experiments in the shock tube, and enabled an axial magnetic-field solenoid to be placed coaxially over the shock tube.

Two 0 - 20 Torr,Wallace & Tiernan FA 160 absolute pressure gauges (Nos. MM11353 & KK041879) were used to set the initial pressure p_o immediately before each run. These have a certified accuracy of 0.33% FSD and were returned for recalibration if they differed by more than twice this amount. They also agreed with a liquid-Nitrogen trapped accurate McLeod gauge, constructed by Dr. M. A. Byrne, to within 0.5% FSD. In use these gauges required at least a day's outgassing if not kept under vacuum, and generally required several minutes to reach a steady reading at 1 Torr pressure. It was demonstrated that this delay was due to the gauges, and was longer than the settling time of the tube and

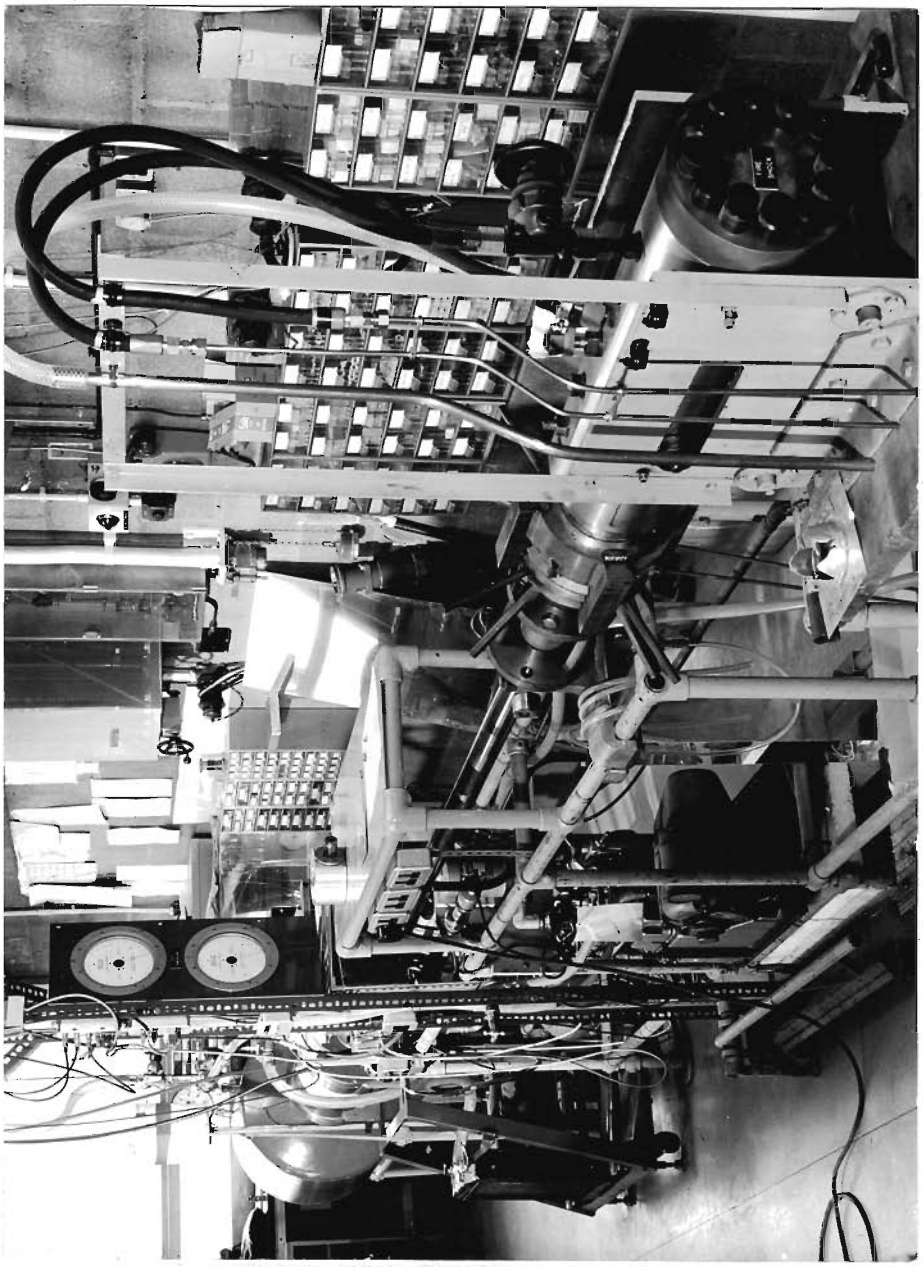


Fig.3 View of Shock Tube from driver end.

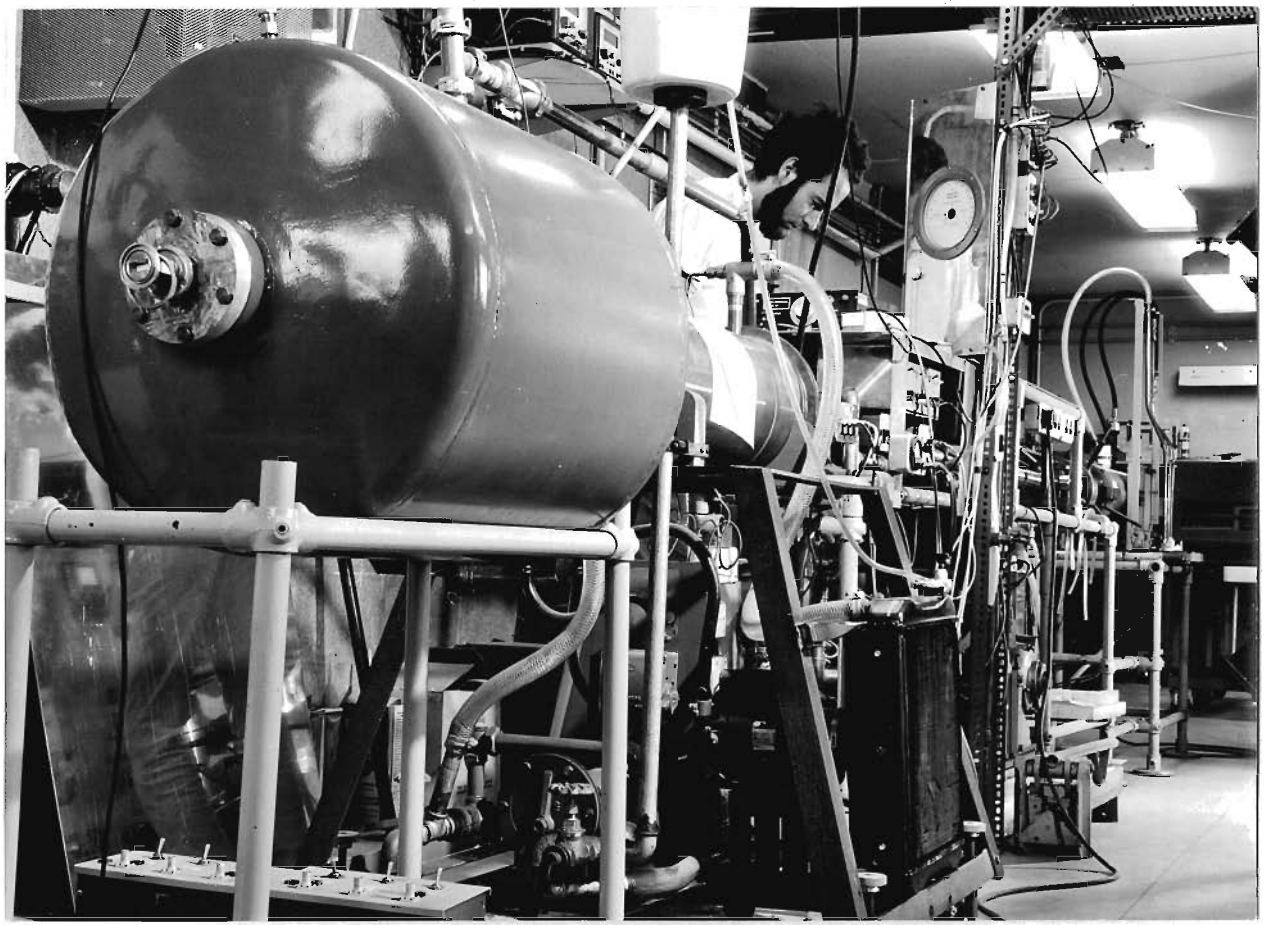


Fig.4 View of Shock Tube from dump-tank end.

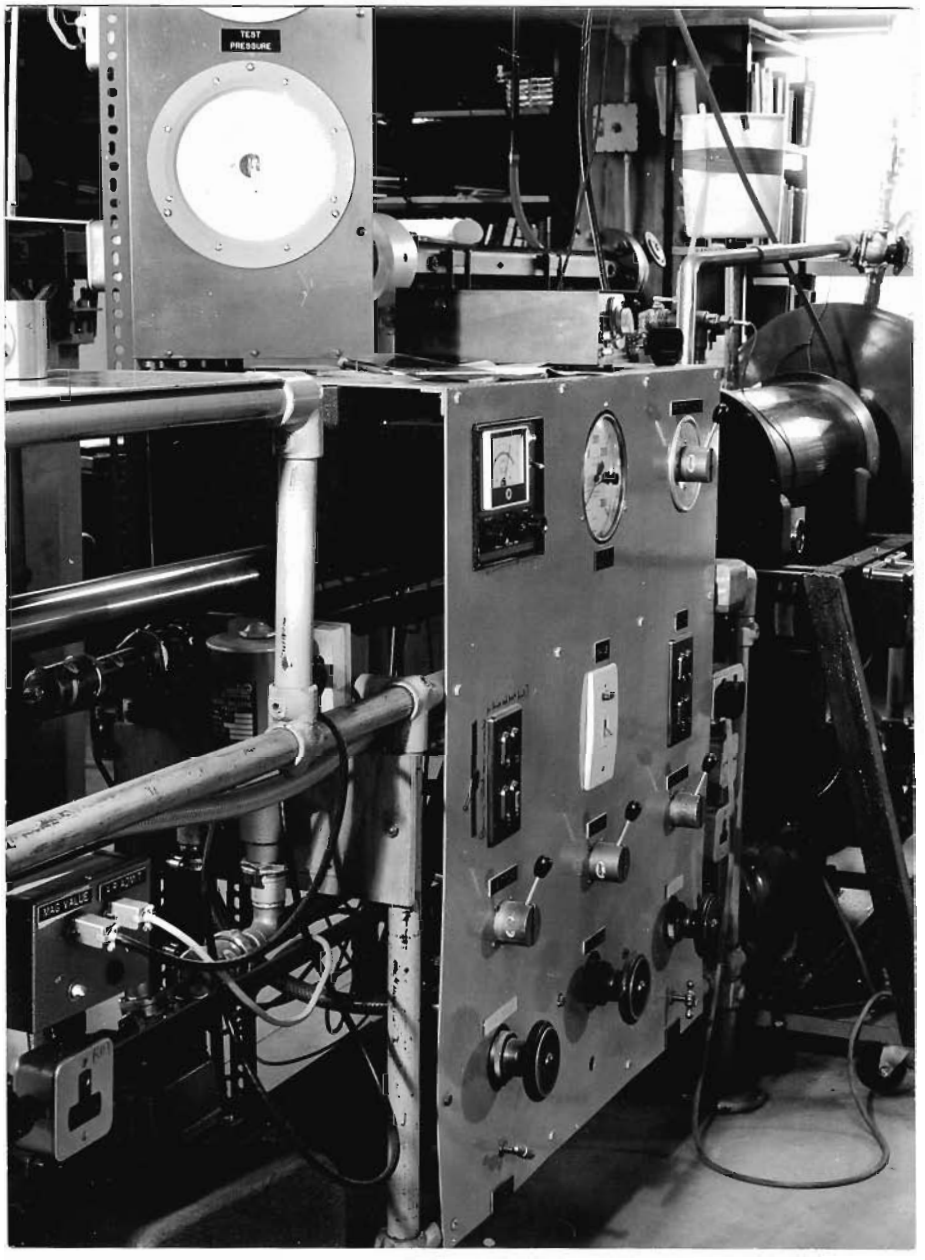


Fig.5 Shock Tube control panel and firing station.

vacuum system.

The shock Mach number was varied by changing the thickness of the half-hard aluminium diaphragms, and for lower Mach numbers by introducing up to 200 Torr of Nitrogen into the driver before firing with the thinnest (24 SWG) diaphragm. Woolgar (17) describes the quick change clamping mechanism used. The diaphragms were unscored, and, except for on a very few occasions, opened cleanly, with no large aluminium particles being projected down the tube.

The system designed by Woolgar was retained to measure the shock speed. Three platinum thin-film heat gauges [see Schultz (18)], spaced at 305 mm intervals just upstream of the experimental section, trigger fast rise-time pulse amplifiers, which in turn start and stop two Advance TC2A, 1MHz timers. These timers, using crystal-controlled clocks, are accurate to within a microsecond, and were checked against the BBC standard frequency signal.

On exchanging, in turn, the counters, the pulse amplifiers and the thin film gauges, the two counters seldom differed by more than a microsecond on a given shock tube run. From this it can be concluded that the delays inherent in the timing were the same at all three stations, that the shock attenuation in the experiment section is negligible, and that the system is accurate for timing the shock to $\pm$ 1 μs. Thus, for a Mach 10 shock, the shock speed can be measured to within 2%.

Microwave techniques could also be used to measure shock velocities [see Dunn & Blum (19)], but these are generally not as accurate as the method chosen.

Table 1 : Shock Tube Details.

Material : stainless steel.	
Driven Section (Channel) :-	
Total length	4.2 m
Length to experiment station	3.7 m
Internal diameter	44.45 mm ($1\frac{3}{4}$ ")
Wall thickness	3.175 mm ($\frac{1}{8}$ ")
Driver :-	
Volume	$3.58 \times 10^{-3} m^3$
Length	0.787 m
Internal diameter	76.2 mm (3")
Wall thickness	63.5 mm ($2\frac{1}{2}$")
Maximum design pressure	135 atm.
Maximum pressure used	1×10^7 N/m^2 (1500 p.s.i.)
Dump tank :-	
Material : stainless steel.	
Length	0.70 m
Diameter	0.55 m
Diaphragms :-	
Material :- half hard aluminium sheet.	
Thickness	0.559 - 2.642 mm (24 - 12 SWG)
Initial pressures (p_o)	0.1, 1, 3, 10 Torr
Mach Number range used :	M = 8 - 14
Test gas :	Dry Air
Driver gas :	Hydrogen
Electron density range :	10^{17} - 3×10^{19}/m^3

After each run the shock tube was pumped down to less than 1 Torr, flushed with dry Nitrogen and pumped by a two-stage rotary vacuum pump to less than 1×10^{-2} Torr. When running with air it was not felt necessary to pump further, as any leakage into the tube will be also of air. The time between runs, including changing the diaphragm and examining the experimental apparatus in the flow for impact damage, was about one hour.

In addition the tube was stored under vacuum and regularly pumped for a few days to outgas any impurities from the walls.

Before the experimental measurements were made, the tube was run with an accelerometer strapped to the rear of the dump tank. Using a driver pressure of about 10^7 N/m^2 (1500 p.s.i.)N_2 driving into 2 Torr Air, a transient acceleration of 4.5 g was measured with a superimposed fast (500 Hz) oscillation, due to dump tank resonance, with a peak acceleration of 35 g. The tube, which is solidly mounted, recoiled some 2 mm , while the driver moved 20 mm on its recoil springs.

A total of 359 successful runs were made on this shock tube.

2.5 The Test Gas:- Air.

As indicated in section 2.2, Air is a convenient test gas for shock tube ionisation work in that the ionisation takes place extremely rapidly behind the shock. The main ion present, NO^+, has a low ionisation potential of 9.5 eV [(20) P.735], which considerably reduces the chance of impurity ions in the shock tube.

However, at elevated temperatures air is no longer a simple mixture, as can be seen in Table 2.

Table 2 Comparison of equilibrium composition by mole fraction of dry Air behind incident shock with the composition at room temperature. [From Hilsenrath & Klein (9)]. $M_s = 11$ $T = 3800^{\circ}K$ $p_o = 1$ Torr $\frac{\rho}{\rho_a} = 1.537 \times 10^{-2}$

Molecule	Mole fraction Room Temperature	Mole fraction behind shock
N_2	7.808×10^{-1}	6.528×10^{-1}
O_2	2.095×10^{-1}	2.169×10^{-2}
NO	0	3.140×10^{-2}
CO	0	2.764×10^{-4}
CO_2	3.3×10^{-4}	6.434×10^{-6}
NO_2	0	1.977×10^{-6}
N_2O	0	4.598×10^{-7}
N_2^+	0	2.845×10^{-12}
O_2^+	0	1.119×10^{-9}
O_2^-	0	9.425×10^{-18}
NO^+	0	2.684×10^{-6}
CO^+	0	1.183×10^{-13}
O^-	0	1.926×10^{-8}
N^+	0	1.289×10^{-13}
N^{++}	0	0
O^+	0	9.648×10^{-11}
O^{++}	0	0
A^+	0	4.430×10^{-14}
A^{++}	0	0
C^+	0	5.833×10^{-17}
C^{++}	0	0
Ne^+	0	3.123×10^{-24}
N	0	1.305×10^{-3}
O	0	2.845×10^{-1}
A	9.340×10^{-3}	8.004×10^{-3}
C	0	8.918×10^{-11}
Ne	3.000×10^{-5}	2.571×10^{-5}
Electrons	0	2.666×10^{-6}

It can be seen from Table 2 that the dominant change carriers are NO^+ and electrons. The next most common ions, O^- and O_2^+, have concentrations of 0.7% and 0.04% of that of NO^+.

In all the calculations used here, the shock tables of Lewis & Burgess (6) and the equilibrium Air tables of Hilsenrath & Klein (9) are used. These tables are computations based on experimentally observed properties of the constituents of Air, together with some theoretical values if the former are not available.

Bulk thermodynamic properties such as pressure, density, and temperature are dominated by well known gas properties and single dissociation reactions, and hence these tables can be expected to yield accurate values.

However, the equilibrium electron density, for the temperature range under consideration, is dominated by multi-stage reactions producing the NO^+ ion, such as:

$$N_2 \rightleftharpoons 2N$$

$$O_2 \rightleftharpoons 2O$$

$$N_2 + O_2 \rightleftharpoons 2NO$$

$$N + O \rightleftharpoons NO$$

$$N + O \rightleftharpoons NO^+ + e$$

$$NO \rightleftharpoons NO^+ + e$$

and any uncertainties in the equilibrium constants for these reactions is going to compound errors in the computed electron density.

The initial air temperature in the shock tube is taken to be 300 K°(practical variations being small) and the sound speed for Air at 300°K was taken from Ref.6 to be 347.326 m/s and used for computing the Mach number.

Figs. 6, 7 show the computed electron densities and electron

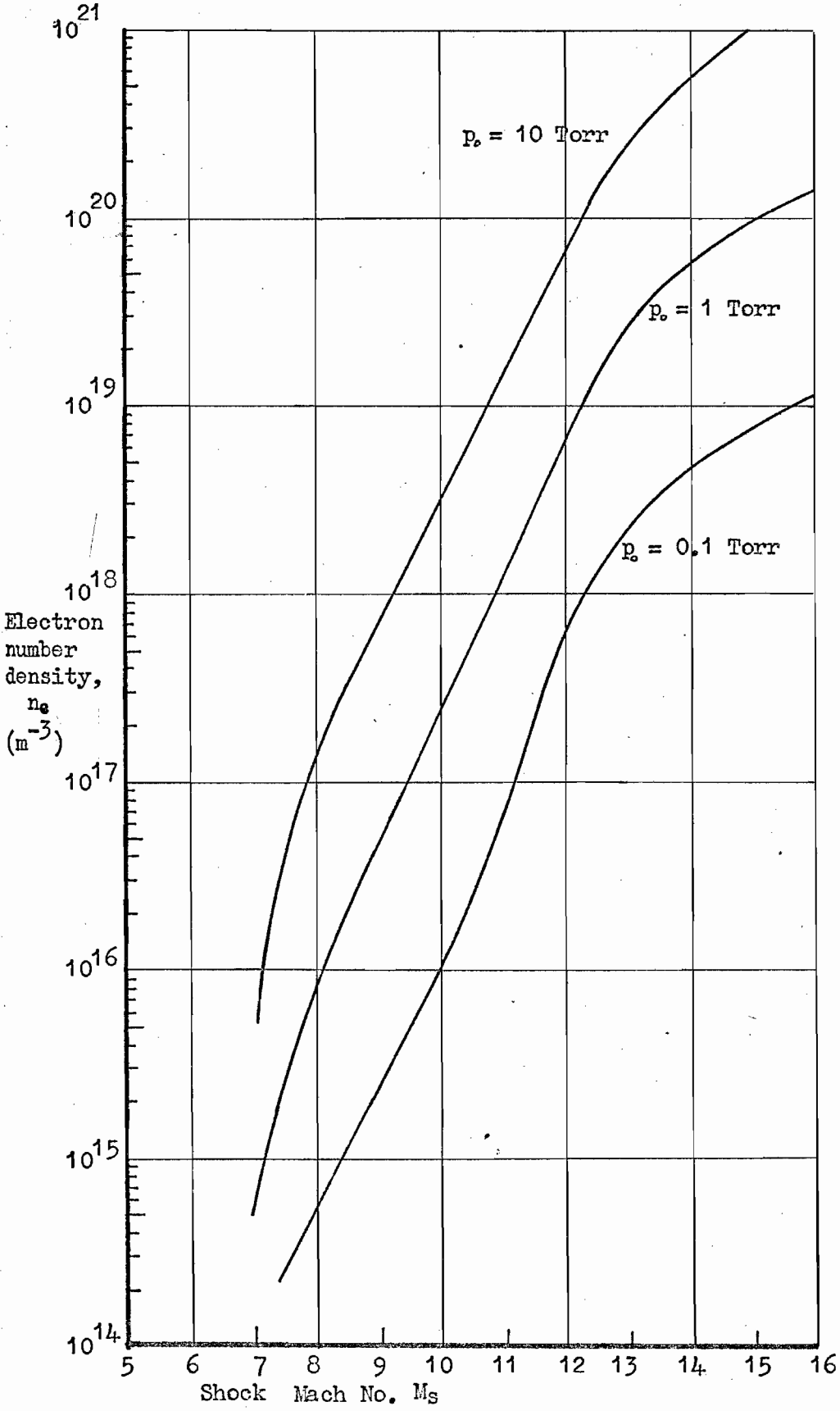


Fig.6 Equilibrium electron number density behind incident shock in dry Air for different initial pressures.

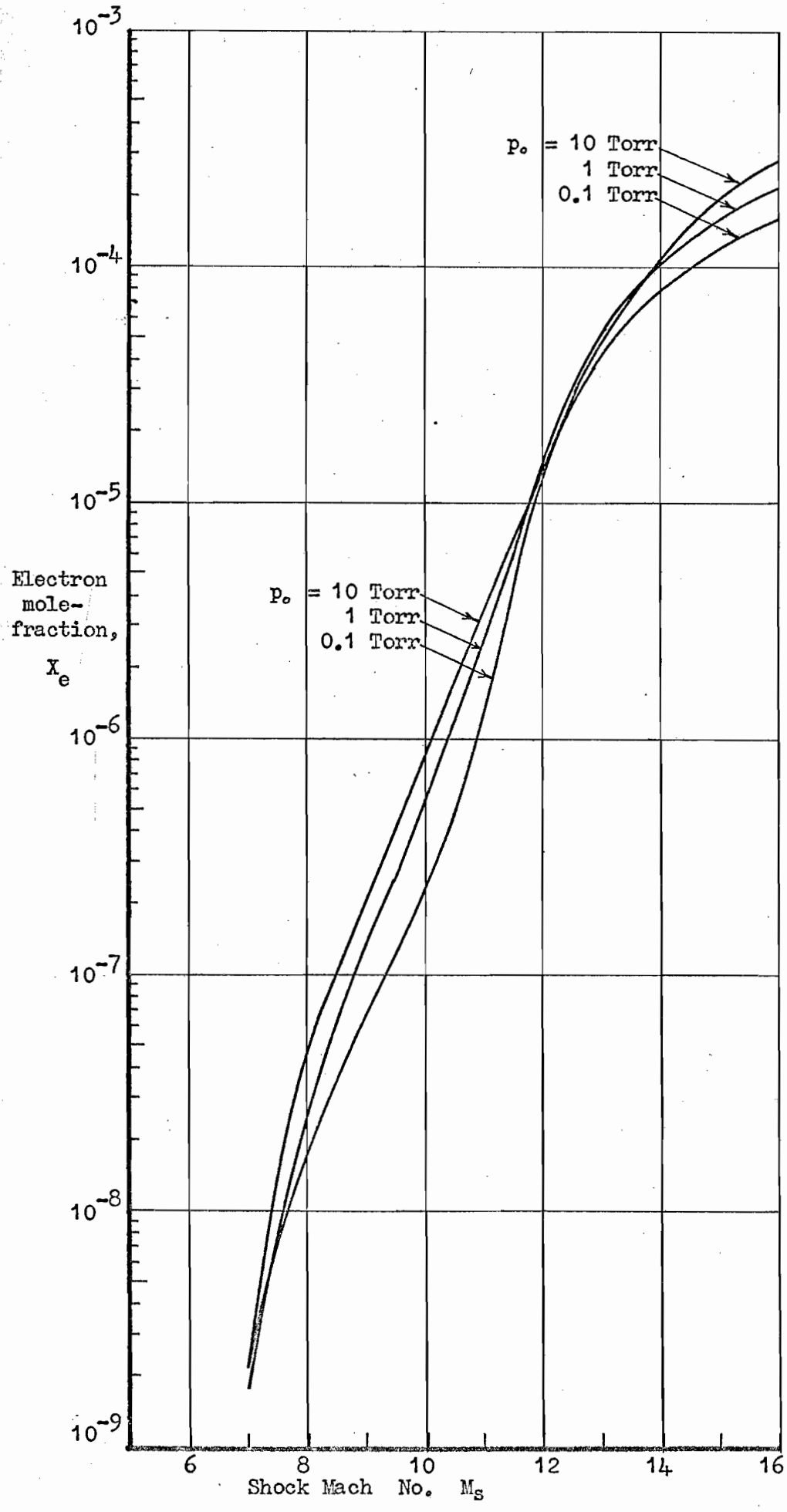


Fig.7 Electron mole-fraction behind incident shock in dry Air for different initial pressures.

mole fractions in Air for $M_s = 7 - 16$, and various initial pressures. These were obtained by using interpolation of the tables in (9) for values of temperature and density obtained from (6). For Mach numbers above 15 they are in accord with the lower end of the curves given by Laird & Heron (5).

Table 3 gives a summary of the most important parameters in Air behind a typical shock.

The molecule m. f. p. is based on that of N_2 in N_2 [(20) p.35] and that of the ions from the suggestion [(20) p.439] that the elastic sphere cross sections for ion-neutral collisions is about twice that for neutral-neutral collisions. The electron m.f.p. is derived from the electron collision frequency and the mean thermal velocity:-

$$\lambda_e = \frac{\bar{c}}{\nu} \qquad (2.1)$$

$$\bar{c} = \sqrt{\frac{8kT_e}{\pi m_e}} \qquad (2.2)$$

In these experiments ordinary room Air was used as the test gas, as earlier work [e.g. Lin, Neale & Fyfe (10)] has shown that no noticeable difference is observed when using pure artificially-mixed Air.

To dry the Air, and to filter out any suspended solids, an on-line silica-gel Air dryer was designed and constructed (Fig. 8). The silica-gel chamber was built inside an electrically-heated oil bath, so that the silica-gel could be heated in situ to 150°C for up to 24 hours while being continuously vacuum pumped, and then used to dry the shock tube Air without being allowed to come up to atmospheric pressure. In this way the silica-gel was maintained in a highly absorbent state, and the test gas was efficiently dried by being passed through the dryer immediately before admission to the test section.

Table 3

Typical parameters for region behind incident shock in Air.

PARAMETER	p_o = 1 Torr	p_o = 10 Torr
Mach No. Ms	11	11
Microwave frequency $\frac{\omega}{2\pi}$	9 GHz	9 GHz
" " ω	5.65×10^{10}/s	5.65×10^{10}/s
Electron density n_e	$1.3 \times 10^{18}/m^3$	$1.5 \times 10^{19}/m^3$
Collision frequency ν	2.5×10^{10}/s	2.2×10^{11}/s
Plasma frequency $\omega_p = \sqrt{\frac{n_e e^2}{m_e \varepsilon_o}}$	6.3×10^{10}/s	2.2×10^{11}/s
$\frac{\omega_p}{2\pi}$	10 GHz	35 GHz
Normalised plasma frequency $\frac{\omega_p}{\omega}$	1.1	3.9
Normalised collision frequency $\frac{\nu}{\omega}$	0.44	3.9
Ionisation $X_e = n_e/n_o$	2.7×10^{-6}	3.5×10^{-6}
Temperature T	3800 °K	4100 °K
Temperature in eV	0.33 eV	0.35 eV
Pressure (atm.)	0.24 Atm.	2.0Atm.
Pressure (N/m^2)	2.4×10^4 N/m^2	2×10^5 N/m^2
Density (Total) (NTP atmosphere = 1.3 kg/m^3)	0.02 kg/m^3	0.18 kg/m^3
Debye length $\lambda_d = \sqrt{\frac{\varepsilon_o k T_e}{n_e e^2}}$	3.7×10^{-6}	1.2×10^{-6}
Approximate neutral m.f.p.	4×10^{-6} m	5×10^{-7} m
Approximate ion m.f.p.	2×10^{-6} m	3×10^{-7} m
Approximate electron m.f.p.	1.5×10^{-5} m	2×10^{-6} m

[The mean free paths hereare order of magnitude only and are based on simple collision models.]

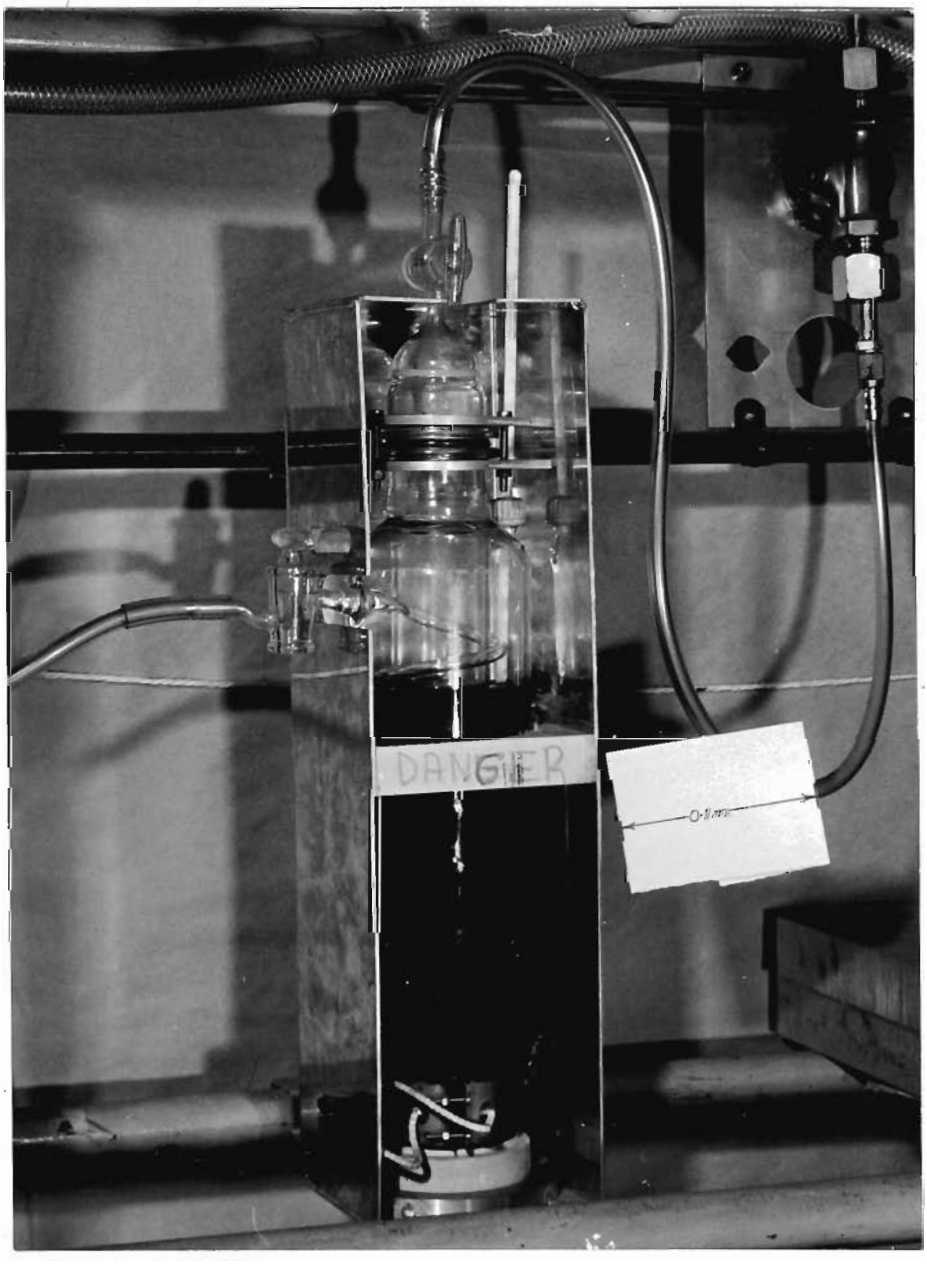


Fig.8 On-line Silica-gel Air-dryer.

The effect of drying the Air is described in Chapter 3, and it was found that pumping and outgassing times on the shock tube were reduced.

An attempt to compare dried and non-dried Air, using a mass-spectrometer, was frustrated by the large "background" contamination, especially of water, in the instrument used.

3. THE FLAT PLATE ELECTROSTATIC PROBE.

3.1 The Electrostatic Probe as a Preliminary Diagnostic.

As was made clear in the introduction, the work to be described is primarily concerned with the use of microwave diagnostics. These, however, have poor spatial resolution, and so preliminary electrostatic probe experiments were made in order to further define the plasma generated by the shock tube used.

It must be emphasised here, that, as the probe used was measuring the saturated ion current in a collision-dominated régime, it was not expected to give an accurate absolute measurement of ion density in the manner of the collisionless Langmuir probe.

The electrostatic probe is useful, however, in studying the uniformity of the flow and the length of plasma behind the shock, as well as indicating the ion density bythe use of a grossly simplified theory.

The "collisionless" Langmuir single (21, 22) and double (23, 24) probes are effective diagnostic devices in the low neutral-density régime, where the mean free paths of the charged particles is greater than the Debye length, λ_d, which is given (20) by :-

$$\lambda_d = \sqrt{\frac{\varepsilon_0 k T_e}{n_e e^2}} \qquad (3.1)$$

where k is Boltzmann's constant,
T_e is electron temperature,
n_e is electron number density,
e is electronic charge.

If this does not hold, then charged particles moving towards the probe will experience collisions in the "sheath", approximately λ_d thick, surrounding the probe, and will modify the current collected

by the probe.

In the limit, as neutral density increases, the movement of ions becomes collision dominated, and the full mobility and diffusion equations must be solved. Elegant solutions of these equations in the spherically symmetric, non-flowing case have been obtained by, among others, Su & Lam (25), Cohen (26) and Su & Sonin (27), and Cozens & von Engel (28) have analysed the flat-plate double-probe.

Unfortunately for the experimentalist, any attempt to put these treatments to any practical use is dogged by other phenomena affecting the probe currents. Collisions in the sheath of an ion collecting probe may result in recombination, and random walk processes (28) can enable some electrons to reach the probe surface in spite of a negative bias voltage.

The higher neutral gas density will result in greater heat transfer to a cold probe surface from the hot plasma. If the probe is allowed to approach the plasma temperature (and in a collision dominated plasma the electron, ion and neutral gas temperatures are equal), thermionic emission, secondary emission and other surface effects will change the nett probe current. If the probe is cooled, then there will be temperature gradients near the probe, causing changes in the mobility of ions in this region, and changing the temperature dependent equilibrium ionisation near the probe.

When the electrostatic probe is used in a weakly ionised plasma flowing at supersonic velocities, the recovery of ion and electron temperature and density in the freestream flow from the measured electrostatic probe current is further complicated by the presence of shock waves and boundary layers near the probe.

Consider the probe geometries practical for use in a flowing collision dominated (high pressure) plasma :-

(a). The stagnation point electrostatic probe (see Fig. 9).

Brundin (29) has analysed this probe, in which ions pass through a standing shock before reaching the probe. The abrupt increase in neutral density and temperature through the standing shock, together with the temperature gradient to the cold probe, make analysis in other than the "frozen ionisation " case extremely difficult. Also, in Air, (10, 11), the rapid ionisation through the standing shock would result in an anomalously high electron and ion density in the region between the shock and the probe.

(b). The thin transverse wire electrostatic probe.

As used by Radcliffe & Hobson (30) these consist of fine wires stretched across the shock tube. The use of low density collisionless probe theory is justified by the use of fine 0.24 mm diameter probes and by comparison of the results obtained with those from microwave diagnostics.

(c). Flat plate electrostatic probes.

These may be wall mounted (Fig. 10) (31), or inset into a sharp edge flat plate parallel to the flow (Fig.11). The wall mounted probe has the disadvantage of having a growing boundary layer, whereas the flat plate probe has a steady attached boundary layer for the duration of the plasma flow. Both these probes have the advantage of not subjecting the ions to strongshocks on the way to the probe. They are, of course, still subject to errors arising from the temperature and density gradients in the boundary layer, and collisions in the sheath.

Bienkowski (32) has analysed the electrostatic sheath for

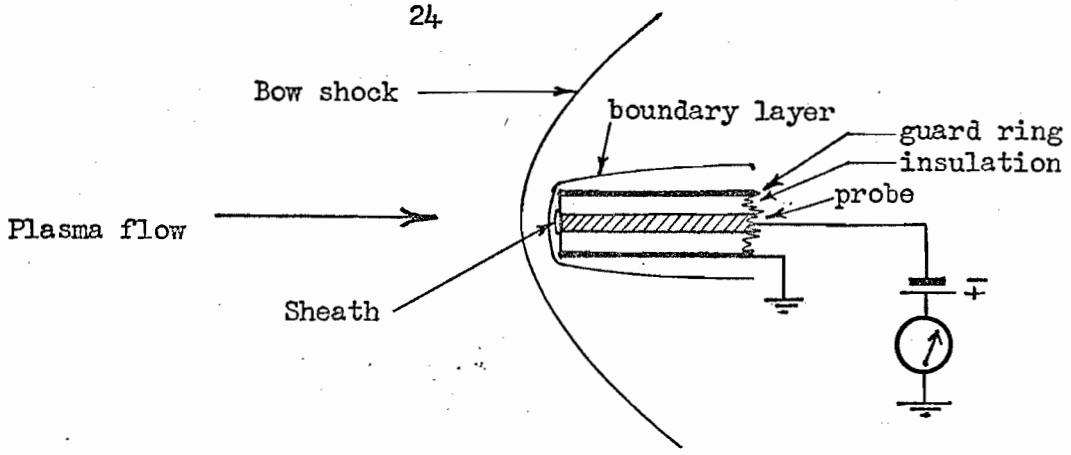


Fig.9 Stagnation point electrostatic probe.

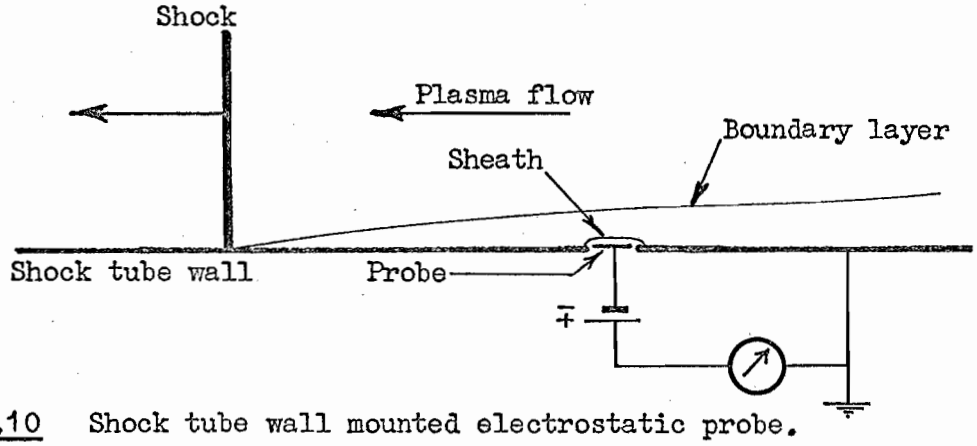


Fig.10 Shock tube wall mounted electrostatic probe.

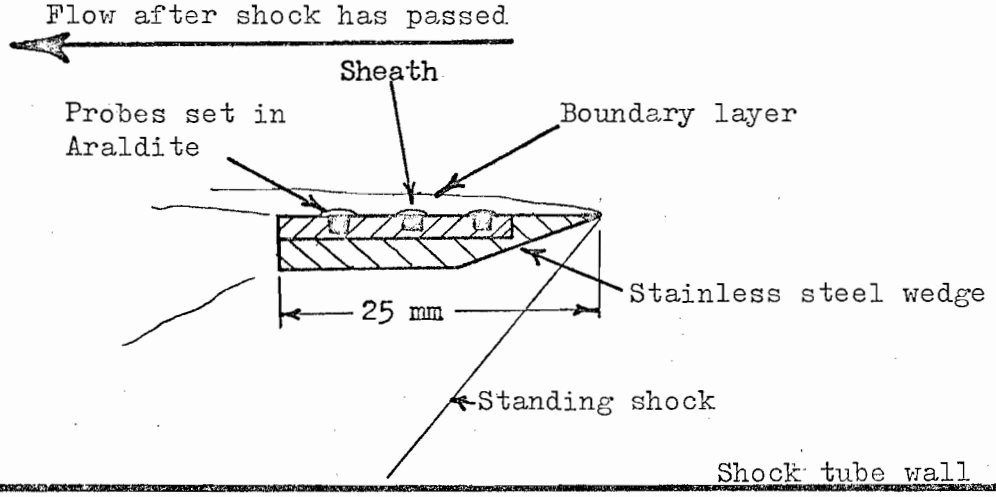


Fig.11 Flat-plate mounted electrostatic probe (as used).

this probe for various ratios of mean free path to Debye length, and Bredfeldt, Scharfman, Guthart & Morita (33) have conducted experiments in shock tubes with low initial pressure (p_o = 0.1 Torr) in Air, in which they compare their results with a theory assuming zero order boundary layer analysis and a collision-free sheath. Their experiments indicate that , when using a negatively biased probe working in the saturated ion current mode and for low ion densities, ($n_i < 10^{18}$ /m^3), the n_i at the sheath edge is between 20% and 80% of the free stream n_i.

Laird's analysis [(1) p.55] of the diffusion of ions through the boundary layer to the probe assumes that the sheath thickness $\lambda_d << \delta$, where δ is the velocity boundary-layer thickness (34, 35, 36). He also assumes the ambipolar Schmidt Number, S, constant, where

$$S = \frac{\mu}{\rho D_a} , \qquad (3.2)$$

$$D_a = \frac{2kT}{e} K_i , \qquad (3.3)$$

and μ is the coefficient of viscosity,
D_a is the coefficient of ambipolar diffusion,
and K_i is the ionic mobility.

From this he derives, using a Blasius laminar boundary-layer profile (34), an equation relating the freestream ion density n_i and the probe saturated ion current j_+ :

$$n_{i_e} = 2.12 \left(\frac{2\rho_e x}{u_e \mu_e}\right)^{\frac{1}{2}} \frac{j_+}{e} S_e^{\frac{2}{3}} \qquad (3.4)$$

In equation (3.4) the subscript e refers to conditions at the freestream edge of the boundary layer, and x is the distance from the flat plate leading edge to the flush probe.

Laird's analysis of his results (for p_o = 2 Torr) using equation (3.4) gave ion densities differing by a factor of 10 from the equilibrium electron densities (Fig. 6), assuming quasi-neutrality ($n_i = n_e$).

Unfortunately, the low ionisation potentials (V_i) obtained from $j_+ : 1/T$ plots of his readings led him to believe that the dominant ion was due to Sodium contamination (V_i = 5.1 eV for Na^+) and consequently he used the D_a for Na^+ in N_2 in equation (3.4).

It is not intended to examine here fully the boundary layer equations used by Laird, for the author's main interests lie in the use of microwaves, but in section 3.3 it will be shown that Na^+ contamination is unlikely, and that the underlying assumptions of equation (3.4), together with the difficulty of evaluating S_e for NO^+ ions in hot air make the use of equation (3.4) a poor practical diagnostic method.

3.2 Construction and Use of Flat Plate Electrostatic Probe.

In order to attempt some comparison with Laird's (1) results, an electrostatic probe having the same dimensions was fabricated. As Laird's probe, made of brass and supported only at one end, had shown permanent distortion under heavy shock loads, stainless steel (EN58B) was now used for both the probe body and the wire probes. The far end of the probe was supported by a slot, machined in a ring, inserted in the 63 mm long, probe mounting cylinder, which could be inserted into the shock tube with the inner walls aligned. The probe was removed from the side of the probe mount between runs to check leading edge damage.

Fig.11 shows a full-scale cross-section of the positioning of the probe in the shock tube. As shown in Fig. 12, the probes are made from stainless steel wire, cast in "Araldite" casting-resin into

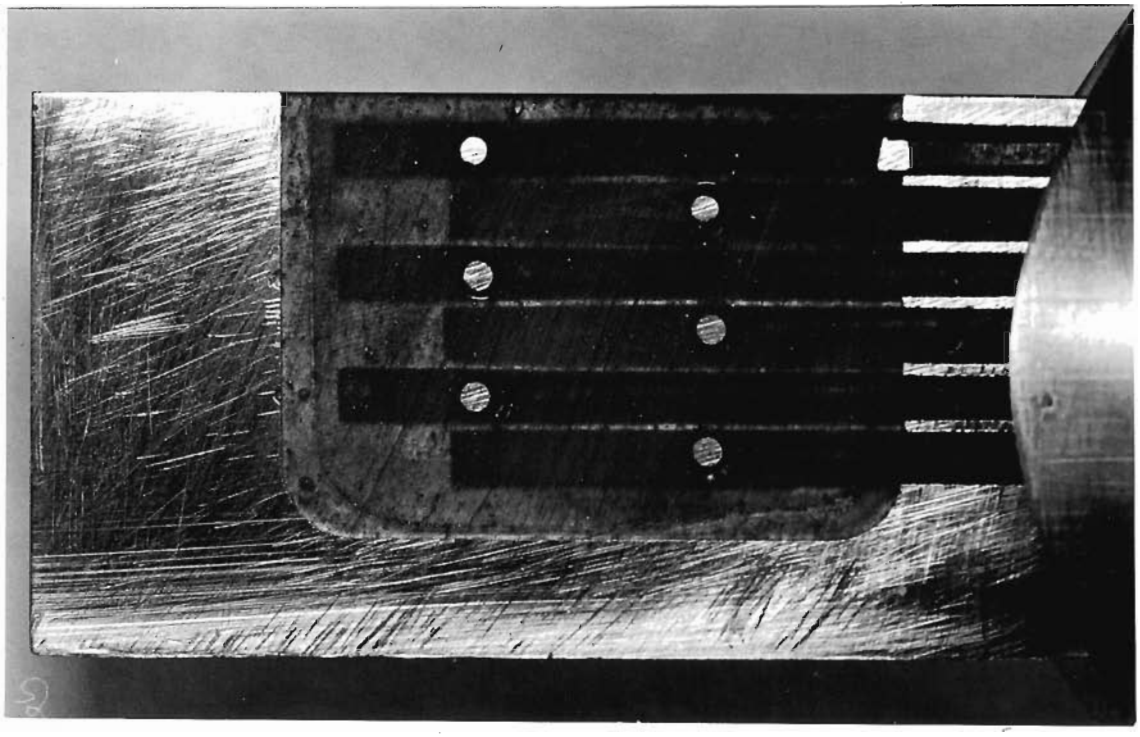


Fig.12 Flat-plate electrostatic probe: top surface showing 6 probes. Leading edge lowermost, streamwise dimension = 25 mm.

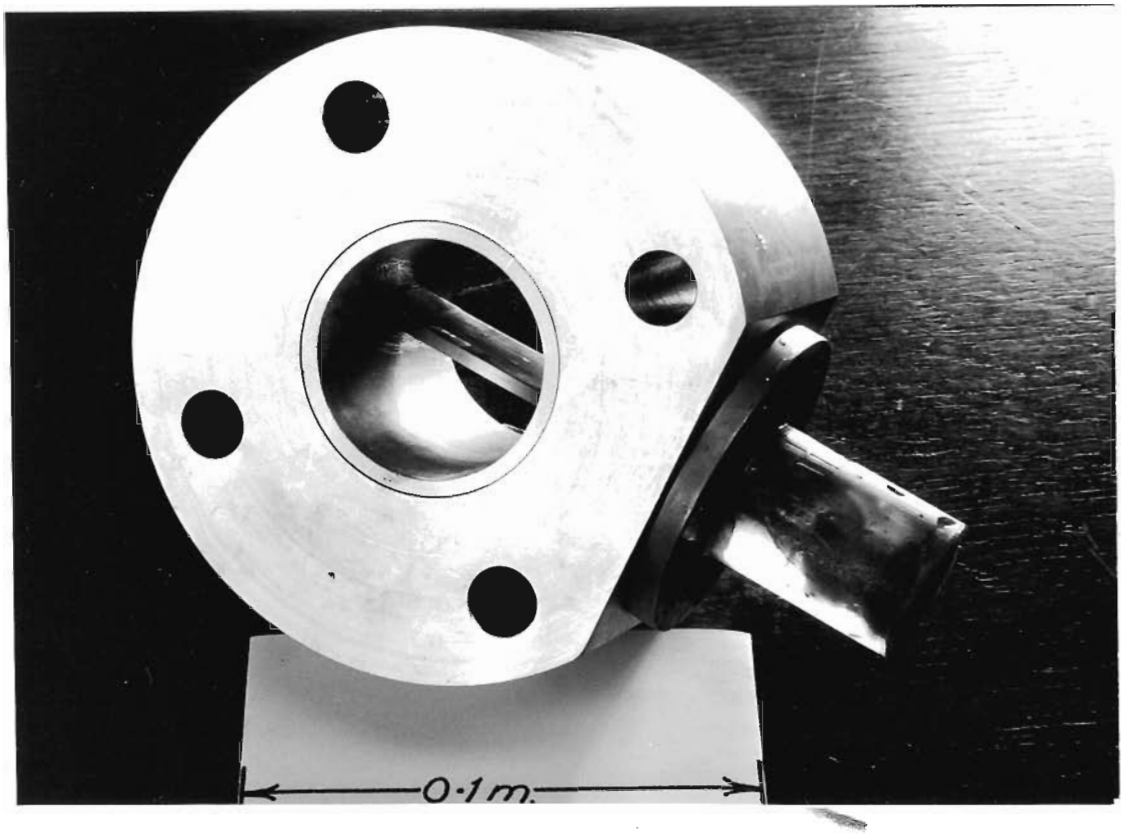


Fig.13 Flat-plate electrostatic probe in mount. Leading edge towards camera.

the probe body. The top flat surface was then ground flush, and the leading edge (included angle 26°) sharpened as much as possible, (no measurements of the sharpness were made) by stoning the lower, inclined face. The six probes, numbered from the leading edge, were placed in two lines (Probe Numbers 1,3,5 and 2,4,6) symmetrical about the shock tube centreline, and 10.2 mm apart. Initially an earthed conducting guard plate was placed around the probes, but was discarded when it became apparent that it had little effect on the saturated ion current.

The leading edge to probe distances, and the longitudinal and transverse probe diameters were measured on an optical measuring machine (S.I.P. Universal Measuring Machine MU 214 B). The probes were then microphotographed, and their images projected to fit the measured diameters scaled by a factor of 50:1. The image of the probe perimeter was then traced out and measured with a planimeter.

Table 4 : Probe Dimensions.

Probe number	Centreline to leading edge. mm.	Longitudinal diameter mm.	Transverse diameter mm.	Area m^2
1	9.314 $\pm$ 0.002	1.218 $\pm$ 0.002	1.217 $\pm$ 0.002	$1.16 \pm 0.01 \times 10^{-6}$
2	11.746	1.253	1.250	1.23×10^{-6}
3	14.854	1.223	1.218	1.17×10^{-6}
4	17.231	1.283	1.268	1.26×10^{-6}
5	20.332	1.060	1.110	0.97×10^{-6}
6	22.856	1.160	1.149	1.04×10^{-6}

Fig. 14 shows the simple biassing circuit used to maintain the negative voltage required for positive ion saturation currents.

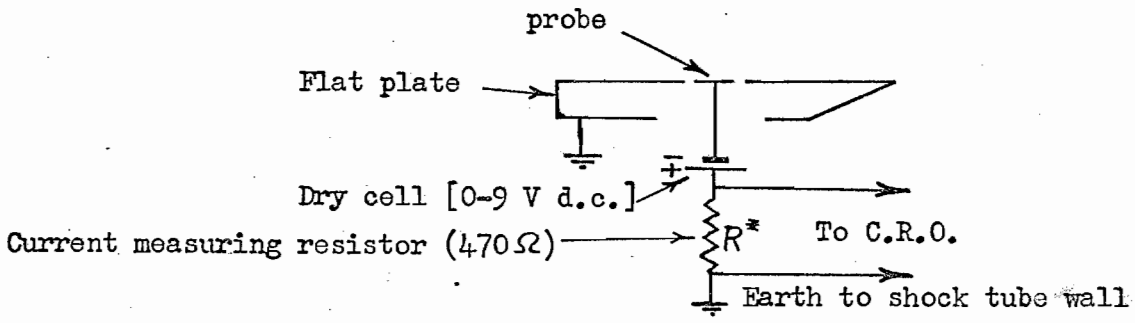


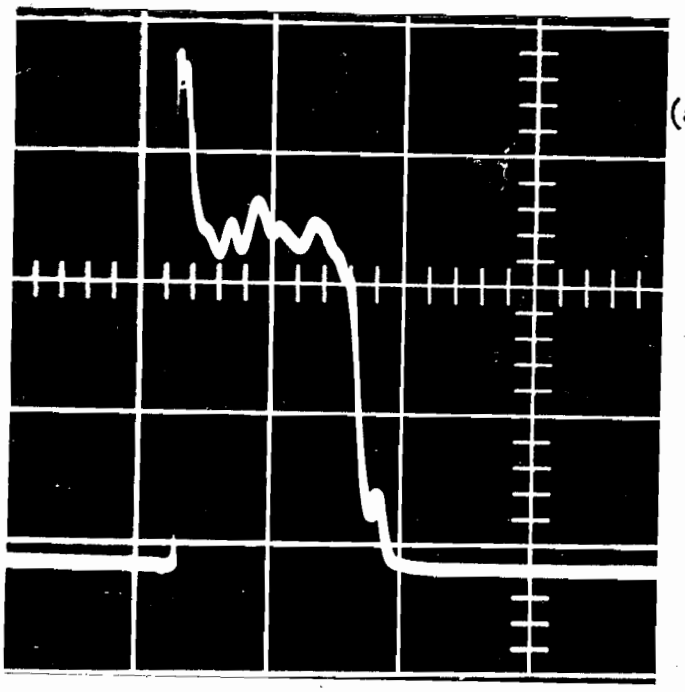
Fig.14 Electrostatic probe biassing circuit.

Three Tektronix Type 551 dual-beam oscilloscopes (with Polaroid cameras), triggered via a time delay from the last shock-tube platinum thin-film gauge (p.10), were used to record the probe currents. The circuit was satisfactory in terms of response time and sensitivity. The resistor R^* was measured to an accuracy of 0.1% .

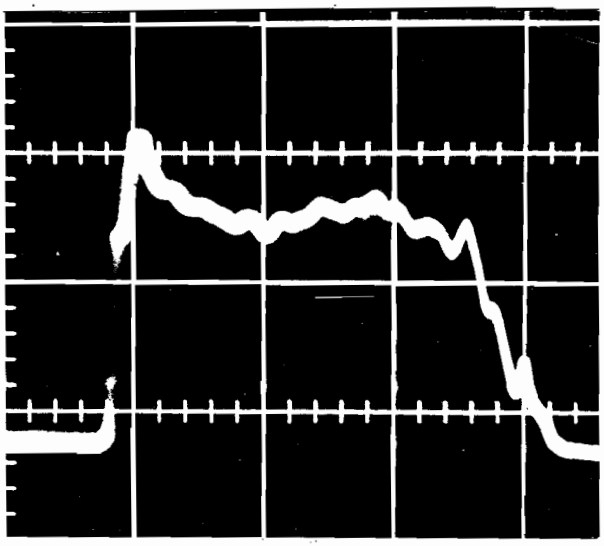
Typical traces for p_o = 1, 3 & 10 Torr (probe 1) are shown in Fig. 15. The traces for probes 2 & 3 were essentially similar in shape, but reduced in height. The initial, zero - current, line before the run provides a reference zero and thus there are no slow oscilloscope zero - drift problems.

It can be seen in Fig. 15 that each trace consists of a sharp peak, caused by the initial ionisation overshoot in Air (10, 11) and the growth of the boundary layer, followed by a plateau and terminated by a more gentle fall after the arrival of the contact - surface as cold hydrogen is convected into the boundary layer.

Assuming only a monotonic variation of ion density with probe current, these traces would seem to justify the crucial assumption of a high ionisation rate behind the shock for Air followed by a period of near equilibrium ionisation.



(a). Run 119. Probe 1.
p_o = 1 Torr Air
20μs/division
M_s = 12.8
j_+ = 248 A/m^2



(b). Run 102. Probe 1.
20 μs/division
p_o = 3 Torr of Air
M_s = 10.5
j_+ = 16.8 A/m^2



(c). Run 35. Probes 1 & 2.
20 μs/division
p_o = 10 Torr of Air
M_s = 10.3
j_+ = 31.0 A/m^2

Fig.15 Typical electrostatic probe traces.

Unfortunately, a flow disturbance generated by an unevenness in front of the probes caused irregular traces (see Fig. 15(c),probe 2) on the line of probes 2,3,5, and this irregularity was repeated on each of the probe traces in turn on a given run. Consequently it was decided to discard readings from these probes.

The estimated accuracy of the probe current readings, taking into account the fluctuations of any one trace and the calibration of the oscilloscopes used, is $\pm$ 10%.

3.3 Shock Tube Test Time.

The electrostatic probe traces show clearly the arrival of the shock (the onset of ion current) and the arrival of the contact surface (the final drop from the plateau current), and the time between these may be used to measure the test time, and hence predict the length of plasma available for microwave reflection experiments.

Mirels has analysed the effects of shock tube wall boundary layer on the test time by considering the "leakage" of shocked gas past the contact surface via the boundary layer, both in the low pressure case , where the boundary layer is laminar (13,14), and in the high pressure turbulent boundary layer case(15). In each case he published convenient graphs enabling the prediction of test times.

Fig. 16 shows Mirels' predicted laminar and turbulent boundary layer test-times for the shock tube used here, together with the ideal (no boundary layer) test time (14) predicted from shock tables (6) for M_s = 8 - 14 and p_o = 1,3,10 Torr.

Mirels (15) gives as a criterion that for $dp_o \leqslant 0.5$ the

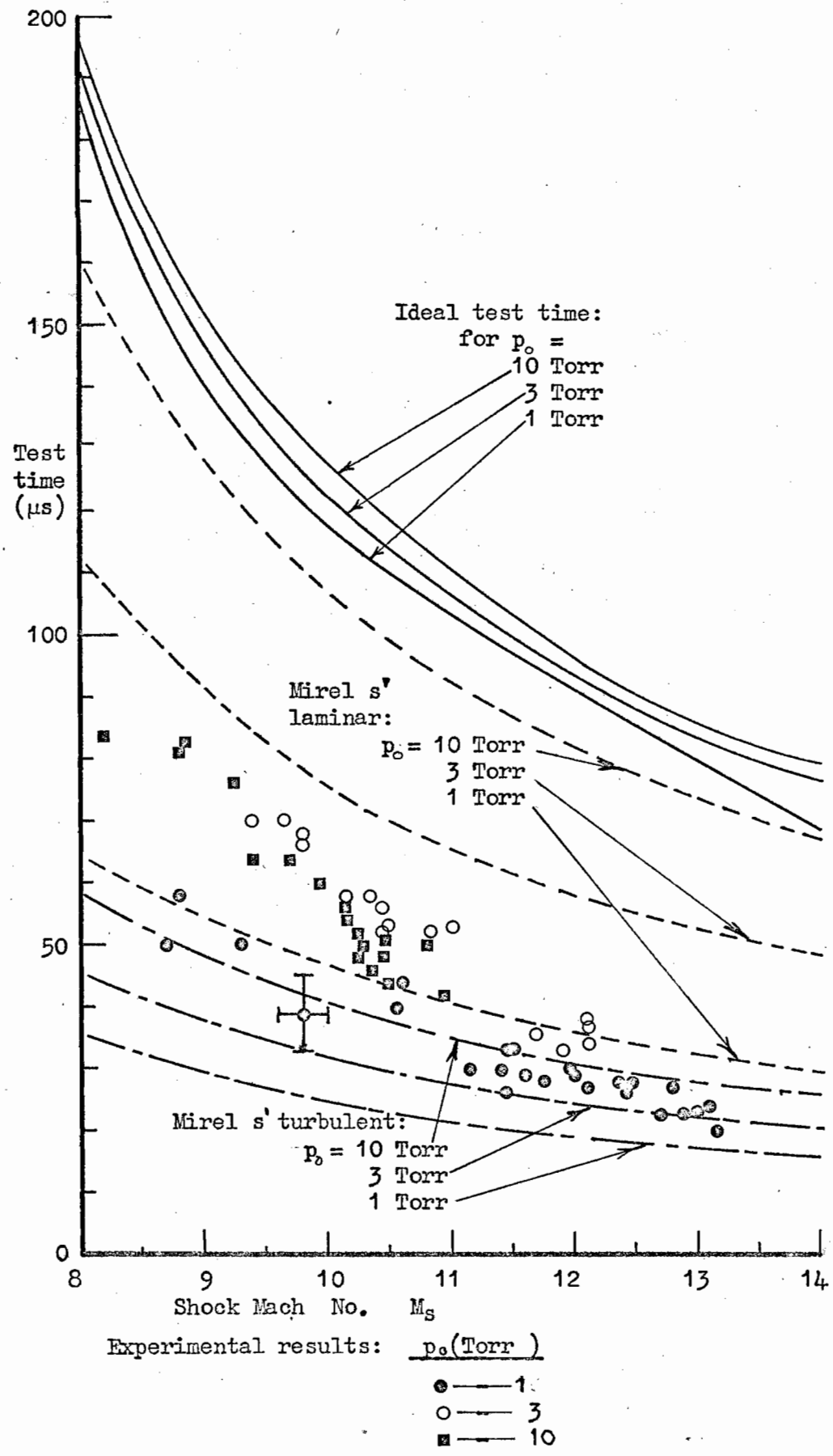


Fig.16 Comparison of experimental shock tube test times with those predicted by Mirels (14,15). Test gas: dry Air.

boundary layer is laminar, and for $d p_o \geq 5$ it is turbulent (d is the shock tube diameter in inches, and p_o is in cm of Hg). Here the appropriate values are $d p_o$ = 0.18, 0.54 and 1.8 for p_o = 1,3 and 10 Torr respectively. In spite of his criteria being for Argon, and these results being for Air, the experimental results plotted on Fig. 16 show that the p_o = 1 Torr points lie close to Mirels' laminar theory (Air) indicating that the boundary layer is laminar, and for p_o = 3 and 10 Torr the experimental test times lie between the laminar and turbulent theoretical curves, indicating a transitional boundary layer.

Thus we see that in the low pressure case Mirels' theory for the laminar boundary case is in reasonable agreement with the experimental test times, and for higher pressures his turbulent theory underestimates the transitional boundary layer test times by a factor of about 2.

From Fig. 16, the minimum test length for this series of experiments corresponds to a test time, τ, of 25 μs at Ms = 13;

i.e. minimum test length $l = a_o M_s \tau$ (3.5)

$\doteqdot$ 0.12 m

3.4 Ion Number Density.

We now wish toexamine the applicability of Laird's saturation ion current equation,

$$n_{i_e} = .2{\cdot}12 \left(\frac{2\rho_e x}{u_e \mu_e}\right)^{\frac{1}{2}} \frac{j_+}{e} S_e^{\frac{3}{2}} \qquad (3.4)$$

(see p.25), to the interpretation of experimental results described here.

Firstly the question of whether the ion current was in fact

saturated was investigated by carrying out a number of experiments at one M_s and with different bias battery voltages.

As can be seen from Fig. 17, there is not a final saturation current, but there is a plateau region at about -6 volts bias, relative to the shock tube walls. As the electron temperature is low at 0.33 eV, this -6V, when added to the +ve plasma-wall potential, is certainly sufficient to prevent electrons reaching the probe surface. For bias voltages below -9V, effects such as sheath growth and field penetration into the plasma again increase the ion current.

Thus -6V is seen to be a suitable probe bias-voltage for the measurement of saturated ion current.

From equation (3.4) for a given run

$$j_+ \propto \frac{1}{\sqrt{x}} \qquad (3.6)$$

where x is the distance from the leading edge of the flat plate. In Fig. 18 a plot of the currents for probes 1,3,5 over a series of 6 runs at the same M_s show that this relationship is verified to the accuracy of the experiments. A plot similar to Fig. 18 was obtained at p_o = 10 Torr.

Unfortunately, equation (3.4), as well as being derived on the assumption of a constant Schmidt Number, requires the evaluation of the viscosity, , and either the ambipolar diffusion coefficient, D , or the mobility, K_+, of NO^+ ions in the hot air at the boundary layer edge.

The viscosity of high temperature air can be obtained from Hansen (7), but the mobility of NO^+ in air in the temperature range 3,000 - 4,000°K is not well known. Sinnot, Golden and Varney (37) give NO^+ in air mobilities at pressures of 0.2 Torr and temperatures of 300°K, and Young et al.(38) have measured NO^+ in N_2

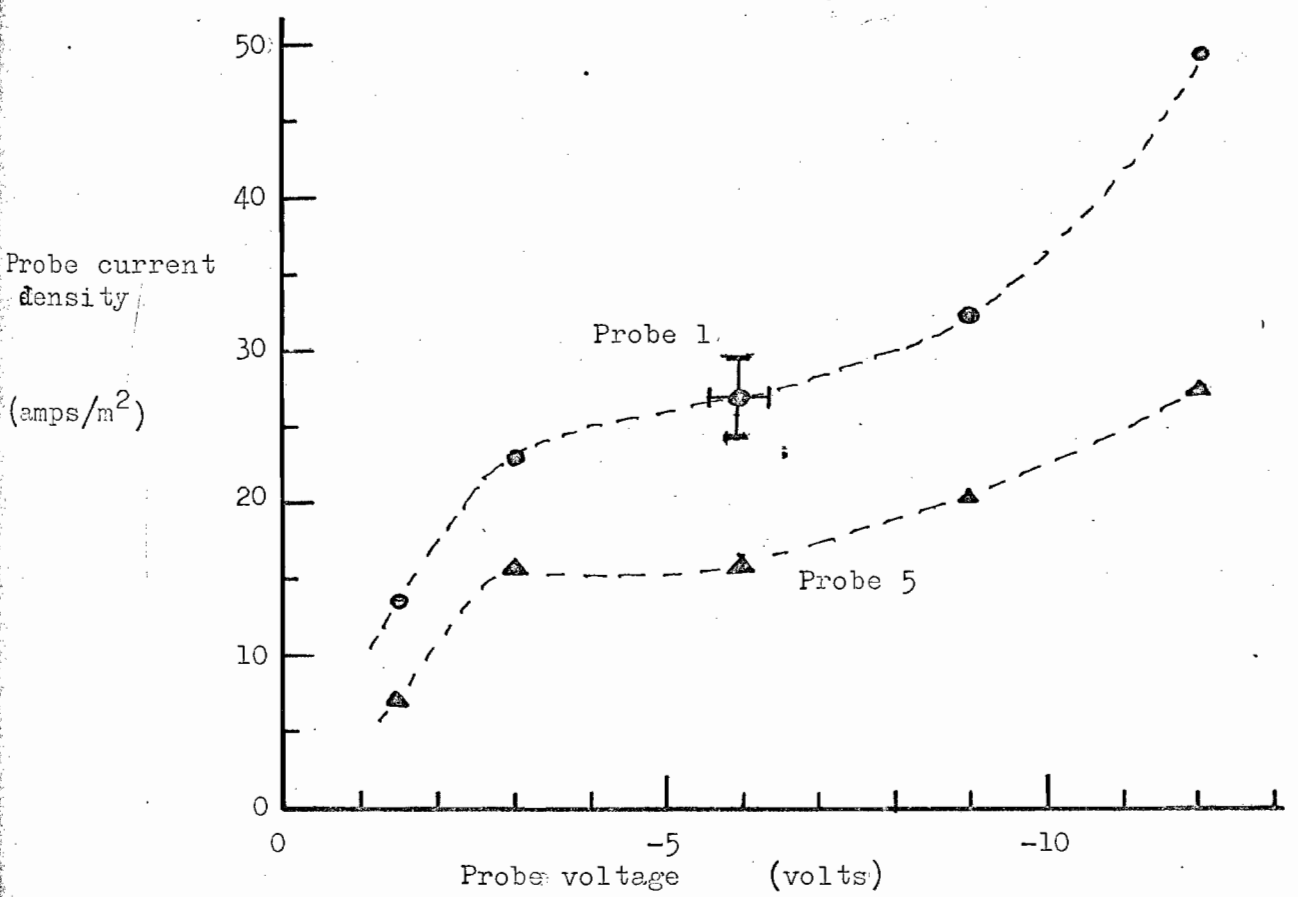


Fig. 17 Electrostatic probe current variation with bias voltage at constant n_e.

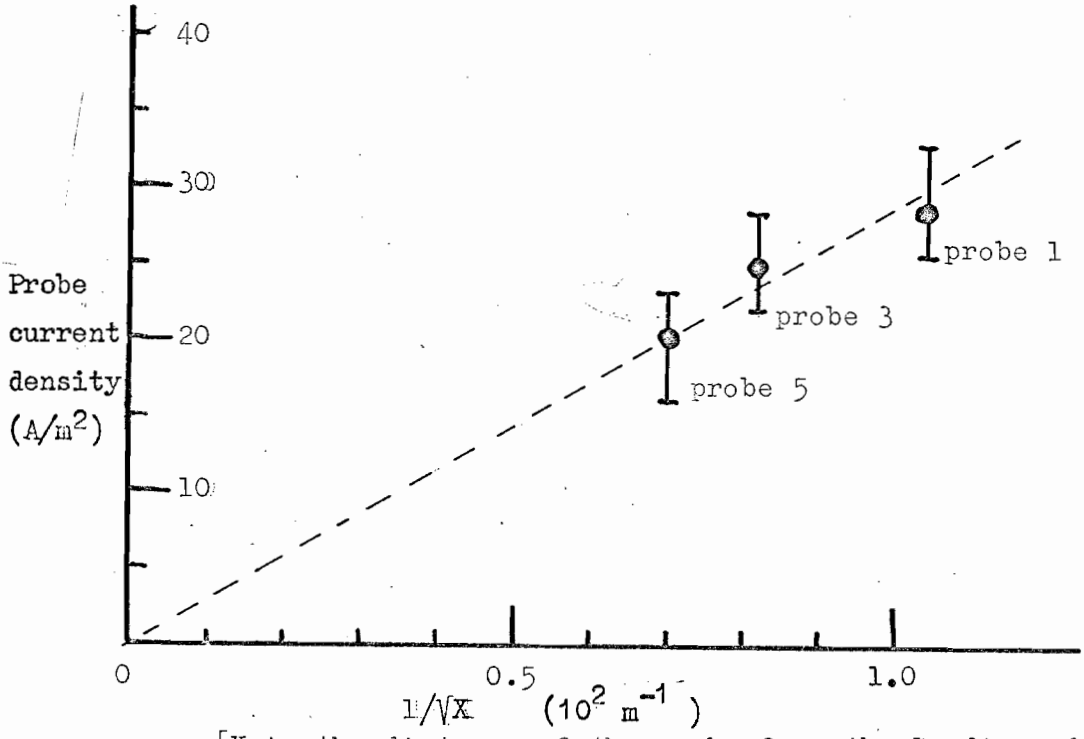
Bias voltage =-1.5 to -12

Test gas: dry Air

p_o = 2 Torr

M_s = 11.0± 0.2

T = 3790°K



[X is the distance of the probe from the leading edge.]

p_o = 2 torr probe bias voltage = −6 volts
M_s = 11 T_2 = 3795°K **Test gas: dry Air**
Readings are the average of 6 runs.

Fig.18

Plot of probe current density v. 1/√(distance from leading edge) .

under similar low temperature conditions. There is a temptation to use simple hard-sphere collision models to extrapolate these to the 4,000°K required, but an examination of the work of Dalgarno (39,40) will show that such simple extrapolations over a factor of 10 in temperature would be most unlikely to yield valid estimates.

Thus, practical use of equation (3.4) is severely hampered by the lack of definitive values of S_e.

Laird, in (1), used the mobility of Na^+ in N_2 in Equation(3.4), and obtained results which disagreed to a factor of 10 with the equilibrium ion density (assuming quasi - neutrality, so that $n_i = n_e$).

The relative magnitudes of the probe diameter, boundary layer thickness (from Mirels), Debye shielding distance and free-stream ion mean free path for p_o = 1 & 10 Torr with varying M_s are plotted in Fig.19 , for probe 1 (see p.17 for m.f.p.). As probe 1 is near the leading edge of the plate, the boundary layer over it is still laminar at p_o = 10 Torr.

Note that the 99% velocity boundary layer thickness δ_u is less than the probe diameter, and that

$$\left.\begin{aligned} \lambda_d &<< \delta_u \\ \lambda_i &<< \delta_u \end{aligned}\right\} \qquad (3.7)$$

where λ_d = Debye length,

λ_i = free - stream NO^+ m.f.p.

It can be seen from Fig.19 that there are many collisions in the boundary layer. As the neutral m.f.p. $\sim 2\lambda_i$, the ions in the boundary layer will be at near equilibrium with the local boundary layer flow. Also since the probe and flat plate remain at near 300 °K during the 30 μs running time, then there are extreme temperature gradients, of the order of 10^7 °K/m through the boundary layer,

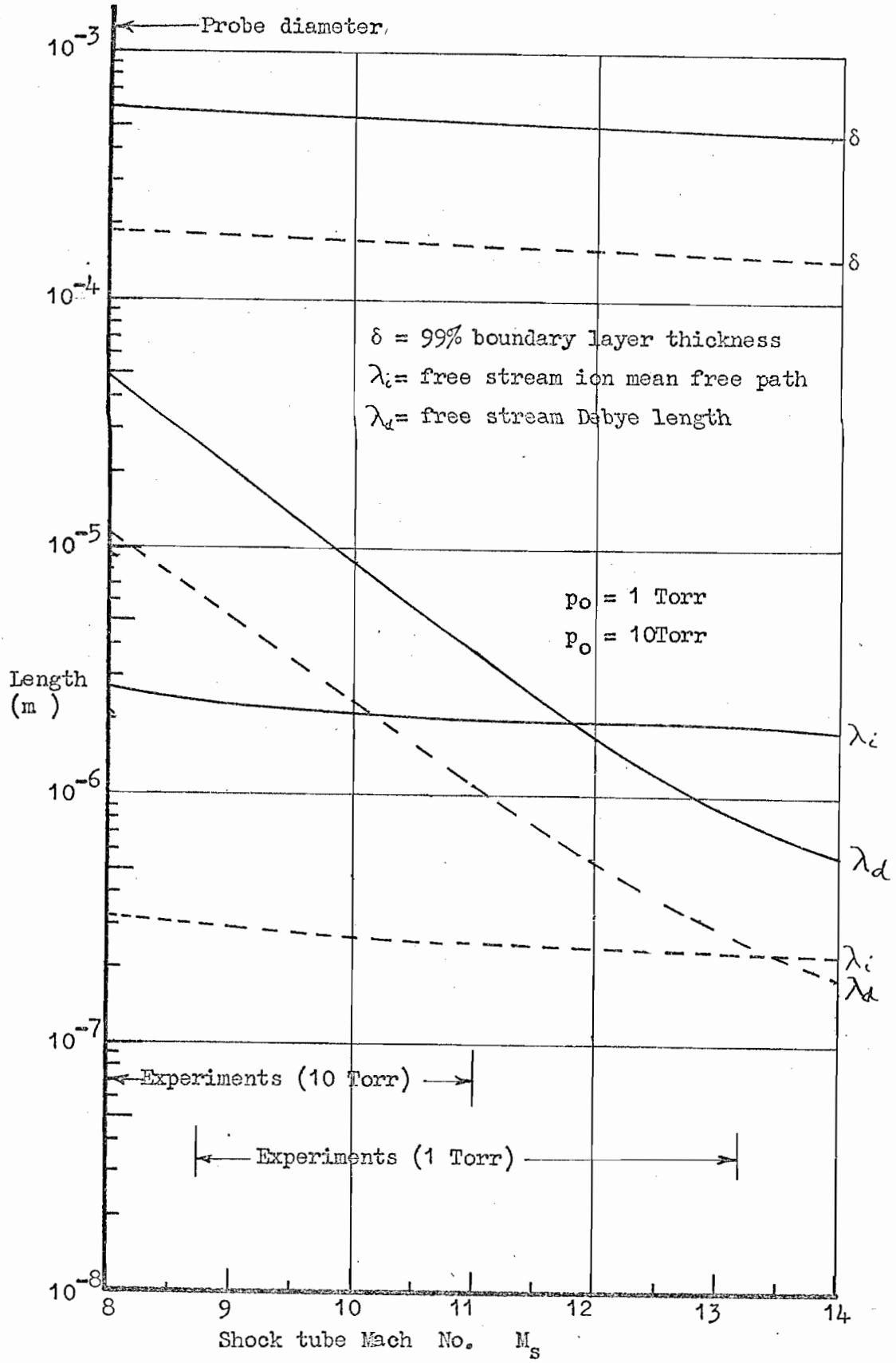


Fig.19 Comparison between boundary layer thickness, ion mean free path, and Debye length in the free stream behind the incident shock in Air.

implying high density gradients also, since pressure is constant across the boundary layer. Equations (3.2) & (3.3) on p.25 show that, as the viscosity μ and ambipolar diffusion coefficient D_a are highly dependent on T, it is unlikely that the constant S assumption is valid in the derivation of Equation (3.4).

At first glance Fig. 19 might seem to indicate that there are relatively few collisions in the sheath as, except for low M_s, $\lambda_i \sim \lambda_d$. However, since the neutral flow temperature at the sheath edge is very close to the probe temperature (300 ^oK), the gas density will be some ten times greater than in the free-stream, and hence the ion m.f.p. will be at least a factor of 10 times smaller than the λ_i shown. Then it becomes apparent that, except at very high M_s, when large n_e leads to small λ_d, there are an appreciable number of collisions in the sheath.

Laird's (1) assumption of impurity Na^+ ions as the dominant species was based on his interpretation of the apparent ionisation potential derived from an Arrhenius (n_e : 1/T) plot of his p_o = 2 Torr Air shock tube runs.

To do this, the reactions leading up to the production of NO^+ ions in equilibrium with the plasma are approximated to a simple ionisation reaction described by Saha's equation [(7) p.92]

$$\log_{10}\left(\frac{X_e^2}{1-X_e^2}\,p\right) = -\frac{5050}{T}V_i + 2.5\log_{10}T \qquad (3.8)$$

where $X_e = n_e / n_o$,

and V_i is the apparent ionisation potential.

In shock tube experiments, where M_s is the varied parameter, p varies slowly, and so, neglecting variations in $\log_{10}T$, we obtain the gradient of a $\log_{10}X_e$: 1/T plot:-

$$\frac{d(\log_{10}X_e)}{d(1/T)} = -2,525\ V_i \qquad (3.9)$$

where V_i is in volts.

In a shock tube $\frac{\partial n_o}{\partial M_s} \ll \frac{\partial n_e}{\partial M_s}$, and so V_i can be obtained from the gradient of a log n_e : 1/T or log n_i :1/T plot. T is obtained from shock tables (6) for measured p_o and M_s.

Any fears that the slow variation of parameters other than T and n_e in the shock tube plasma with M_s might invalidate this technique were allayed by using shock tube (6) and equilibrium Air tables (9) to predict the apparent ionisation potentials that should be obtained as the temperature is increased by increasing the Mach number for given p_o:-

Table 5 Theoretical apparent ionisation potentials for shock ionised Air.

p_o (Torr)	V_i (eV)
1	9.25
10	9.7

These agree closely with the accepted value of 9.5 eV for NO^+ (20).

If equation (3.4) were to be interpreted as

$$n_i = Cj_+ \qquad (3.10)$$

where C is nearly constant with varying M_s at a given p_o, then a plot of log j_+ : 1/T will give estimates of the ionisation potential.

The experimental electrostatic probe results were then plotted against 1/T in Figs. 20,21,22, for initial shock tube pressures

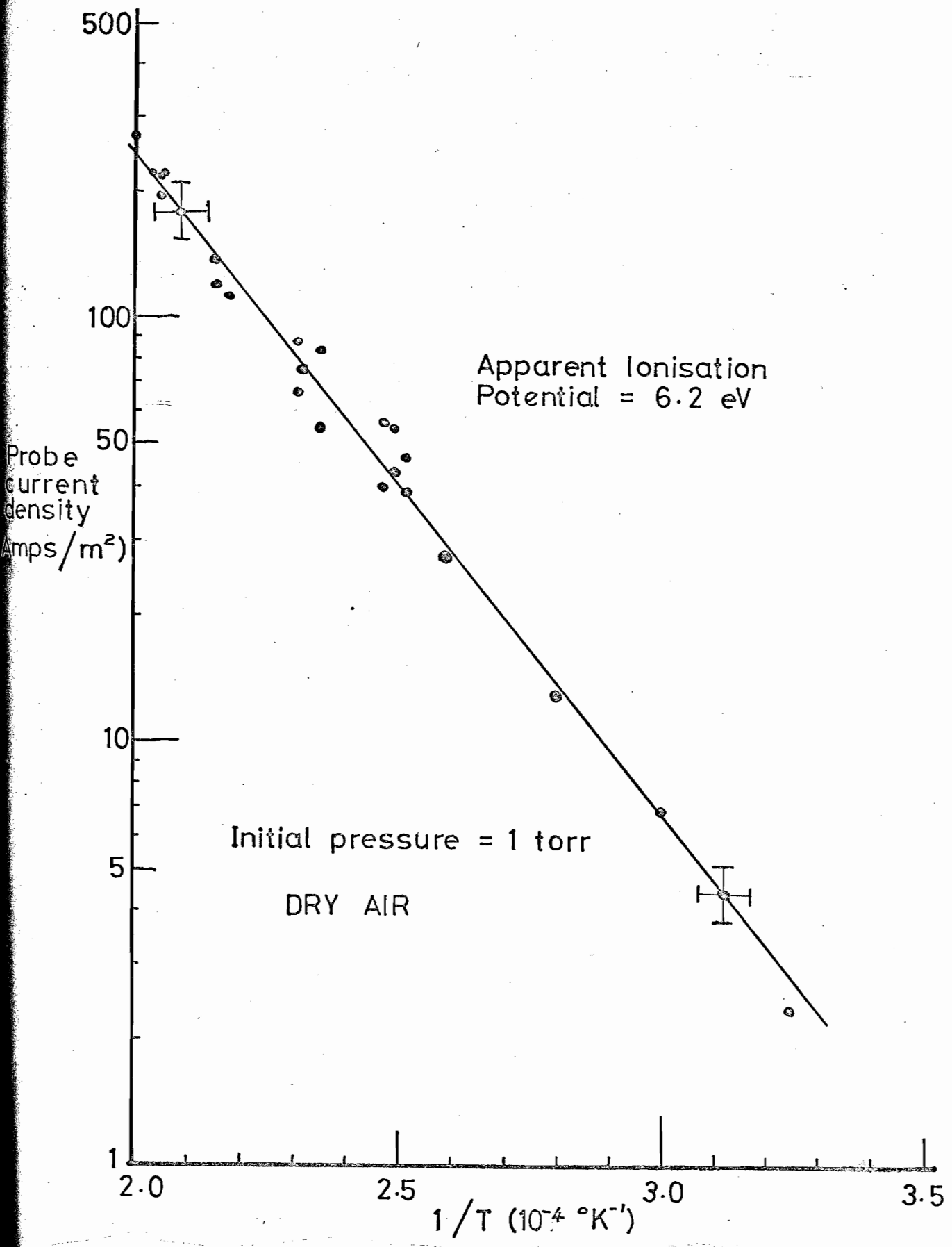


Fig. 20 Determination of Apparent Ionisation potential V from electrostatic probe results by use of j_+ : 1/T plot. p_o = 1 Torr dry Air

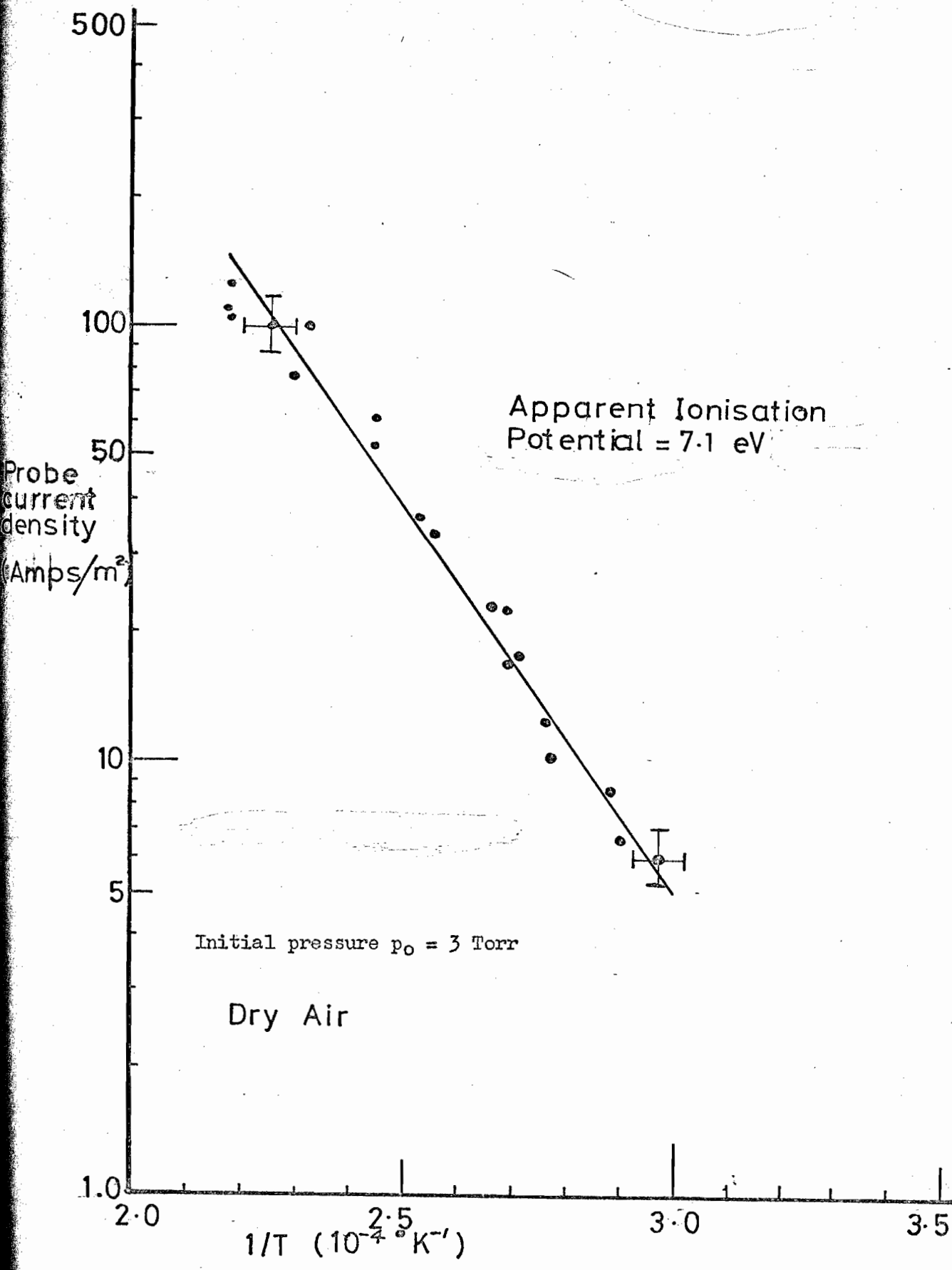


Fig.21 Determination of apparent ionisation potential V_I from electrostatic probe results by use of j_+ : 1/T plot. p_o = 3 Torr dry Air

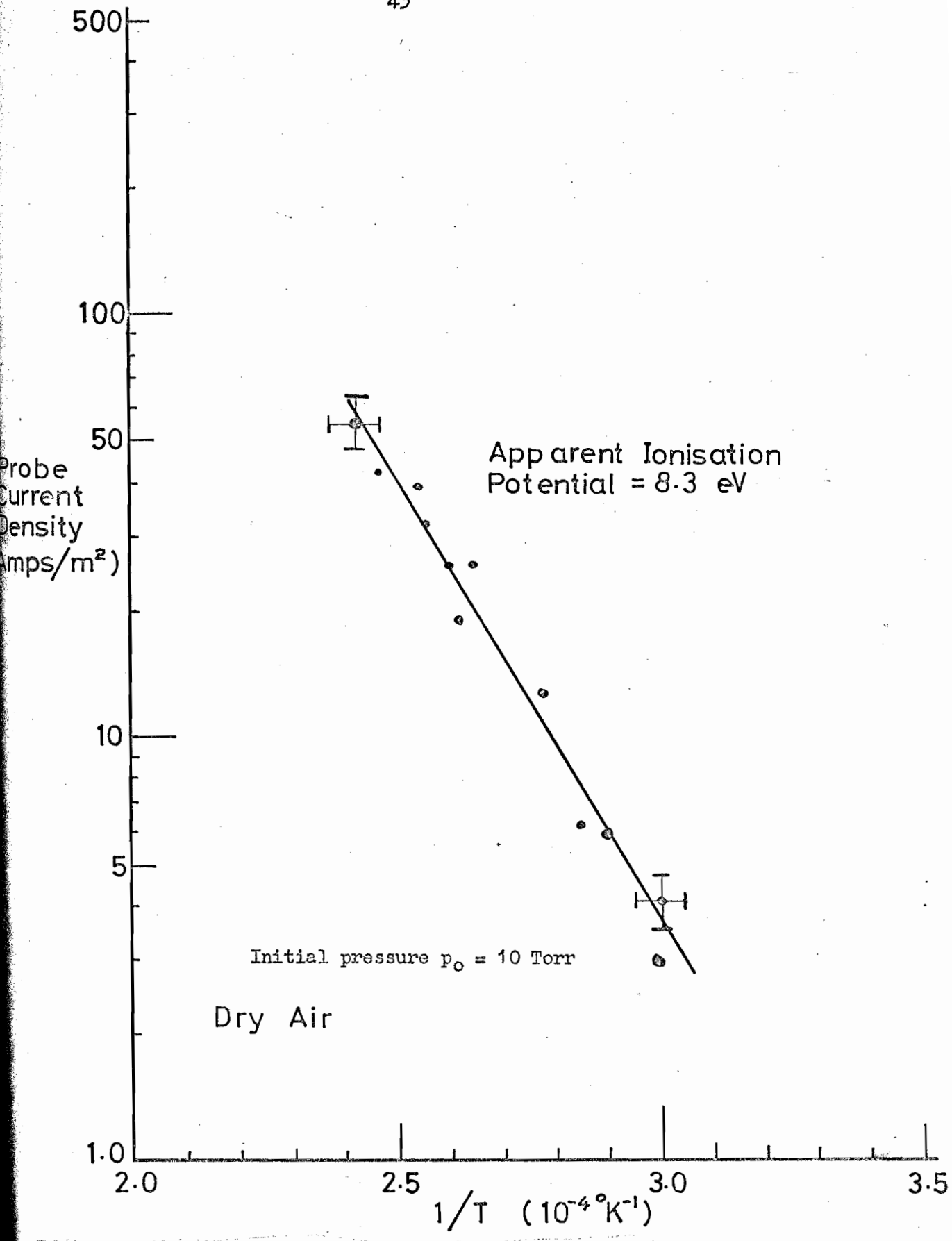


Fig.22 Determination of apparent ionisation potential V_I from electrostatic probe, results by use of $j_+ : 1/T$ plot.
p_o = 10 Torr dry Air

of 1, 3 and 10 Torr, and the gradients thus obtained are shown in Table 6 below:

Table 6 Experimental apparent ionisation potentials for shock ionised Air.

p_o (Torr)	V_i (eV)
1	6.2 ± 1.0
3	7.1 ± 1.5
10	8.3 ± 2.0

The estimates of the standard errors for these measurements are pessimistic in that they were computed on the assumption that the errors in ion current are wholly random, and in fact the measurements of apparent V_i are probably more accurate than indicated.

Laird (2) obtained a V_i of 6.1 ± 2.3 eV at $p_o = 2$ Torr, and concluded he had Na^+ ($V_i = 5.1$ eV) in the shock tube. However, the present experiments were made in a shock tube that had not been used for Na-line reversal spectroscopic measurements, and from Table 6 it can be seen that the apparent ionisation potential changes with shock tube pressure. It may be concluded then, that the simplification of equation (3.4) to equation (3.10) is not valid at low shock tube pressures, but becomes increasingly valid as the initial pressure p_o increases.

It is now apparent that equation (3.4) is not suitable for the estimation of ion density from measured saturation ion current on the type of electrostatic probe used, and that some attempt should be made to use a simplified theory in order to make use of the experimental data obtained.

When the probe is used, as it was, in the saturated ion current mode, the vertical ion current is conserved in the region immediately above the probe, and the probe current may be related (28,33)

to the ion flux at the sheath (a near local- Maxwellian velocity-distribution is assumed ($\lambda_\alpha \not\approx \lambda_i$) for the ions):

$$j_+ = \frac{e n_i \bar{c}}{4} \tag{3.11}$$

where $$\bar{c} = \left(\frac{8kT_i}{\pi m_i}\right)^{\frac{1}{2}} \tag{3.12}$$

In the case of the flat plate electrostatic probe used here the temperature T is not the free-stream temperature, but that of the probe, since $\lambda_i << \delta_w$ (Fig.19). Taking T = 300°K, and the ion to be NO^+, with a molecule mass of 5.3136×10^{-26} kg, we get

$$n_i = 5.604 \times 10^{16} \; j_+ \; m^{-3} \tag{3.13}$$

where j_+ is in amps / m^2.

The n_i thus measured is the measured ion density at the sheath edge, but is not necessarily the free-stream ion density.

Figs. 23, 24, 25 show the sheath edge ion number density, n_e, plotted against M_s for p_o = 1, 3, and 10 Torr of Air from probe 1 data. A scale showing the measured ion current density is included to enable the reader to recover the raw data, and the computed equilibrium electron density (p45) curves are plotted by comparison.

Surprisingly the sheath edge ion number density turns out to give a very reasonable estimate of the free-stream (where $n_i = n_e$) ion density. In the low pressure, p_o = 1 Torr, case, this agreement is particularly good in the range M_s = 10.5 - 12.5, and even at the extremes is within a factor of 2 of the predicted equilibrium density, which later microwave experiments show is a good estimate of the electron density behind the shock. At higher, p_o = 10 Torr, pressures, the sheath edge ion density is, as would be expected, lower than the predicted equilibrium free - stream level, but still is within a factor of 3 for most of the range. A possible explanation for the higher measured sheath density in the p_o = 1 Torr case would be

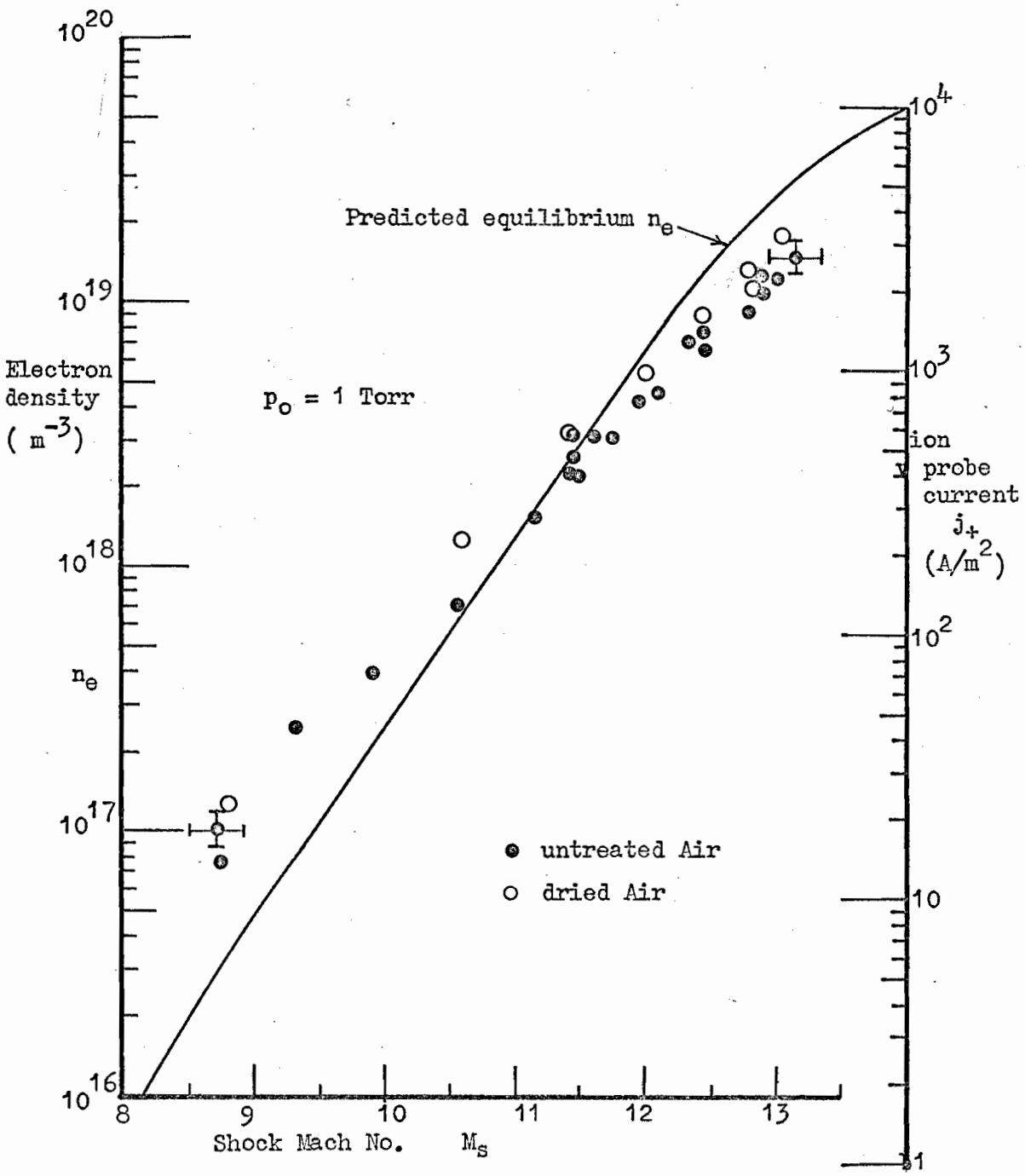


Fig.23 Sheath edge ion number density from electrostatic probe results. p_o = 1 Torr dry Air.

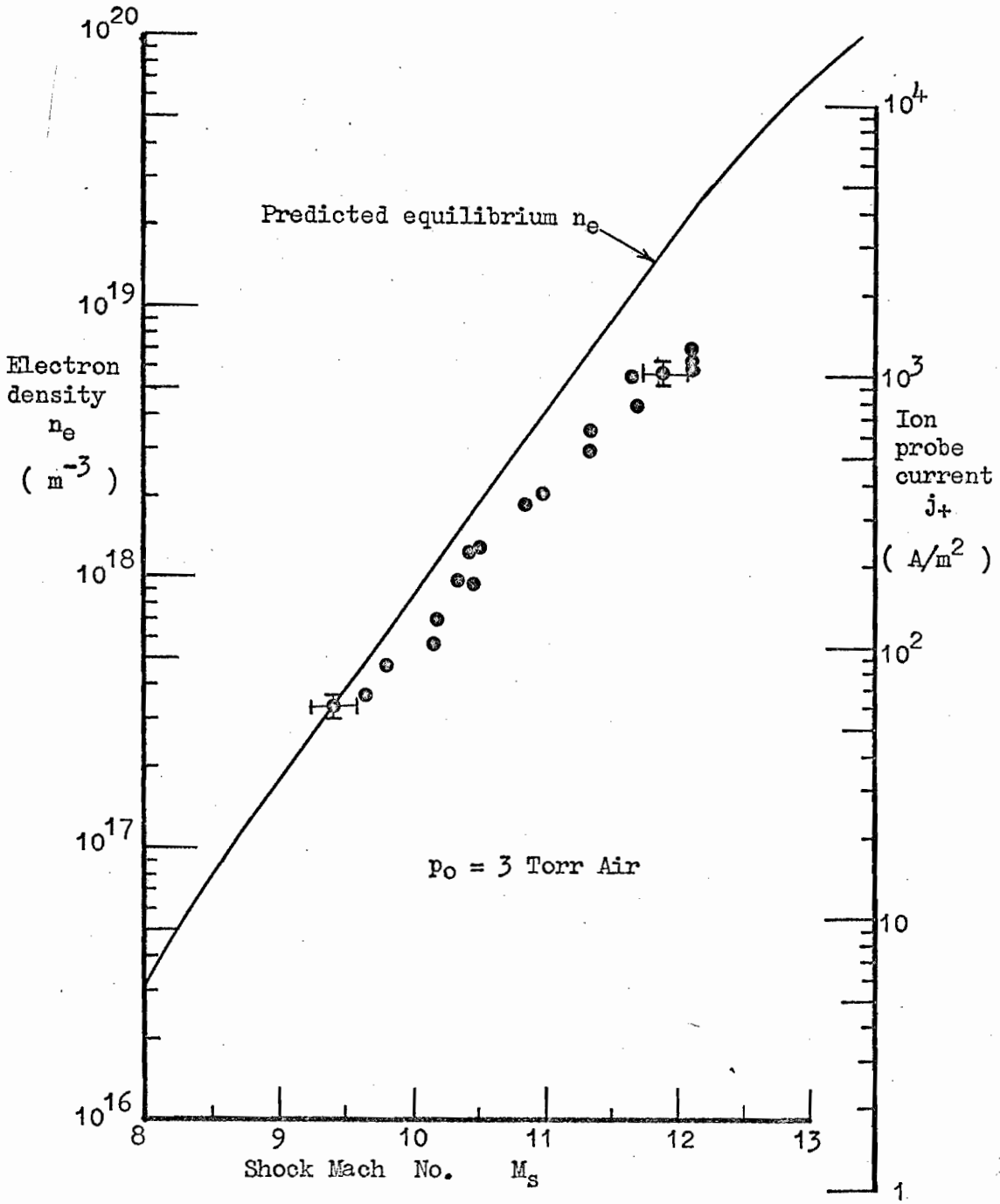


Fig.24 Sheath edge ion number density from electrostatic probe results. p_o = 3 Torr Air.

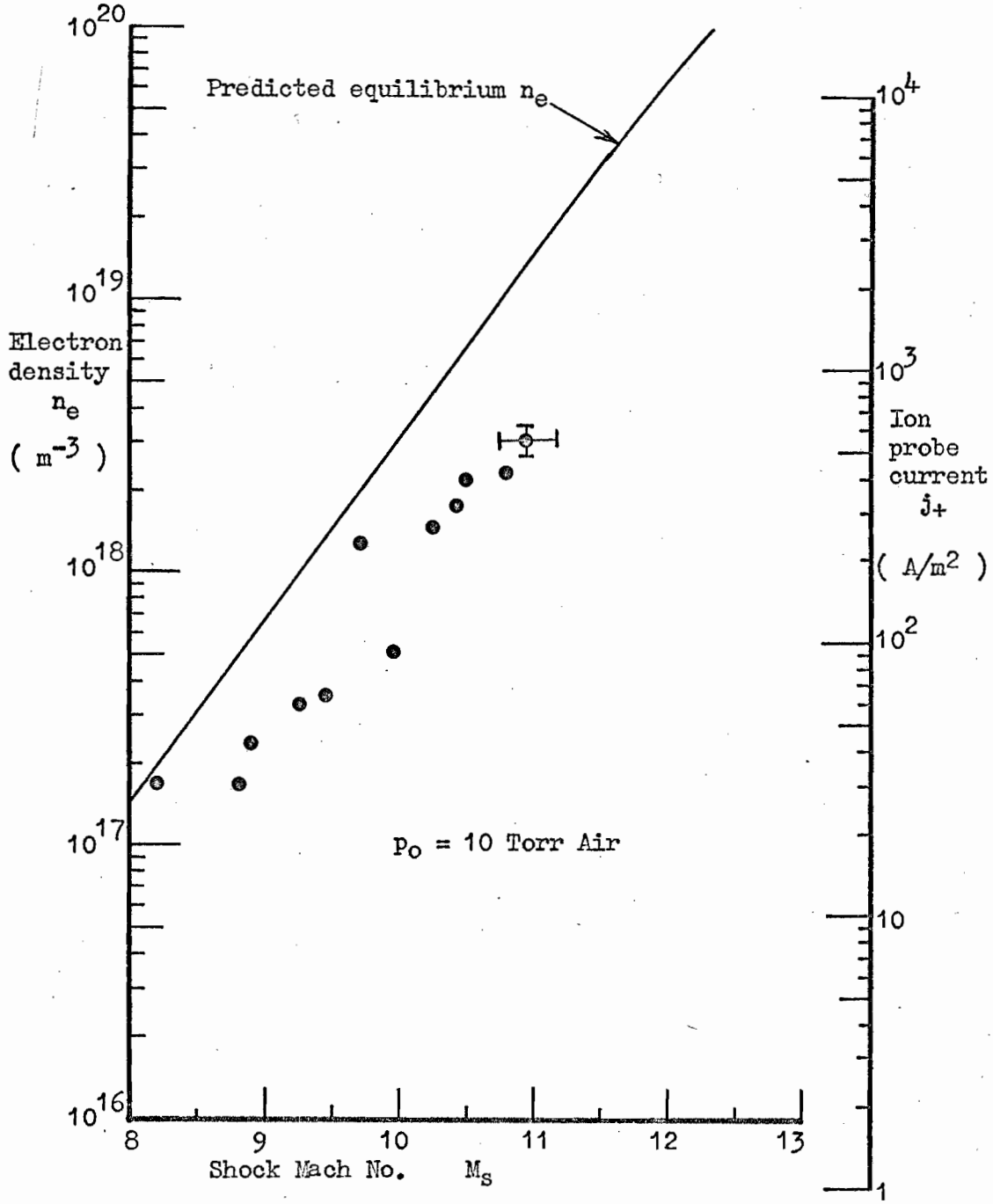


Fig.25 Sheath edge ion number density from electrostatic probe results. p_o = 10 Torr Air.

that the sheath edge ion temperature is in fact higher than the 300 ^{o}K used in interpreting Equation (3.12). This low assumed temperature would then have the effect of increasing the computed ion density, and would compensate for the decrease of ion density through the boundary layer predicted by Bredfeldt et al. (33).

It is noted that Radcliffe & Hobson (30), using thin wire probes in a shock tube, use the simple theory (Equations 3.11, 3.12) for ion collection and recover ion densities in Argon which agree with their microwave results.

For most of the electrostatic probe runs the Air used was unpurified room Air. However, the Air-dryer described on p.17 was used for later runs, and, as the points on Fig.23 show, a slight increase of sheath-edge ion density was observed. There was, however, no change in the slope observed, and so the apparent ionisation potentials observed (p.44) would not be changed. The decrease of ion density with the presence of water vapour, for a given p_o and M_s behind Air-shocks, is in accord with that observed by Aronsen & Levine (41).

The Air-dryer was kept in use for the later microwave runs, as the use of dry Air reduced the pump-down times between shock tube runs.

A few electrostatic probe runs were carried out in pure Argon. The ionisation rate behind the shock in Argon (42) is much slower than in Air, and as can be seen from the probe trace in Fig. 26, the ion density is still increasing at the arrival of the contact surface. This confirms that shock heated Argon, unlike Air, does not reach an equilibrium ionisation level within the running time available, for the Ms and p_o ranges used here.

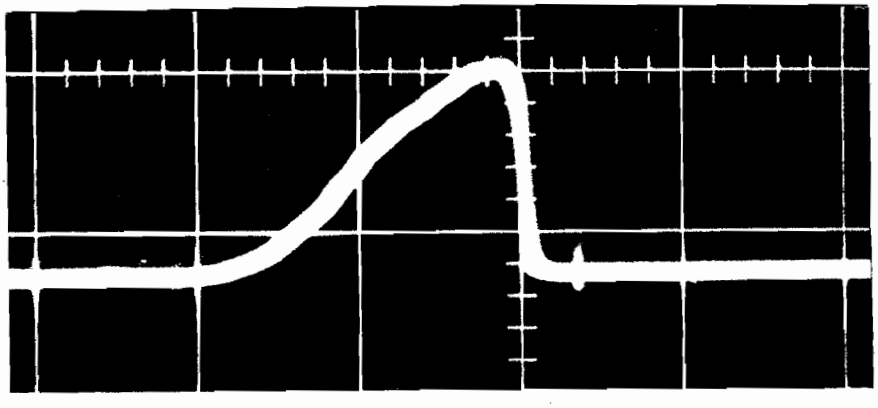


Fig.26 Electrostatic probe current trace in Argon behind incident shock. Peak Ion current = 121 A/m^2

50 μs/division p_o = 1 Torr Argon

M_s = 7.44

4. MICROWAVE REFLECTION WITHOUT MAGNETIC FIELD.

4.1 Introduction.

Before studying the propagation of microwaves through a collisionally damped plasma (collisional plasma) in the presence of a strong magnetic field, it was first necessary to conduct experiments with the microwave system in order to calibrate both the microwave equipment and the shock tube.

Low power microwave measurements are commonly used to determine electron densities in laboratory plasmas. They have the advantage of not disturbing the plasma to a great extent, but unfortunately have a spatial resolution limited to the order of the microwave wavelength, which in turn is determined effectively by the electron density in the plasma to be examined.

In addition, the geometry of the plasma, together with any internal inhomogeneity, must be considered carefully.

The general field of microwave diagnostics is well covered by Heald & Wharton (44), and general propagation of microwaves through plasmas by Ginzburg (45). The electron densities produced by the shock tube described here (Chapter 2) limit the useful microwave frequencies to those near 9 GHz.

Laird (1) has listed in detail the various geometries used with shock tubes at this order of frequency, and so only a brief summary is given here:-

(a) External transverse geometry.

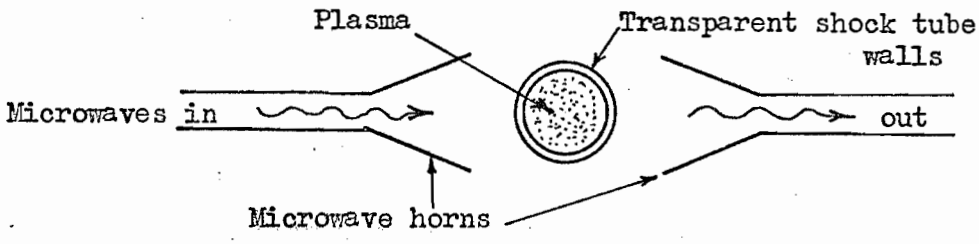


Fig.27 External transverse microwave geometry.

Bad geometrically, as the amount of microwave signal reaching the second horn depends on the refraction through the shock tube walls and plasma. The growing boundary layers behind the shock change the effective diameter of the plasma.

(b) Internal transverse reflection probe.

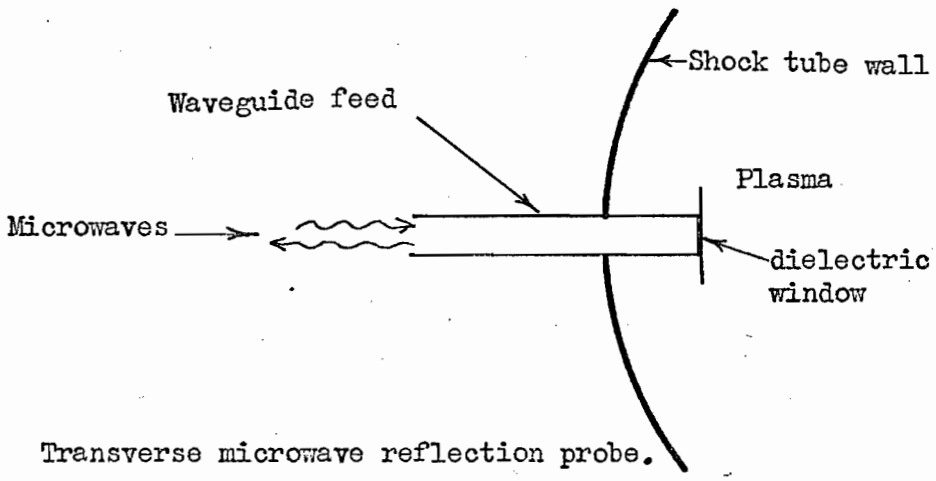


Fig.28 Transverse microwave reflection probe.

As used by Lin, Neal & Fyfe (10), this requires that shock tube diameter >> microwave wavelength. This is certainly not satisfied with 30 mm waves in a 45 mm diameter shock tube.

(c) Longitudinal probe in reflected shock.

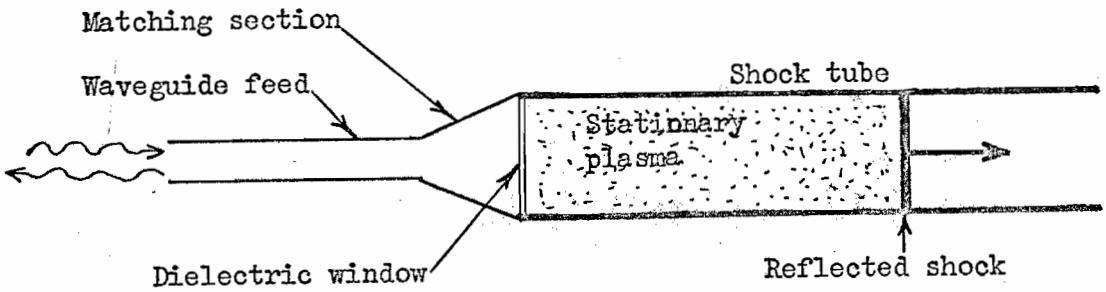


Fig.29 Longitudinal probe in reflected shock.

This system is used by Takeda & Tsukishima (46, 47), and has the apparent advantage that the position of the front reflecting face of the plasma is stationary and hence known. Thus, by using, for example, a four wire probe system, both the amplitude and phase of the reflected wave can be measured. In practice, a growing thermal boundary layer on the shock tube end-face reduces the accuracy of phase measurements, and the region behind the reflected shock is by no means uniform (49).

(d) Waveguide used as shock tube.

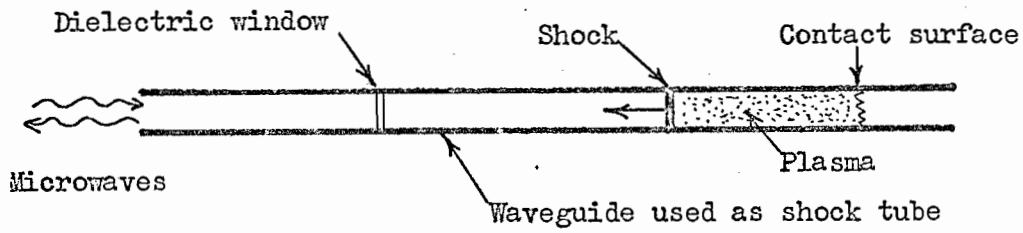


Fig.30 Waveguide shock-tube.

As used by Yamanaka & Nakai (48) this system uses waveguide

as the shock tube and the microwaves are reflected by the plasma behind the incident shock. Unfortunately, the small dimensions (22.86 mm x 10.16 mm) of 9 GHz waveguide curtails the running time for low pressure shocks (14) and the thickness of the plasma slab must be considered in interpreting the microwave reflection results.

(e) Waveguide inside shock tube .

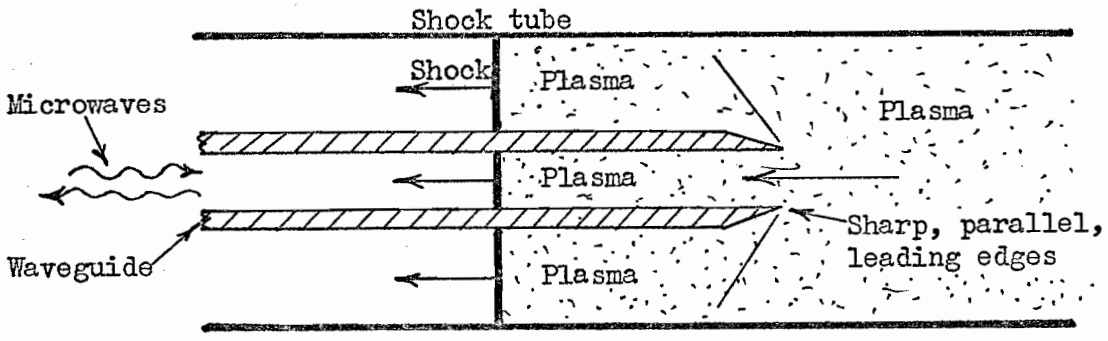


Fig.30a Waveguide inside shock tube.

As developed and used by Laird (1), this system uses a rectangular waveguide mounted axially inside a larger shock tube. This waveguide punches the centre out of the plasma behind the shock and microwaves are reflected from this as it travels down the waveguide. The plasma, being from the center of the tube, is relatively undisturbed and the boundary layers inside the waveguide are small. As the plasma is generated within the larger shock tube, a sufficient length of plasma of known parameters can be examined. A single,stationary, microwave diode and probe can be used and the movement of the plasma in the guide allows standing waves to be displayed on a time-swept oscilloscope. The incident shock (in Air) in the waveguide ensures a sharp front boundary to the plasma, and allows

simple reflection formulae to be used. However, the difficulty of ascertaining the exact position of the shock front in the waveguide at any instant precludes accurate measurement of the phase of the reflected wave.

The choice of microwave system used in the present work is finally dictated by the later work with an axial magnetic field applied. If a coaxial plasma - filled line, with an axial magnetic field, can be used, then a theoretical analysis becomes feasible. Structural considerations show that for a coaxial line, system (e), as used by Laird, is the preferred system, and the magnetic field can then be applied by surrounding the shock tube with a coaxial solenoid.

4.2 Analysis of reflection from Plasma.

Convention for propagation constants.

In the literature of microwave - plasma interactions, many conventions abound for the wave propagation constants (wave numbers). The conventions used here are:-

all waves propagating along the waveguide or coaxial line vary as $e^{j(\omega t - k_o k z)}$, where the z - axis is in the direction of propagation. ω is the circular frequency of the wave and $\frac{\omega}{2\pi}$ (Hz) is the cyclic frequency.

$$k_o = \frac{\omega}{c} = \omega\sqrt{\varepsilon_o \mu_o} \qquad (4.1)$$

is the free-space wave number and k is the normalised (non-dimensional) wave number. As k is usually complex, we divide it into its real and imaginary parts:-

$$k = k^r + j\,k^i \qquad (4.2)$$

[$j = \sqrt{-1}$ as usual]

Thus the wave propagation varies as

$$e^{j(\omega t - k_o k z)} = e^{j\omega t} e^{-jk_o(k^r + jk^i)z}$$

$$= e^{j\omega t} e^{-jk_o k^r z} e^{k_o k^i z} . \qquad (4.3)$$

For a forward propagating , attenuating,wave,

$k^r > 0$ and $k^i < 0$.

i.e. k^r = normalised propagation constant.

$-k^i$ = normalised attenuation constant.

For free space transverse electromagnetic (TEM) waves,

$k^r = k = 1$ and $k^i = 0$.

Other conventions for propagation constants.

(a) Bers (50) uses waves propagating as $e^{j(\omega t - kz)}$

and $e^{j\omega t - \gamma z}$ where

$\gamma = j\,k$ and $\gamma = \alpha + j\,\beta$ (4.4)

are the non-normalised propagation constants.

Conversions:-

Bers		Present work
k	=	$k_o k$
γ	=	$j\,k_o k$
α	=	$-k_o k^i$
β	=	$k_o k^r$

(4.5)

(b) Heald & Wharton (44) use propagation constants as above but introduce further normalised constants:-

Heald & Wharton		Present work
$\chi = \alpha/k^o$	=	$-k^i$
$\mu = \beta/k^o$	=	k^r

(4.6)

In the following analysis of plasma - microwave interaction the following assumptions are made:-

(a) Only the interaction of the electromagnetic wave with the electrons is considered. The ions are regarded as contributing to a stationary background of positive charge-density required to neutralise the electrons.

(b) The effects of electron collisions with ions and neutral molecules are considered to be due to a viscous drag force $m_e \nu \underset{\sim}{v}$, where m_e is the electron mass, and $\underset{\sim}{v}$ is the electron velocity due to the oscillating electromagnetic field. ν is known as the "collision frequency" and is , more exactly, the collision frequency for momentum transfer (51).

(c) The microwave energy density is very much lower than the mean random thermal energy of the electrons, so that microwave heating of the electrons ~~and wave - trapping of the electrons~~ does not occur. Laird (1) has shown that for the low (< 10mW) microwave power used, electron heating is neglible.

Note that the electronic charge, e , is taken to be a positive constant.

Maxwell's Equations.

Assuming that all quantities vary as $e^{j\omega t}$, we have,

$$\left.\begin{aligned} \nabla \times \underset{\sim}{E} &= -j\omega\mu_0 \underset{\sim}{H}, \\ \nabla \times \underset{\sim}{H} &= j\omega\varepsilon_0 \underset{\sim}{E} + \underset{\sim}{J}, \\ \nabla \cdot \underset{\sim}{D} &= \rho, \\ \nabla \cdot \underset{\sim}{B} &= 0, \\ \nabla \cdot \underset{\sim}{J} &= -j\omega\rho, \\ \underset{\sim}{B} = \mu_0 \underset{\sim}{H} \quad &\text{and} \quad \underset{\sim}{D} = \varepsilon_0 \underset{\sim}{E} \end{aligned}\right\} \qquad (4.7)$$

where ρ is the mean charge density in this case.

Consider the motion of an electron, velocity $\underset{\sim}{v}$:-

$$m_e \frac{d\underset{\sim}{v}}{dt} + m_e \nu \underset{\sim}{v} = -e \underset{\sim}{E}. \qquad (4.8)$$

i.e. $$(j\omega + \nu)\underset{\sim}{v} = -\frac{e}{m_e}\underset{\sim}{E}$$

Current density $$\underset{\sim}{J} = -n_e e \underset{\sim}{v}, \qquad (4.9)$$

so that $$\underset{\sim}{J} = \frac{n_e e^2}{m_e}\frac{1}{(j\omega+\nu)}\underset{\sim}{E}. \qquad (4.10)$$

Substituting (4.10) into the second of Maxwell's equations (4.7) we get

$$\nabla \times \underset{\sim}{H} = j\omega\varepsilon_0\left(1 + \frac{n_e e^2}{j\omega m(j\omega+\nu)}\right)\underset{\sim}{E}$$

$$= j\omega\varepsilon_0\varepsilon\underset{\sim}{E}, \qquad (4.11)$$

where $\varepsilon_0\varepsilon$ is the equivalent dielectric-coefficient of the plasma.

If we define the plasma frequency ω_p by

$$\omega_p = \sqrt{\frac{n_e e^2}{\varepsilon_0 m_e}} \qquad (4.12)$$

$$\left[\frac{\omega_p}{2\pi} = 8.979\sqrt{n_e}\ \text{Hz} \quad \text{for } n_e \text{ in } m^{-3}\right]$$

then the relative dielectric constant is given by

$$\varepsilon_0\varepsilon = \varepsilon_0\left(1 - \left(\frac{\omega_p}{\omega}\right)^2 \frac{1}{(1 - j\frac{\nu}{\omega})}\right), \qquad (4.13)$$

and is complex for $\frac{\nu}{\omega} \neq 0$.

Also, if we define $\underset{\sim}{D}' = \varepsilon \underset{\sim}{D}$, then the plasma behaves as a dielectric with dielectric constant given by (4.13).

The normalised parameters describing the plasma are the

normalised plasma frequency $\frac{\omega_p}{\omega}$

and the normalised collision frequency $\frac{\nu}{\omega}$.

Some writers use the U.R.S.I. symbols

$X = \left(\frac{\omega_p}{\omega}\right)^2$ and $Y = \frac{\nu}{\omega}$,

but here the simple normalised frequencies are retained.

The propagation constant is given by

$$k_0 k = k_0 \varepsilon^{\frac{1}{2}} = k_0 \sqrt{1 - \left(\frac{\omega_p}{\omega}\right)^2 \frac{1}{(1 - j\frac{\nu}{\omega})}} \qquad (4.14)$$

Reflection from semi - infinite plasma - filled coaxial line.

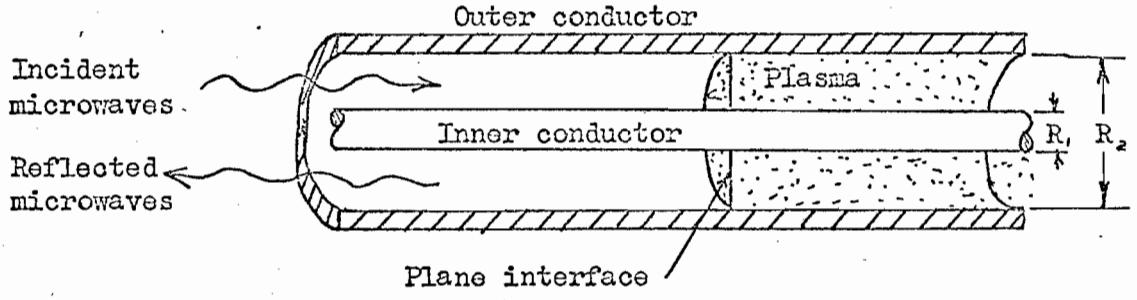


Fig.31 Reflection of microwaves from uniform plasma in coaxial line.

By choice of sufficiently large $\frac{\nu}{\omega}$, and hence k_i, the wave in the plasma attenuates rapidly, and within a few wavelengths the reflection may be considered to be the same as from a semi - infinite plasma (1). The impedance of an empty coaxial line is given [(53)p.136] by

$$Z_0 = \frac{1}{2\pi} \left(\frac{\mu_0}{\varepsilon_0}\right)^{\frac{1}{2}} \log \frac{R_2}{R_1}$$

where R_1 and R_2 are the inner and outer diameters, and for the plasma - filled line the equivalent equation is

$$Z = \frac{1}{2\pi}\left(\frac{\mu_0}{\varepsilon_0 \varepsilon}\right)^{\frac{1}{2}} \log \frac{R_2}{R_1}$$

The voltage reflection coefficient R_v is given by

$$R_v = \frac{Z - Z_0}{Z + Z_0} = \frac{Z - Z_0}{Z + Z_0} \qquad (4.15)$$

$$= \frac{1 - \frac{Z_0}{Z}}{1 + \frac{Z_0}{Z}} \qquad (4.16)$$

and the power reflection coefficient by

$$R_p = R_v^* R_v \quad .$$

R_v shall be used in preference to R_p here.

It will be appreciated that R_v is, in general, a complex quantity, but that a standing wave probe in the coaxial line measures the magnitude $|R_v|$:-

Voltage standing wave ratio,

$$\text{VSWR} = \frac{\text{maximum line voltage}}{\text{minimum line voltage}}$$

$$= \frac{1 + |R_v|}{1 - |R_v|} \qquad (4.17)$$

A computer program was written to compute R_v in magnitude and phase for different values of the non - dimensional parameters $\frac{\omega_p}{\omega}$ & $\frac{\nu}{\omega}$. Fig. 32 shows a plot of $|R_v|$ against $\frac{\omega_p}{\omega}$ for various $\frac{\nu}{\omega}$ and Fig. 33 a plot of R_v on the complex plane. Fig. 32 agrees with the plot of R_p ($=|R_v|^2$) given by Hochstim (54) and the polar plot in Fig.33 with that of Yamanaka & Nakai (48).

Note that the presence of electron collisions enables the reflection of microwaves to be used as a diagnostic at frequencies below the plasma frequency.

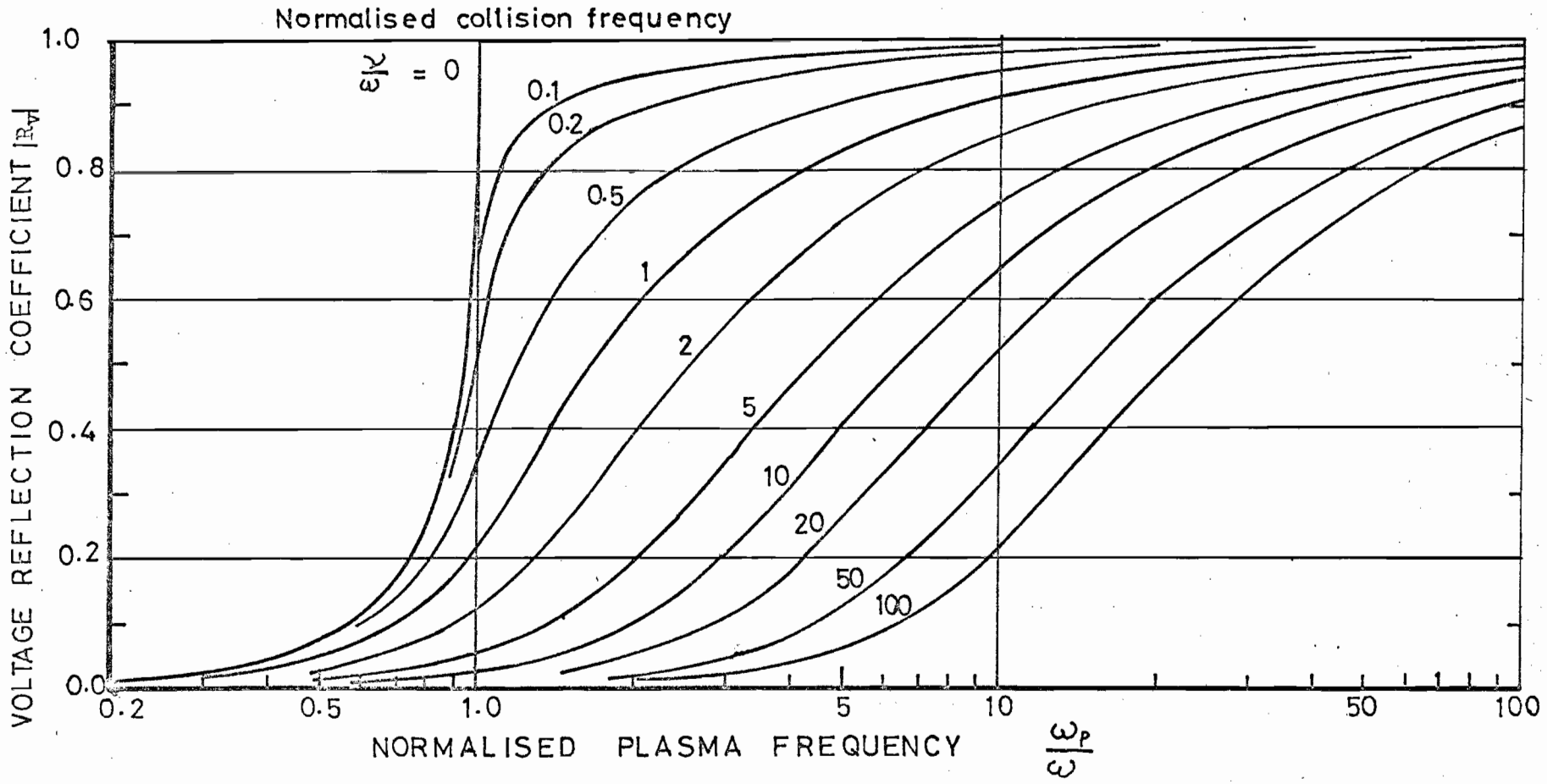


Fig.32 Voltage reflection curves for reflection at a plane interface of plasma (Parameters ω_p, ν), in coaxial line or free space. For waveguide replace $\frac{\omega_p}{\omega}$ by $\frac{\omega_p}{\omega}\left(1-\left(\frac{\omega_{c0}}{\omega}\right)^2\right)^{-\frac{1}{2}}$. No magnetic field.

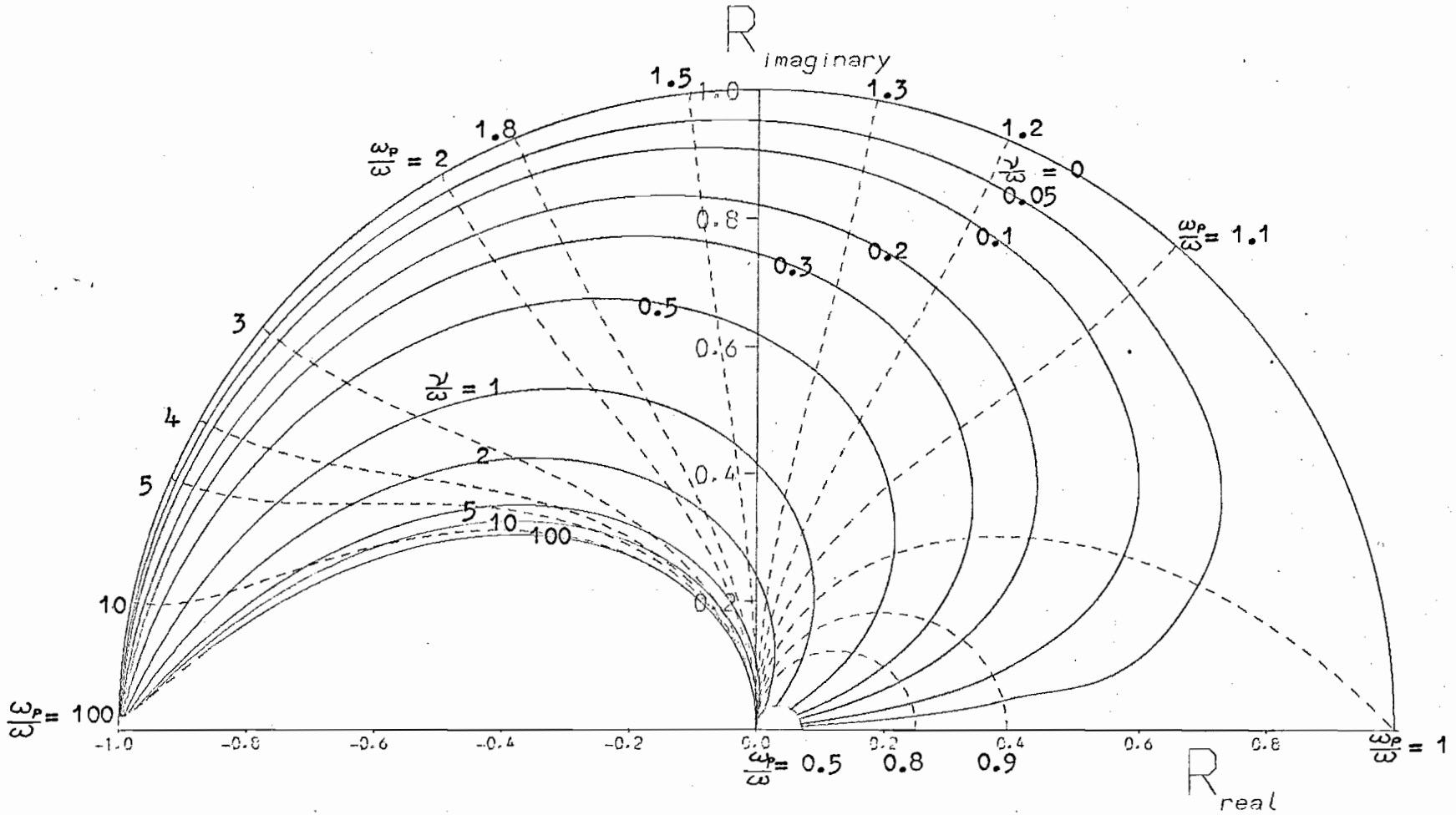


Fig.33 Complex Voltage Reflection Coefficient R_v for Semi-infinite Plasma.

No Magnetic Field. Parameters, $\frac{\omega_p}{\omega}, \frac{\nu}{\omega}$

Reflection from semi - infinite plasma - filled rectangular waveguide.

Following the treatment in Collin [(53) p.172], the wave impedance of a waveguide filled with plasma of permittivity μ_0 and dielectric constant ε_0 is given by

$$Z = \frac{j\omega\mu_0}{\Gamma} = \frac{j\omega\mu_0}{\sqrt{(k_{c0}^2 - k_1^2)}}$$

where $k_{co} = \frac{2\pi}{\lambda_{co}}$, is the cut - off wave number of the waveguide mode, and $k_1 = \frac{2\pi}{\lambda} = \frac{\omega}{\sqrt{(\mu_0 \varepsilon_0 \varepsilon)}}$ is the propagation constant of TEM waves in the plasma. If k_0 is the free - space wave number, as before, then

$$k_1 = \omega\sqrt{\mu_0\varepsilon_0\varepsilon} = k_0\sqrt{\varepsilon} \quad .$$

Note that k_{co} is a function of the geometry of the waveguide and not of the dielectric constant of the plasma.

Then $$Z = \frac{j\omega\mu_0}{\sqrt{(k_{c0}^2 - k_0^2\varepsilon}} \qquad (4.18)$$

For the empty waveguide we define the cut - off frequency

$$\omega_{c0} = \sqrt{\mu_0\varepsilon_0}\, k_{co} \quad .$$

Then (4.18) becomes

$$Z = \frac{\mu_0^{\frac{3}{2}}\varepsilon_0^{\frac{1}{2}}}{\omega\sqrt{\left(\varepsilon - \left(\frac{\omega_{c0}}{\omega}\right)^2\right)}} \quad . \qquad (4.19)$$

For the empty waveguide, $\varepsilon = 1$ and

$$Z_0 = \frac{\mu_0^{\frac{3}{2}}\varepsilon_0^{\frac{1}{2}}}{\omega\sqrt{\left(1 - \left(\frac{\omega_{c0}}{\omega}\right)^2\right)}} \quad .$$

Then $$\frac{Z_0}{Z} = \sqrt{\frac{\varepsilon - \left(\frac{\omega_{c0}}{\omega}\right)^2}{1 - \left(\frac{\omega_{c0}}{\omega}\right)^2}}$$

$$= \sqrt{\frac{1 - \left(\frac{\omega_p}{\omega}\right)^2 \frac{1}{(1 - j\frac{\nu}{\omega})} - \left(\frac{\omega_{c0}}{\omega}\right)^2}{1 - \left(\frac{\omega_{c0}}{\omega}\right)^2}}$$

$$\frac{Z_0}{Z} = \sqrt{1 - \left[\left(\frac{\omega_p}{\omega}\right)^2 \left(1 - \left(\frac{\omega_{co}}{\omega}\right)^2\right)^{-1}\right] \frac{1}{\left(1 - j\frac{\nu}{\omega}\right)}} \qquad (4.20)$$

As in the case of the coaxial line, the reflection coefficient from a semi - infinite plasma filling a waveguide is given by

$$R_v = \frac{1 - \frac{Z_0}{Z}}{1 + \frac{Z_0}{Z}} \qquad (4.15)$$

But for a coaxial line,

$$\frac{Z_0}{Z} = \sqrt{\varepsilon} = \sqrt{1 - \left(\frac{\omega_p}{\omega}\right)^2 \frac{1}{\left(1 - j\frac{\nu}{\omega}\right)}} \qquad (4.21)$$

We define an equivalent waveguide normalised plasma frequency

$$\left(\frac{\omega_p}{\omega}\right)_w = \frac{\omega_p}{\omega}\left(1 - \left(\frac{\omega_{co}}{\omega}\right)^2\right)^{-\frac{1}{2}} \qquad (4.22)$$

Then, in a waveguide,

$$\frac{Z_0}{Z} = \sqrt{1 - \left(\frac{\omega_p}{\omega}\right)_w^2 \frac{1}{\left(1 - j\frac{\nu}{\omega}\right)}} \qquad (4.23)$$

Equation (4.23) is of the same form as (4.21), and so any expression derived for the reflection from a plasma in a coaxial line may be used for a waveguide if $\frac{\omega_p}{\omega}$ is replaced by $\left(\frac{\omega_p}{\omega}\right)_w$.

Thus Figs 32 & 33 can also be used to predict the reflection coefficient for plasma - filled waveguides.

In particular, for X-band (~~25.4~~ 22.8 mm x ~~12.7~~ 10.2 mm) waveguide (cut off frequency = 6.557 GHz) with 9 GHz microwaves,

$$\frac{\omega_p}{\omega} = 0.68497 \left(\frac{\omega_p}{\omega}\right)_w$$

[The above waveguide - coaxial line correspondence only holds for uniform isotropic plasmas.]

4.3 Construction and calibration of Coaxial microwave probe.

The coaxial microwave probe was fabricated from General Radio GR - 900 series precision components. Centerless - ground, stress - relieved, silver - layered brass inner (6.20395 mm diameter) and outer (14.2875 mm diameter) conductors were used with type 900-BT connectors (VSWR < 1.006 at 9 GHz) to fabricate a 50 ohm, low loss, air line which projected in from the rear of the dump tank along the axis of the shock tube. This line terminated in the 152.4 mm long coaxial probe shown, in position, in Fig.34.

The inner and outer conductors are screwed onto the end of the air line, as shown, and may be removed to allow inspection of the PTFE support-bead and vacuum - seal between shock tube runs. This bead, which is identical to those in the 900-BT connectors, is mounted in machined matching recesses in the inner and outer conductors, and is cold - bonded with Araldite epoxy resin to them to give an efficient vacuum seal and to resist the peak pressure behind the reflected shock. In use the bead proved adequate, suffering only slight ablation and minor surface damage after some 142 successful shock tube runs.

The impedance of the bead is matched to the 50 ohm air -line by changes in the inner and outer conductor diameters, and in practice the measured VSWR at 9 GHz was less than that (1.03) of the 900-W50 50 ohm load used to terminate the line during measurements.

A second, O - ring, vacuum seal is used just inside the mouth of the dump tank, where the coaxial line is mounted in a 41 mm diameter support tube, which is mounted in turn on the dump tank end flange.

A 200 mm length of low - loss, flexible, 50 ohm, coaxial cable , using GR 900-C9 precision connectors, was used to insulate

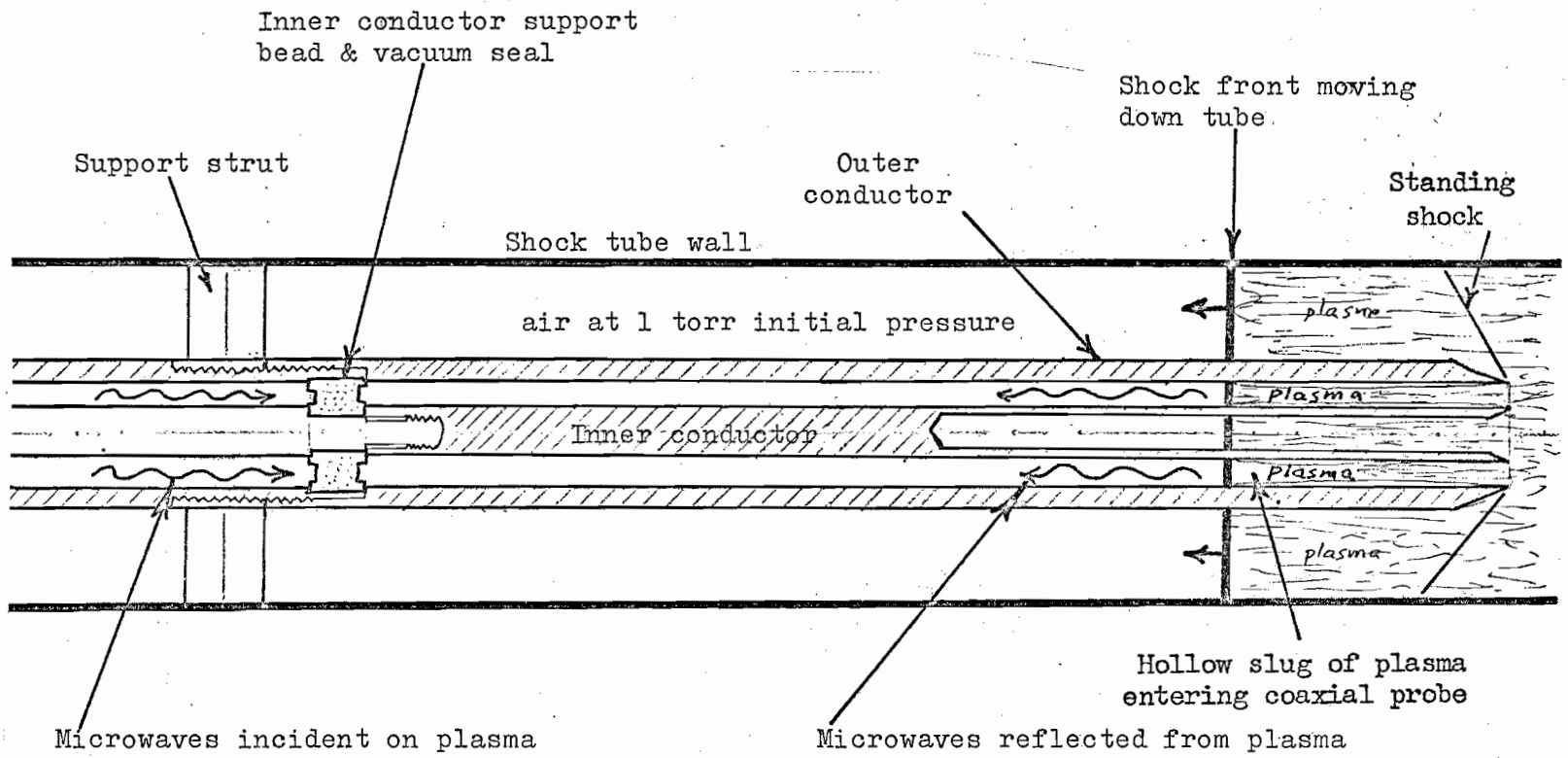


Fig.34 Coaxial microwave probe in position in shock tube.

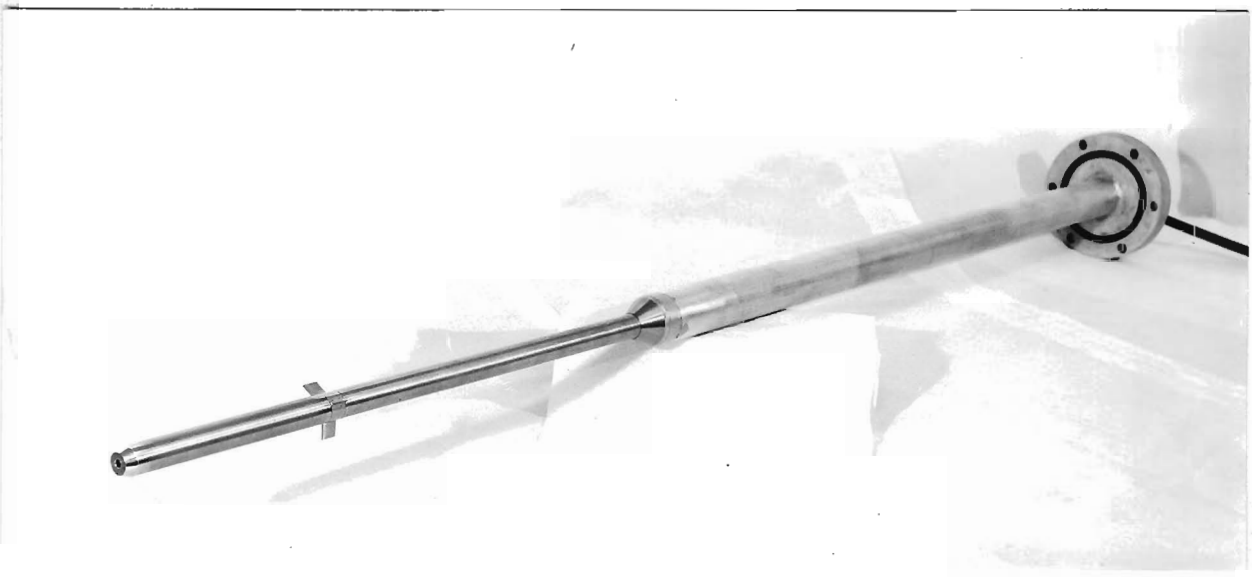


Fig.35 Coaxial microwave probe and support tube.

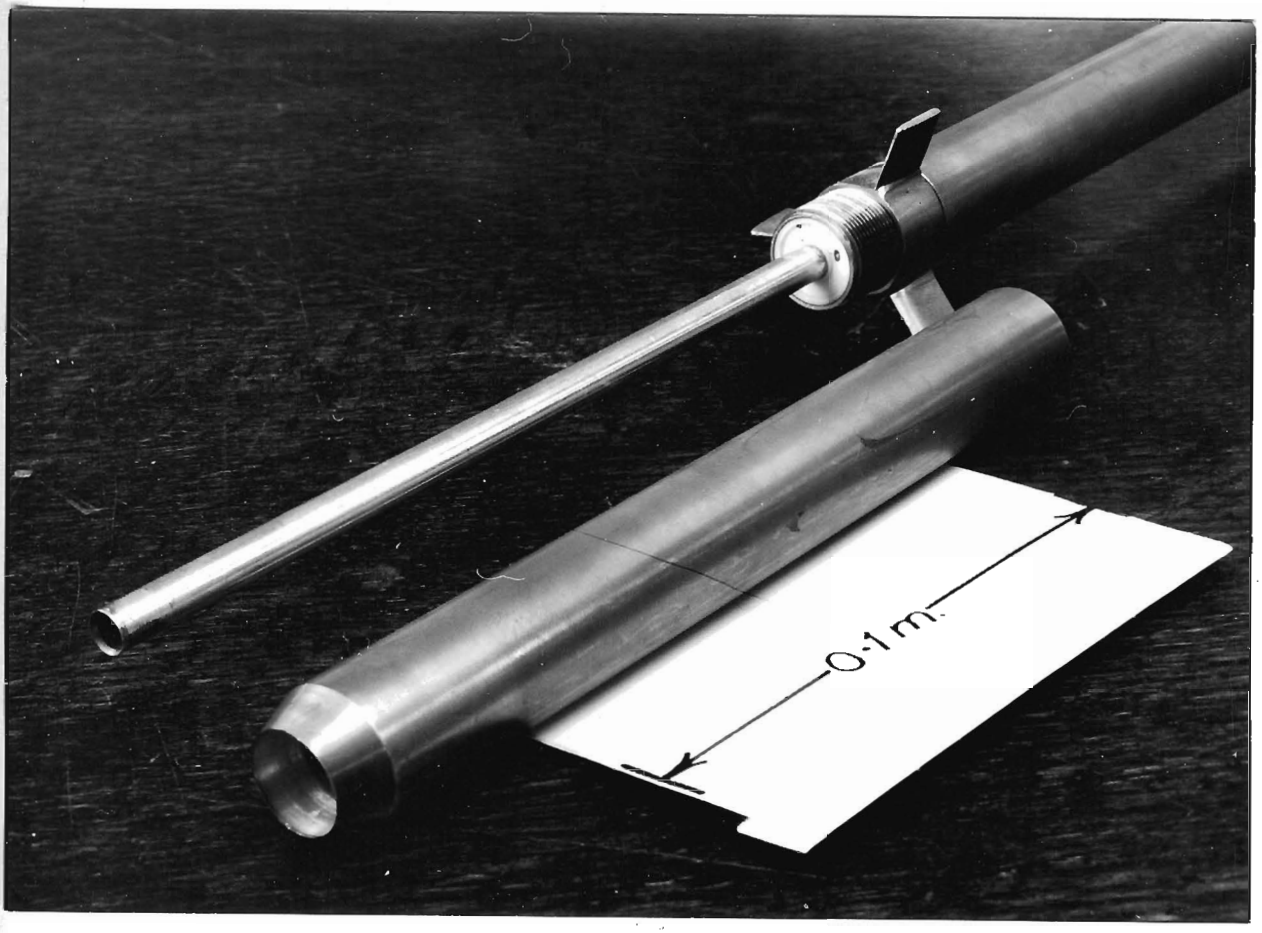


Fig.36 Coaxial probe with outer conductor removed to show inner conductor and support bead.

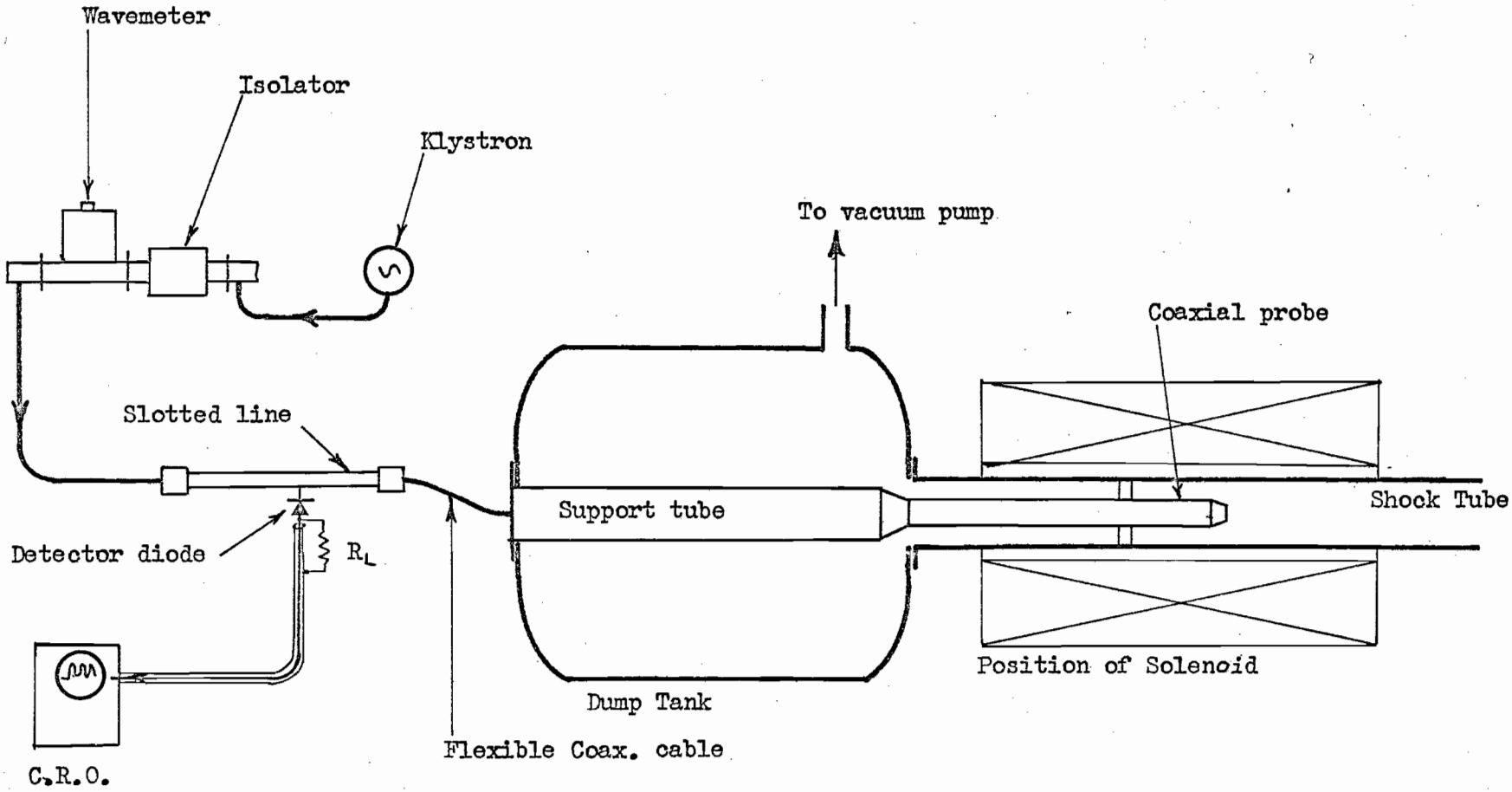


Fig.37 Coaxial probe mounted in shock tube with microwave system.

the 900-LB slotted line and standing wave probe from the mechanical shocks associated with the firing of the shock tube.

Fig. 35 shows the complete probe and support tube, Fig. 36 shows in detail the probe with the outer conductor removed, and Fig. 37 shows the mounting of the probe in the shock tube , together with the microwave system used.

The ends of the inner and outer conductors were carefully machined to give a sharp edge, with the inner faces parallel to the flow, to avoid the generation of standing shocks between them, and the inner conductor was drilled to a depth sufficient to prevent the reflected shock inside it from returning to the main flow during the running time. Great care was taken between runs to keep the mouth of the coaxial probe sharp and parallel to the flow, and to keep the inner and outer conductors coaxial.

As can be seen in Fig.34,the final 154 mm length of the inner conductor is supported only at the bead end, and faces into the shock tube flow. In practice this proved sufficiently rigid to withstand the dynamic forces of the hypersonic plasma-flow without bending.

A tendency for the inner conductor to become unscrewed during a run was initially treated by using "Loctite" epoxy thread-locking compound. Unfortunately, this introduced an effective series impedance into the inner conductor and gave rise to incorrect reflection measurements. A final cure was effected by "soldering" Indium onto the contact surfaces of the inner and outer conductors. This provided effective electrical continuity of the conductor skin, and, being a soft metal, provided mechanical locking.

Microwave system.

[see Fig. 37]

A Saunders CLC 7 - 12 tunable , low power, klystron was used in the CW mode as a microwave source. The signal was then passed through an X - band waveguide isolator and calibrated wavemeter (these being available, and thus cheaper than coaxial components). The signal was then transformed back to a coaxial cable and passed, via a GR874-LK10L adjustable length air line, through the 900-LB precision slotted-line and into the rear end of the coaxial probe.

Essentially the simplest microwave circuit possible was chosen, and all components from the detector probe to the plasma reflection interface were of the GR- 900, low loss, low VSWR, type. In this way reflections originating from connectors, and other discontinuities, were kept extremely low, and the added complication of matching stubs and the like was not required. The 900-BT connectors used have a VSWR < 1.01 at 9 GHz.

The attenuation in the air line,and in the flexible coaxial cable, can be measured and the measured value of R_v corrected.

The slotted - line probe - carriage (55) carried an adjustable tuner with an adjustable fine wire probe, and a 1N23 type microwave diode. Initially this was connected, by a short length of coaxial cable, to the 1 MΩ , 1 mV/cm input of the 1A6 plug-in of a Tectronix 551 oscilloscope, using a 500 kΩ shunt load resistor at the diode. Unfortunately the rise-time of the system (including the capacitance of the coaxial cable),in response to a square-wave input, was too great. By reducing the load resistor to 330Ω an acceptable rise-time (< 0.3 μs) was achieved, but at the expense of a vastly reduced voltage signal at the oscilloscope input.

As there wereno attenuators in the circuit, the microwave power level was adjusted by changing the klystron cavity coupling-probe insertion-depth, and the detected signal from the diode by adjusting he detector probe insertion into the coaxial slotted line.

Ideally, it should be possible to obtain low-power microwave diodes having a guaranteed square-law response. In practice the diodes commercially available are seldom exact square-law devices, and so must be calibrated.

If we define a response index n by

$$V_d \sim (V_m)^n \qquad (4.24)$$

where V_d = diode output voltage,
and V_m = microwave voltage,

then, in practice, n varies with the diode load-resistance, and, crucially, n also varies vastly from diode to diode.

A selection process was undertaken, and some 30 different diodes (the encapsulation being the only limit to the choice) were calibrated to choose those with the lowest n. In this batch some diodes had an n as high as 5 (5th law diodes!). Finally, two diodes (a IN23B and a IN21B), having sufficiently high output and an n of 1.9— 2.2, were selected.

The method used to calibrate the index of the diode is the self-consistent method described by Montgomery [(56) p.497], which requires only an accurately calibrated vernier scale on the slotted line and a stable microwave source. No calibrated microwave attenuators are needed. This method uses the fact that, when the line is fully short-circuited (S/C) or open-circuited (O/C) at the load end, the envelope voltage of the standing waves in the slotted line is given

by:

$$V_m = \left| 2\, V_o \sin 2\pi \left(\frac{x - x_o}{\lambda} \right) \right| \qquad (4.25)$$

as shown in Fig. 38.

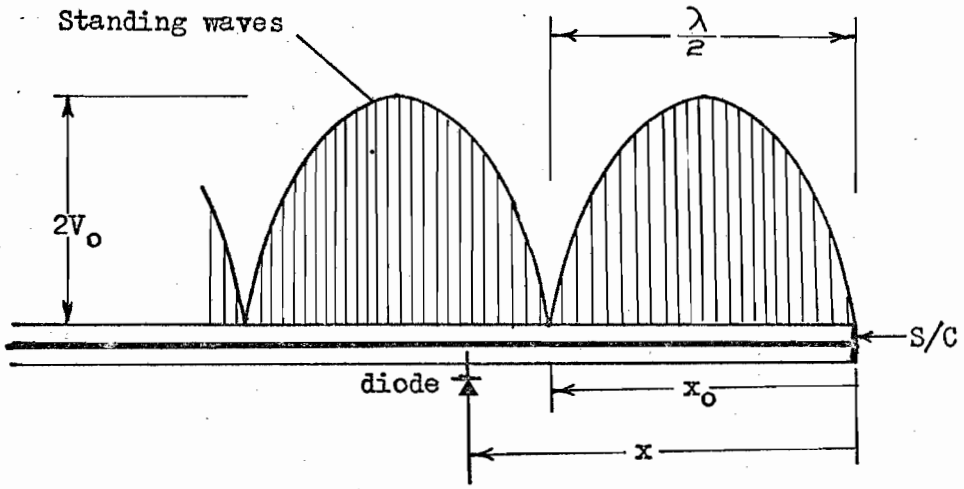


Fig.38 Diode calibration.

λ = wavelength of microwaves.

Combining Equations (4.24) and (4.25) and taking logarithms, we get:

$$\log_{10} V_d = \text{Const.} + n \log_{10} \left(\sin 2\pi \frac{(x - x_o)}{\lambda} \right) \qquad (4.26)$$

The required index n is then the slope of the $\log_{10} V_d : \log_{10} \left(\sin 2\pi \frac{(x - x_o)}{\lambda} \right)$ curve as shown in Fig. 39. This method proved extremely accurate in practice, as it depends only on the self-consistency of the slotted-line linear-scale.

For the diodes used, n drifted only slowly with time, and it was found that calibration was necessary only every few days. By restricting the diodes to very low signal levels, the constancy of the particular power law of the diode in use was ensured during shock tube runs.

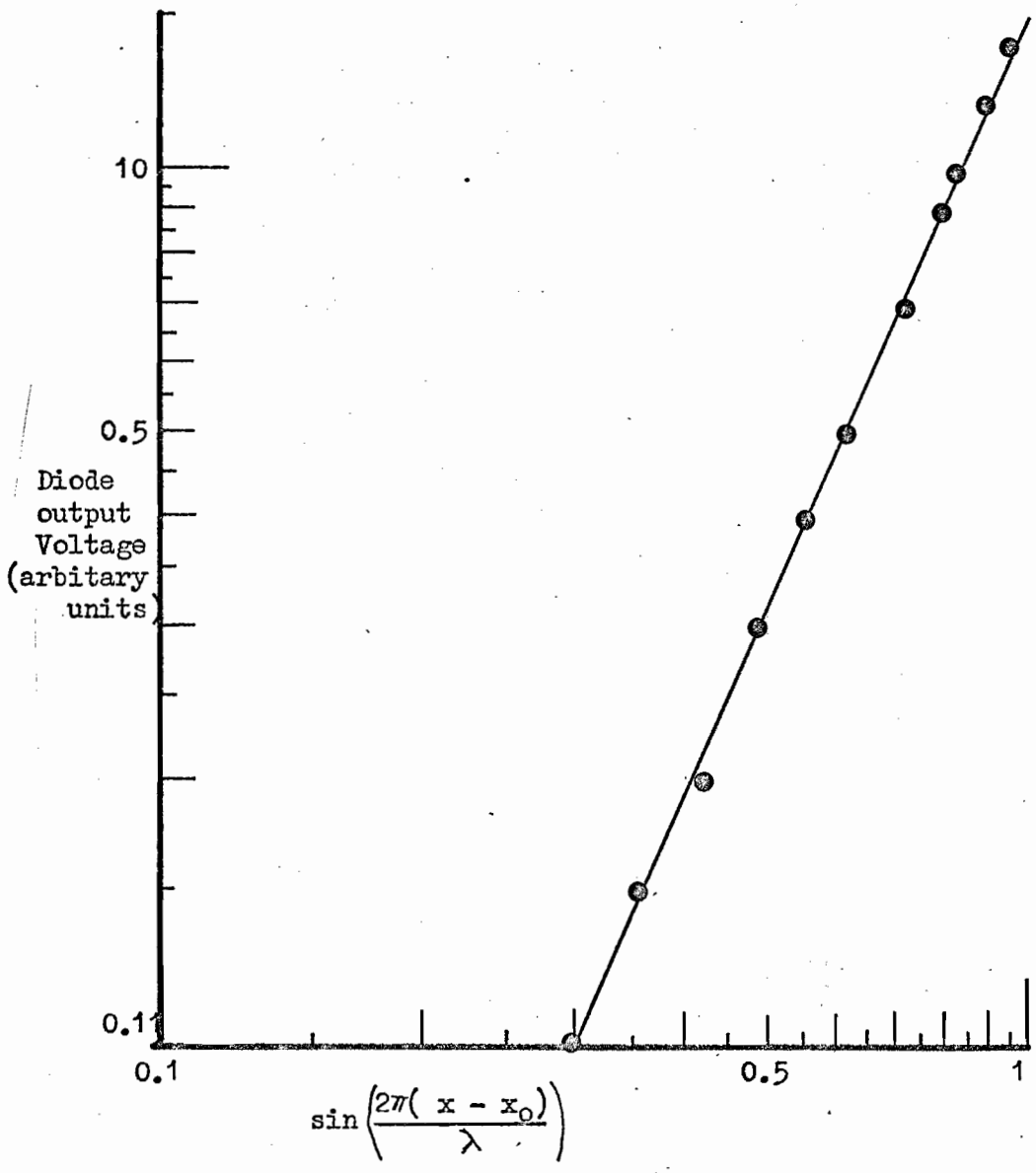


Fig.39 Calibration curve for 1N23B microwave diode.

$n = 2.2 \pm 0.1$ (12/6/1968)

$R_L = 330\,\Omega$

The attenuation, α , in the Air-line between the detector and the plasma reduces the measured reflection coefficient by a factor α^2 :-

$$R_{eff} = \alpha^2 R_{plasma} \qquad (4.27)$$

α^2 was measured by replacing the outer conductor of the probe by an equal length adaptor to take a 900-WO O/C termination ($R > 0.999$) The reflection coefficient ($R_{eff.} = \alpha^2$ in this case) was then measured by using the 'width of minimum' technique (55), and the measured reflection coefficient corrected to give the true plasma reflection coefficient. The coaxial probe used gave $\alpha^2 = 0.88 \pm 0.01$ at a microwave frequency of 9 GHz.

A further, at first less obvious, correction must be made for the effective source reflection, R_S , of the microwave-source system.

Again all the attenuations and reflections in the microwave-source system are lumped together to give an effective source reflection coefficient , connected to the slotted line by a lossless matched transmission line (an application of Thévenin's theorem!).

In normal reflection coefficient measurements, where the source to load distance is constant and the detector is moved along the slotted line to detect the maxima and minima of the standing wave, the source reflection effects do not change with probe movement and may be neglected. However, when the detector is stationary and the load is moved to detect the maxima and minima, the changing electrical line length will change the effective source voltage V_S (Fig.40).

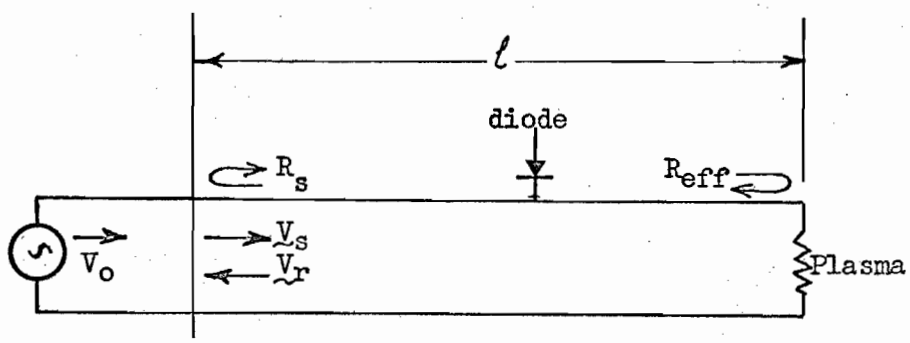


Fig.40 Microwave source reflection.

Here $$\underset{\sim}{V}_s = \underset{\sim}{V}_o + R_s \underset{\sim}{V}_r$$
$$= \underset{\sim}{V}_o + R_{eff} R_s e^{j\frac{4\pi\ell}{\lambda}} \underset{\sim}{V}_s .$$

i.e. $$\underset{\sim}{V}_s = \frac{\underset{\sim}{V}_o}{1 + R_{eff} R_s e^{j\frac{4\pi\ell}{\lambda}}} \qquad (4.28)$$

From Equation (4.27) it can be seen that V_s varies from a maximum of $\frac{V_o}{1 - R_{eff} R_s}$ to a minimum of $\frac{V_o}{1 + R_{eff} R_s}$ when ℓ is changed by $\frac{\lambda}{4}$.

If ℓ is adjusted so that at a minimum of the standing wave, V_s is at a maximum, then the measured minimum voltage will be

$$V_{min} = V_o \frac{(1 - R_{eff})}{(1 - R_{eff} R_s)} .$$

If, then, without moving the detector, the load is moved towards the detector by $\frac{\lambda}{4}$, the voltage maximum will be

$$V_{max} = V_o \frac{(1 + R_{eff})}{(1 + R_{eff} R_s)}$$

and the measured VSWR will be

$$S = \frac{V_{max}}{V_{min}} = \frac{(1 + R_{eff})(1 - R_{eff} R_s)}{(1 - R_{eff})(1 + R_{eff} R_s)} \qquad (4.29)$$

(4.29) is then solved for R_{eff} in terms of the measured VSWR. To measure R_s, the coaxial probe is replaced by an O/C at the end of the slotted line, and the variation of the maximum ($2V_s$) voltage is measured, while changing the length of the adjustable line between the source and the slotted line. For the system used at 9 GHz, $R_s = 0.02$, growing to 0.08 at 7.5 GHz.

The choice of V_s maximum at the standing wave minimum was to reduce S and thus increase the maximum R_{plasma} that could be measured. The alternative viable choice of V_s minimum at the standing wave minimum has the opposite effect, and any intermediate setting would involve the use of a Smith Chart to recover R_{eff}.

The attenuation α^2 also serves to increase the maximum R_{plasma} which can be measured for a given maximum S.

An Algol computer program was written to compute R_{plasma} from the measured maximum and minimum detector diode voltages, corrected for R_s, α, and the diode n, and the Mach No. M_s from the shock speed measuring system output (p.10).

A further program computed n_e, ω_p, $\frac{\omega_p}{\omega}$, $\frac{\nu}{\omega}$ for given R_{plasma} and collision frequency ν. The "Regula Falsi" iteration scheme was used to find the roots of Equations (4.12), (4.13) and (4.16) (p.60) for the variable n_e.

4.4 Construction and Calibration of Rectangular Waveguide Probe.

As a further check on the coaxial microwave probe results, an X-band probe of the same length was fabricated from ~~25.4~~ 22.8 mm x ~~12.7~~ 10.2 mm rectangular waveguide (W.G. 16), as shown in Fig. 41.

Additional strength to withstand the internal pressure (4 MN / m^2 max) behind the reflected shock inside the guide is provided by shrink-fitting a larger waveguide (having internal dimensions equal to the external dimensions of the X-band) over the X-band waveguide. This doubled the effective wall thickness, to 2.54 mm .

The vacuum seal and microwave window differed from the coaxial probe in that it was positioned at the first waveguide joint outside the dump tank.

This seal was effected by clamping a 0.25 mm thick Mylar diaphragm between a choke waveguide flange (carrying an O-ring) on the near end of the probe and a plane waveguide flange. This gave a VSWR of 1.14 . A lower VSWR of 1.03 was obtained by inserting a 27 mm long PTFE matching-plug behind the diaphragm, and tuning the microwave frequency to give the minimum VSWR (9.11 GHz).

As the diaphragm bows under the reflected shock pressure, the matching plug was pushed back into contact with the diaphragm after each run.

The diaphragm seal was pressure tested (using water) to 8 MN / m^2 at room temperature, and in practice proved able to stand the combined high pressure and temperature behind the reflected shock in all but one very high M_s , p_o = 10 Torr, run. There was

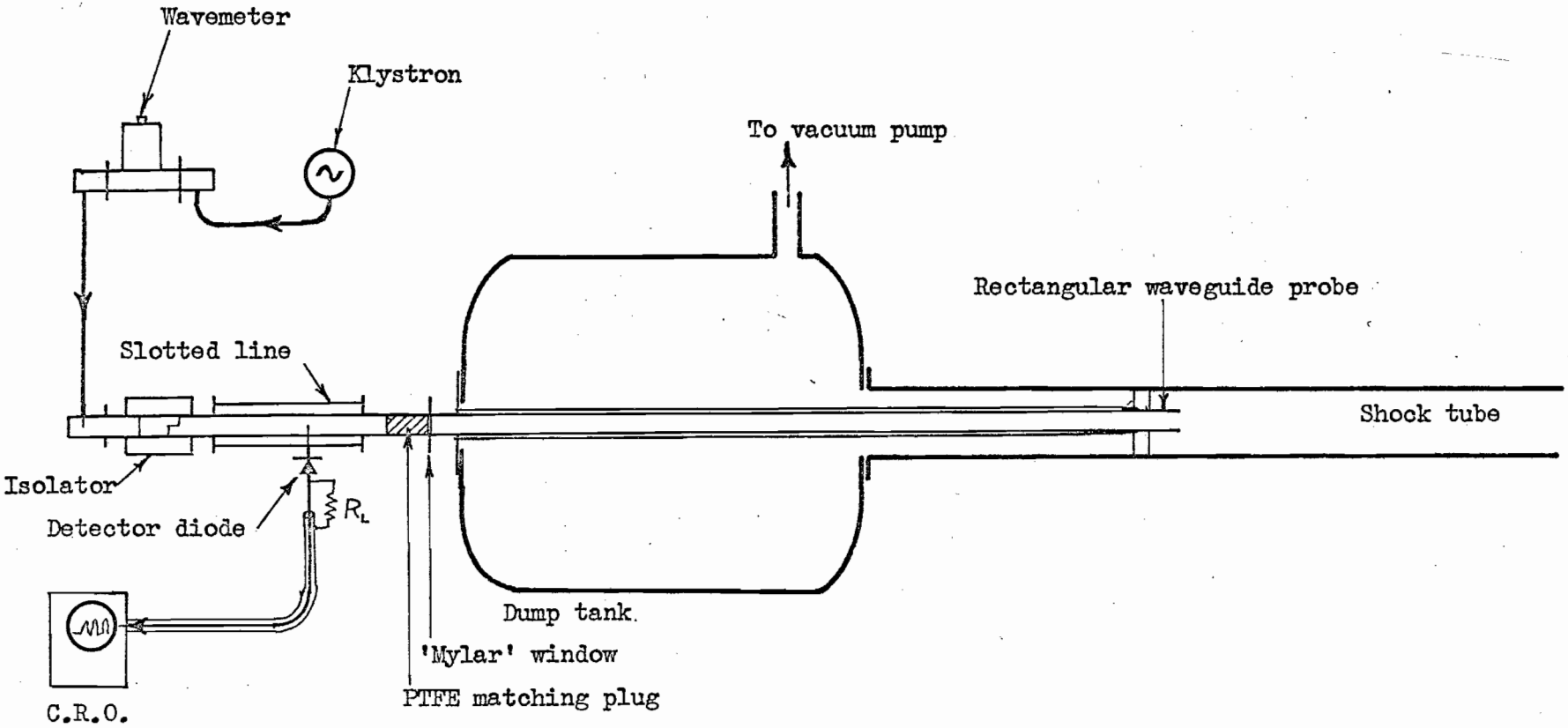


Fig.41 Rectangular waveguide probe mounted in shock tube with microwave system.

some ablation of the Mylar, and consequently the diaphragms were changed every few runs.

As with the coaxial probe, the attenuation ($\alpha^2 = 0.89 \pm 0.01$) and source reflection ($R_s = 0.02 \pm 0.01$) were measured and corrected. As shown on p.64 all the analysis for reflection in a coaxial line can be used with waveguide by replacing $\frac{\omega_p}{\omega}$ by

$$\left(\frac{\omega_p}{\omega}\right)_w = \frac{\omega_p}{\omega} \frac{1}{\left(1-\left(\frac{\omega_{co}}{\omega}\right)^2\right)^{\frac{1}{2}}}$$

where ω_{co} is the waveguide cut-off frequency. Thus the computer programs developed for the analysis of coaxial line results were used, with slight modification, for the waveguide probe results.

As the encapsulation required by the detector-diode mount on the X-band rectangular-waveguide slotted-line differed from that of the coaxial slotted-line, diodes having index $n \sim 2$ were again chosen from a selection of 30. An AEI C59-B diode, having an n of 2.1 ± 0.1 , was finally used.

4.5 Electron Collision Frequency.

If both the magnitude and phase of the microwave reflection coefficient from the plasma could have been measured, then it would, in principle, have been possible to extract both the electron density and the electron collision frequency for momentum transfer from experimental results. Similarly, if only the magnitude of the reflection coefficient were measured, as has been done here, then by taking experimental results at two different frequencies, it should be possible to set up simultaneous equations from Equations (4.12), (4.13) &(4.16) whose solution would give values of n_e and ν .

Unfortunately, the microwave system used limited the frequency spread to the range from 7.5 to 9.5 GHz. The loci of curves of constant $|R_v|$ at 9 and 7.5 GHz (the two frequencies used with the coaxial probe) on the $\nu : \omega_p$ plane for given p_o and M_s are nearly parallel, and so small errors in the measurement of $|R_v|$ cause large movements in the intersection points of the two curves. This makes extraction of both n_e and ν to any accuracy very difficult.

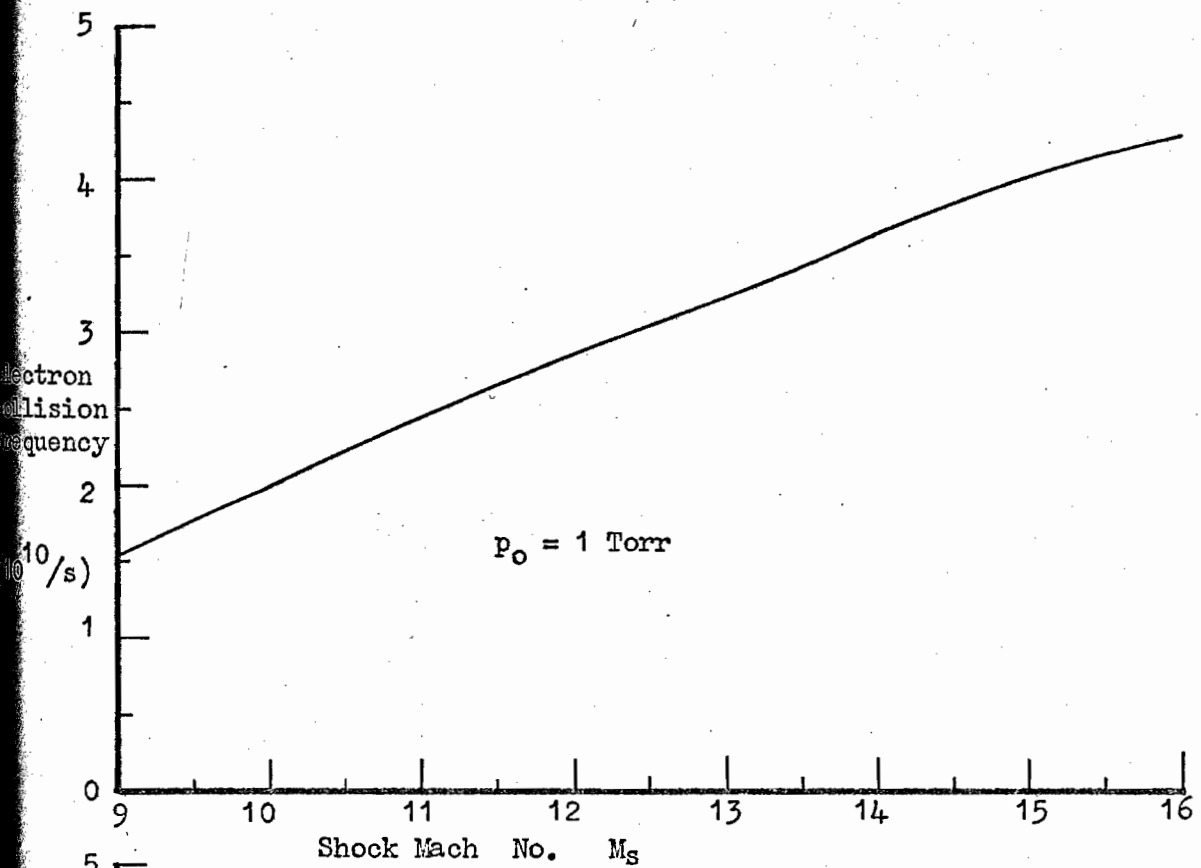
The method employed here was to use the best available published estimates of collision frequency in the evaluation of n_e from experimental results, and then to see if these values of n_e are the same at 9 and 7.5 GHz.

In analysing his rectangular waveguide results, Laird (1) assumed for $p_o = 2$ Torr that $\nu = 3.5 \times 10^{10}$ /sec , and was approximately constant for the range of M_s used.

Shkarofsky, Bachynski and Johnson (51) have carefully compiled the best estimates of the electron collision cross-sections for the main constituent molecules of high temperature Air, and have computed the electron collision frequencies for monoenergetic electrons in terms of Air temperature and density. They have also (52) averaged these over a Maxwellian distribution of electron velocities for equal electron and gas temperatures. Fig. 4 of (52) gives ν in terms of temperature and density: from these curves, by using (as before) the shock tube charts of Lewis & Burgess (6), values of ν in terms of p_o and M_s were obtained.

Fig. 42 shows these curves of $\nu : M_s$ for $p_o = 1$ and 10 Torr, used to compute n_e from the microwave probe results.

Note that, contrary to Laird's assumption of constant ν , ν does vary by a factor of at least 2 in the range $M_s = 8 - 12$.



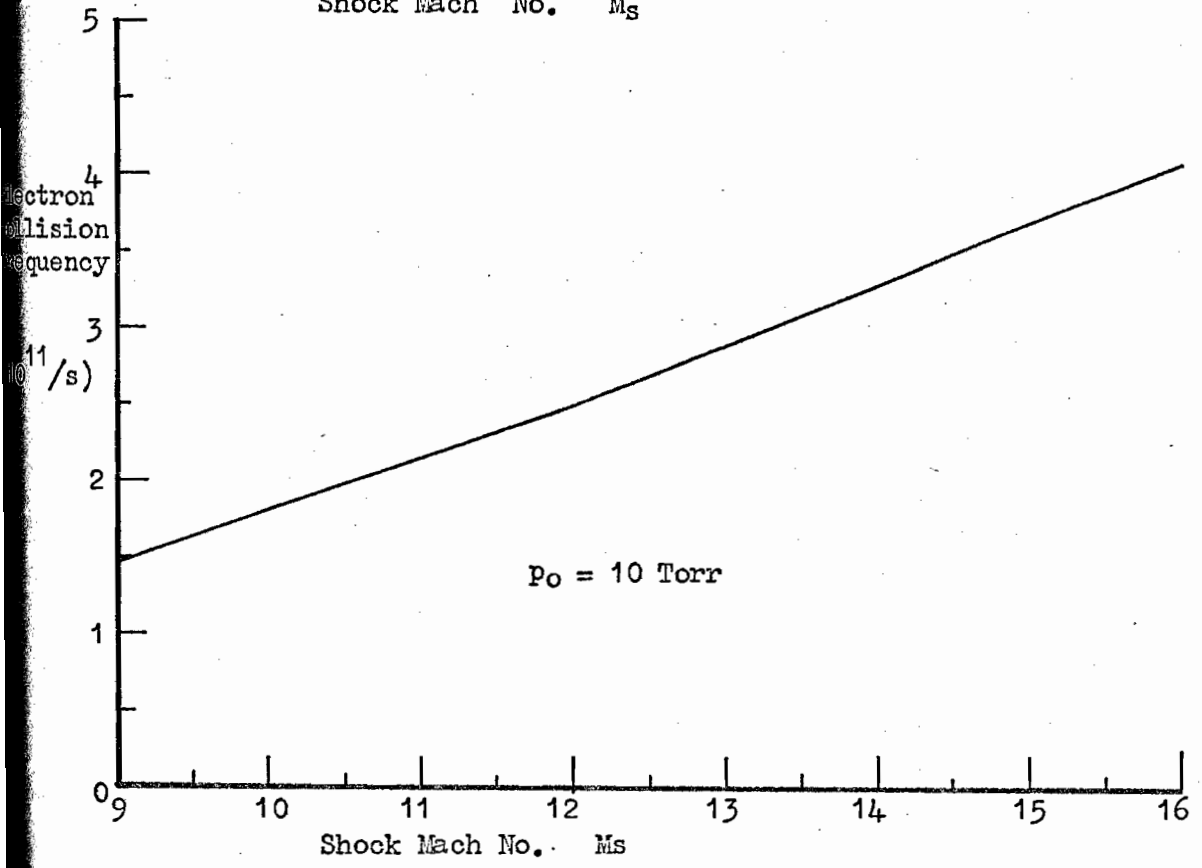


Fig 42 Electron collision frequency behind incident shock.

Based on Bachynski, Johnson & Scharofsky (52).

4.6 Electron Density : Experimental Results.

The coaxial probe was used at frequencies of 9 and 7.5 GHz for shock tube runs having initial pressures of p_o = 1 and 10 Torr dry Air and a range of Mach numbers of M_s = 9 - 13.5.

Later, the rectangular X-band waveguide probe was used at 8.98 and 9.11 GHz (different matching-plugs) for runs having p_o = 1, 10 Torr and M_s = 9 - 12. The X-band probe was not used at 7.5 GHz , partly because this is near the cut-off frequency, and partly because previous coaxial runs had confirmed the values of ν used.

Typical probe standing wave oscilloscope traces are shown in Fig. 43 (coaxial probe) and Fig. 44 (rectangular waveguide probe).

By considering the reflection from a slab of lossy ($\nu > 0$) plasma as its thickness increases, Laird (1) has shown that, for the values of ν and n_e to be considered, a plasma slab greater than 3 wavelengths thick may be considered to be infinitely thick.

An alternative approach is to consider the attenuation of the transmitted wave through the slab :-

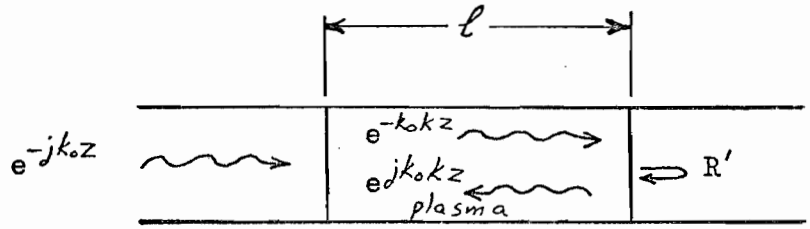


Fig. 45 Transmission through slab.

The fraction of the magnitude of the transmitted wave which, after reflection from the back face of the slab, reaches the front

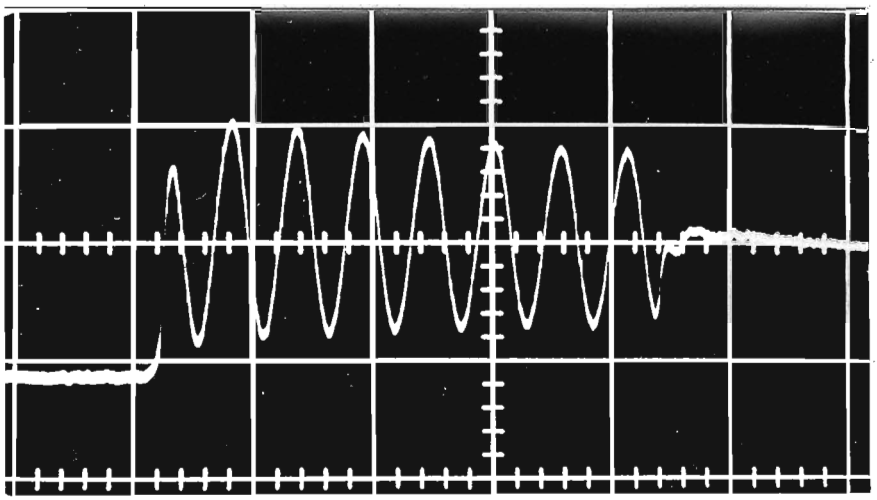


Fig.43 Typical coaxial microwave probe trace: Run 188

2 mV/division

10 μs/division

Microwave frequency = 7.5 GHz

p_o = 10 Torr Air

$|R_v| = 0.413$

$\frac{\omega_p}{\omega} = 3.211$

$\frac{\nu}{\omega} = 4.265$

$n_e = 7.2 \times 10^{18}/m^3$

$M_s = 10.6$

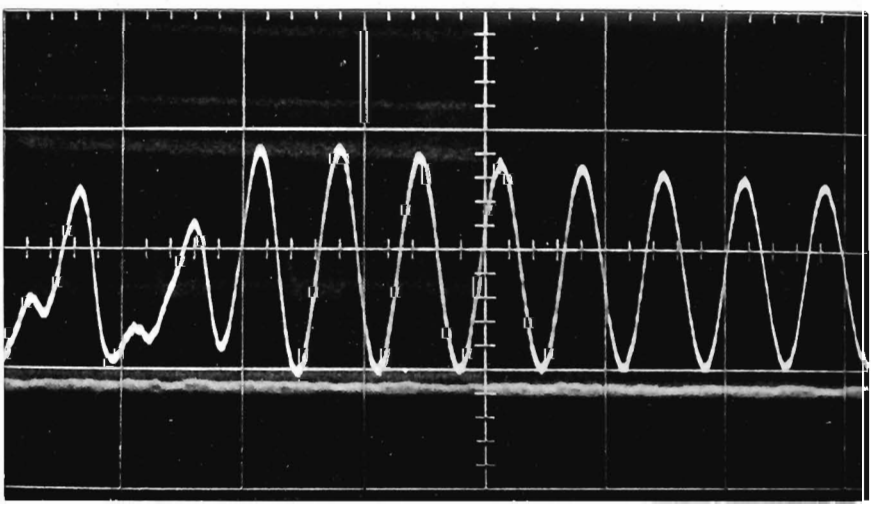


Fig.44 Typical rectangular waveguide probe trace: Run 285

2 mV/division

10 μs/division

Microwave frequency =8.98 GHz

p_o = 1 Torr

$M_s = 10.3$

$|R_v| = 0.559$

$\frac{\omega_p}{\omega} = 0.792$

$\frac{\nu}{\omega} = 0.376$

$n_e = 6.3 \times 10^{18}/m^3$

face again

$$= e^{-2k_0 k^i \ell} R'$$

(see p.55), where R' is the voltage reflection coefficient of the rear face. Taking as a criterion that this fraction should be less than 1% if the slab is to be considered infinitely thick, and taking the extreme case where $R' = 1$, we find that, for 9 GHz microwaves, and a probe length of 152 mm,

$$-k^i \geq 0.065 \ .$$

For ν as given in Fig. 42 for $p_o = 1$ Torr, this corresponds to

$$\frac{\omega_p}{\omega} \geq 0.6 \qquad (4.30)$$

according to tables prepared from Equations (4.13) and (4.14) for shock tube plasmas. Since $\frac{\nu}{\omega} = 0.363$ for $\frac{\omega_p}{\omega} = 0.6$ we find that $|R'| = 0.101$ and so the lower limit on $\frac{\omega_p}{\omega}$ in Equation (4.30) is extremely pessimistic.

Most of the experiments at $p_o = 1$ Torr, and all of those at 10 Torr satisfy Equation (4.30), and those low M_s runs at $p_o = 1$ Torr would certainly satisfy the 1% criterion, as R' decreases rapidly with $\frac{\omega_p}{\omega}$ for $\frac{\omega_p}{\omega} < 1$. Thus the length of plasma in the coaxial probe may be considered equivalent to a semi-infinite plasma. A similar analysis is valid for the rectangular waveguide probe.

Coaxial Probe Results.

Fortunately an open coaxial line is not well matched to the propagating modes of the circular waveguide formed by the shock tube wall, and so presents a near open - circuit termination up to the time that the shock enters the line. The slotted line probe was moved to a voltage minimum of the standing wave due to this O/C and the

small magnitude of this minimum measured before each run. This voltage minimum is traced out during each run just before the standing wave pattern (Fig.43), and enables the true signal zero to be determined in spite of any oscilloscope-zero drift immediately before the run.

Measurements were taken on the maximum and minimum approximately $\frac{\lambda}{2}$ before the shock reflecting from the bead terminated the standing wave trace (Fig.43).

Figs. 46 & 47 show plots of n_e: M_s for p_o = 1 & 10 Torr dry Air, together with the predicted equilibrium density from Fig.6. The computed electron densities for runs at microwave frequencies of 9 GHz (circles) and 7.5 GHz (squares) are plotted for $\nu = \nu_c$ (the collision frequencies given in Fig.42) [blocked in points] and also for $\nu = 10\nu_c$ and $\nu = 0.1\,\nu_c$ (outlined points).

Since $n_e \sim \left(\frac{\omega_p}{\omega}\right)^2$, it can be seen from the $|R_v|$: $\frac{\omega_p}{\omega}$ Plot in Fig.33 that, for regions of very high $|R_v|$ and very low $|R_v|$, n_e is very sensitive to variations in $|R_v|$. The error bars for n_e in Figs. 46 & 47 were computed by perturbing the measured variables V_{max}, V_{min}, α^2, and n over their estimated ranges of accuracy, using the computer programs previously written. As expected, they show that the estimated accuracy is poor for p_o = 1 Torr at high M_s, and for p_o = 10 Torr at low M_s.

Examination of Figs 46 & 47 shows that for $\nu = \nu_c$ the 9 and 7.5 GHz results are consistent, but they separate slightly for $\nu = 10\nu_c$ and for $\nu = 0.1\,\nu_c$. From this it is concluded that the values of electron collision frequency used (i.e. ν_c), derived from those given by Bachynski, Johnston & Shkarofsky (52) are correct to within a factor of 2.

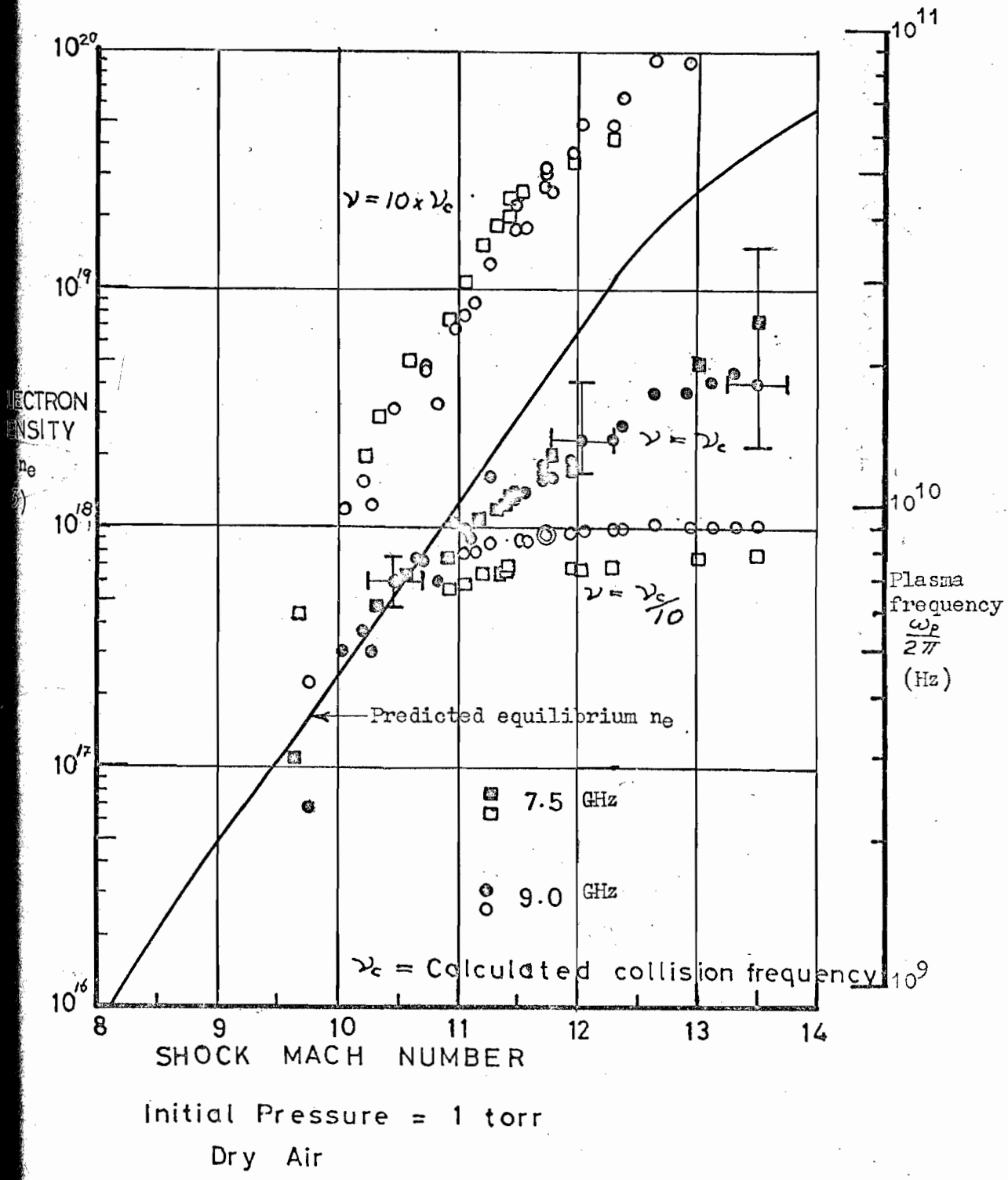


Fig.46 Electron number density behind incident shock, from coaxial probe results. p_o = 1 Torr.

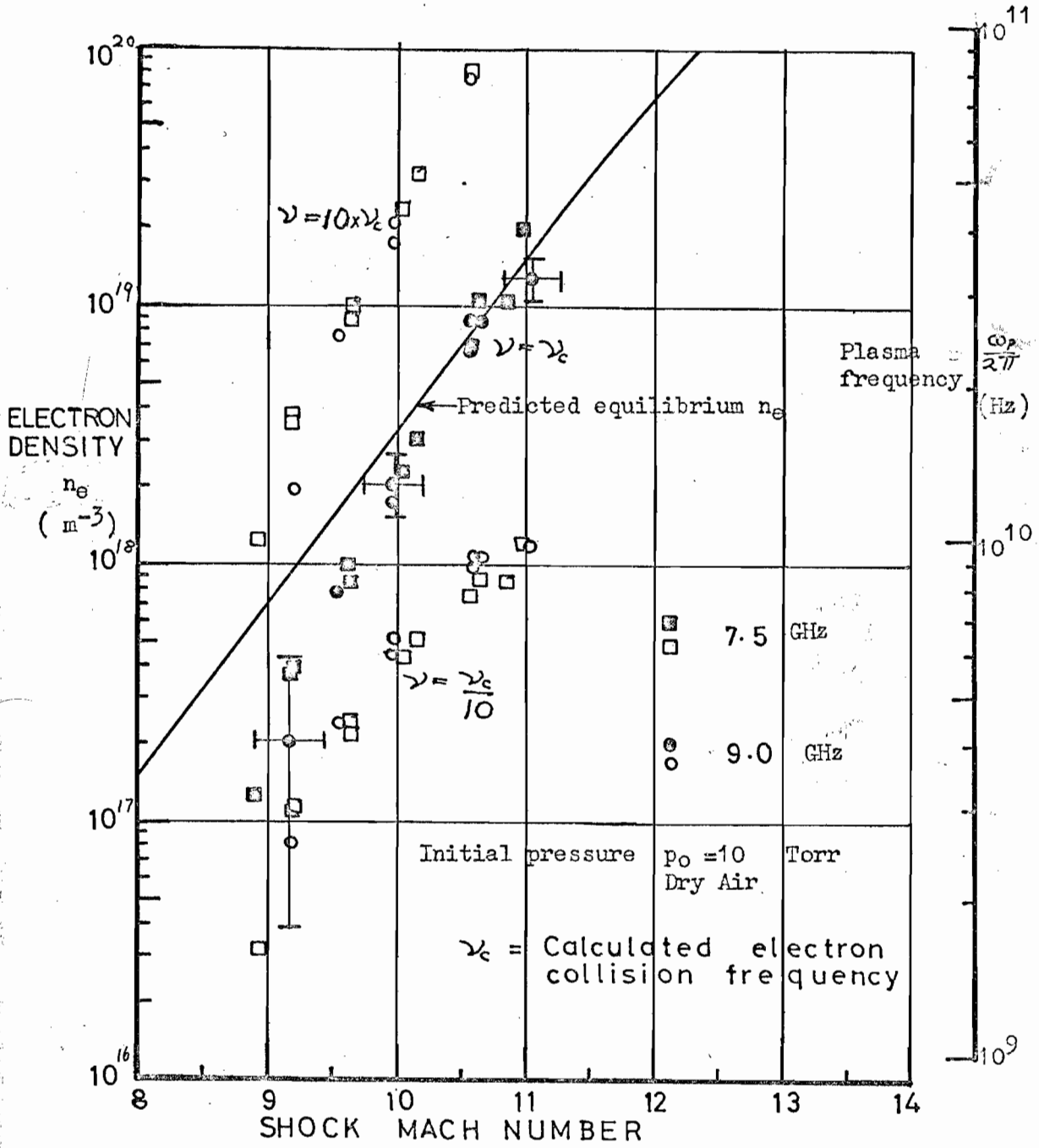


Fig.47 Electron number density behind incident shock from microwave coaxial probe results. p_o = 10 Torr.

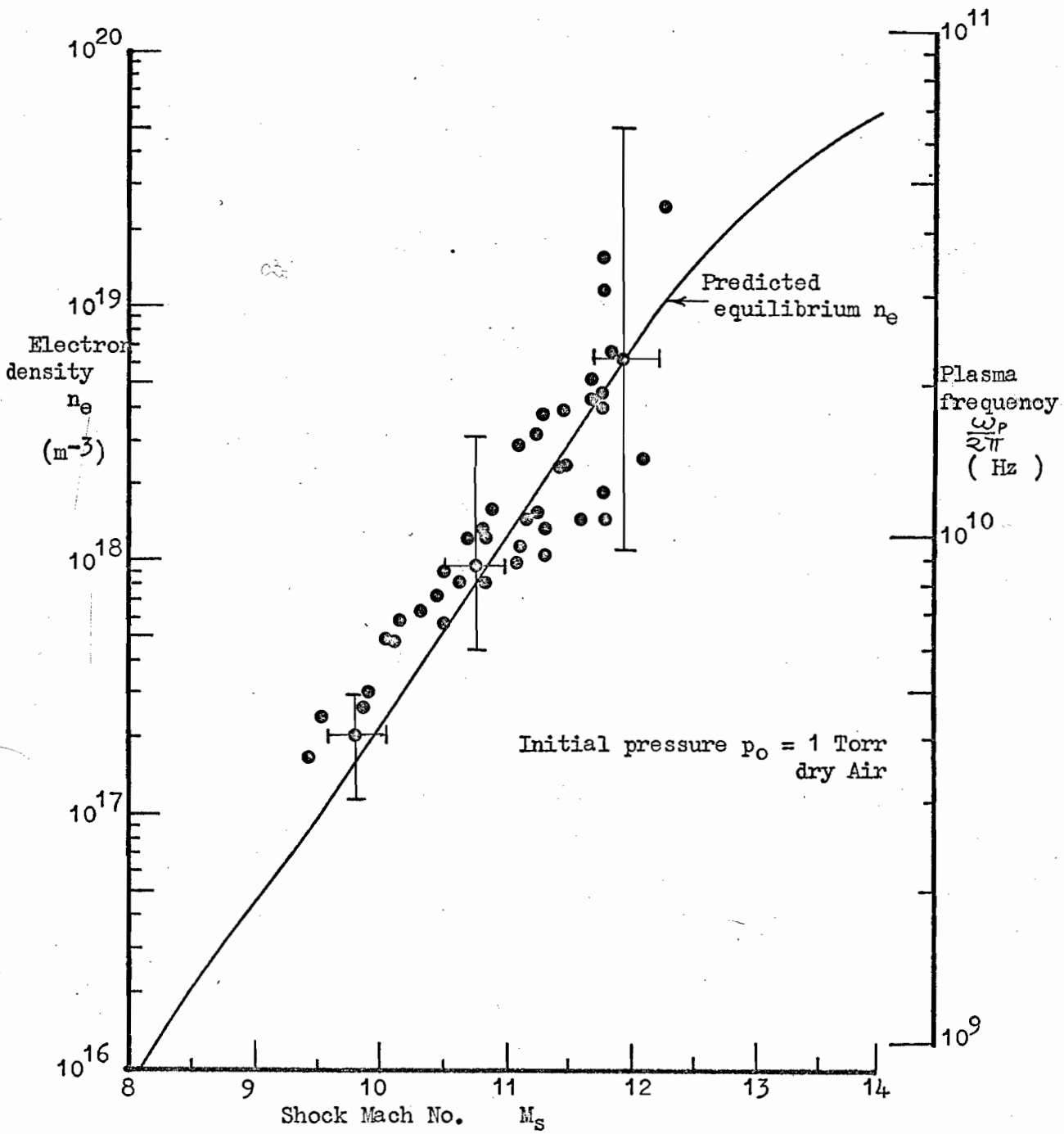


Fig.48 Electron number density behind incident shock from microwave rectangular waveguide probe resuls. p_o = 1 Torr.

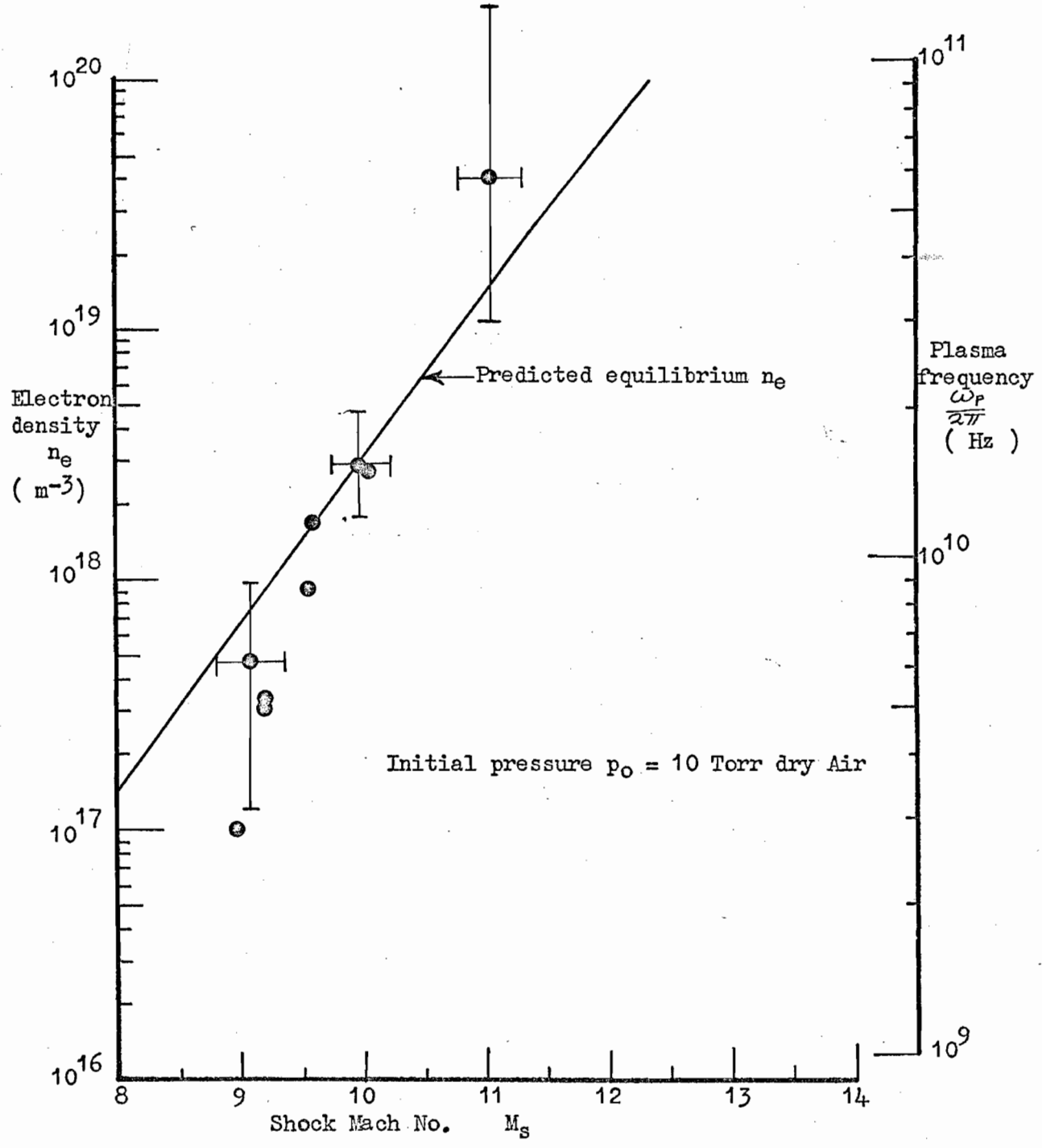


Fig.49 Electron number density behind incident shock from microwave rectangular waveguide probe results. p_o = 10 Torr.

A scale of plasma frequency [$\frac{\omega_p}{2\pi} = 8.979\sqrt{n_e}$ Hz] is also given on Figs.46 - 49 .

Figs. 48 & 49 show the equivalent results for the rectangular waveguide probe, for microwave frequencies of 8.98 and 9.11 GHz and for $\nu = \nu_c$.

The maximum and minimum measurements were taken at the same number of wavelengths from the probe orifice as with the coaxial probe.

As will be seen from the initial waves for a typical waveguide probe run (Fig.44), the rectangular waveguide TE_{10} mode couples with cylindrical waveguide modes in the shock tube, and so the method of obtaining a zero-line used in the coaxial probe case cannot be used. In spite of photographing zero-lines before and after each shock tube run, some oscilloscope drift was encountered, and, as can be seen in Fig. 48, the scatter of experimental results is greater than for the coaxial probe results. This is aggravated at high M_s . With estimates of this possible zero-drift included, the estimated accuracy of the electron density results (computed in the same manner as the coaxial accuracies) is poorer than in the coaxial case. This can be seen in the greater spread of the error bars in Figs. 48 & 49 as compared with those in Figs. 46 & 47.

The coaxial and waveguide results agree well with each other for $p_o = 10$ Torr and are close to the equilibrium electron density curve.

At $p_o = 1$ Torr the waveguide probe results again agree well with the equilibrium curve (albeit with a large scatter), but the coaxial probe results diverge below the equilibrium electron densities at high Mach numbers.

Fig. 50 shows the plasma entry orifices of both probes. The inner and outer walls of the coaxial probe are only 4.04 mm apart, whereas the faces of the waveguide are 10.16 mm apart. The growing boundary layers behind the shock reduce the effective electron density far more in the coaxial probe than in the waveguide. This is accentuated at low p_o and at high M_s , when n_e is high. At $M_s = 13.5$ the 99% velocity boundary layer thickness is 0.9 mm [for $p_o = 1$ Torr] one wavelength behind the shock..

Another effect is due to the attenuation of the shock by these boundary layers. Most of the plasma in the probe has been created in the shock tube before reaching the orifice of the probe. There is, however, a short (5 - 10 mm) section immediately behind the shock which has been created by the slightly slower shock in the coaxial probe, and this will have a slightly smaller n_e . At low M_s , n_e is low, $k^i < 1$, this section is relatively transparent to microwaves, and the main reflection processes occur in the shock tube produced plasma. However, at high M_s , and high n_e , k^i increases until at $\frac{\omega_p}{\omega} = 3$, $k^i = -2.5$, the transmitted wave attenuates rapidly, and the main reflection processes occur in the region of lower electron density just behind the shock, giving a low measured n_e .

Measurement of the distance between successive minima of the reflection trace does show apparent shock attenuation, but the changing phase of the reflection coefficient as the length of plasma in the probe grows makes absolute measurements of this inaccurate.

The shock in the rectangular waveguide probe , of course, attenuates much less, and this effect is negligible.



Fig.50 Comparison of coaxial and rectangular microwave probe orifices.

Nevertheless, the curves in Figs. 46 - 49 proved a calibration of the shock tube - probe system for the plasma parameters $\frac{\omega_p}{\omega}$ and $\frac{\nu}{\omega}$ in terms of p_o and M_s, to sufficient accuracy so that one could proceed with confidence to conduct experiments with an axial magnetic field applied to the plasma.

Furthermore, the rectangular waveguide probe results confirm the validity of using the computed equilibrium electron density curves of Fig.6 to predict the electron and ion number densities behind the incident shock in Air, and justify the use of these curves in Chapter 3 for comparison with the electrostatic probe results.

5. MICROWAVE REFLECTION WITH AXIAL MAGNETIC FIELD APPLIED.

5.1 Introduction.

When a d.c. magnetic field is applied to a plasma, the effective dielectric constant for microwave interaction is no longer a scalar, but becomes a 3 x 3 tensor. This introduces anisotropy into the plasma- microwave interaction. The propagation of microwaves through this magnetised plasma can no longer be analysed by extensions of free-space and empty- waveguide theory, and Maxwell's equations must be solved again for the anisotropic case.

Radcliffe (61) has studied this phenomenon in the case of the Earth's magnetic field acting on the ionosphere, and Allis, Buchsbaum & Bers (50) have written a general theoretical treatment for waves propagating in anisotropic plasmas, both unbounded and in waveguides. Generally they have looked at the limit of zero electron collision frequency when analysing particular cases in detail.

The mathematics of microwave propagation in a magnetised plasma waveguide are equivalent to those of propagation in a ferrite-filled waveguide. Brodwin & Miller (57) have analysed the quasi-TEM mode propagation in a ferrite-filled coaxial line, and Gabriel & Brodwin (62, 63) have extended this treatment to cover generalised inhomogeneous anisotropic media.

For plasma experiments in the laboratory, boundaries are an unfortunate necessity. Ideally a boundary geometry which allows the simplest experimental system, together with the simplest theoretical analysis, would be chosen. In the case of the highly collisionally damped plasma produced by a pressure-driven shock tube, the rectangular waveguide geometry described in Chapter 4 is an excellent experimental

choice. Unfortunately, the rectangular geometry is not readily amenable to theoretical analysis when an axial magnetic field is applied.

Consequently, the coaxial transmission line geometry described in Chapter 4 has been used, and a theoretical analysis of this is given in Appendix A.

Franklin (58) has analysed the reflection of microwaves in a plasma-filled coaxial line for the particular case of zero electron collision frequency.

In the present work, an analysis, using rotating coordinate systems, is given for the non-zero electron collision frequency case and the results are compared with experimental results in Air using the coaxial microwave probe in an axial magnetic field.

Some experiments with the rectangular waveguide probe in the magnetic field were also carried out.

5.2 Theory of microwave reflection from magnetised plasma.

A field analysis of the propagation of microwaves in a coaxial line filled with a uniform magnetised plasma is given in Appendix A. In addition to the plasma parameters

$\frac{\omega_p}{\omega}$ = normalised plasma frequency,

and $\frac{\nu}{\omega}$ = normalised electron collision frequency

described in Chapter 4, the effect of the applied axial magnetic field is characterised by the parameter

$$\frac{\omega_c}{\omega} = \frac{e B_1}{\omega m_e} = \text{normalised cyclotron frequency.}$$

[A magnetic field of 1 T gives $\frac{\omega_c}{2\pi}$ = 27 GHz .]

Appendix B summarises the rotating coordinate system used in Appendix A . Appendix C describes the computer program used to solve the equations in Appendix A.

This computer program was used to compute the normalised plasma propagation wave number, $k = k^r + j\,k^i$, and the voltage reflection coefficient $|R_v|$, over the range $\frac{\omega_p}{\omega} = 0.1$ to 10 for values of $\frac{\omega_c}{\omega} = 0.1, 0.5, 1, 1.5, 2, 5$ and $\frac{\nu}{\omega} = 0, 0.1, 0.5, 1, 5$. Similar computations had already been made for the simpler case of $\frac{\omega_c}{\omega} = 0$, from the equations in Section 4.2.

Figs. 51, 52, 53, 54, & 55 show the computed real (k^r) and imaginary (k^i) parts of the magnetized plasma wave number for the ranges given above, and Figs. 56, 57, 58, 59, & 60 show $|R_v|$ plotted against $\frac{\omega_p}{\omega}$. These should be compared with the $\frac{\omega_c}{\omega} = 0$ case in Fig. 32 .

It should be made clear that the curves in Figs 51 - 60, although in non-dimensional form, are not completely universal, but apply only to a given ratio of inner and outer conductor diameter to the free-space wavelength λ_o :

$$R_1 k_o = 0.58513$$

$$R_2 k_o = 1.3475$$

where $k_o = \omega\sqrt{\mu_o \varepsilon_o} = \frac{2\pi}{\lambda_o}$

Solutions for other values of $R_1 k_o$ and $R_2 k_o$ could be computed by changing the appropriate constants in the procedure 'diseq' in the program in Appendix C, Section C.2 .

In all cases, the curves for $\frac{\omega_c}{\omega} = 0.1$ were too close to the field-free $\frac{\omega_c}{\omega} = 0$ curves to be plotted. As $\frac{\nu}{\omega}$ increases, the curves

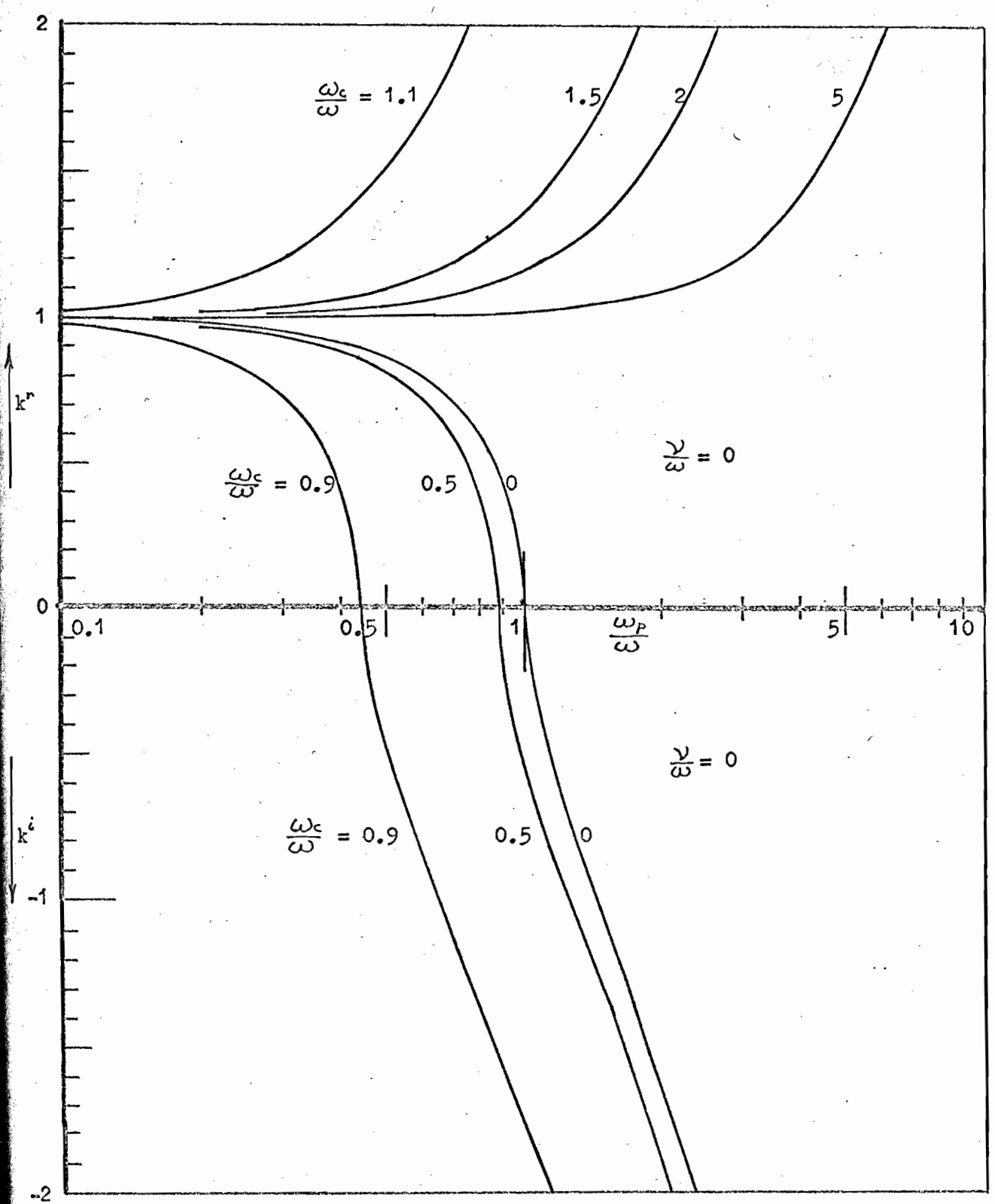


Fig.51 . Computed real and imaginary parts of wave number $k = k^r + jk^i$ for plasma filled coaxial line ($R_1 k_o = 0.585$, $R_2 k_o = 1.348$) with axial magnetic field. Normalised electron collision frequency $\frac{\nu}{\omega} = 0$.

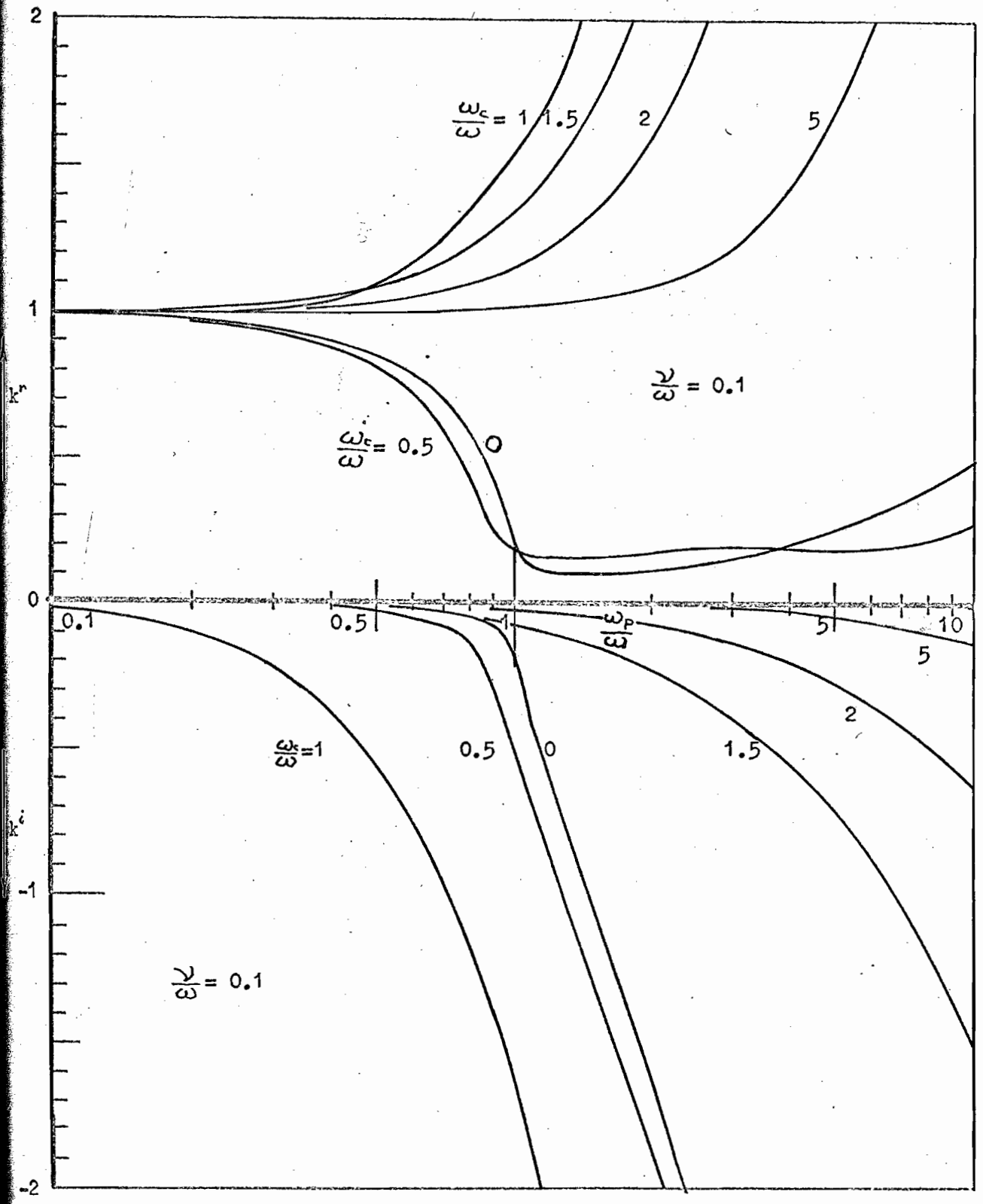


Fig.52 . Computed real and imaginary parts of wave number $k = k^r + jk^i$ for plasma filled coaxial line ($R_1 k_0 = 0.585$, $R_2 k_0 = 1.348$) with axial magnetic field. Normalised electron collision frequency $\frac{\nu}{\omega} = 0.1$.

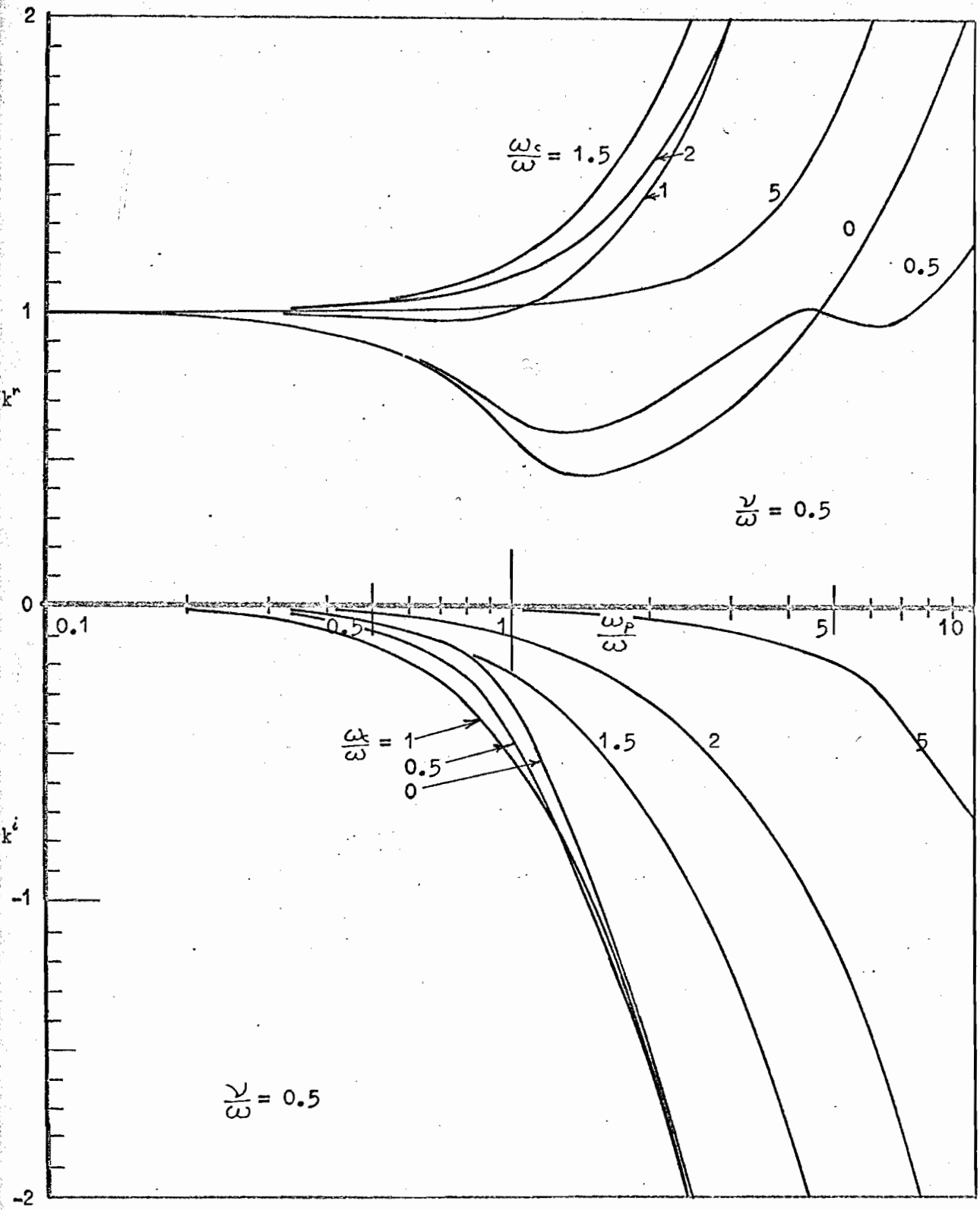


Fig. 53 . Computed real and imaginary parts of wave number $k = k^r + jk^i$ for plasma filled coaxial line ($R_1 k_o = 0.585$, $R_2 k_o = 1.348$) with axial magnetic field. Normalised electron collision frequency $\frac{\nu}{\omega} = 0.5$.

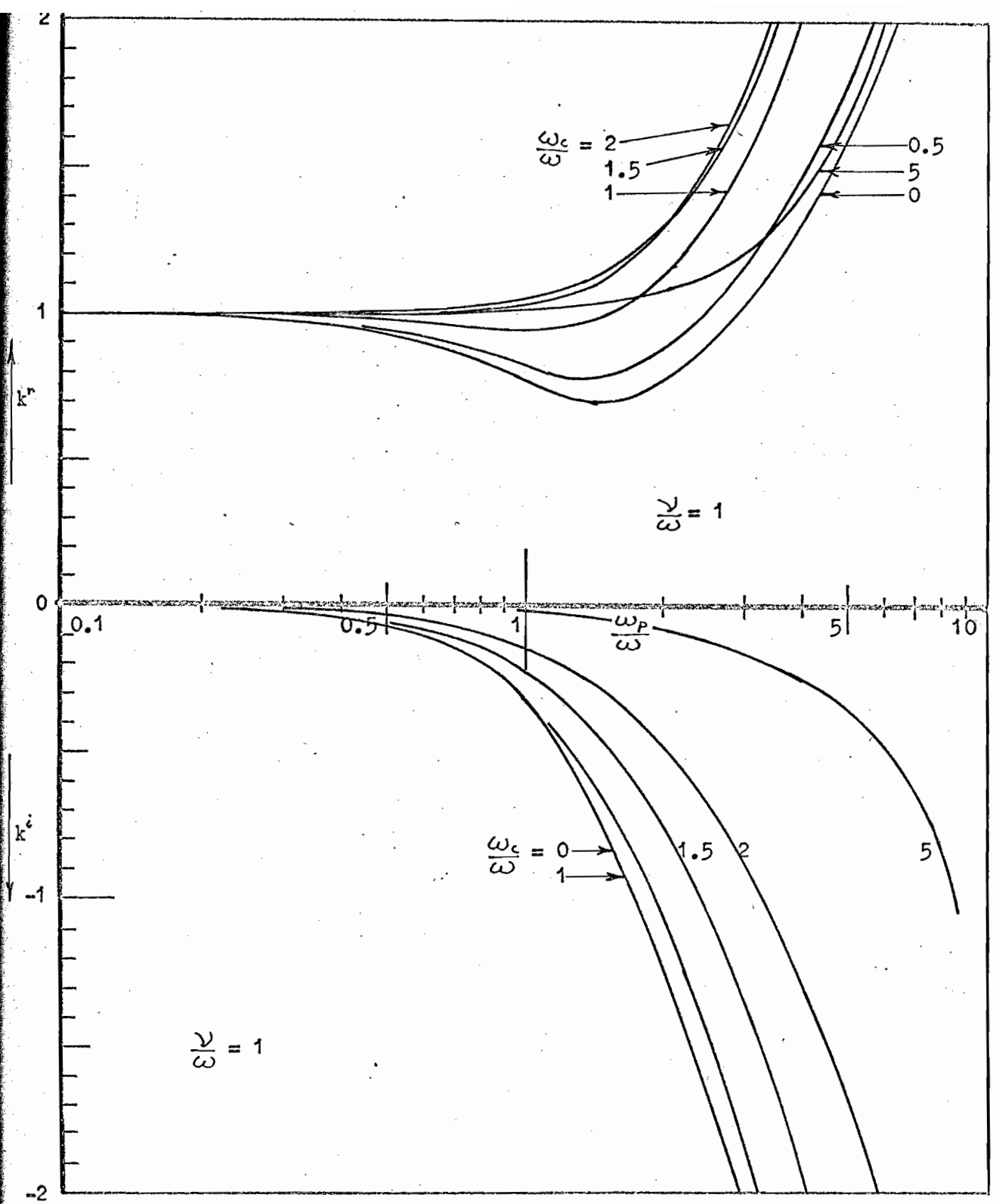


Fig. 54 . Computed real and imaginary parts of wave number $k = k^r + jk^i$ for plasma filled coaxial line ($R_1 k_o = 0.585$, $R_2 k_o = 1.348$) with axial magnetic field. Normalised electron collision frequency $\frac{\nu}{\omega} = 1$.

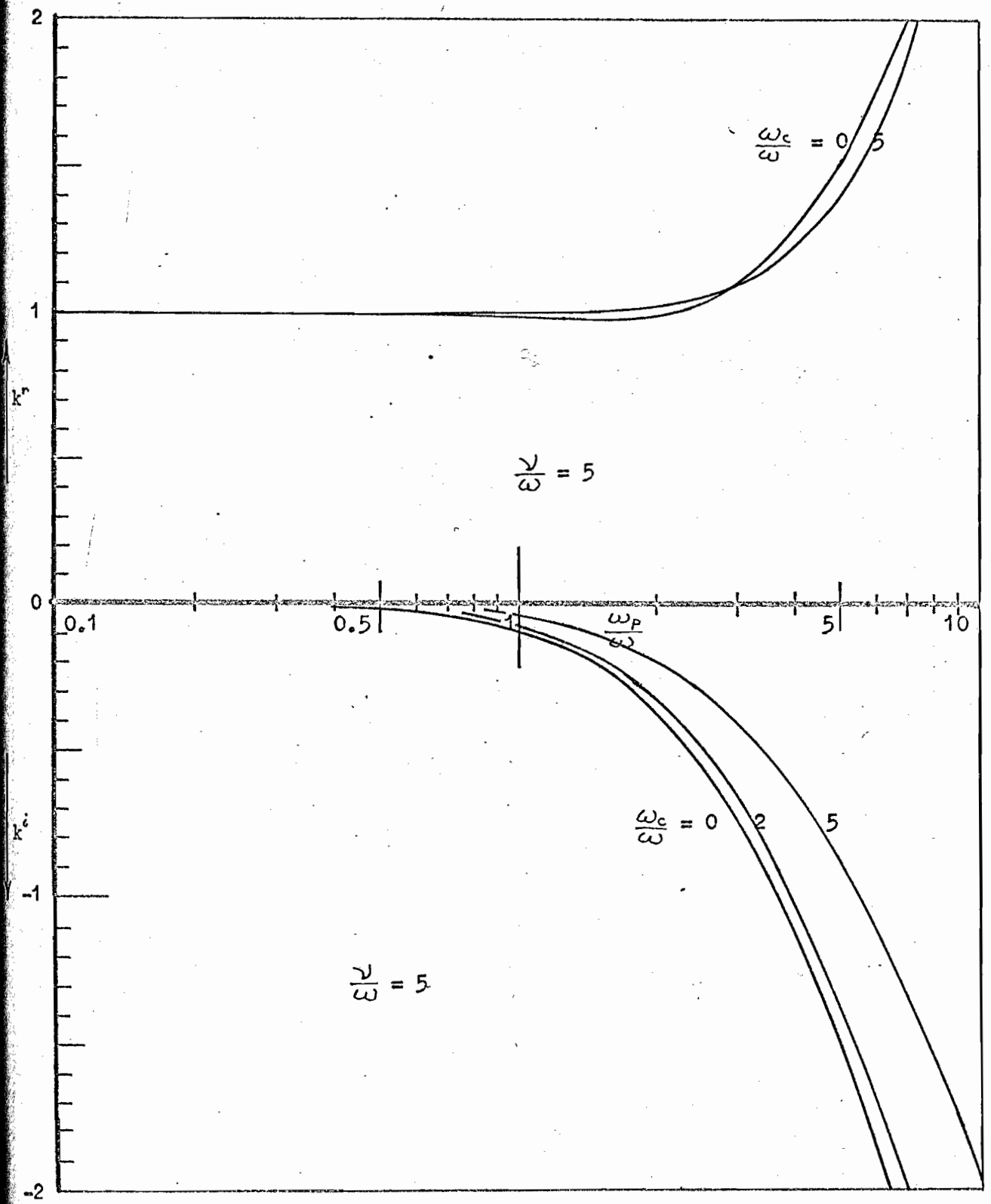


Fig. 55 . Computed real and imaginary parts of wave number $k = k^r + jk^i$ for plasma filled coaxial line ($R_1 k_o = 0.585$, $R_2 k_o = 1.348$) with axial magnetic field. Normalised electron collision frequency $\frac{\nu}{\omega} = 5$.

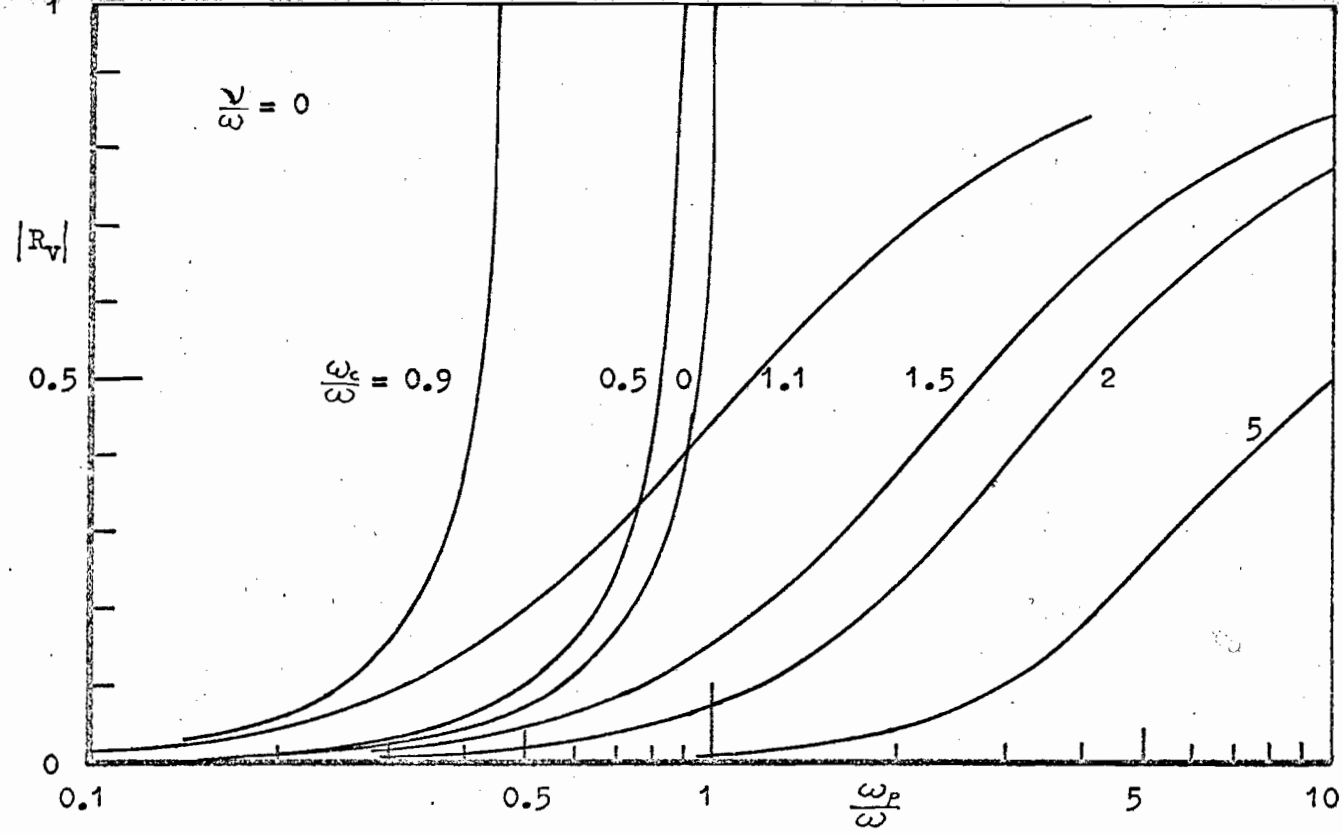


Fig. 56 . Computed Reflection Coefficient $|R_v|$ for plasma-filled coaxial line ($R_1 k_0 = 0.585$, $R_2 k_0 = 1.348$) with axial magnetic field applied. Normalised electron collision frequency $\frac{\nu}{\omega} = 0$.

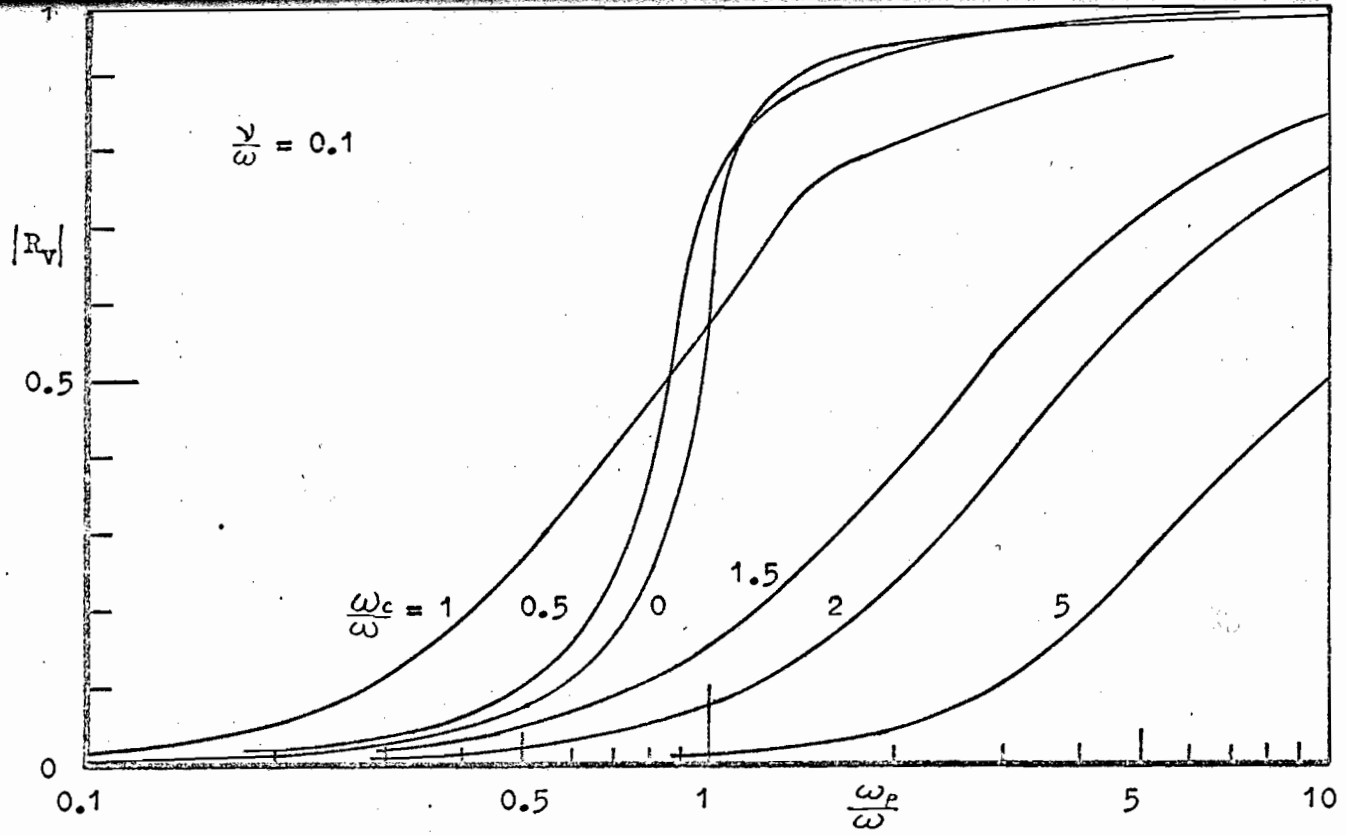


Fig. 57 . Computed Reflection Coefficient $|R_v|$ for plasma-filled coaxial line ($R_1 k_0 = 0.585$, $R_2 k_0 = 1.348$) with axial magnetic field applied. Normalised electron collision frequency $\frac{\nu}{\omega} = 0.1$.

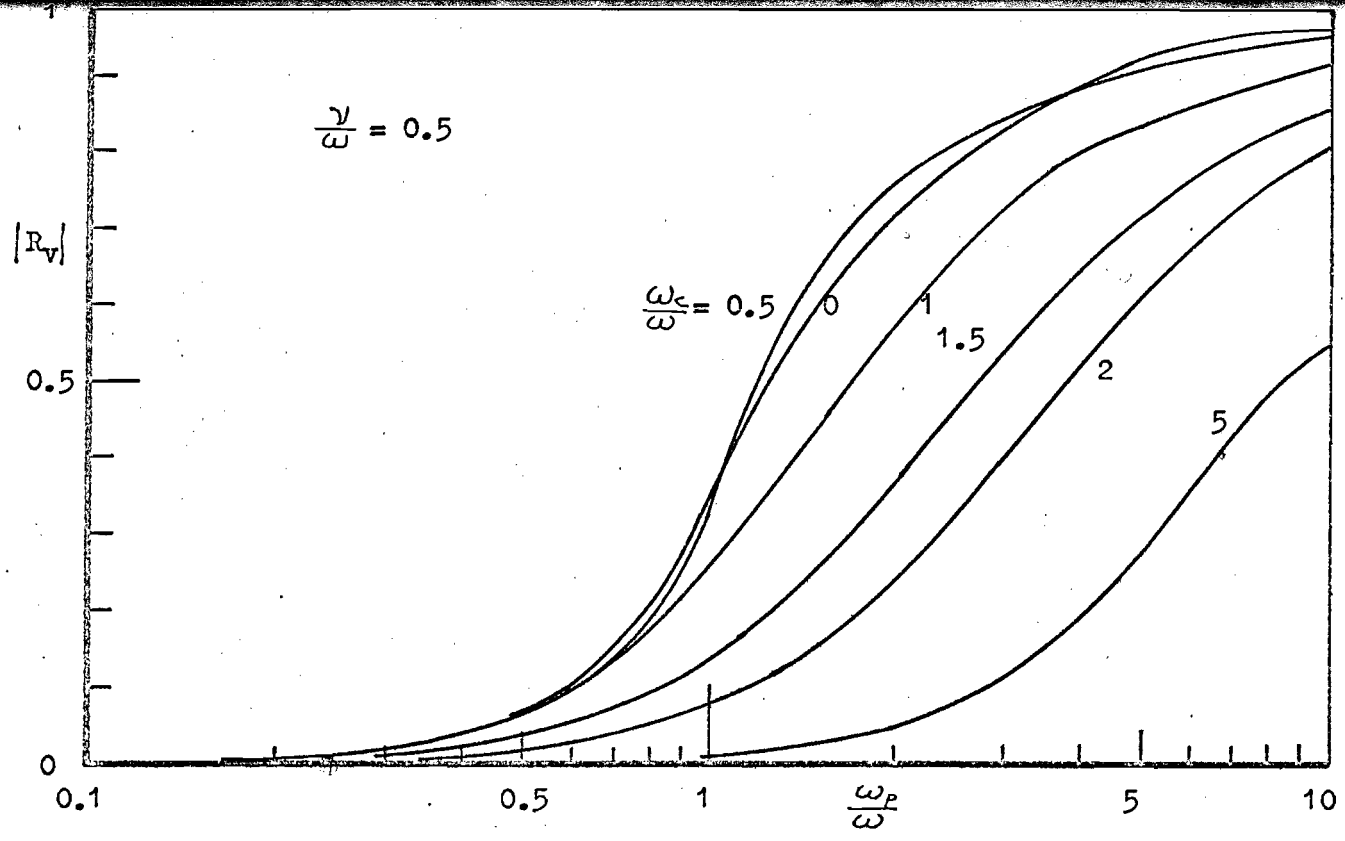


Fig. 58 . Computed Reflection Coefficient $|R_v|$ for plasma-filled coaxial line ($R, k_o = 0.585$, $R_2 k_o = 1.348$) with axial magnetic field applied. Normalised electron collision frequency $\frac{\nu}{\omega} = 0.5$.

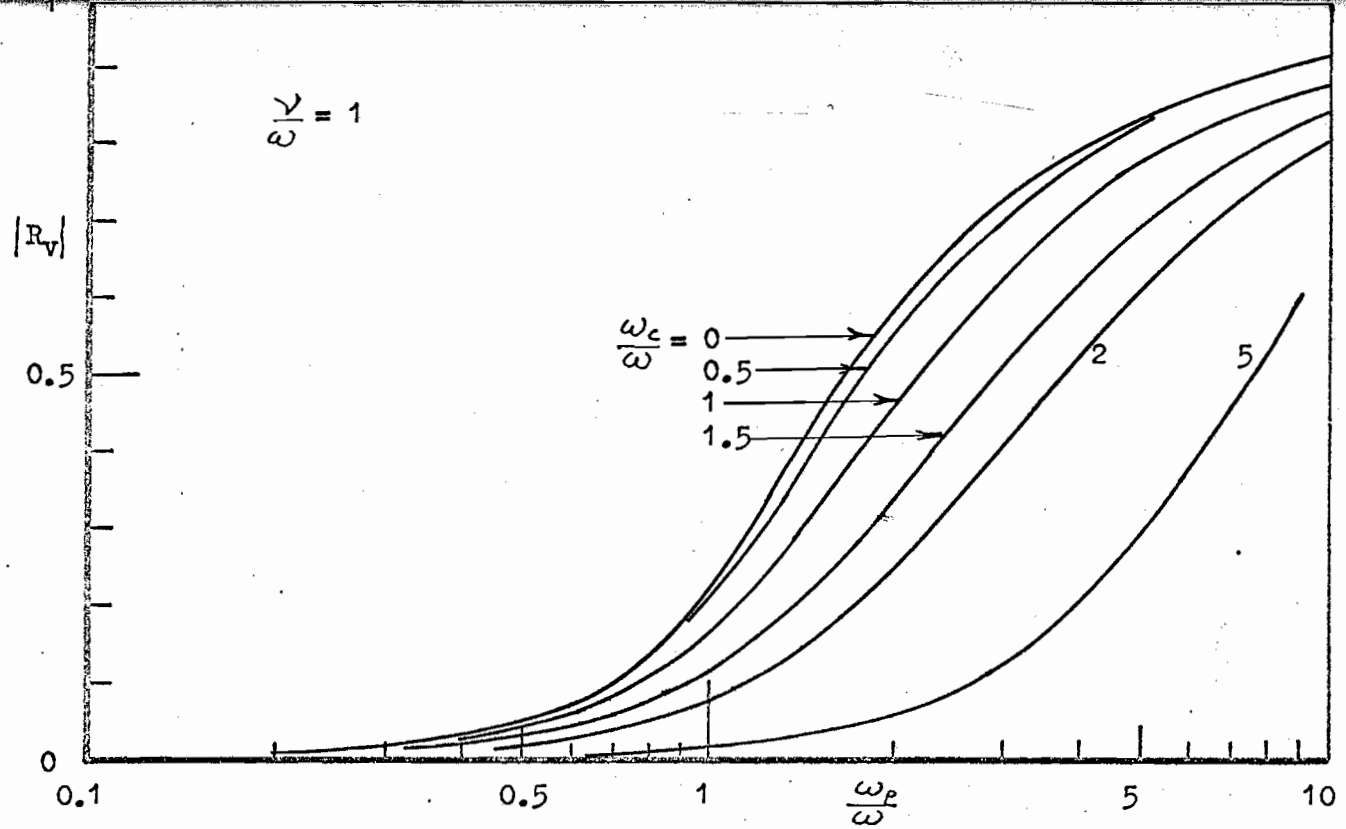


Fig. 59 . Computed Reflection Coefficient $|R_v|$ for plasma-filled coaxial line ($R_1 k_0 = 0.585$, $R_2 k_0 = 1.348$) with axial magnetic field applied. Normalised electron collision frequency $\frac{\nu}{\omega} = 1$.

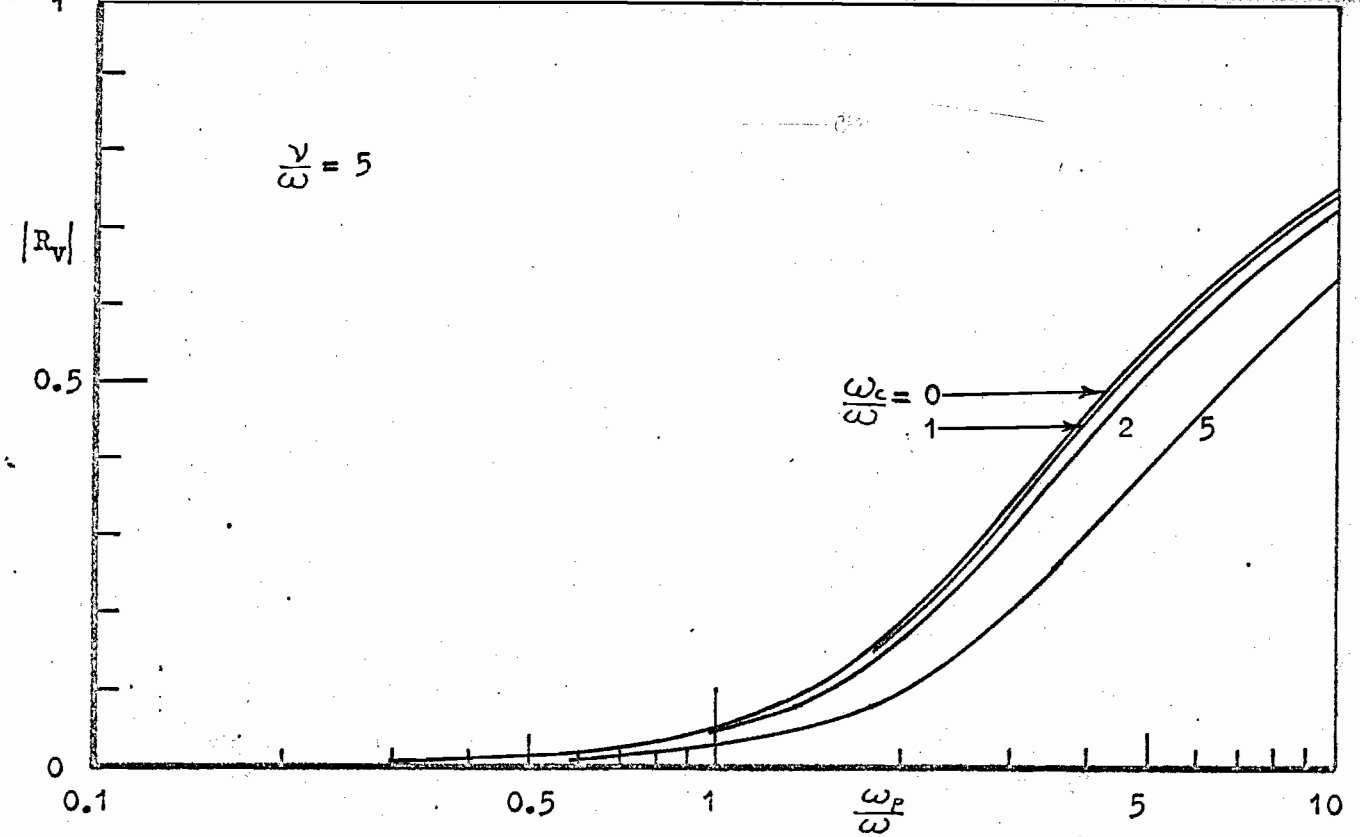


Fig. 60 . Computed Reflection Coefficient $|R_v|$ for plasma-filled coaxial line ($R_1 k_0 = 0.585$, $R_2 k_0 = 1.348$) with axial magnetic field applied. Normalised electron collision frequency $\frac{\nu}{\omega} = 5$.

for $\frac{\omega_c}{\omega} = 0.5$ approach the $\frac{\omega_c}{\omega} = 0$ curve, and for $\frac{\nu}{\omega} = 5$, even the "cyclotron resonance" $\frac{\omega_c}{\omega} = 1$ curve closely approaches the $\frac{\omega_c}{\omega} = 0$ curve.

In the collision free ($\nu = 0$) case, $\frac{\omega_c}{\omega} = 1$ is a resonance condition for which $k \rightarrow \infty$ and $|R_v| = 1$. The curves for $\frac{\omega_c}{\omega} = 0.9$ & 1.1 are thus included in Figs. 51 & 56.

The computer program occasionally ran into regions in $(\frac{\omega_p}{\omega}, \frac{\nu}{\omega}, \frac{\omega_c}{\omega})$ space in which it did not converge onto a solution, even with decreased step length. In such cases, the curves were terminated before the full $\frac{\omega_p}{\omega}$ range was covered.

Jumping from the quasi - TEM mode solution to higher modes was also a problem during computation : for this reason, the values of k^r for $\frac{\omega_p}{\omega} > 4$ in the $\frac{\omega_c}{\omega} = 0.5$ curve in Fig. 53 should be treated with care.

The electron collision free results shown in Figs 51, 56 are similar to those computed by Franklin (58), but do not agree exactly. An analysis of the limiting behavior of the solutions as $\frac{\omega_c}{\omega} \rightarrow 0$ showed that the results in Figs. 51, 56 tended exactly to the magnetic field free solutions (computed by a completely different method) given in Section 4.2, whereas Franklin's curves only closely approached these field free solutions.

Comparison of the mathematical analysis in both cases showed that identical solutions should have been obtained, and so it is felt that a minor error in the computer program used by Franklin would account for the discrepancy.

Inspection of Figs. 51 - 60 shows that as the collision

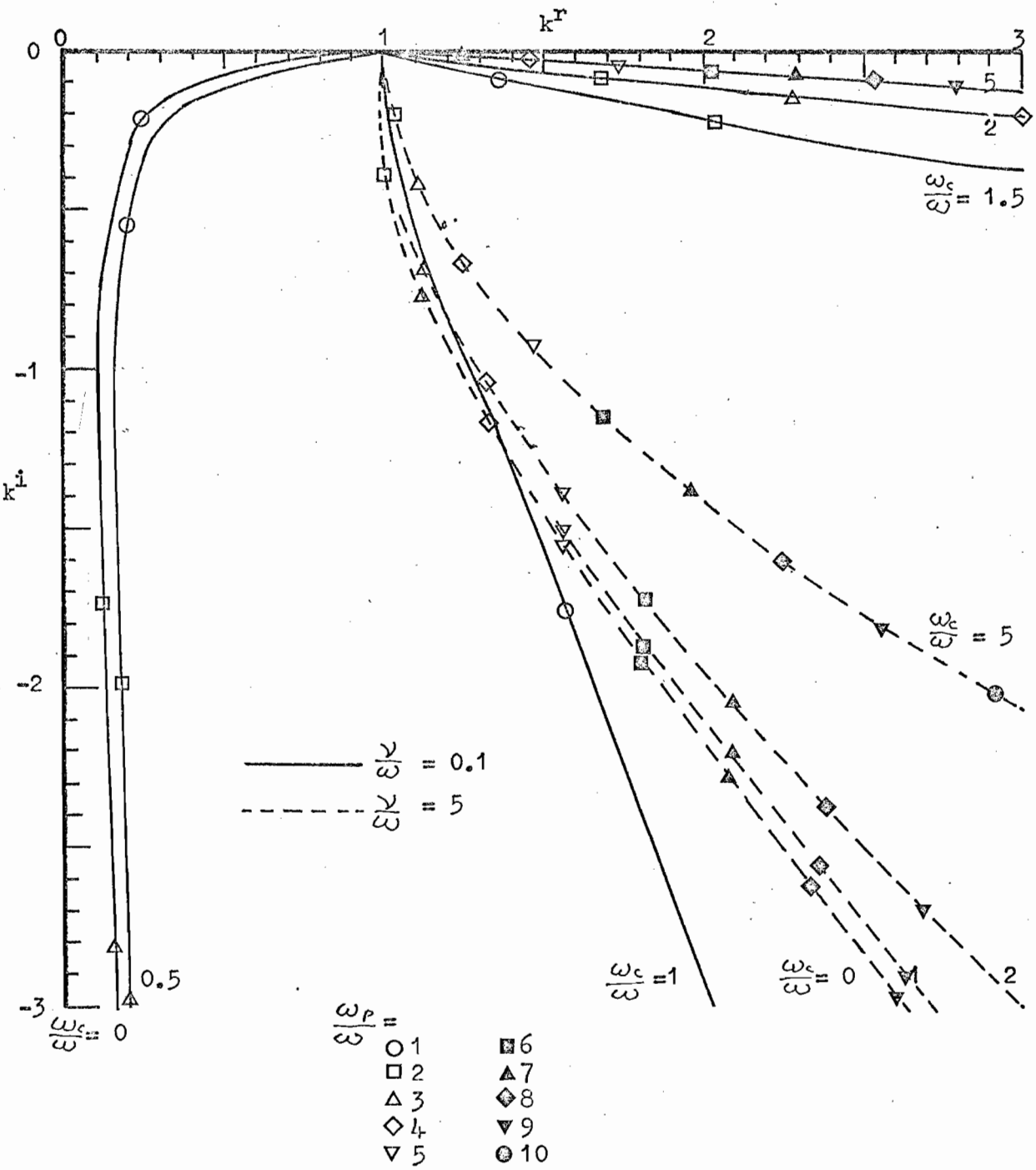


Fig.61 Loci of $k = k^r + jk^i$ on the complex plane for increasing $\frac{\omega_p}{\omega}$ and various $\frac{\omega_c}{\omega}$, for the values of $\frac{\nu}{\omega} = 0.1, 5$

frequency $\frac{\nu}{\omega}$ increases, the change of k and $|R_v|$ with magnetic field decreases. This effect is shown more dramatically in Fig. 61, which shows the root loci of k, on the complex plane, as $\frac{\omega_p}{\omega}$ increases for $\frac{\nu}{\omega} = 0.1$ and 5. In the limiting case, $\frac{\nu}{\omega} = 0$, k is either completely real (propagating wave) or completely imaginary (evanescent wave). For $\frac{\nu}{\omega} = 0.1$ the root loci are close to the axes, but as $\frac{\nu}{\omega}$ increases, they converge until, when $\frac{\nu}{\omega} = 5$, all the values of k lie in a narrow fan with its apex at (1, 0).

From Figs. 51 - 55 it can also be seen that application of a magnetic field to the coaxial line allows propagation to take place beyond the field-free plasma cut-off $\omega = \omega_p$. In the $\nu = 0$ limit, all waves propagate for $\omega_c > \omega$.

5.3 Construction and calibration of axial magnetic field solenoid.

A d.c. solenoid to the specifications given in Table 7 was manufactured to order by the Oxford Instrument Company.

Table 7 : Specifications and performance of 0.6 T solenoid.

Length	0.75 m
Outside diameter	0.26 m
Clear bore	44.4 mm
Max. field	0.51 T at 80 Amps.
Field calibration	$64.0 \pm 0.2 \times 10^{-3}$ T / Amp.
99% field length in centre of magnet	220 mm
Max. inclination of H at inner edge of shock tube	15° at ends of magnet

Max.current	80 Amps.
D.c. voltage required	216
Power dissipated	17 kW
Conductor	4.5 mm x 3 mm Lewmex (insulated copper)
Cooling system	closed circuit with fan-cooled radiator
Coolant	Shell Diala - B transformer oil
Coolant flow	5 gallons / min.

The solenoid was supplied from a laboratory step-variable 0 - 216 V d.c. power supply (lead - acid batteries) through the control circuit shown in Fig.62.

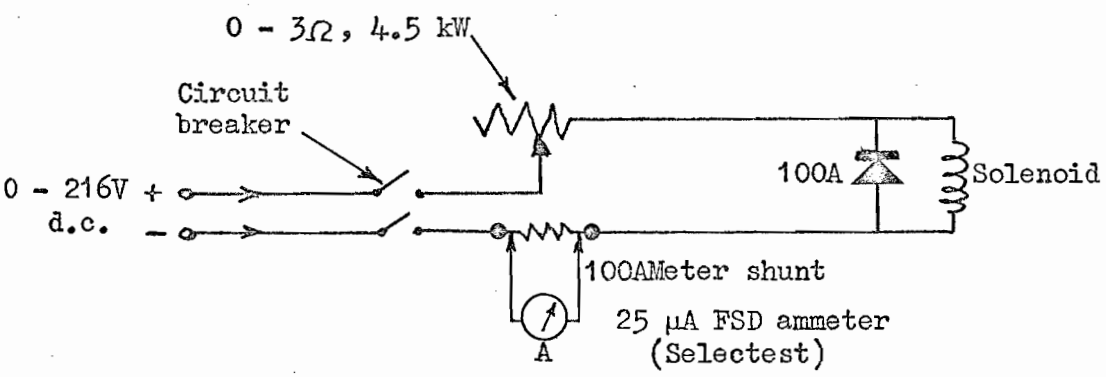


Fig.62 Solenoid control circuit.

Meter errors were eliminated by using the same meter both during magnet calibration and when using the magnet for shock tube runs.

A Nuclear Magnetic Resonance (NMR) probe was used to calibrate the magnetic field produced. The accuracy of the NMR probe, which utilises the proton spin resonance in a magnetic field (at a frequency

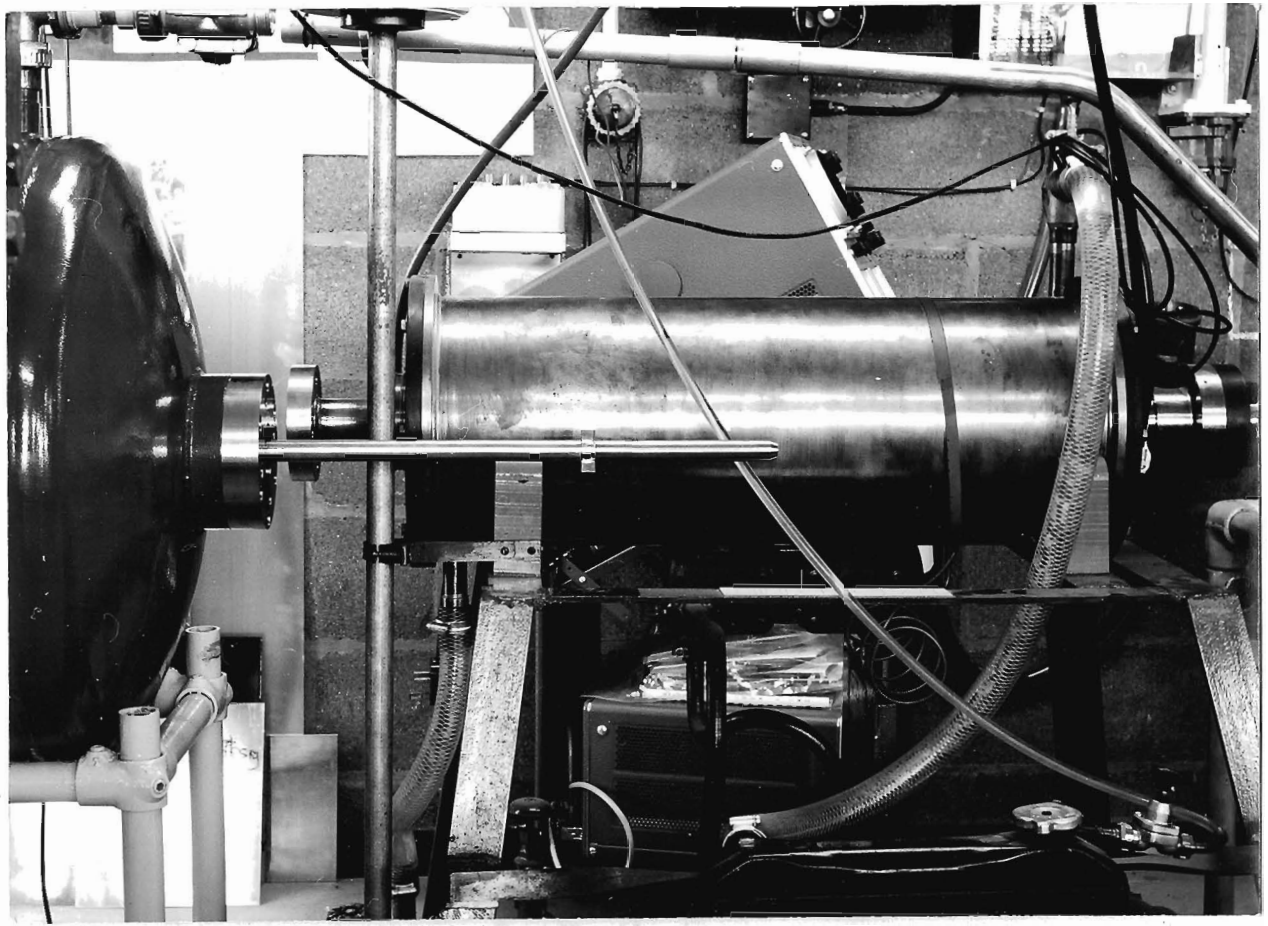


Fig.63 Microwave coaxial probe shown next to solenoid in position it would occupy inside shock tube.

of 0.425759 MHz/Tesla), is only limited by the frequency meter used. In this case the Hewlett Packard meter used was crystal controlled to 1 part in 10^5 in frequency.

The solenoid was found to have a centre length of 220 mm in which the axial field was greater than 99% of the maximum field.

For the shock tube experiments the magnet was centered about the coaxial probe as shown in Fig. 37. The photograph in Fig. 63 shows the probe positioned beside the solenoid at approximately the position it would occupy inside the shock tube.

During shock tube runs the solenoid current was continuously monitored and kept at the required value.

To determine whether the magnetic field produced by the solenoid would influence the bulk flow and electron density behind the shock, the electrostatic probe described in Section 3.2 was mounted in the shock tube, immediately behind the solenoid. It was found that there was no detectible difference between the traces for $B_1 = 0$ and $B_1 = 5T$ for the same p_0 and M_s.

5.4 Experimental results : magnetised plasma - filled coaxial line.

The design, construction, and use of the coaxial microwave probe is described in Chapter 4.

The shock tube runs were repeated over the same range of M_s for $p_0 = 1$ Torr, for solenoid fields giving $\frac{\omega_c}{\omega} = 0.5,\ 1\ \&\ 1.5$. The lower shock tube initial pressure, $p_0 = 1$ Torr , was chosen as the theoretical curves in Section 5.3 show that the influence of

the magnetic field on R_v is greater for low $\frac{\nu}{\omega}$.

As can be seen in Fig. 64, the standing wave trace is similar to the $B_1 = 0$ trace in Fig. 43.

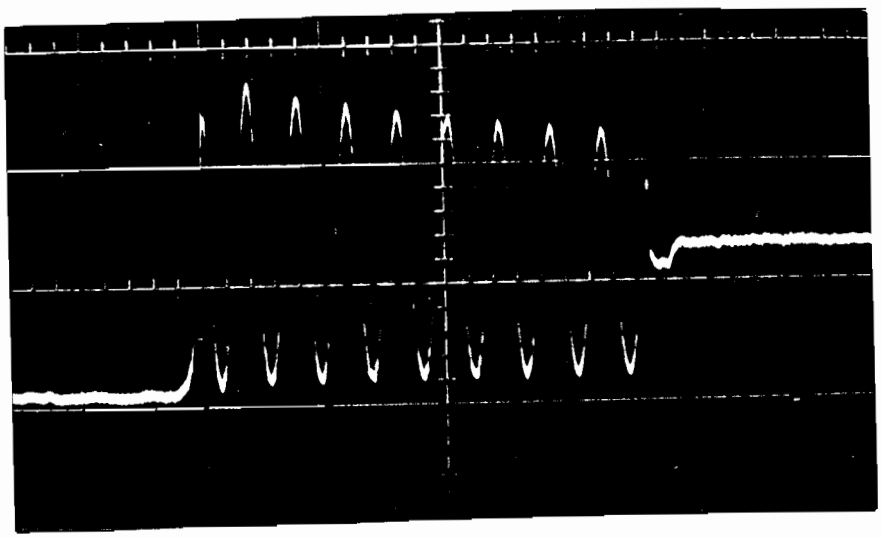


Fig.64 Run 261. Typical microwave coaxial probe trace with axial magnetic field applied. $|R_v| = 0.61$
2 mV/division $\frac{\omega_p}{\omega} = 1.45$
10 μs/division $\frac{\nu}{\omega} = 0.45$
Microwave frequency = 9 GHz $\frac{\omega_c}{\omega} = 0.5$
p_o = 1 Torr dry Air
M_s = 11.9

A best fit curve through the $n_e : M_s$ results in Fig. 46 was used to give a calibration of $\frac{\omega_p}{\omega} : M_s$. This was used to convert the experimental results described above from a M_s scale to an $\frac{\omega_p}{\omega}$ scale.

The experimental $\frac{\omega_p}{\omega} : M_s$ calibration was also used with the $\nu : M_s$ curve, for $p_o = 1$ Torr, in Fig. 42 [based on (52)] to give the $\frac{\nu}{\omega} : \frac{\omega_p}{\omega}$ calibration curve shown in Fig. 65, from which it can be seen that $\frac{\nu}{\omega}$ varies from 0.3 to 0.55 in the range of used. This $\frac{\nu}{\omega} : \frac{\omega_p}{\omega}$ calibration only applies for the particular

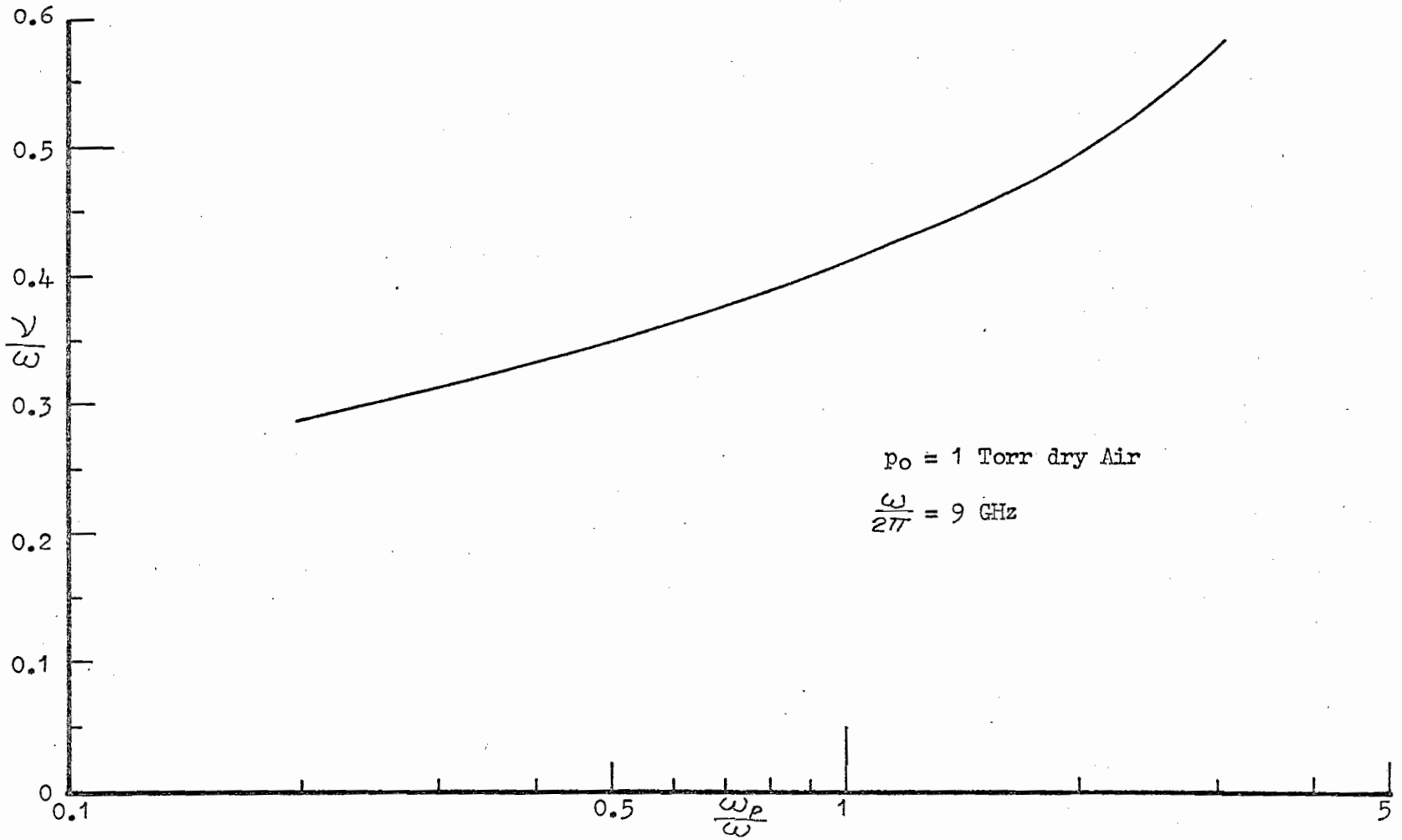


Fig. 65 Calibration curve for $\frac{\nu}{\omega}$ in terms of $\frac{\omega_p}{\omega}$, from coaxial probe results. This calibration is only valid for the particular experimental system used, and for p_o = 1 Torr dry Air with a microwave frequency of 9 GHz .

experimental conditions used. The variation in $\frac{\nu}{\omega}$ is due to the changing T and ρ behind the shock as M_s increases.
This calibration was then used to compute the theoretical reflection coefficient $|R_v|$, using the computer program listed in Section C.2 , for $\frac{\omega_c}{\omega} = 0.5, 1$ & 1.5 . As $\frac{\nu}{\omega}$ varies with $\frac{\omega_p}{\omega}$, the curves obtained are not the same as those of constant $\frac{\nu}{\omega}$ in Figs. 51 - 55 .

Fig. 66 shows these curves together with the experimental results for $\frac{\omega_c}{\omega} = 0.5, 1$ & 1.5 . The experimental results for $\frac{\omega_c}{\omega} = 0$ are not included, for they have already been used to calibrate the $\frac{\omega_p}{\omega}$ axis, and thus would automatically lie on the $\frac{\omega_c}{\omega} = 0$ curve.

The curves for $\frac{\omega_c}{\omega} = \frac{\nu}{\omega} = 0$, and for $\frac{\omega_c}{\omega} = 0$ with $\frac{\nu}{\omega}$ as given by Fig. 65 are also shown.

The accuracy of both the experimental $|R_v|$ in Fig.66, and of the experimental $n_e : M_s$ in Fig. 46 depends on both systematic and random experimental errors. The calibration method used for the $\frac{\omega_p}{\omega}$ scale, where exactly the same apparatus and methods are used for the $B_1 = 0$ and the $B_1 \neq 0$ shock tube runs, effectively cancels out the effects of the systematic errors, especially as B_1 is known to within 1%. Hence in Fig. 66 only the random errors are significant. As these are all too obvious from the distribution of experimental points, no error bars are added.

This technique is justified in that we are interested in comparing theory and experiment in $(|R_v|, \frac{\omega_p}{\omega}, \frac{\omega_c}{\omega})$ space, and systematic errors in $n_e : M_s$ and $|R_v| : M_s$ are effectively cancelled out.

Examination of Fig.66 shows that for $\frac{\omega_c}{\omega} = 0.5$ and $\frac{\omega_c}{\omega} = 1.5$ agreement between experiment and theory is extremely good, but that for low $\frac{\omega_p}{\omega}$ the $\frac{\omega_c}{\omega} = 1$ results are above the computed curve. A clue to this behaviour can be seen in Fig.67, which shows curves

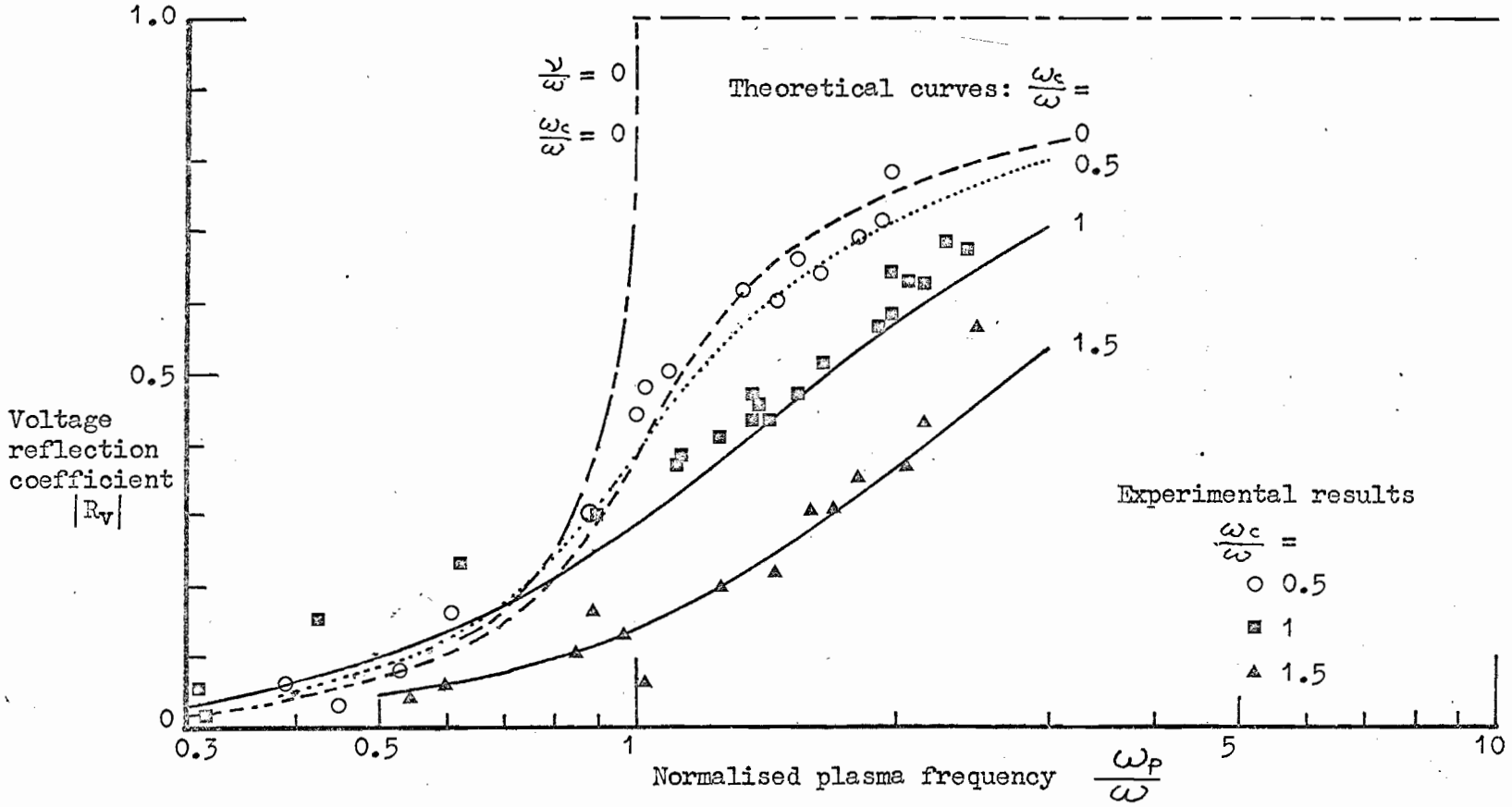


Fig.66 Microwave reflection from magnetised plasma-filled coaxial line: experimental results for $\frac{\omega_c}{\omega}$ = 0.5, 1 & 1.5 . Theoretical curves are given for the appropriate values of $\frac{\omega_p}{\omega}$ and $\frac{\nu}{\omega}$.

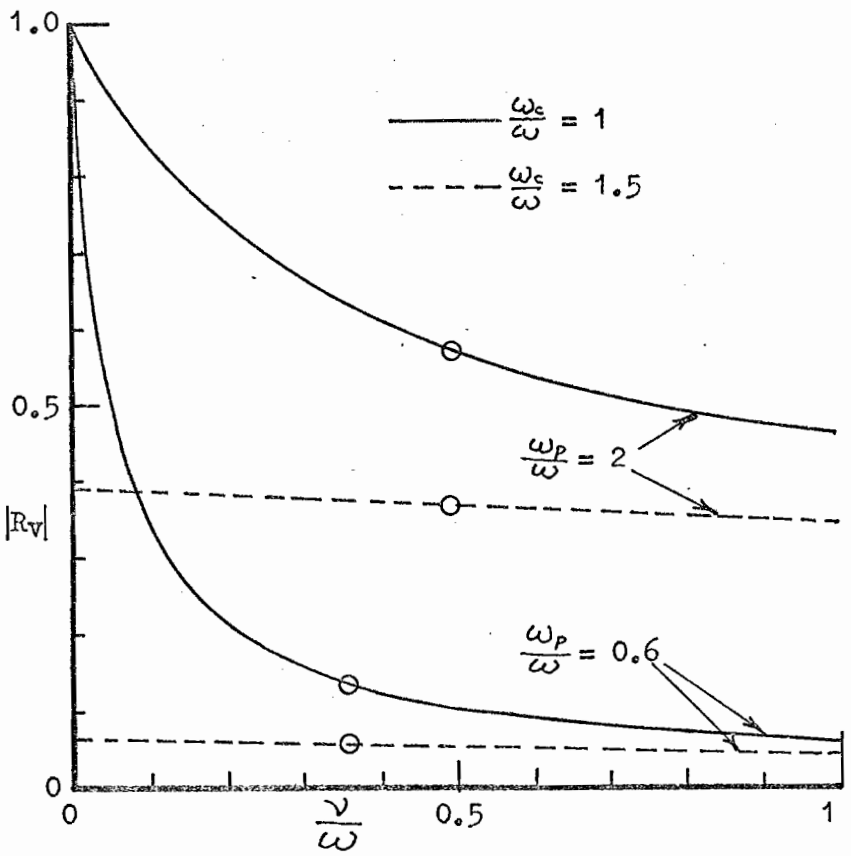


Fig.67 Theoretical variation of the voltage reflection coefficient R_v with electron collision frequency for $\frac{\omega_c}{\omega} = 1$ & 1.5 .

The appropriate experimental values of $\frac{\nu}{\omega}$ are ringed.

of theoretical $|R_v|$: $\frac{\nu}{\omega}$ for $\frac{\omega_c}{\omega} = 1$ and 1.5 at $\frac{\omega_p}{\omega} = 0.6$ and 2. [The values of $\frac{\nu}{\omega}$ corresponding to those in Fig.66 are circled.]

$\frac{\omega_c}{\omega} = 1$ is an unusual case in that it is a damped cyclotron resonance and is extremely sensitive to $\frac{\nu}{\omega}$, whereas the $\frac{\omega_c}{\omega} = 1.5$ curves are almost completely insensitive to $\frac{\nu}{\omega}$. The model describing electron collision effects in Section 4.5 is a fairly primitive one and from Fig.67 it is apparent that a small error in the effective electron collision frequency would account for the discrepancy between theory and experiment in the $\frac{\omega_c}{\omega} = 1$ curves.

It is felt that the results in Fig.66 constitute an experimental verification of the theoretical model used in the analysis of microwave reflection from a magnetized-plasma filled coaxial line.

5.5 Experimental results: Magnetized plasma filled rectangular waveguide.

As the rectangular microwave probe described in Chapter 4 was available, further experiments, with $p_o = 1$ Torr, were carried out at a microwave frequency of 9.11 GHz with the axial magnetic field applied. A calibration of $M_s : \frac{\omega_p}{\omega}\left(1-\left(\frac{\omega_{co}}{\omega}\right)^2\right)^{-\frac{1}{2}}$ (See p.64) was obtained from Fig.48 and the experimental results plotted in Fig.68, for $\frac{\omega_c}{\omega} = 1$ and $\frac{\omega_c}{\omega} = 1.5$. A calibration of $\frac{\nu}{\omega}$: $\frac{\omega_p}{\omega}\left(1-\left(\frac{\omega_{co}}{\omega}\right)^2\right)^{-\frac{1}{2}}$ was similarly obtained.

As is explained in Appendix A, the rectangular waveguide boundary conditions do not allow simple solutions of the anisotropic wave equations, (A.31) & (A.32), and approximations must be considered. In the TE_{10} mode, the only propagating mode in X-band waveguide at 9 GHz,

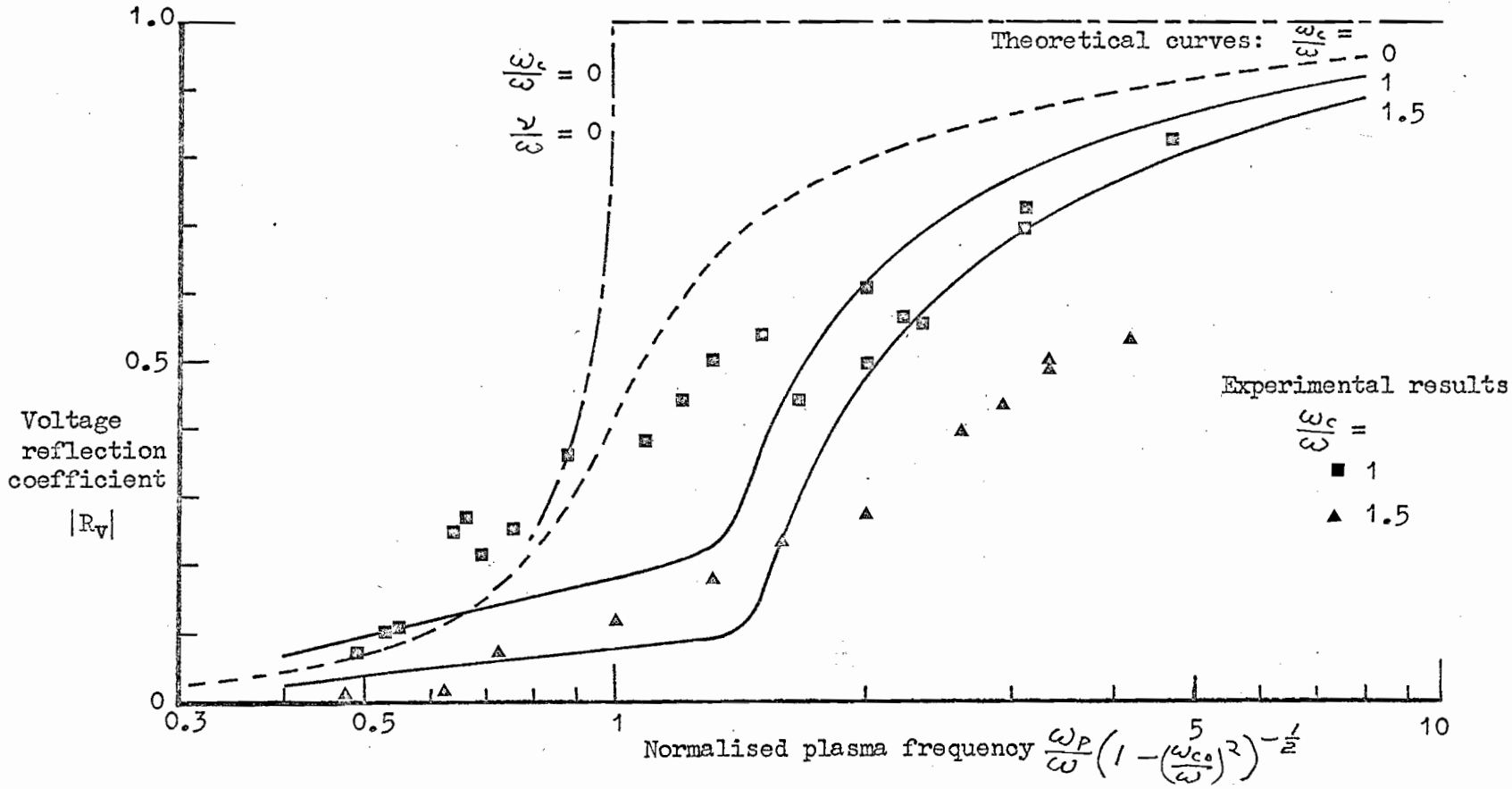


Fig. 68 Microwave reflection from magnetised plasma-filled rectangular waveguide: experimental results for $\frac{\omega_c}{\omega} = 1$ & 1.5 . The theoretical curves are for the incident-component free-space approximation.

the $\underset{\sim}{E}$ vector is constrained to lie parallel to the short waveguide walls. Therefore, a possible approximation for microwave reflection might be to consider the component of the free-space reflection from a plasma boundary in the plane of the incident wave (incident component approximation), as analysed in Appendix A, Section A.3, adjusted by replacing $\frac{\omega_p}{\omega}$ by $\frac{\omega_p}{\omega}\left(1-\left(\frac{\omega_{co}}{\omega}\right)^2\right)^{-\frac{1}{2}}$ for the waveguide.

Equations (A.15) have been used to compute curves of free-space incident-component reflection coefficient R_x for $\frac{\omega_c}{\omega} = 1$ & 1.5 and are shown on Fig.68. Curves of $\frac{\nu}{\omega} = 0$ and $\frac{\omega_c}{\omega} = 0$ are also given from Chapter 4.

It can be seen in Fig.68 that the experimental points do not agree with the theoretical curves, the step in the latter being completely absent in the former. In fact, the experimental curves follow more closely the coaxial line theoretical curves of Fig.66.

It is concluded that the free-space reflection coefficient is not a good approximation for that in a rectangular waveguide with magnetic field applied. A similar analysis with the power reflection coefficient R_p of Equation (A.16) yields similar disagreement with experimental results.

The effect of the magnetic field can be seen quite clearly on the standing wave trace in the rectangular waveguide. As seen in Fig.69, the plasma behind the shock travels beyond the magnetic field and into a field-free ($\frac{\omega_c}{\omega} < 0.1$) region, in which the measured $|R_v|$ agrees well with that measured with $B_t = 0$ in Fig.48, again confirming that the magnetic field does not disturb the plasma flow.

As the measured VSWR in the magnetic field region is smaller, it can be measured more accurately than the VSWR in the $B_t = 0$ region. This effect can be used to measure the $B_t = 0$ reflection

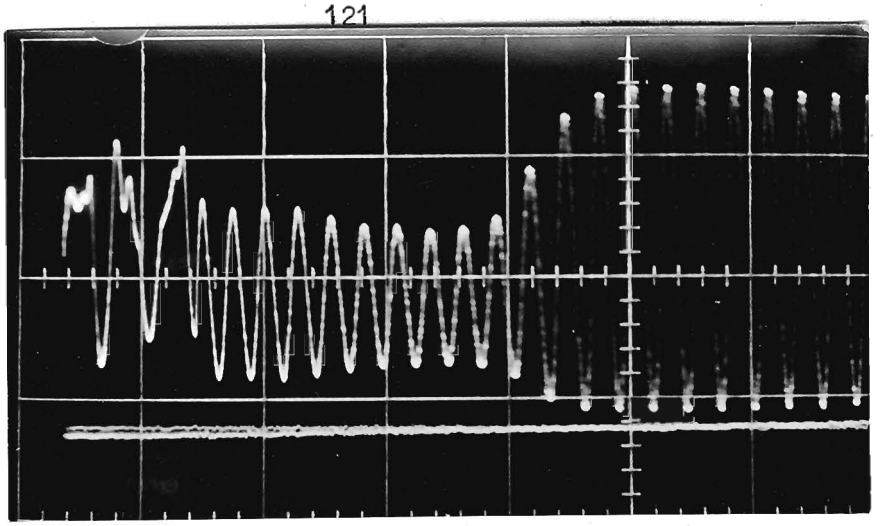


Fig. 69 Run 342 . Typical rectangular waveguide probe trace with axial magnetic field applied.

2 mV/division
20 μs/division
Microwave frequency = 9.11 GHz
p_o = 1 Torr dry Air
M_s = 11.1

$|R_v|$ = 0.49 in magnetic field
$|R_v|$ = 0.85 in B = 0
$\frac{\omega_p}{\omega}$ = 3.02
$\frac{\nu}{\omega}$ = 0.41
$\frac{\omega_c}{\omega}$ = 1.5

coeffecients to greater accuracy. If V_{1m} , V_{2m} , R_m and V_{2o} , V_{2o} , R_o are the measured maximum and minimum standing wave voltages and reflection coefficients in the magnetic and no magnetic field regions respectively, and V is the incident wave voltage, then

$$V_{2m} = V (1 + R_m) ,$$

$$V_{2o} = V (1 + R_o) .$$

i.e.
$$R_o = \frac{V_{2o}}{V_{2m}} (1 + R_m) - 1 . \qquad (5.1)$$

Equation (5.1) was used to recover additional $n_e{:}M_s$ points for $B_1 = 0$ from the results with magnetic field applied. This proved particularly useful at high M_s when the values thus obtained were plotted in Fig. 48 .

6 CONCLUSION.

Since detailed conclusions are included at the ends of Chapters 1 - 5, only a summary need be given here.

The shock tube described in Chapter 1 behaved as a satisfactory source of collision dominated, slightly ionised, dry Air plasma. It was run some 359 times, at initial pressures p_o of 0.1 - 10 Torr of dry Air, and for Mach Nos. ranging from 8 - 14 , and it produced plasmas having 10^{17} - 3 x 10^{19} electrons / m^3.

The initial flat-plate electrostatic probe experiments, at p_o = 1, 3 and 10 Torr in dry Air, showed that the ion density rapidly reached a steady value behind the shock, and that the sheath edge ion density (computed on the assumption that sheath edge ions are at the probe surface temperature) is of the same order as the free- stream equilibrium ion density behind the incident shock.

It was also demonstrated that the low apparent ionisation potential measured by Laird (1) was not due to Na^+ contamination, but that it increased with increasing shock tube initial pressure.

Microwave reflection experiments using a coaxial line probe and a rectangular line probe were successfully used to calibrate further the electron density and electron collision frequency behind the shock in dry Air for p_o = 1 and 10 Torr and M_s = 8 - 14.

The results for both probes at p_o = 10 Torr and for the rectangular waveguide probe at p_o = 1 Torr agree with the theoretical equilibrium electron density, but boundary layer effects reduced the effective electron density in the coaxial probe at high Mach numbers

for $p_o = 1$ Torr. Using the $p_o = 1$ Torr results (giving $\frac{\nu}{\omega} \sim 0.4$) as a calibration of $\frac{\omega_p}{\omega} : M_s$ and $\frac{\nu}{\omega} : M_s$ for each probe, voltage reflection coefficients have been measured for $\frac{\omega_p}{\omega} = 0.3 - 5$ with axial magnetic fields applied (giving $\frac{\omega_c}{\omega} = 0.5, 1, 1.5$).

A full analysis, using rotating coordinate techniques, of the reflection of microwaves from an anisotropic magnetised plasma in a coaxial line has been given, and a computer program used to obtain wave numbers and reflection coefficients over the ranges $\frac{\omega_p}{\omega} = 0.1 - 10$, $\frac{\nu}{\omega} = 0 - 5$, $\frac{\omega_c}{\omega} = 0 - 5$. In the coaxial probe case the experimental results agreed excellently with the reflection coefficients predicted by this theoretical analysis.

It was shown that the free-space reflection coefficient approximation does not agree with the measured reflection coefficients obtained with the rectangular waveguide probe in a magnetized plasma.

APPENDIX A Field Theory of Microwave Propagation in a Coaxial Transmission Line filled with Anisotropic Plasma.

A.1 Introduction.

In this appendix the field theory of electromagnetic wave propagation through a plasma with a d.c. magnetic field parallel to the wave propagation vector is developed. The wave equations are then solved for the case of propagation along a coaxial line with an axial magnetic field applied.

The use of rotating coordinates (Appendix B), which are described briefly by Allis & Buchsbaum (50) and Heald & Wharton (44), simplifies and shortens the field analysis, which otherwise broadly follows that of Bers (50). The analysis of propagation with coaxial conducting boundaries follows the analysis of propagation in magnetised ferrites given by Brodwin & Miller (57) and that for collisionless plasmas by Franklin (58).

A.2 The anisotropic dielectric tensor.

The assumptions used here are those of Section 4.2 (p.57), with the addition of a steady magnetic field $\underset{\sim}{B}_1 = B\hat{k}$ in the z - direction.

Maxwell's equations again become (Equation 4.7) :-

$$\left.\begin{aligned} \nabla \times \underset{\sim}{E} &= -j\omega\mu_0 \underset{\sim}{H}, \\ \nabla \times \underset{\sim}{H} &= j\omega\varepsilon_0 \underset{\sim}{E} + \underset{\sim}{J}, \\ \nabla \cdot \underset{\sim}{D} &= \rho, \\ \nabla \cdot \underset{\sim}{B} &= 0, \\ \nabla \cdot \underset{\sim}{J} &= -j\omega\rho. \end{aligned}\right\} \qquad (A.1)$$

It is assumed that, as the microwave power is low, $B_1 >> B$, the microwave-frequency magnetic field, and that the electron motion is non-relativistic.

Again the plasma frequency, $\omega_p = \sqrt{\dfrac{n_e e^2}{\varepsilon_0 m_e}}$,

and we define the cyclotron frequency $\omega_c = \dfrac{e B_1}{m_e}$.

Then the equation of motion of an electron, velocity $\underset{\sim}{v}$, including the Lorentz force (59) is:-

$$m_e \frac{d\underset{\sim}{v}}{dt} + m_e \nu \underset{\sim}{v} = -e\left(\underset{\sim}{E} + \underset{\sim}{v} \times \underset{\sim}{B_1}\right) \qquad (A.2)$$

i.e. $$(j\omega + \nu)\underset{\sim}{v} = -\frac{e}{m_e}\left(\underset{\sim}{E} + \underset{\sim}{v} \times \underset{\sim}{B_1}\right)$$

$$= -\frac{e}{m_e}\underset{\sim}{E} - \begin{bmatrix} 0 & \omega_c & 0 \\ -\omega_c & 0 & 0 \\ 0 & 0 & 0 \end{bmatrix} \underset{\sim}{v}$$

$$-\frac{e\underset{\sim}{E}}{m_e} = \begin{bmatrix} (j\omega+\nu), & \omega_c, & 0 \\ -\omega_c, & (j\omega+\nu), & 0 \\ 0, & 0, & (j\omega+\nu) \end{bmatrix} \underset{\sim}{v}$$

But current density $\underset{\sim}{J} = -n_e e \underset{\sim}{v}$, from which we get

$$\underset{\sim}{E} = \frac{1}{\omega_p^2 \varepsilon_0} \begin{bmatrix} j\omega+\nu, & \omega_c, & 0 \\ -\omega_c, & j\omega+\nu, & 0 \\ 0, & 0, & j\omega+\nu \end{bmatrix} \underset{\sim}{J}$$

$$= \underset{\approx}{R}\,\underset{\sim}{J}$$

where $\underset{\approx}{R}$ is the resistivity tensor. Inverting $\underset{\approx}{R}$ we get the conductivity tensor

$$\underset{\approx}{R}^{-1} = \frac{\omega_p^2 \varepsilon_0}{\left[(j\omega+\nu)^2 + \omega_c^2\right]} \begin{bmatrix} j\omega+\nu & -\omega_c & 0 \\ \omega_c & j\omega+\nu & 0 \\ 0 & 0 & \frac{(j\omega+\nu)^2+\omega_c^2}{j\omega+\nu} \end{bmatrix}$$

Now

$$\begin{aligned} \nabla \times \underset{\sim}{H} &= j\omega\varepsilon_0 \underset{\sim}{E} + \underset{\sim}{J} \\ &= j\omega\varepsilon_0 \left(\underset{\approx}{I} + \frac{\underset{\approx}{R}^{-1}}{j\omega\varepsilon_0} \right) \underset{\sim}{E} \\ &= j\omega\varepsilon_0 \underset{\approx}{\varepsilon} \underset{\sim}{E} , \end{aligned} \qquad \text{(A.3)}$$

where the relative dielectric tensor is defined as

$$\underset{\approx}{\varepsilon} = \underset{\approx}{I} + \frac{\underset{\approx}{R}^{-1}}{j\omega\varepsilon_0}$$

$$= \begin{bmatrix} 1 - \frac{\left(\frac{\omega_p}{\omega}\right)^2 \left(1 - j\frac{\nu}{\omega}\right)}{\left(1-j\frac{\nu}{\omega}\right)^2 - \left(\frac{\omega_c}{\omega}\right)^2} , & -j\frac{\left(\frac{\omega_p}{\omega}\right)^2 \frac{\omega_c}{\omega}}{\left(1-j\frac{\nu}{\omega}\right)^2 - \left(\frac{\omega_c}{\omega}\right)^2} , & 0 \\ j\frac{\left(\frac{\omega_p}{\omega}\right)^2 \frac{\omega_c}{\omega}}{\left(1-j\frac{\nu}{\omega}\right)^2 - \left(\frac{\omega_c}{\omega}\right)^2} , & 1 - \frac{\left(\frac{\omega_p}{\omega}\right)^2 \left(1 - j\frac{\nu}{\omega}\right)}{\left(1-j\frac{\nu}{\omega}\right)^2 - \left(\frac{\omega_c}{\omega}\right)^2} , & 0 \\ 0 , & 0 , & 1 - \frac{\left(\frac{\omega_p}{\omega}\right)^2}{1 - j\frac{\nu}{\omega}} \end{bmatrix} \qquad \text{(A.4)}$$

$$= \begin{bmatrix} \varepsilon_{11} , & -j\varepsilon_{12} , & 0 \\ j\varepsilon_{12} , & \varepsilon_{11} , & 0 \\ 0 , & 0 , & \varepsilon_{33} \end{bmatrix}$$

where

$$\left.\begin{aligned} \varepsilon_{11} &= 1 - \frac{\left(\frac{\omega_p}{\omega}\right)^2 \left(1 - j\frac{\nu}{\omega}\right)}{\left(1-j\frac{\nu}{\omega}\right)^2 - \left(\frac{\omega_c}{\omega}\right)^2} \\ \varepsilon_{12} &= \frac{\left(\frac{\omega_p}{\omega}\right)^2 \frac{\omega_c}{\omega}}{\left(1-j\frac{\nu}{\omega}\right)^2 - \left(\frac{\omega_c}{\omega}\right)^2} \\ \varepsilon_{33} &= 1 - \frac{\left(\frac{\omega_p}{\omega}\right)^2}{\left(1 - j\frac{\nu}{\omega}\right)} \end{aligned}\right\} \qquad \text{(A.5)}$$

Note that if $\frac{\omega_c}{\omega} = 0$, $\varepsilon_{12} = 0$, $\varepsilon_{11} = \varepsilon_{33}$, and the zero magnetic field results of p.58 are recovered.

Define the effective electric displacement $\underset{\sim}{D}'$ by

$$\underset{\sim}{D}' = \varepsilon_0 \underset{\approx}{\varepsilon} \underset{\sim}{E} \tag{A.6}$$

Then
$$\begin{aligned} \nabla . \underset{\sim}{D}' &= \varepsilon_0 \nabla . (\underset{\approx}{\varepsilon} \underset{\sim}{E}) \\ &= \nabla . \varepsilon_0 \left(\underset{\approx}{I} + \frac{\underset{\approx}{R}^{-1}}{j\omega\varepsilon_0} \right) \underset{\sim}{E} \\ &= \nabla . \underset{\sim}{D} + \frac{\nabla . \underset{\sim}{J}}{j\omega} \\ &= \rho - \rho \\ &= 0 \end{aligned} \tag{A.7}$$

since $\nabla . \underset{\sim}{J} = -\frac{\partial \rho}{\partial t} = j\omega\rho$.

In rotating coordinates, using the transformations in Appendix B, Equation (B.4),

$$\begin{aligned} \underset{\approx}{\varepsilon}_{rot} &= \underset{\approx}{U} \underset{\approx}{\varepsilon} \underset{\approx}{U}^{-1} \\ &= \frac{1}{2} \begin{bmatrix} 1 & -j & 0 \\ 1 & j & 0 \\ 0 & 0 & \sqrt{2} \end{bmatrix} \begin{bmatrix} \varepsilon_{11} & -j\varepsilon_{12} & 0 \\ j\varepsilon_{12} & \varepsilon_{11} & 0 \\ 0 & 0 & \varepsilon_{33} \end{bmatrix} \begin{bmatrix} 1 & 1 & 0 \\ j & -j & 0 \\ 0 & 0 & \sqrt{2} \end{bmatrix} \\ &= \frac{1}{2} \begin{bmatrix} 2(\varepsilon_{11} + \varepsilon_{12}) & 0 & 0 \\ 0 & 2(\varepsilon_{11} - \varepsilon_{12}) & 0 \\ 0 & 0 & 2\varepsilon_{33} \end{bmatrix} . \end{aligned}$$

Define
$$\underline{\underline{\varepsilon}}_{rot} = \begin{bmatrix} \varepsilon_\ell & 0 & 0 \\ 0 & \varepsilon_r & 0 \\ 0 & 0 & \varepsilon_{33} \end{bmatrix} \tag{A.8}$$

where
$$\left.\begin{aligned} \varepsilon_\ell &= \varepsilon_{11} + \varepsilon_{12} = 1 - \frac{\left(\frac{\omega_p}{\omega}\right)^2}{1 + \frac{\omega_c}{\omega} - j\frac{\nu}{\omega}} \\ \varepsilon_r &= \varepsilon_{11} - \varepsilon_{12} = 1 - \frac{\left(\frac{\omega_p}{\omega}\right)^2}{1 - \frac{\omega_c}{\omega} - j\frac{\nu}{\omega}} \\ \varepsilon_{33} &= 1 - \frac{\left(\frac{\omega_p}{\omega}\right)^2}{1 - j\frac{\nu}{\omega}} \end{aligned}\right\} \tag{A.9}$$

Conversely
$$\left.\begin{aligned} \varepsilon_{\parallel} &= \frac{1}{2}\left(\varepsilon_{\ell} + \varepsilon_{r}\right) \\ \varepsilon_{12} &= \frac{1}{2}\left(\varepsilon_{\ell} - \varepsilon_{r}\right) \end{aligned}\right\} \qquad (A.10)$$

Thus the transposition into the rotating coordinate system reduces the anisotropic dielectric tensor in Equation (A.4) to a tensor having purely diagonal terms. In unbounded plasma propagation this enables the electromagnetic waves to be resolved into three uncoupled waves, and also facilitates analysis of the bounded case.

A.3 Propagation of TEM waves along the magnetic field in an unbounded uniform plasma.

From Maxwell's Equations (A.1) & (A.3) we get the wave equation:-

$$\begin{aligned} \nabla\times\nabla\times\underset{\sim}{E} &= -j\omega\mu_0\,\nabla\times\underset{\sim}{H} \\ &= \mu_0\varepsilon_0\,\underline{\underline{\varepsilon}}\,\omega^2\underset{\sim}{E} \\ &= k_0^2\,\underline{\underline{\varepsilon}}\,\underset{\sim}{E} \end{aligned} \qquad (A.11)$$

where $k_0 = \frac{\omega}{c} = \omega\sqrt{\mu_0\varepsilon_0}$ is the free-space wave number.

As these are TEM waves, $\underset{\sim}{E}$ is a function of z only (not of x, y or ℓ, r or ρ, θ in Cartesian, rotating, cylindrical coordinate systems respectively).

Let $\underset{\sim}{E} = \underset{\sim}{E_0}\,e^{-jk_0kz}$ as before. Then, in rotating coordinates, using Equation (B.10),

$$\begin{aligned} \nabla\times\underset{\sim}{E} &= j\begin{bmatrix} \frac{\partial E_z}{\partial r} - \frac{\partial E_\ell}{\partial z} \\ -\frac{\partial E_z}{\partial \ell} + \frac{\partial E_r}{\partial z} \\ \frac{\partial E_\ell}{\partial \ell} - \frac{\partial E_r}{\partial r} \end{bmatrix} \\ &= j\begin{bmatrix} jk_0kE_\ell \\ -jk_0kE_r \\ 0 \end{bmatrix} \end{aligned}$$

and $\nabla \times \nabla \times \underset{\sim}{E} = \begin{bmatrix} k_o^2 k^2 E_\ell \\ k_o^2 k^2 E_r \\ 0 \end{bmatrix}$

Equation (A.11) becomes

$$k_o^2 \begin{bmatrix} k^2 E_\ell \\ k^2 E_r \\ 0 \end{bmatrix} = k_o^2 \begin{bmatrix} \varepsilon_\ell E_\ell \\ \varepsilon_r E_r \\ \varepsilon_{33} E_z \end{bmatrix} \qquad \text{(A.12)}$$

From Equation (A.12) we get two independently propagating waves, left-hand and right-hand polarised, having normalised propagation constants:- (ordinary) $k_\ell^2 = \varepsilon_\ell = \varepsilon_{11} + \varepsilon_{12}$

and (extraordinary) $k_r^2 = \varepsilon_r = \varepsilon_{11} - \varepsilon_{12}$

and a longitudinal, non-propagating, wave $\varepsilon_{33} = 0$, which need not be considered here.

Reflection from a plane boundary.

As the ordinary and extraordinary waves are uncoupled, they can be treated in the manner of plane waves reflected from a semi - infinite isotropic medium of dielectric coefficients $\varepsilon_o \varepsilon_\ell$ and $\varepsilon_o \varepsilon_r$ respectively. Thus the voltage reflection coefficients are

$$\left.\begin{aligned} R_\ell &= \frac{1 - \varepsilon_\ell^{\frac{1}{2}}}{1 + \varepsilon_\ell^{\frac{1}{2}}} = \frac{1 - k_\ell}{1 + k_\ell} \\ \text{and} \quad R &= \frac{1 - \varepsilon_r^{\frac{1}{2}}}{1 + \varepsilon_r^{\frac{1}{2}}} \qquad \frac{1 - k_r}{1 + k_r} \end{aligned}\right\} \qquad \text{(A.13)}$$

Consider the reflection of an incident TEM wave, propagating in the z - direction and polarised in the x - direction, on the free-space plasma interface at $z = 0$, as shown in Fig.(A.1):-

the incident wave $\underset{\sim}{E}_{xi} = E_o \hat{i}$.

This may be resolved into rotating components by Equation (B.2):-

$$\underset{\sim}{E}_{\ell i} = \frac{1}{\sqrt{2}} E_o \hat{\ell}$$

and $$\underset{\sim}{E}_{ri} = \frac{1}{\sqrt{2}} E_o \hat{r} .$$

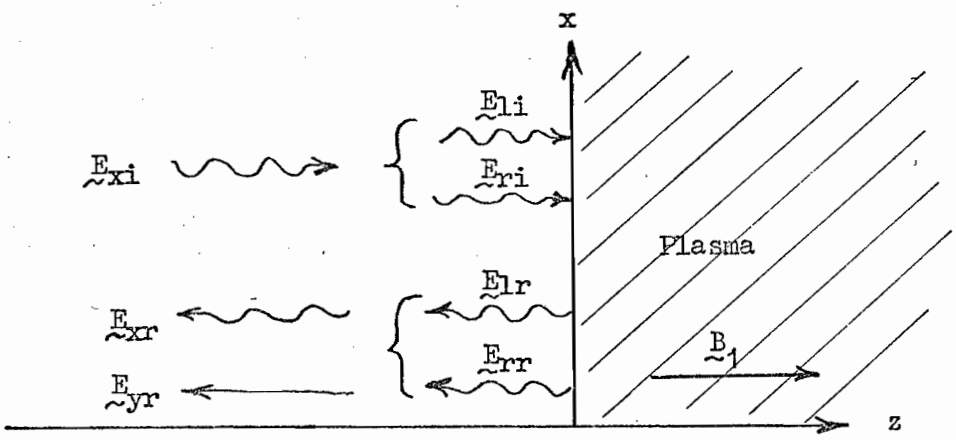


Fig. 70 Unbounded magnetised-plasma — vacuum interface.

The reflected waves are;-

$$\underset{\sim}{E}_{\ell r} = \frac{E_o}{\sqrt{2}} \frac{1 - k_\ell}{1 + k_\ell} \hat{\ell} ,$$

$$\underset{\sim}{E}_{rr} = \frac{E_o}{\sqrt{2}} \frac{1 - k_r}{1 + k_r} \hat{r} . \qquad (A.14)$$

Equation (A.14) is then transformed back into the Cartesian frame to give the reflected waves

$$\underset{\sim}{E}_{xr} = \frac{1}{\sqrt{2}} \left(E_{\ell r} + E_{rr} \right) \hat{i}$$

$$= E_o \frac{1 - k_\ell k_r}{(1 + k_\ell)(1 + k_r)} \hat{i}$$

and $$\underset{\sim}{E}_{yr} = E_o \frac{k_\ell - k_r}{(1 + k_\ell)(1 + k_r)} \hat{j}$$

The x and y components of the voltage reflection coefficient are then given by

$$\left.\begin{aligned} R_x &= \frac{E_{xr}}{E_o} = \frac{1 - k_\ell k_r}{(1+k_\ell)(1+k_r)} \\ R_y &= \frac{E_{yr}}{E_o} = \frac{k_\ell - k_r}{(1+k_\ell)(1+k_r)} \end{aligned}\right\} \quad (A.15)$$

The power reflection coefficient R_p is given by

$$\begin{aligned} R_p &= \frac{E_{xr}\, E_{xr}^{*} + E_{yr}\, E_{yr}^{*}}{E_o^2} \\ &= \left|\left(\frac{1 - k_\ell k_r}{(1+k_\ell)(1+k_r)}\right)^2\right| + \left|\left(\frac{k_\ell - k_r}{(1+k_\ell)(1+k_r)}\right)^2\right| \end{aligned} \quad (A.16)$$

where E^{*} is the complex conjugate of E. Note that, since R_x & R_y are in general complex quantities, since k_ℓ & k_r are complex,

$$R_p \neq \left|R_x^2 + R_y^2\right|.$$

A.4 Solution of Maxwell's equations for propagation of EM waves in anisotropic plasma in a waveguide.

When a solution to Maxwell's equations is required for a wave propagating in a waveguide, such as in the coaxial geometry to be considered here, Equation (A.11) can no longer be used as the left- and right- hand waves are no longer uncoupled.

Transverse variations in the wave vectors are now possible. It is assumed that, in rotating coordinates, all field vectors vary as $A(\ell, r)\, e^{-jk_o k z}$, where the wave is propagating in the z - direction.

Using Equations (B.9) & (B.10), Maxwell's equations (A.1) now become:-

$$\nabla \times \underset{\sim}{E} = j \begin{bmatrix} \frac{\partial E_z}{\partial r} + jk_o k E_\ell \\ -\frac{\partial E_z}{\partial \ell} - jk_o k E_r \\ \frac{\partial E_\ell}{\partial \ell} - \frac{\partial E_r}{\partial r} \end{bmatrix} = -j\omega\mu_o \begin{bmatrix} H_\ell \\ H_r \\ H_z \end{bmatrix}, \qquad \text{(A.17)}$$

$$\nabla \times \underset{\sim}{H} = j \begin{bmatrix} \frac{\partial H_z}{\partial r} + jk_o k H_\ell \\ -\frac{\partial H_z}{\partial \ell} - jk_o k H_r \\ \frac{\partial H_\ell}{\partial \ell} - \frac{\partial H_r}{\partial r} \end{bmatrix} = j\omega\varepsilon_o \begin{bmatrix} \varepsilon_\ell E_\ell \\ \varepsilon_r E_r \\ \varepsilon_{33} E_z \end{bmatrix} \qquad \text{(A.18)}$$

$$\nabla . \underset{\sim}{D}' = \nabla . \left(\varepsilon_o \underset{\approx}{\varepsilon} \underset{\sim}{E} \right) = 0,$$

from which $$\varepsilon_\ell \frac{\partial E_\ell}{\partial \ell} + \varepsilon_r \frac{\partial E_r}{\partial r} - jk_o k \varepsilon_{33} E_z = 0, \qquad \text{(A.19)}$$

$$\nabla . \underset{\sim}{H} = \frac{\partial H_\ell}{\partial \ell} + \frac{\partial H_r}{\partial r} - jk_o k H_z = 0 \qquad \text{(A.20)}$$

Taking, respectively, the ℓ components of (A.17) & (A.18) and then the r components, we have,

$$\begin{bmatrix} -jk_o k , -\omega\mu_o \\ \omega\varepsilon_o\varepsilon_\ell , -jk_o k \end{bmatrix} \begin{bmatrix} E_\ell \\ H_\ell \end{bmatrix} = \begin{bmatrix} \frac{\partial E_z}{\partial r} \\ \frac{\partial H_z}{\partial r} \end{bmatrix} \qquad \text{(A.21)}$$

and

$$\begin{bmatrix} -jk_o k , \omega\mu_o \\ -\omega\varepsilon_o\varepsilon_r , -jk_o k \end{bmatrix} \begin{bmatrix} E_r \\ H_r \end{bmatrix} = \begin{bmatrix} \frac{\partial E_z}{\partial \ell} \\ \frac{\partial H_z}{\partial \ell} \end{bmatrix} \qquad \text{(A.22)}$$

Equations (A.21) & (A.22) can now be inverted to give the transverse components of the field vectors in terms of the transverse derivatives of the longitudinal components E_z & H_z .

$$\begin{bmatrix} E_\ell \\ H_\ell \end{bmatrix} = \frac{1}{k_0^2(\varepsilon_\ell - k^2)} \begin{bmatrix} -jk_0 k \;,\; \omega\mu_0 \\ -\omega\varepsilon_0\varepsilon_\ell \;,\; -jk_0 k \end{bmatrix} \begin{bmatrix} \frac{\partial E_z}{\partial r} \\ \frac{\partial H_z}{\partial r} \end{bmatrix} \qquad (A.23)$$

$$\begin{bmatrix} E_r \\ H_r \end{bmatrix} = \frac{1}{k_0^2(\varepsilon_r - k^2)} \begin{bmatrix} -jk_0 k \;,\; -\omega\mu_0 \\ \omega\varepsilon_0\varepsilon_r \;,\; -jk_0 k \end{bmatrix} \begin{bmatrix} \frac{\partial E_z}{\partial \ell} \\ \frac{\partial H_z}{\partial \ell} \end{bmatrix} \qquad (A.24)$$

It remains to find a solution to Maxwell's equations in terms of E_z & H_z. By multiplying the z - component of Equation (A.17) by ε_r and adding this to Equation (A.19) we get

$$(\varepsilon_\ell + \varepsilon_r)\frac{\partial E_\ell}{\partial \ell} = jk_0 k \varepsilon_{33} E_z - \omega\mu_0 \varepsilon_r H_z \,,$$

and similarly by adding the z- component of Equation (A.18) to Equation(A.20),

$$2\frac{\partial H_\ell}{\partial \ell} = \omega\varepsilon_0\varepsilon_{33} E_z + jk_0 k H_z \,.$$

i.e.
$$\begin{bmatrix} \frac{\partial E_\ell}{\partial \ell} \\ \frac{\partial H_\ell}{\partial \ell} \end{bmatrix} = \begin{bmatrix} j\frac{k_0 k \varepsilon_{33}}{(\varepsilon_\ell + \varepsilon_r)} \;,\; -\frac{\omega\mu_0 \varepsilon_r}{(\varepsilon_\ell + \varepsilon_r)} \\ \frac{\omega\varepsilon_0\varepsilon_{33}}{2} \;,\; \frac{jk_0 k}{2} \end{bmatrix} \begin{bmatrix} E_z \\ H_z \end{bmatrix} \qquad (A.25)$$

Differentiate Equation (A.21) w.r.t. ℓ :-

$$\begin{bmatrix} -jk_0 k \;,\; -\omega\mu_0 \\ \omega\varepsilon_0\varepsilon_\ell \;,\; -jk_0 k \end{bmatrix} \begin{bmatrix} \frac{\partial E_\ell}{\partial \ell} \\ \frac{\partial H_\ell}{\partial \ell} \end{bmatrix} = \begin{bmatrix} \frac{\partial^2 E_z}{\partial \ell \partial r} \\ \frac{\partial^2 H_z}{\partial \ell \partial r} \end{bmatrix} \qquad (A.26)$$

Substituting (A.25) in (A.26) we get, by matrix multiplication,

$$\begin{bmatrix} \frac{\partial^2 E_z}{\partial \ell \partial r} \\ \frac{\partial^2 H_z}{\partial \ell \partial r} \end{bmatrix} = \begin{bmatrix} \frac{k_0^2 \varepsilon_{33}(2k^2 - \varepsilon_\ell - \varepsilon_r)}{2(\varepsilon_\ell + \varepsilon_r)} \;,\; -j\frac{\omega\mu_0 k_0 k(\varepsilon_\ell - \varepsilon_r)}{2(\varepsilon_\ell + \varepsilon_r)} \\ j\frac{\omega\varepsilon_0 k_0 k \varepsilon_{33}(\varepsilon_\ell - \varepsilon_r)}{2(\varepsilon_\ell + \varepsilon_r)} \;,\; -\frac{k_0^2(2\varepsilon_\ell\varepsilon_r - k^2(\varepsilon_\ell + \varepsilon_r))}{2(\varepsilon_\ell + \varepsilon_r)} \end{bmatrix} \begin{bmatrix} -E_z \\ H_z \end{bmatrix} \qquad (A.27)$$

In order to conform with the notation of Bers (50) we define, using Equations (A.9) & (A.10), the following parameters:-

$$\left.\begin{aligned}
a &= -\frac{k_o^2\varepsilon_{33}(2k^2-\varepsilon_e-\varepsilon_r)}{(\varepsilon_e+\varepsilon_r)} &&= -\frac{k_o^2\varepsilon_{33}(k^2-\varepsilon_{11})}{\varepsilon_{11}} \\
b &= -j\frac{\omega\mu_o k_o k(\varepsilon_e-\varepsilon_r)}{(\varepsilon_e+\varepsilon_r)} &&= -j\frac{\omega\mu_o k_o k\,\varepsilon_{12}}{\varepsilon_{11}} \\
c &= \frac{k_o^2(2\varepsilon_e\varepsilon_r-k^2(\varepsilon_e+\varepsilon_r))}{(\varepsilon_e+\varepsilon_r)} &&= \frac{k_o^2(\varepsilon_{11}^2-\varepsilon_{12}^2-k^2\varepsilon_{11})}{\varepsilon_{11}} \\
d &= j\frac{\omega\varepsilon_o k_o k(\varepsilon_e-\varepsilon_r)\varepsilon_{33}}{(\varepsilon_e+\varepsilon_r)} &&= j\frac{\omega\varepsilon_o k_o k\,\varepsilon_{12}\varepsilon_{33}}{\varepsilon_{11}}
\end{aligned}\right\} \quad (A.28)$$

Since, from Equation (B.12),

$$\nabla_T^2 = \frac{\partial^2}{\partial x^2} + \frac{\partial^2}{\partial y^2} = 2\frac{\partial^2}{\partial l\,\partial r} ,$$

Equations (A.27) can be expressed as

$$\nabla_T^2 E_z + a\,E_z = b\,H_z \qquad (A.29)$$

and $$\nabla_T^2 H_z + c\,H_z = d\,E_z \qquad (A.30)$$

Substituting (A.29) into (A.30) we get the biharmonic equation

$$\nabla_T^4 E_z + (a + c)\nabla_T^2 E_z + (ac - bd)\,E_z = 0 \qquad (A.31)$$

and similarly

$$\nabla_T^4 H_z + (a + c)\nabla_T^2 H_z + (ac - bd)\,H_z = 0 \qquad (A.32)$$

We attempt to find separable solutions E_{z1} , H_{z1} and E_{z2} , H_{z2} which satisfy the harmonic equation

$$(\nabla_T^2 + p_i)E_{zi} = 0 , \quad i = 1, 2 \qquad (A.33)$$

where p_1 & p_2 are the transverse wave numbers which satisfy the equation:

$$p_i^4 - (a + c)p_i^2 + (ac - bd) = 0 \qquad (A.34)$$

Using (A.33) in (A.29) and (A.30),

$$H_z = a E_z + \nabla_T^2 E_z$$
$$= a E_{z1} + a E_{z2} - p_1^2 E_{z1} - p_2^2 E_{z2}$$
$$= h_1 E_{z1} + h_2 E_{z2} \qquad (A.35)$$

where $$h_i = \frac{a - p_i^2}{b} = \frac{d}{c - p_i^2} \quad , \quad i = 1, 2 . \qquad (A.36)$$

A.5 Particular Solution in Longitudinally Magnetized Coaxial Line.

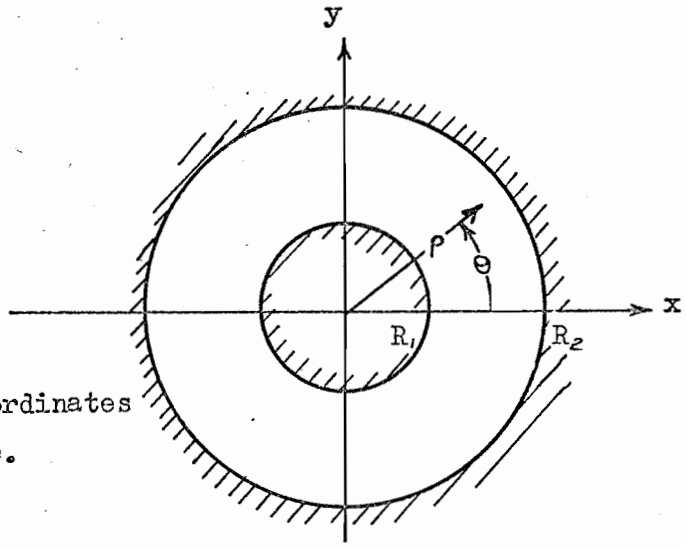


Fig.71
Cylindrical coordinates in coaxial line.

To solve Equation (A.33) with coaxial, infinitely-conducting, boundaries, the left- and right- hand rotating coordinates (ℓ , r , z) are transformed into cylindrical polar coordinates (ρ , Θ, z), using the transformations given in Appendix B.

We look for solutions of the form

$$E_{zi} = R(\rho)\textcircled{H}(\Theta) .$$

Then Equation (A.33) becomes, using Equation (B.17):-

$$\frac{\rho^2}{R}\frac{\partial^2 R}{\partial \rho^2} + \frac{\rho}{R}\frac{\partial R}{\partial \rho} + \rho^2 p_i^2 + \frac{1}{\textcircled{H}}\frac{\partial^2 \textcircled{H}}{\partial \Theta^2} \qquad (A.37)$$

Separating the variables, and noting that $\textcircled{H}(\theta) = \textcircled{H}(\theta + 2\pi)$ in coaxial geometry, we have,

$$\frac{\partial^2 \textcircled{H}}{\partial \theta^2} = -n \textcircled{H}$$

or $$\textcircled{H} = C e^{\pm jn\theta} \qquad (A.38)$$

for $n = 0, 1, 2, 3, \ldots\ldots\ldots$

Then $$\frac{\partial^2 R}{\partial \rho^2} + \frac{1}{\rho}\frac{\partial R}{\partial \rho} + \left(p_i^2 - \frac{n^2}{\rho}\right)R = 0 \qquad (A.39)$$

This is Bessel's equation of order n and has solutions (60),

$$R = A J_n(p_i \rho) + B Y_n(p_i \rho), \qquad (A.40)$$

where J_n, Y_n, are Bessel's functions of the first and second kind of order n.

The nth azimuthal mode family of solutions for E_z and H_z is then given by :-

$$\begin{aligned}(E_n)_z &= \sum_{i=1,2} [A_i J_n(p_i\rho) + B_i Y_n(p_i\rho)] e^{\pm jn\theta} \\ (H_n)_z &= \sum_{i=1,2} h_i [A_i J_n(p_i\rho) + B_i Y_n(p_i\rho)] e^{\pm jn\theta}\end{aligned} \qquad (A.41)$$

Transverse components of $\underset{\sim}{E}$, $\underset{\sim}{H}$.

It is now necessary to determine the radial and azimuthal components of $\underset{\sim}{E}$, $\underset{\sim}{H}$ in terms of E_z, H_z.

Using Equation (B.19), the ρ, θ components of $\underset{\sim}{E}$, $\underset{\sim}{H}$ are given by

$$\begin{bmatrix} E_\rho \\ H_\rho \\ E_\theta \\ H_\theta \end{bmatrix} = \frac{1}{2}\begin{bmatrix} e^{j\theta} & 0 & e^{-j\theta} & 0 \\ 0 & e^{j\theta} & 0 & e^{-j\theta} \\ j e^{j\theta} & 0 & -j e^{j\theta} & 0 \\ 0 & j e^{j\theta} & 0 & -j e^{j\theta} \end{bmatrix} \begin{bmatrix} E_\ell \\ H_\ell \\ E_r \\ H_r \end{bmatrix} \qquad (A.42)$$

Equations (A.23) and (A.24) can be combined to give

$$\begin{bmatrix} E_\ell \\ H_\ell \\ E_r \\ H_r \end{bmatrix} = \frac{1}{k_0^2} \begin{bmatrix} 0 & 0 & -j\frac{k_0 k}{(\varepsilon_\ell - k^2)} & \frac{\omega\mu_0}{(\varepsilon_\ell - k^2)} \\ 0 & 0 & \frac{-\omega\varepsilon_0\varepsilon_\ell}{(\varepsilon_\ell - k^2)} & -j\frac{k_0 k}{(\varepsilon_\ell - k^2)} \\ -j\frac{k_0 k}{(\varepsilon_r - k^2)} & -\frac{\omega\mu_0}{(\varepsilon_r - k^2)} & 0 & 0 \\ \frac{\omega\varepsilon_0\varepsilon_r}{(\varepsilon_r - k^2)} & -j\frac{k_0 k}{(\varepsilon_r - k^2)} & 0 & 0 \end{bmatrix} \begin{bmatrix} \frac{\partial E_z}{\partial \ell} \\ \frac{\partial H_z}{\partial \ell} \\ \frac{\partial E_z}{\partial r} \\ \frac{\partial H_z}{\partial r} \end{bmatrix} \qquad \text{(A.43)}$$

Finally, from (B.16), we have

$$\begin{bmatrix} \frac{\partial}{\partial \ell} \\ \frac{\partial}{\partial r} \end{bmatrix} = \frac{1}{\sqrt{2}} \begin{bmatrix} e^{j\theta} & j\frac{e^{j\theta}}{\rho} \\ e^{-j\theta} & -j\frac{e^{-j\theta}}{\rho} \end{bmatrix} \begin{bmatrix} \frac{\partial}{\partial \rho} \\ \frac{\partial}{\partial \theta} \end{bmatrix}$$

which leads to

$$\begin{bmatrix} \frac{\partial E_z}{\partial \ell} \\ \frac{\partial H_z}{\partial \ell} \\ \frac{\partial E_z}{\partial r} \\ \frac{\partial H_z}{\partial r} \end{bmatrix} = \frac{1}{\sqrt{2}} \begin{bmatrix} e^{j\theta} & 0 & j\frac{e^{j\theta}}{\rho} & 0 \\ 0 & e^{j\theta} & 0 & j\frac{e^{j\theta}}{\rho} \\ e^{-j\theta} & 0 & -j\frac{e^{-j\theta}}{\rho} & 0 \\ 0 & e^{-j\theta} & 0 & -j\frac{e^{-j\theta}}{\rho} \end{bmatrix} \begin{bmatrix} \frac{\partial E_z}{\partial \rho} \\ \frac{\partial H_z}{\partial \rho} \\ \frac{\partial E_z}{\partial \theta} \\ \frac{\partial H_z}{\partial \theta} \end{bmatrix} \qquad \text{(A.44)}$$

By multiplying the matrices of Equations (A.42), (A.43) & (A.44) together, we get, after slight rearrangement,

$$\begin{bmatrix} E_\rho \\ H_\rho \\ E_\theta \\ H_\theta \end{bmatrix} = \frac{1}{k_o^2(\varepsilon_e - k^2)(\varepsilon_r - k^2)} \begin{bmatrix} -jk_o k(\varepsilon_e+\varepsilon_r-2k^2), & -\omega\mu_o(\varepsilon_e-\varepsilon_r), & \frac{k_o k}{\rho}(\varepsilon_e-\varepsilon_r), & -j\frac{\omega\mu_o}{\rho}(\varepsilon_e+\varepsilon_r-2k^2) \\ -\omega\varepsilon_o k^2(\varepsilon_e-\varepsilon_r), & -jk_o k(\varepsilon_e+\varepsilon_r-2k^2), & j\frac{\omega\varepsilon_o}{\rho}\left(2\varepsilon_e\varepsilon_r - k^2(\varepsilon_e+\varepsilon_r)\right), & \frac{k_o k}{\rho}(\varepsilon_e-\varepsilon_r) \\ -k_o k(\varepsilon_e-\varepsilon_r), & j\omega\mu_o(\varepsilon_e+\varepsilon_r-2k^2), & -j\frac{k_o k}{\rho}(\varepsilon_e+\varepsilon_r-2k^2), & -\frac{\omega\mu_o}{\rho}(\varepsilon_e-\varepsilon_r) \\ -j\omega\varepsilon_o\left(2\varepsilon_e\varepsilon_r - k^2(\varepsilon_e+\varepsilon_r)\right), & -k_o k(\varepsilon_e-\varepsilon_r), & -\frac{\omega\varepsilon_o k^2}{\rho}(\varepsilon_e-\varepsilon_r), & -j\frac{k_o k}{\rho}(\varepsilon_e+\varepsilon_r-2k^2) \end{bmatrix} \begin{bmatrix} \frac{\partial E_z}{\partial \rho} \\ \frac{\partial H_z}{\partial \rho} \\ \frac{\partial E_z}{\partial \theta} \\ \frac{\partial H_z}{\partial \theta} \end{bmatrix} \quad \text{(A.45)}$$

Equation (A.45) is the transform of Equations (A.23) & (A.24) from rotating coordinates to cylindrical coordinates.

As eventually only the quasi-TEM mode will be considered, we shall here consider only modes which are axisymmetric (independant of θ), and hence take $n = 0$.

Then $\frac{\partial E_z}{\partial \theta} = \frac{\partial H_z}{\partial \theta} = 0$, and the third and fourth columns of the matrix in Equation (A.45) need not be explicitly evaluated. Then, in terms of the longitudinal solutions in Equations (A.41), we have, with $n = 0$,

$$\frac{\partial E_{oz}}{\partial \rho} = \sum_{i=1,2} p_i \left[A_i J_o'(p_i \rho) + B_i Y_o'(p_i \rho)\right]$$

and $$\frac{\partial H_{oz}}{\partial \rho} = \sum_{i=1,2} h_i p_i \left[A_i J_o'(p_i \rho) + B_i Y_o'(p_i \rho)\right],$$

where $J_n' = \frac{\partial J_n}{\partial \rho}$ etc.

From this, $(E_o)_\rho$, $(H_o)_\rho$, $(E_o)_\theta$, and $(H_o)_\theta$ can be evaluated with the aid of Equation (A.45).

In particular,

$$(E_o)_\theta = \frac{1}{k_o^2(\varepsilon_\ell - k^2)(\varepsilon_r - k^2)} \sum_i p_i \left[-k_o k(\varepsilon_\ell - \varepsilon_r) + j h_i \omega \mu_o (\varepsilon_\ell + \varepsilon_r - 2k^2)\right] \times \left[A_i J_o'(p_i \rho) + B_i Y_o'(p_i \rho)\right]$$

$$= \sum_i G_i \left[A_i J_o'(p_i \rho) + B_i Y_o'(p_i \rho)\right] \qquad (A.46)$$

where $$G_i = \frac{1}{k_o^2(\varepsilon_\ell - k^2)(\varepsilon_r - k^2)} p_i \left[-k_o k(\varepsilon_\ell - \varepsilon_r) + j h_i \omega \mu_o (\varepsilon_\ell + \varepsilon_r - 2k^2)\right] \qquad (A.47)$$

Boundary conditions.

For an infinitely-conducting boundary, the component of $\underset{\sim}{E}$ tangential to the surface, $= \underset{\sim}{E}_t = 0$ at the boundary.

For coaxial geometry, with inner ($\rho = R_1$) and outer ($\rho = R_2$) boundaries assumed to have infinite conductivity, the boundary conditions are

$$E_z(R_1) = E_z(R_2) = E_\theta(R_1) = E_\theta(R_2) = 0 \qquad (A.48)$$

Using Equations (A. 41) with n = 0 and Equation (A.46), these boundary conditions can be written

$$\begin{bmatrix} J_0(p_1R_1), & Y_0(p_1R_1), & J_0(p_2R_1), & Y_0(p_2R_1) \\ J_0(p_1R_2), & Y_0(p_1R_2), & J_0(p_2R_2), & Y_0(p_2R_2) \\ G_1J_0'(p_1R_1), & G_1Y_0'(p_1R_1), & G_2J_0'(p_2R_1), & G_2Y_0'(p_2R_1) \\ G_1J_0'(p_1R_2), & G_1Y_0'(p_1R_2), & G_2J_0'(p_2R_2), & G_2Y_0'(p_2R_2) \end{bmatrix} \begin{bmatrix} A_1 \\ B_1 \\ A_2 \\ B_2 \end{bmatrix} = 0 \qquad (A.49)$$

Equation (A.49) is an equation whose solutions give values of the constants A_1, B_1, A_2, B_2 for the given boundaries R_1 & R_2. A necessary condition that a solution should exist is the determinantal equation

$$\Delta = \begin{vmatrix} J_0(p_1R_1), & Y_0(p_1R_1), & J_0(p_2R_1), & Y_0(p_2R_1) \\ J_0(p_1R_2), & Y_0(p_1R_2), & J_0(p_2R_2), & Y_0(p_2R_2) \\ G_1J_0'(p_1R_1), & G_1Y_0'(p_1R_1), & G_2J_0'(p_2R_1), & G_2Y_0'(p_2R_1) \\ G_1J_0'(p_1R_2), & G_1Y_0'(p_1R_2), & G_2J_0'(p_2R_2), & G_2Y_0'(p_2R_2) \end{vmatrix} = 0 \qquad (A.50)$$

Equation (A.50), together with

$$p_i^4 - (a + c)p_i^2 + (ac - bd) = 0 \qquad (A.34)$$

is the dispersion equation for the quasi-TEM mode in a uniform, axially magnetized plasma in a coaxial guide, and has as solutions values of k, the wave number for waves propagating in the plasma.

For a plasma with collisions, the terms in Equation (A.50) are complex Bessel's functions of complex argument, and computed solutions must be used. A digital computer program which solves

Equation (A.50) for given $\frac{\omega_p}{\omega}$, $\frac{\nu}{\omega}$ and $\frac{\omega_c}{\omega}$ is described in Appendix C.

In general there is an infinite series of complex values of k which satisfy Equation (A.50), corresponding to the infinite number of discrete axially symmetric modes which can exist in a plasma-filled coaxial line. As will be shown, for reflection measurements only the fundamental quasi-TEM mode will be considered. This mode degenerates into the coaxial TEM mode as $\frac{\omega_c}{\omega} \rightarrow 0$.

For computation purposes G_i is further simplified by using Equations (A.28), to give

$$ac - bd = \frac{2 k_o^4 \varepsilon_{33} (\varepsilon_e - k^2)(\varepsilon_r - k^2)}{(\varepsilon_e + \varepsilon_r)} \qquad (A.51)$$

Then, from Equation (A.47),

$$G_i = \frac{2 p_i k_o^2}{j\omega \varepsilon_o (ac - bd)} \left(-d - h_i a\right).$$

Since p_i^2, p_j^2 ($j \neq i$) are the solutions of Equation (A.34),

$$p_i^2 + p_j^2 = a + c ,$$

so, from Equation (A.36),

$$h_i = \frac{a - p_i^2}{b} = \frac{p_j^2 - c}{b} .$$

Then

$$G_i = \frac{2 p_i k_o^2}{j\omega \varepsilon_o (ac - bd) b} \left(-bd + ac - p_j^2 a\right)$$

$$= \frac{2 p_i k_o^2}{j\omega \varepsilon_o b} \left[1 - \frac{p_j^2 a}{(ac - bd)}\right] . \qquad (A.52)$$

It can be seen that the factor $\frac{2 p_i k_o^2}{j\omega \varepsilon_o b}$ has poles only if $\omega = 0$ or $\varepsilon_e = \varepsilon_r$ (i.e. $\frac{\omega_c}{\omega} = 0$), and that this factor is a common factor

of rows 3 & 4 of the determinant in Equation (A.50). Thus for computation we can replace G_i by

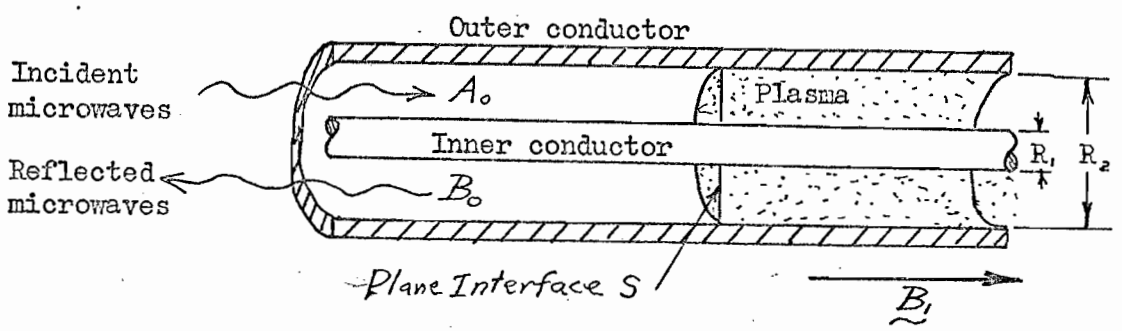
$$g_i = p_i \left[1 - \frac{p_j^2 a}{(ac - bd)} \right] . \qquad (A.53)$$

A.6 Reflection from Magnetized Plasma in Coaxial Line.

In this treatment the method used by Brodwin & Miller (57) for reflection in a ferrite-filled coaxial line is adapted to the plasma-filled line.

It is stressed that, in using the quasi-TEM mode approximation, it is nowhere assumed that other modes are ignored. The prime approximation is that on integrating across the plasma-vacuum boundary, the coupling between these higher modes and the TEM mode in the empty line is small. As the plasma to be considered is lossy, any higher modes will be damped, and, with poor coupling to the exciting TEM mode, will be of small amplitude.

Consider the vacuum-plasma interface in the coaxial line:-



Let A_o and B_o be the coefficients for the incident and reflected modes in the empty waveguide. The modes in the empty wqveguide are then $\underset{\sim}{E}_{TEM}$ & $\underset{\sim}{H}_{TEM}$ and the higher modes

$$\sum_{m=1}^{\infty} B_m \underset{\sim}{E}_m \quad \text{and} \quad \sum_{m=1}^{\infty} B_m \underset{\sim}{H}_m \ .$$

The plasma modes (m = 1 for the quasi-TEM mode) are $\sum_{m=1}^{\infty} T_m \underset{\sim}{E}_m^p$ and $\sum_{m=1}^{\infty} T_m \underset{\sim}{H}_m^p$. The subscript t denotes transverse components.

Matching transverse components across the interface S of the empty-line and plasma modes gives

$$\sum_{m=1}^{\infty} T_m (\underset{\sim}{E}_m^p)_t = (A_o + B_o)(\underset{\sim}{E}_{TEM})_t + \sum_{m=1}^{\infty} B_m (\underset{\sim}{E}_m)_t \qquad (A.54)$$

$$\& \sum_{m} T_m (\underset{\sim}{H}_m^p)_t = (A_o - B_o)(\underset{\sim}{H}_{TEM})_t - \sum_{m=1}^{\infty} B_m (H_m)_t \qquad (A.55)$$

Form the scalar product of Equation (A.54) with $(E_{TEM})_t^*$ and intergrate across S , remembering that the empty guide modes are mutually orthoganal:

$$\sum_{m=1}^{\infty} T_m \int_0^{2\pi}\int_{R_1}^{R_2} (\underset{\sim}{E}_{TEM})_t^* \cdot (\underset{\sim}{E}_m^p)_t \rho \, d\rho \, d\theta = (A_o + B_o) \int_0^{2\pi}\int_{R_1}^{R_2} |(\underset{\sim}{E}_{TEM})_t|^2 \rho \, d\rho \, d\theta .$$

But $(\underset{\sim}{E}_{TEM})_t = \underset{\sim}{E}_\rho = \frac{E_o}{2\pi\rho} e^{j(\omega t - k_o k z)} \hat{\rho}$,

and so $\sum_{m=1}^{\infty} E_o T_m \int_{R_1}^{R_2} (\underset{\sim}{E}_m^p)_\rho \, d\rho = \frac{A_o + B_o}{2\pi} E_o^2 \log \frac{R_2}{R_1}$. (A.56)

Similarly, using $\underset{\sim}{H}_{TEM} = \underset{\sim}{H}_\theta = \frac{|\underset{\sim}{E}_\rho|}{\sqrt{\frac{\mu_o}{\varepsilon_o}}} \hat{\theta}$,

we get (A.57)

$$\sum_{m=1}^{\infty} T_m \frac{E_o}{\sqrt{\frac{\mu_o}{\varepsilon_o}}} \int_{R_1}^{R_2} (\underset{\sim}{H}_m^p)_\theta \, d\theta = \frac{A_o - B_o}{2\pi \frac{\mu_o}{\varepsilon_o}} E_o^2 \log \frac{R_2}{R_1} .$$

Put (A.58)

$$I_m = \int_{R_1}^{R_2} (\underset{\sim}{E}_m^p)_\rho \, d\rho$$

$$J_m = \int_{R_1}^{R_2} (\underset{\sim}{H}_m^p)_\theta \, d\rho$$

$$\text{Then} \quad \sum_{m=1}^{\infty} T_m E_o I_m = \frac{A_o + B_o}{2\pi} E_o^2 \log \frac{R_2}{R_1}$$

$$\text{and} \quad \sum_{m=1}^{\infty} T_m E_o J_m = \frac{A_o - B_o}{2\pi\sqrt{\frac{\mu_o}{\varepsilon_o}}} E_o \log \frac{R_2}{R_1} \qquad \text{(A.59)}$$

If all but the axisymmetric quasi-TEM mode (m = 1) are neglected, then Equations (A.59) give:

$$\frac{I_1}{J_1} = \frac{(A_o + B_o)}{(A_o - B_o)}\sqrt{\frac{\mu_o}{\varepsilon_o}} \; . \qquad \text{(A.60)}$$

Using Equation (A.45),

$$I_1 = \int_{R_1}^{R_2} (\underset{\sim}{E}_1^p)_\rho \, d\rho$$

$$= \frac{1}{k_o^2(\varepsilon_\ell - k^2)(\varepsilon_r - k^2)} \int_{R_1}^{R_2} \left[-jk_o k(\varepsilon_\ell + \varepsilon_r - 2k^2)\frac{\partial E_z}{\partial \rho} - \omega\mu_o(\varepsilon_\ell - \varepsilon_r)\frac{\partial H_z}{\partial \rho}\right] d\rho.$$

$$= \frac{-\omega\mu_o(\varepsilon_\ell - \varepsilon_r)}{k_o^2(\varepsilon_\ell - k^2)(\varepsilon_r - k^2)} \left[H_z(R_2) - H_z(R_1)\right],$$

since $E_z(R_1) = E_z(R_2) = 0$, as they satisfy the boundary conditions at the conductor surfaces.

Similarly, $J_1 = \int_{R_1}^{R_2} (\underset{\sim}{H}_1^p)_\theta \, d\rho$

$$= \frac{1}{k_o^2(\varepsilon_\ell - k^2)(\varepsilon_r - k^2)} \int_{R_1}^{R_2} \left[-j\omega\varepsilon_o(2\varepsilon_\ell\varepsilon_r - k^2(\varepsilon_\ell + \varepsilon_r))\frac{\partial E_z}{\partial \rho} - k_o k(\varepsilon_\ell - \varepsilon_r)\frac{\partial H_z}{\partial \rho}\right] d\rho.$$

$$= \frac{-k_o k(\varepsilon_\ell - \varepsilon_r)\left(H_z(R_2) - H_z(R_1)\right)}{k_o^2(\varepsilon_\ell - k^2)(\varepsilon_r - k^2)} \; .$$

$$\frac{I_1}{J_1} = \frac{\omega\mu_o}{k_o k} = \sqrt{\frac{\mu_o}{\varepsilon_o}}\,\frac{1}{k} \; .$$

since $k_o = \omega\sqrt{\varepsilon_o\mu_o}$.

Thus Equation (A.60) becomes

$$\sqrt{\frac{\mu_o}{\varepsilon_o}}\,\frac{1}{k} = \frac{A_o + B_o}{A_o - B_o}\sqrt{\frac{\mu}{\varepsilon_o}}$$

Then the voltage reflection coefficient

$$R_v = \frac{B_o}{A_o} = \frac{1 - k}{1 + k} \qquad (A.61)$$

Thus, if coupling with all but the fundamental quasi-TEM mode in the magnetised plasma-filled coaxial line is neglected, the reflection coefficient from a plasma-vacuum interface in the coaxial line is related to the wave number of the quasi-TEM mode in the same way as for the TEM mode in a magnetic field free plasma-filled coaxial line.

Equation (A.61) was used to compute $|R_v|$ in Appendix C.

Appendix B Rotating Coordinates.

In the analysis of wave propagation in a magnetized plasma waveguide given in Appendix A, left- and right- hand rotating coordinates are used.

As these coordinate systems exhibit unusual vector operator properties, a summary of the matrix transformations used and some of the vector operators in the rotating system are given here.

B.1 Definition.

We define the left- and right- hand rotating coordinate system in terms of the Cartesian coordinate system [$\underset{\sim}{r} = (x, y, z)$] by the transformation

$$\begin{bmatrix} \ell \\ r \\ z \end{bmatrix} = \frac{1}{\sqrt{2}} \begin{bmatrix} 1 & -j & 0 \\ 1 & j & 0 \\ 0 & 0 & \sqrt{2} \end{bmatrix} \begin{bmatrix} x \\ y \\ z \end{bmatrix} \qquad (B.1)$$

i.e. $\underset{\sim}{u} = \underset{\approx}{U}\,\underset{\sim}{r}$

[$j = \sqrt{-1}$]

The inverse transform is then

$$\begin{bmatrix} x \\ y \\ z \end{bmatrix} = \frac{1}{\sqrt{2}} \begin{bmatrix} 1 & 1 & 0 \\ j & -j & 0 \\ 0 & 0 & \sqrt{2} \end{bmatrix} \begin{bmatrix} \ell \\ r \\ z \end{bmatrix} \qquad (B.2)$$

or $\underset{\sim}{r} = \underset{\approx}{U}^{-1}\,\underset{\sim}{u}$,

where $\underset{\approx}{U}\,\underset{\approx}{U}^{-1} = \underset{\approx}{U}^{-1}\,\underset{\approx}{U} = \underset{\approx}{I}$.

The unit vectors in the rotating coordinate frame are $\hat{\ell}$, $\hat{r}$, $\hat{z}$.

B.2 Transformation of matrices.

In the x , y , z frame

$$\underset{\sim}{A}_{l} = \underset{\approx}{S}_{l}\,\underset{\sim}{B}_{l} .$$

Then in the rotating system

$$\begin{aligned} A_r &= \underset{\approx}{U}\,\underset{\sim}{A}_{l} = \underset{\approx}{U}\,\underset{\approx}{S}_{l}\,\underset{\sim}{B}_{l} \\ &= \underset{\approx}{U}\,\underset{\approx}{S}_{l}\,\underset{\approx}{U}^{-1}\,\underset{\sim}{B}_{r} \\ &= \underset{\approx}{S}_{r}\,\underset{\sim}{B}_{r} \end{aligned}$$

i.e. $$\underset{\approx}{S}_{r} = \underset{\approx}{U}\,\underset{\approx}{S}_{l}\,\underset{\approx}{U}^{-1} \qquad (B.3)$$

and $$\underset{\approx}{S}_{l} = \underset{\approx}{U}^{-1}\,\underset{\approx}{S}_{r}\,\underset{\approx}{U} \qquad (B.4)$$

B.3 Vector manipulations.

Scalar product :-

$$\begin{aligned} \underset{\sim}{A}^{T}\cdot\underset{\sim}{B} &= A_xB_x + A_yB_y + A_zB_z \\ &= [\,A_x\,,\,A_y\,,\,A_z\,]\begin{bmatrix} B_x \\ B_y \\ B_z \end{bmatrix} \\ &= [\,A_\ell\,,\,A_r\,,\,A_z\,]\,(\underset{\approx}{U}^{-1})^{T}\,(\underset{\approx}{U}^{-1})\begin{bmatrix} B_\ell \\ B_r \\ B_z \end{bmatrix} \end{aligned}$$

$$\underset{\sim}{A}^{T}\cdot\underset{\sim}{B} = A_\ell B_r + A_r B_\ell + A_z B_z \qquad (B.5)$$

Similarly it can be shown that the vector product is given by

$$\underset{\sim}{A}\times\underset{\sim}{B} = \begin{vmatrix} \hat{\imath} & \hat{\jmath} & \hat{k} \\ A_x & A_y & A_z \\ B_x & B_y & B_z \end{vmatrix}$$

$$= j\begin{vmatrix} \hat{\ell} & \hat{r} & \hat{k} \\ A_r & A_\ell & A_z \\ B_r & B_\ell & B_z \end{vmatrix} \qquad (B.6)$$

Note the transposition of components in the first and second columns.

B.4 Differential vector operators.

$$\begin{bmatrix} \frac{\partial}{\partial x} \\ \frac{\partial}{\partial y} \\ \frac{\partial}{\partial z} \end{bmatrix} = \begin{bmatrix} \frac{\partial \ell}{\partial x} & , & \frac{\partial r}{\partial x} & , & \frac{\partial z}{\partial x} \\ \frac{\partial \ell}{\partial y} & , & \frac{\partial r}{\partial y} & , & \frac{\partial z}{\partial y} \\ \frac{\partial \ell}{\partial z} & , & \frac{\partial r}{\partial z} & , & \frac{\partial z}{\partial z} \end{bmatrix} \begin{bmatrix} \frac{\partial}{\partial \ell} \\ \frac{\partial}{\partial r} \\ \frac{\partial}{\partial z} \end{bmatrix}$$

$$= \frac{1}{\sqrt{2}} \begin{bmatrix} 1 & , & 1 & , & 0 \\ -j & , & j & , & 0 \\ 0 & , & 0 & , & \sqrt{2} \end{bmatrix} \begin{bmatrix} \frac{\partial}{\partial \ell} \\ \frac{\partial}{\partial r} \\ \frac{\partial}{\partial z} \end{bmatrix}$$

$$= \underset{\approx}{U}^{T} \begin{bmatrix} \frac{\partial}{\partial \ell} \\ \frac{\partial}{\partial r} \\ \frac{\partial}{\partial z} \end{bmatrix} \qquad (B.7)$$

Thus

$$\nabla. \equiv \hat{\imath} \frac{\partial}{\partial x} + \hat{\jmath} \frac{\partial}{\partial y} + \hat{k} \frac{\partial}{\partial z}$$

$$= \underset{\approx}{U}^{T} \begin{bmatrix} \frac{\partial}{\partial \ell} \\ \frac{\partial}{\partial r} \\ \frac{\partial}{\partial z} \end{bmatrix} \qquad \text{in } x, y, z \text{ coordinates}$$

$$= \underset{\approx}{U}\,\underset{\approx}{U}^{T} \begin{bmatrix} \frac{\partial}{\partial \ell} \\ \frac{\partial}{\partial r} \\ \frac{\partial}{\partial z} \end{bmatrix} \qquad \text{in } \ell, r, z \text{ coordinates}$$

i.e. $$\nabla. = \hat{\ell} \frac{\partial}{\partial r} + \hat{r} \frac{\partial}{\partial \ell} + \hat{k} \frac{\partial}{\partial z} \qquad (B.8)$$

Then

$$\text{div } \underset{\sim}{A} \equiv \nabla. \underset{\sim}{A} = \frac{\partial A_\ell}{\partial \ell} + \frac{\partial A_r}{\partial r} + \frac{\partial A_z}{\partial z} \qquad (B.9)$$

This is of the same form as in Cartesian coordinates, where

$$\nabla . \underset{\sim}{A} = \frac{\partial A_x}{\partial x} + \frac{\partial A_y}{\partial y} + \frac{\partial A_z}{\partial z}$$

From (B.6) and (B.8)

$$\text{Curl } \underset{\sim}{A} \equiv \nabla \times \underset{\sim}{A} = j \begin{vmatrix} \hat{\ell}, & \hat{r}, & \hat{k} \\ \frac{\partial}{\partial \ell}, & \frac{\partial}{\partial r}, & \frac{\partial}{\partial z} \\ A_r, & A_\ell, & A_z \end{vmatrix}$$

$$= j \begin{bmatrix} \frac{\partial A_z}{\partial r} - \frac{\partial A_\ell}{\partial z} \\ -\frac{\partial A_z}{\partial \ell} + \frac{\partial A_r}{\partial z} \\ \frac{\partial A_\ell}{\partial \ell} - \frac{\partial A_r}{\partial r} \end{bmatrix} \qquad \text{(B.10)}$$

The Laplacian operator ∇^2 becomes

$$\begin{aligned} \nabla^2 &= \frac{\partial^2}{\partial x^2} + \frac{\partial^2}{\partial y^2} + \frac{\partial^2}{\partial z^2} \\ &= \nabla . (\nabla) \\ &= 2 \frac{\partial^2}{\partial \ell \partial r} + \frac{\partial^2}{\partial z^2} \\ &= \nabla_T^2 + \frac{\partial^2}{\partial z^2} \end{aligned} \qquad \text{(B.11)}$$

where the transverse Laplacian operator

$$\nabla_T^2 = \frac{\partial^2}{\partial x^2} + \frac{\partial^2}{\partial y^2} = 2 \frac{\partial^2}{\partial \ell \partial r} \qquad \text{(B.12)}$$

B.5 Transformation of rotating coordinates to cylindrical coordinates.

We define cylindrical coordinates (ρ, Θ, z) by

$$\left.\begin{aligned} x &= \rho \cos \Theta \\ y &= \rho \sin \Theta \\ z &= z \end{aligned}\right\} \qquad \text{(B.13)}$$

Combining (B.13) with (B.1), and noting that

$e^{j\theta} = \cos\theta + j\sin\theta$, we have

$$\left.\begin{aligned} \ell &= \frac{1}{\sqrt{2}}\rho e^{-j\theta} \\ r &= \frac{1}{\sqrt{2}}\rho e^{j\theta} \end{aligned}\right\} \qquad (B.14)$$

and the inverse transformation is

$$\left.\begin{aligned} \rho &= \sqrt{2\ell r} \\ \theta &= -j\frac{1}{2}(\log r - \log \ell) \end{aligned}\right\} \qquad (B.15)$$

The differentials are given by

$$\begin{aligned} \frac{\partial}{\partial \ell} &= \frac{\partial \rho}{\partial \ell}\frac{\partial}{\partial \rho} + \frac{\partial \theta}{\partial \ell}\frac{\partial}{\partial \theta} \\ &= \frac{e^{j\theta}}{\sqrt{2}}\left(\frac{\partial}{\partial \rho} + \frac{j}{\rho}\frac{\partial}{\partial \theta}\right) \end{aligned}$$

and similarly (B.16)

$$\frac{\partial}{\partial r} = \frac{e^{-j\theta}}{\sqrt{2}}\left(\frac{\partial}{\partial \rho} - \frac{j}{\rho}\frac{\partial}{\partial \theta}\right)$$

The transverse Laplacian operator

$$\nabla_T^2 = 2\frac{\partial^2}{\partial \ell\, \partial r} = e^{j\theta}\left[\left(\frac{\partial}{\partial \rho} + \frac{j}{\rho}\frac{\partial}{\partial \theta}\right)\left\{e^{-j\theta}\left(\frac{\partial}{\partial \rho} - \frac{j}{\rho}\frac{\partial}{\partial \theta}\right)\right\}\right]$$

$$= \frac{\partial^2}{\partial \rho^2} + \frac{1}{\rho}\frac{\partial}{\partial \rho} + \frac{1}{\rho^2}\frac{\partial^2}{\partial \theta^2} \qquad (B.17)$$

as would be expected.

The transverse components of a vector $\underset{\sim}{A}$ in terms of ρ, θ components are given by

$$\begin{bmatrix} A_x \\ A_y \end{bmatrix} = \begin{bmatrix} \cos\theta, & -\sin\theta \\ \sin\theta, & \cos\theta \end{bmatrix} \begin{bmatrix} A_\rho \\ A_\theta \end{bmatrix}$$

By (B.1), then

$$\begin{bmatrix} A_\ell \\ A_r \end{bmatrix} = \frac{1}{\sqrt{2}} \begin{bmatrix} 1, & -j \\ 1, & j \end{bmatrix} \begin{bmatrix} \cos\theta, & -\sin\theta \\ \sin\theta, & \cos\theta \end{bmatrix} \begin{bmatrix} A_\rho \\ A_\theta \end{bmatrix}$$

i.e.

$$\begin{bmatrix} A_l \\ A_r \end{bmatrix} = \frac{1}{\sqrt{2}} \begin{bmatrix} e^{-j\theta}, & -je^{-j\theta} \\ e^{j\theta}, & je^{j\theta} \end{bmatrix} \begin{bmatrix} A_\rho \\ A_\theta \end{bmatrix} \qquad (B.18)$$

Inverting this :-

$$\begin{bmatrix} A_\rho \\ A_\theta \end{bmatrix} = \frac{1}{\sqrt{2}} \begin{bmatrix} e^{j\theta}, & e^{-j\theta} \\ je^{j\theta}, & -je^{-j\theta} \end{bmatrix} \begin{bmatrix} A_l \\ A_r \end{bmatrix} \qquad (B.19)$$

Appendix C Program for the computation of the reflection from a magnetised plasma-filled coaxial line.

C.1 Introduction.

The KDF - 9 Algol computer program shown in Section C.2 was written to compute the reflection coefficient from the interface of a plasma-filled coaxial line with an axial magnetic field, using the equations developed in Appendix A.

The input parameters were the non-dimensional plasma frequency $\frac{\omega_p}{\omega}$, the electron collision frequency $\frac{\nu}{\omega}$, and the cyclotron frequency frequency $\frac{\omega_c}{\omega}$.

As the determinantal equation (A.50) cannot be solved directly for k , the method adopted was to guess the solution $k = k^r + j k^i$ for a given $\frac{\omega_p}{\omega}$, $\frac{\nu}{\omega}$, $\frac{\omega_c}{\omega}$, compute the determinant Δ , and then use a two-variable extension of Newton's method to iterate k to reduce the real and imaginary parts of Δ. This was continued until successive values of k^r and k^i agreed to within 10^{-3} .

Once a solution had been found, one of $\frac{\omega_p}{\omega}$, $\frac{\nu}{\omega}$ or $\frac{\omega_c}{\omega}$ was changed slightly, and the value of k just determined used as the first guess for the new root. This was repeated, and so a root was followed as one of the variables changed. This proved successful if the increments in the changed variable were kept small. Too large an increment would cause the solution to "jump" to a higher mode than the fundamental quasi- TEM mode. This was usually obvious on inspection of the computer output. A decisive test for the quasi- TEM mode was to see if the mode being followed tended towards the free-space TEM wave number (computed by a separate program from

Equation (4.14)) as $\frac{\omega_c}{\omega} \to 0$.

The subroutines which compute the Bessel's functions, J_0 , J_1 , Y_0 , Y_1 , $H_0^{(1)}$, $H_0^{(2)}$, $H_1^{(1)}$, $H_1^{(2)}$ were written by D. McKay. They were checked for both real and complex argument and appeared correct to the accuracy of the reference tables consulted.

To ease computation, the dimensions were normalised to $1 / k_0$ (so that $k_0 = 1$) and the radii (6.20395 mm & 14.2875 mm) adjusted in the computation of $J_0(p_i R_1)$ etc.

The normalised radii for a microwave frequency of 9 GHz were

$$R_1 k_0 = 0.58513$$

$$R_2 k_0 = 1.3475 \ .$$

The identities

$$J_0' = -J_1$$

$$Y_0' = -Y_1$$

were used to compute J_0' and Y_0' .

This program, on the computer available, is somewhat time-consuming, as an average of 5 iterations is required for each computation, and so the range of $\frac{\omega_p}{\omega}$, $\frac{\nu}{\omega}$, $\frac{\omega_c}{\omega}$ covered was limited by the computing time available.

The Algol "comment" convention is used to avoid confusion in the print-out of the program given here. There are no "comments" in the actual program tape.

C.2 PROGRAM PRINT OUT.

```
FAEDM16DOAPU
MAG COAX REFLECTION;
SAVE;
TL30J;→

begin library A0,A6,A12,A14;


real procedure modc(a,b);

comment Modulus of complex number x + jy ;

value a,b; real a,b;
if a =0 and b=0 then modc:=0 else
begin a:=abs(a);b:=abs(b); if a>b then modc:= a/ cos(arctan(b/a))
    else modc:=b/cos(arctan(a/b))
end;

procedure sqrtc(a,b,c,d);

comment Square root of x + jy .  All roots have
real part ⩾ 0;

value a,b; real a,b,c,d;
begin real theta; if a>0 then begin theta:=0; goto SOL end;
    if a<0and (b>0or b=0) then begin theta:=3.14159 26535 90;
    goto SOL end;
    if a<0andb<0 then begin theta:=-3.14159 26535 90;
    goto SOL end;
    if a=0and b=0 then begin c:=d:=0;goto RETURN end;
    if a=0 and b>0 then begin c:=d:=sqrt(b/2);
    goto RETURNend;
    if a=0and b<0 then begin c:= sqrt(-b/2); d:=-c;
    goto RETURN end;
    SOL:d:= sqrt(modc(a,b)); a:=(arctan (b/a)+theta)/2;
    c:=d×cos(a);d:=d×sin(a);
RETURN: endsqrtc;



procedure jzsm(x,y,jr,ji,yr,yi);

comment Computes J0 and Y0 of x+jy;

value  x,y;
real  x,y,jr,ji,yr,yi;

begin  real  xx,yy,f,g,fd,gd,a,h,fe,ge,ff,gf,fg,
gg,lr,li,k,wa,wb,tp,xa,ya;
                xa:=abs(x); ya:=abs(y);
    xx:=x↑2-y↑2;yy:=2.0×xa×ya;f:=g:=fd:=gd:=
    fe:=ge:=ff:=gf:=fg:=gg:=
                0.0;
```

```
    for  a:=1.52776628966₁₀-19,-1.98858655989₁₀-15,
    8.87648950577₁₀-12,-1.90128586963₁₀-8,
    2.25848557175₁₀-5,-1.59547049907₁₀-2,
    6.90220568183    ,-1.82980577559₁₀+3,
    2.89641429881₁₀+5,-2.58121327065₁₀+7,
    1.15859974056₁₀+9,-2.09892577626₁₀+10,
    8.73153122922₁₀+10  do
    begin  h:=fxxx-gxyy+a;g:=fxyy+gxxx;f:=h  end;
    for  a:=1.0₁₀-24,1.352₁₀-21,1.211392₁₀-18,
    9.59422464₁₀-16,7.0174900224₁₀-13,
    4.77189321523₁₀-10,2.99848417307₁₀-7,
    1.71790077853₁₀-4,8.79565198610₁₀-2,
    3.91147817736₁₀+1,1.44930559835₁₀+4,
    4.19056361579₁₀+6,8.39570310499₁₀+8,
    8.73153122922₁₀+10  do
    begin  h:=fdxxx-gdxyy+a;gd:=fdxyy+gdxxx;fd:=h  end;
    for  a:=-7.38042951083₁₀-26,-9.97634069863₁₀-23,
    -8.60602031949₁₀-19,-9.86990464621₁₀-16,
    -8.70828788907₁₀-13,-6.68110615768₁₀-10,
    -4.57994302253₁₀-7,-2.80622998236₁₀-4,
    -1.51678240761₁₀-1,-7.05648613251₁₀+1,
    -2.71713120912₁₀+4,-8.12317037590₁₀+6,
    -1.67604925845₁₀+9,-1.78941344066₁₀+11do
    begin  h:=fexxx-gexyy+a;ge:=fexyy+gexxx;fe:=h  end;
    for  a:=-2.62206530322₁₀-17,3.68551979078₁₀-13,
    -1.61922565488₁₀-9,3.26303968134₁₀-6,
    -3.51359697230₁₀-3,2.16649521904    ,
    -7.83579857410₁₀+2,1.64621638910₁₀+5,
    -1.92046321417₁₀+7,1.13036927597₁₀+9,
    -2.76135258252₁₀+10,1.72497098990₁₀+11do

  begin  h:=ffxxx-gfxyy+a;gf:=ffxyy+gfxxx;ff:=h  end;
  for  a:=1.352₁₀-21,1.211392₁₀-18,
  9.59422464₁₀-16,7.0174900224₁₀-13,
  4.77189321523₁₀-10,2.99848417307₁₀-7,
  1.71790077853₁₀-4,8.79565198610₁₀-2,
  3.91147817736₁₀+1,1.44930559835₁₀+4,
  4.19056361579₁₀+6,8.39570310499₁₀+8,
  8.73153122922₁₀+10  do
  begin  h:=fgxxx-ggxyy+a;gg:=fgxyy+ggxxx;fg:=h  end;
  h:=fd↑2+gd↑2;jr:=(fxfd+gxgd) h;ji:=(gxfd-fxgd)/h;
  lr:=0.5xln(x↑2+y↑2);
  li:=if ya>xa then 1.57079632679-arctan(xa/ya)
        else  arctan(ya/xa);
  k:=fg↑2+gg↑2;tp:=0.63661977236676;

  wa:=(fexfg+gexgg)/k+tpxlr;wb:= -(fexgg-gexfg)/k+tpxli;
  yr:=(ffxfd+gfxgd)/h+jrxwa-jixwb;
  yi:=(gfxfd-ffxgd)/h+jrxwb+jixwa;
  if x<0.0 then begin ji :=- ji;
yr:=yr-2.0xji; yi:=2.0xjr-yi end;
  if y< 0.0 then begin ji:= - ji;yi := - yi end ;
end;
```

```
procedure jusm(x,y,jr,ji,yr,yi);
comment Computes J, and Y, of x+jy;

value  x,y;
real  x,y,jr,ji,yr,yi;

begin  real  xx,yy,f,g,fd,gd,a,h,fe,ge,ff,gf,lr,li,wa,
     wb,tp,xa,ya;
                    xa:=abs (x) ; ya:= abs (y);
     xx:=x↑2-y↑2;yy:=2.0×xa×ya;f:=g:=fd:=gd:=
     fe:=ge:=ff:=gf:=0.0;

     for a:=

  1.138620446281₀-19, -1.192075749081₀-15,  4.583876586141₀-12,
 -8.986230377871₀ -9,  1.031307298491₀ -5, -7.395354544091₀ -3,
  3.402777934851₀ +0, -1.005032477271₀ +3,  1.862491994001₀ +5,
 -2.060245822361₀ +7,  1.242263852621₀ +9, -3.441430993921₀+10,
  2.946891789871₀+11
     do
     begin  h:=f×xx-g×yy+a;g:=f×yy+g×xx;f:=h  end;
     for  a:=
  6.007000000021₀-24,  4.608000000011₀-20,  1.107025920001₀-16,
  1.700391813121₀-13,  2.004033208331₀-10,  1.940195641401₀ -7,
  1.582277032861₀ -4,  1.089663768321₀ -1,  6.247619264601₀ +1,
  2.888476192511₀ +4,  1.015405799211₀ +7,  2.421837434141₀ +9,
  2.946891789871₀+11
  do

     begin  h:=fd×xx-gd×yy+a;gd:=fd×yy+gd×xx;fd:=h  end;
     for  a:=
 -4.007020080711₀-20, -1.256294249691₀-16, -2.245398023471₀-13,
 -2.933418568361₀-10, -3.066423119631₀ -7, -2.656636141821₀ -4,
 -1.922447099751₀ -1, -1.149195619191₀ +2, -5.507204553501₀ +4,
 -1.997689732041₀ +7, -4.898998709501₀ +9, -6.111426115361₀+11

     do
     begin  h:=fe×xx-ge×yy+a;ge:=fe×yy+ge×xx;fe:=h  end;
     for  a:=
 -1.735899933601₀-17,  2.030818708121₀-13, -7.924394725481₀-10,
  1.503689071921₀ -6, -1.608304486071₀ -3,  1.035637246011₀ +0,
 -4.108899353261₀ +2,  9.966888355261₀ +4, -1.423713456531₀ +7,
  1.108105312251₀ +9, -4.041152394901₀+10,  4.955908053811₀+11
     do

     begin  h:=ff×xx-gf×yy+a;gf:=ff×yy+gf×xx;ff:=h  end;
     h:=fd↑2+gd↑2;jr:=(f×fd+g×gd)/h;ji:=(g×fd-f×gd)/h;
     a:=xa×ff-ya×gf;  gf:=(ya×ff+xa×gf)/2.0; ff:=a/2.0;
     a:=xa×jr-ya×ji;  ji:=(ya×jr+xa×ji)/2.0;  jr:=a/2.0;
lr:=0.5×ln(x↑2+y↑2);
     li:=if ya > xa then 1.57079632679-arctan(xa ya)
           else  arctan(ya/xa);
     tp:=0.636619772367;

     xx:=x↑2+y↑2;

     wa:=(fe×fd+ge×gd)/h+tp×lr;wb:= -(fe×gd-ge×fd)/h+tp×li;
     yr:=(ff×fd+gf×gd)/h+jr×wa-ji×wb-tp×xa/xx;
     yi:=(gf×fd-ff×gd)/h+jr×wb+ji×wa+tp×ya/xx;
     if x< 0.0 then begin jr := -jr; yr := -yr -2.0 ×ji;
     yi:=yi+2.0×jr; end;
     if y<0.0 then begin  ji := - ji; yi:=-yi; end;
                                                  end;
```

```
procedure hzlg(x,y,har,hai,hbr,hbi);

comment Computes H(1)0 and H(2)0 of x+jy;

 value x,y; real x,y,har,hai,hbr,hbi;
begin real xa,ya,d,xd,yd,fa,fb,fd,ga,gb,gd,
     h,md,ur,ui,vr,vi,a,b,r,
c,s,wa,wb,xn,yn;
xa:=abs (x); ya:= abs(y);
d:=xa↑2+ya↑2; xn:=xa/d; yn:=-ya/d;
     xd:=xn↑2-yn↑2; yd:=2.0×xn×yn;
fa:=fb:=fd:=ga:=gb:=gd:=0.0;  for a:=

 -1.594131046401010+10, -4.035006713171012+12, -4.503290090191013+13,
 -9.832651186101013+13, -6.827213817751013+13, -1.929535663621013+13,
 -2.572545018611012+12, -1.780572076991011+11, -6.822995101421010 +9,
 -1.510357631511010 +8, -1.980620807601010 +6, -1.552157359601010 +4,
 -7.193650544811010 +1, -1.896093418421010 -1, -2.581626163081010 -4,
 -1.387300852251010 -7
do begin h:=fa×xd-ga×yd+a; ga:=fa×yd+ga×xd; fa:=h end; for a:=


  7.002521600001010 +7, -1.663243673601011+11, -3.523138227011012+12,
 -9.859283271871012+12, -7.640581957681012+12, -2.274802969461012+12,
 -3.113072044881011+11, -2.184597891101010+10, -8.435289564981010 +8,
 -1.875493707421010 +7, -2.465918860031010 +5, -1.935599292641010 +3,
 -8.979895881321010 +0, -2.368457276101010 -2, -3.226138545101010 -5,
 -1.734126065311010 -8
do begin h:=fb×xd-gb×yd+a; gb:=fb×yd+gb×xd; fb:=h end; for a:=

 -3.555555555551010+10, -5.015_1020408101012+12, -4.890817555061013+13,
 -1.018761476901014+14, -6.942336422591013+13, -1.946022338291013+13,
 -2.584406970161012+12, -1.785217750621011+11, -6.833410700871010 +9,
 -1.511734004781010 +8, -1.981704560151010 +6, -1.552661144681010 +4,
 -7.194980975501010 +1, -1.896274790261010 -1, -2.581723707671010 -4,
 -1.387300852251010 -7
do
begin h:=fd×xd-gd×yd+a; gd:=fd×yd+gd×xd; fd:=h end;
md:=fd↑2+gd↑2; ur:=(fa×fd+ga×gd)/md;  ui:=(fd×ga-fa×gd)/md;
vr:=(fb×fd+gb×gd)/md;  vi:=(fd×gb-fb×gd)/md;
r:=vr×xn-vi×yn;  vi:=vi×xn+vr×yn;  vr:=r;
r:=sqrt(d); a:=sqrt((xa+r)/2.0);
b:=ya/(2.0×a); s:=xa-0.7853981633974; c:=cos(s); s:=sin(s);
wa:=c×(ur+vi)-s×(ui-vr); wb:=s×(ur+vi)+c×(ui-vr);
fa:=0.7978845608029/(a↑2+b↑2);
if ya <70 then fb:=exp(ya) else fb:=1;
har:=(a×wa+b×wb)×fa/fb; hai:=(a×wb-b×wa)×fa/fb;
wa:=c×(ur-vi)+s×(ui+vr); wb:=s×(vi-ur)+c×(ui+vr);
hbr:=(a×wa+b×wb)×fa×fb; hbi:=(a×wb-b×wa)×fa×fb;
if x< 0.0 then begin hbr := hbr+ 2.0×har; hbi:= -hbi- 2.0×hai;
 har:= -har; end;
if y  < 0.0 then begin fd:=har; har:=hbr; hbr:=fd;
 fd:= hai; hai:= - hbi; hbi:=-fd
                        end;
end;
```

```
procedure hulg(x,y,har,hai,hbr,hbi);

comment Computes H1(1) and H1(2) of x+jy;

 value x,y; real x,y,har,hai,hbr,hbi;
begin real xa,ya,d,xd,yd,fa,fb,fd,ga,gb,gd,h,md,ur,ui,vr,vi,a,b,r,
c,s,wa,wb,xn,yn;
xa:=abs(x); ya:=abs(y);
d:=xa↑2+ya↑2; xn:=xa/d; yn:=-ya/d; xd:=xn↑2-yn↑2; yd:=2.0×xn×yn;
fa:=fb:=fd:=ga:=gb:=gd:=0.0;  for a:=

   6.97684234240₁₀+10,  5.70480712179₁₀+12,  4.78758830900₁₀+13,
   9.56222292613₁₀+13,  6.46444253482₁₀+13,  1.81647692981₁₀+13,
   2.42497839334₁₀+12,  1.68440229249₁₀+11,  6.48062517355₁₀ +9,
   1.44018896014₁₀ +8,  1.89536419915₁₀ +6,  1.49009594322₁₀ +4,
   6.92561289312₁₀ +1,  1.83003126507₁₀ -1,  2.49723460079₁₀ -4,
   1.34461467219₁₀ -7
do begin h:=fa×xd-ga×yd+a; ga:=fa×yd+ga×xd; fa:=h end; for a:=
  -1.14737152000₁₀ +9, -7.93489782336₁₀+11, -1.19354012525₁₀+13,
  -2.98279195729₁₀+13, -2.21685459801₁₀+13, -6.50373006544₁₀+12,
  -8.86669886224₁₀+11, -6.22620439000₁₀+10, -2.40976662559₁₀ +9,
  -5.37344879023₁₀ +7, -7.08602559458₁₀ +5, -5.57777810811₁₀ +3,
  -2.59443280476₁₀ +1, -6.85896387574₁₀ -2, -9.36266010254₁₀ -5,
  -5.04230502070₁₀ -8
do begin h:=fb×xd-gb×yd+a; gb:=fb×yd+gb×xd; fb:=h end; for a:=
   2.13333333333₁₀+10,  3.90095238095₁₀+12,  4.13838408504₁₀+13,
   8.98907185503₁₀+13,  6.28116152520₁₀+13,  1.79034055123₁₀+13,
   2.40617200670₁₀+12,  1.67702273546₁₀+11,  6.46403714952₁₀ +9,
   1.43799088261₁₀ +8,  1.89362880194₁₀ +6,  1.48928722042₁₀ +4,
   6.92347225950₁₀ +1,  1.82973883274₁₀ -1,  2.49707702875₁₀ -4,
   1.34461467219₁₀ -7
do
begin h:=fd×xd-gd×yd+a; gd:=fd×yd+gd×xd; fd:=h end;
md:=fd↑2+gd↑2; ur:=(fa×fd+ga×gd)/md;  ui:=(fd×ga-fa×gd)/md;
vr:=(fb×fd+gb×gd)/md;  vi:=(fd×gb-fb×gd)/md;
r:=vr×xn-vi×yn;  vi:=vi×xn+vr×yn;  vr:=r;
r:=sqrt(d); a:=sqrt((xa+r)/2.0);
b:=ya/(2.0×a); s:=xa-2.35619449019l; c:=cos(s); s:=sin(s);
wa:=c×(ur+vi)-s×(ui-vr); wb:=s×(ur+vi)+c×(ui-vr);
fa:=0.797884560802g/(a↑2+b↑2);
if ya<70 then fb:=exp(ya) else fb:=1;
har:=(a×wa+b×wb)×fa/fb; hai:=(a×wb-b×wa)×fa/fb;
wa:=c×(ur-vi)+s×(ui+vr); wb:=s×(vi-ur)+c×(ui+vr);
hbr:=(a×wa+b×wb)×fa×fb; hbi:=(a×wb-b×wa)×fa×fb;
if x<0.0 then begin hai:= - hai; hbr:= - hbr - 2.0×har;
 hbi:=  hbi-2.0×hai; end;
if y<0.0 then begin fd:=har; har:=hbr; hbr:= fd; fd:=hai;
hai:= - hbi; hbi:=-fd
                        end;

end;
```

```
procedure detcf(ar,ai,x,y);

comment Computes complex 4x4 determinant of
arrays ar(i,k)+j ai(i,k), i,k=1...4;

 value ar,ai;array ar,ai;
real x,y;
begin real e,f,den; integer m,k,s,t,u; array br[1:4],bi[1:4];
m:=1;
for s:=1step 1 until 3 do

begin
k:=0; e:= sqrt(ar[s,s]xar[s,s]+ai[s,s]xai[s,s]);
for t:=1 step 1 until 4-s do
begin f:=sqrt(ar[s+t,s]xar[s+t,s]+ai[s+t,s]xai[s+t,s]);
    if f>e then begin k:=t; e:=f end;
end;
if k≠0 then m:=-m;
for t:=s step 1 until 4 do
begin br[t]:=ar[s,t];bi[t]:=ai[s,t];
    ar[s,t]:=ar[s+k,t];ai[s,t]:=ai[s+k,t];
    ar[s+k,t]:=br[t];ai[s+k,t]:=bi[t];
end;

if ar[s,s]=0 and ai[s,s]=0 then begin x:=y:=0;
 goto RETURN end;

for t:=s+1 step 1  until 4do
beginden:= 1/(ar[s,s]xar[s,s]+ai[s,s]xai[s,s]);
e:=(ar[t,s]xar[s,s]+ai[t,s]xai[s,s])xden;
f:=(ai[t,s]xar[s,s]-ar[t,s]xai[s,s])xden;
    for u:=s+1 step 1  until 4 do
    begin x:= exar[s,u]-fxai[s,u];
y:= exai[s,u]+fxar[s,u];
          ar[t,u]:=ar[t,u]-x; ai[t,u]:=ai[t,u]-y;
    end
end;

end;
e:=ar[1,1]; f:=ai[1,1];
for t:=2 step 1until 4 do
beginden:=exar[t,t]-fxai[t,t];
f:=exai[t,t]+fxar[t,t];
e:=den;
end;
x:=mxe; y:=mxf;
RETURN: end;



procedure bescjy(m,x,y,jr,ji,yr,yi);

comment Computes J0 and Y0 for m=0,  J1  ,Y1
for m=1.  Uses jzsm and jusm for small |z| , but
uses hzlg and hulg with the identities
Jv = 0.5(H(1)v+H(2)v) and Yv=0.5j(H(2)v-H(1)v) for large z .
The transition is smoothed;


value x,y; integer m; real x,y,jr,ji,yr,yi;
```

```
begin real a,b,c,d,z;

z:=x×x+y×y;

if z<81 then
begin if m=0 then jzsm(x,y,jr,ji,yr,yi) else
            jusm(x,y,jr,ji,yr,yi);
end

else
 begin if m=0 then hzlg(x,y,a,b,c,d) else
           hulg(x,y,a,b,c,d);
 if abs(y)<70 then
  begin jr:=0.5×(a+c); ji:=0.5×(b+d);
 yr:=0.5×(b-d); yi:=0.5×(c-a);

          if z<91 then
    begin if m=0 then jzsm(x,y,a,b,c,d) else
              jusm(x,y,a,b,c,d);
     jr:=0.1×((91-z)×a+(z-81)×jr);
      ji:=0.1×((91-z)×b+(z-81)×ji);
     yr:=0.1×((91-z)×c+(z-81)×yr);
      yi:=0.1×((91-z)×d+(z-81)×yi);
     end;
  end
 else if y>69 then
  begin jr:=0.5×c; ji:=0.5×d; yr:=-0.5×d; yi:=0.5×c
  end
  else
   begin jr:=0.5×a; ji:=0.5×b; yr:=0.5×b; yi:=-0.5×a;
   end;
end;
end;



procedure diseq(elr,eli,err,eri,e3r,e3i,kr,ki,disr,disi);

comment Computes the value of the dispersion determinant
  △ in equation (A.50);


value elr,eli,err,eri,e3r,e3i,kr,ki;
real elr,eli,err,eri,e3r,e3i,kr,ki,disr,disi;

begin real pir,pii,pji,pjr,ppir,ppii,ppjr,ppji,
          aar,aai,acr,aci,
    adr,adi,gir,gii,gjr,gji,ccr,cci,elrr,elri,
    kkr,kki,tar,tai,tbr,tbi,tc,tdr,tdi;
array ar[1:4,1:4], ai[1:4,1:4];

kkr:=kr×kr-ki×ki; kki:=2×kr×ki;

if abs(err)>9₁₀9 or abs(eri)>9₁₀9 then
    begin aar:=e3r; aai:=e3i;
    ccr:=2×elr-kkr; cci:=2×eli-kki;
```

```
    acr:=aar+ccr; aci:=aai+cci;
    tar:=elr-kkr; tai:=eli-kki;
    adr:=2x(e3rxtar-e3ixtai); adi:=2x(e3rxtai+e3ixtar);
    goto LZ;
    end;


elrr:=elr+err; elri:=eli+eri;

tar:=2xkkr-elrr; tai:=2xkki-elri;
tbr:=e3rxtar-e3ixtai; tbi:=e3rxtai+e3ixtar;
tc:=elrrxelrr+elrixelri;
aar:=-(tbrxelrr+tbixelri)/tc; aai:=-(tbixelrr-tbrxelri)/tc;

tar:=2x(elrxerr-elixeri); tai:=2x(elrxeri+elixerr);
tbr:=kkrxelrr-kkixelri; tbi:=kkrxelri+kkixelrr;
tdr:=tar-tbr; tdi:=tai-tbi;
ccr:=(tdrxelrr+tdixelri)/tc; cci:=(tdixelrr-tdrxelri)/tc;

acr:=aar+ccr; aci:=aai+cci;

tar:=elr-kkr; tai:=eli-kki;tbr:=err-kkr; tbi:=eri-kki;
tdr:=tarxtbr-taixtbi; tdi:=tarxtbi+taixtbr;
tar:=2x(e3rxtdr-e3ixtdi); tai:=2x(e3rxtdi+e3ixtdr);
adr:=(tarxelrr+taixelri)/tc; adi:=(taixelrr-tarxelri)/tc;
LZ:
tar:=acrxacr-acixaci-4xadr; tai:=2xacrxaci-4xadi;
sqrtc(tar,tai,tbr,tbi);
ppir:=0.5x(acr+tbr); ppii:=0.5x(aci+tbi);
ppjr:=0.5x(acr-tbr); ppji:=0.5x(aci-tbi);
sqrtc(ppir,ppii,pir,pii);
sqrtc(ppjr,ppji,pjr,pji);


tbr:=2x((elr-kkr)x(err-kkr)-(eli-kki)x(eri-kki));
tbi:=2x((elr-kkr)x(eri-kki)+(err-kkr)x(eli-kki));
tar:=elrr-2xkkr; tai:=elri-2xkki;
ta:=tbrxtbr+tbixtbi;
tdr:=(tarxtbr+taixtbi)/ta;
tdi:=(taixtbr-tarxtbi)/ta;

tar:=1-tdrxppjr+tdixppji;
tai:=-tdrxppji-tdixppjr;
gir:=pirxtar-piixtai;  gii:=pirxtai+piixtar;

tar:=1-tdrxppir+tdixppii;
tai:=-tdrxppii-tdixppir;
gjr:=pjrxtar-pjixtai;  gji:=pjrxtai+pjixtar;

bescjy(0,0.58513xpir,0.58513xpii,ar[1,1],ai[1,1],
          ar[1,2],ai[1,2]);
bescjy(1,0.58513xpir,0.58513xpii,tar,tai,tbr,tbi);

ar[3,1]:=-girxtar+giixtai; ai[3,1]:=-girxtai-giixtar;
ar[3,2]:=-girxtbr+giixtbi; ai[3,2]:=-girxtbi-giixtbr;

bescjy(0,1.3475xpir,1.3475xpii,ar[2,1],ai[2,1],
          ar[2,2],ai[2,2]);
bescjy(1,1.3475xpir,1.3475xpii,tar,tai,tbr,tbi);
```

```
ar[4,1]:=-gir×tar+gii×tai; ai[4,1]:=-gir×tai-gii×tar;
ar[4,2]:=-gir×tbr+gii×tbi; ai[4,2]:=-gir×tbi-gii×tbr;

bescjy(0,0.58513×pjr,0.58513×pji,ar[1,3],ai[1,3],
          ar[1,4],ai[1,4]);
bescjy(1,0.58513×pjr,0.58513×pji,tar,tai,tbr,tbi);

ar[3,3]:=-gjr×tar+gji×tai; ai[3,3]:=-gjr×tai-gji×tar;
ar[3,4]:=-gjr×tbr+gji×tbi; ai[3,4]:=-gjr×tbi-gji×tbr;

bescjy(0,1.3475×pjr,1.3475×pji,ar[2,3],ai[2,3],
          ar[2,4],ai[2,4]);
bescjy(1,1.3475×pjr,1.3475×pji,tar,tai,tbr,tbi);

ar[4,3]:=-gjr×tar+gji×tai; ai[4,3]:=-gjr×tai-gji×tar;
ar[4,4]:=-gjr×tbr+gji×tbi; ai[4,4]:=-gjr×tbi-gji×tbr;

detcf(ar,ai,disr,disi);

end;



real f1,f2,wp,nu,wc,elr,eli,err,eri,e3r,e3i,
     kar,kai,kbr,kbi,kcr,kci,
     ta,dabr,dabi,dbar,dbai,dbbr,dbbi,drr,dri,
     dir,dii,tai,tar,
     tbr,tbi,tcr,tci,refl;
integer n;
open(20); open(30);


f1:=format([ss-d.ddd10+nd]); f2:=format([ss-d.ddd10+ndc]);

kcr:=1; kci:=1;


comment This section reads values of ωp/ω, ν/ω, ωc/ω, for each
calculation;

START: wp:=read(20); if wp=0 then goto FINISH;
nu:=read(20);
wc:=read(20);
kbr:=read(20);
if kbr=0 then   begin kbr:=kcr; kbi:=kci
                end
     else begin         kbi:=read(20)
          end;

kar:=kbr+10-4; kai:=kbi+10-4;


ta:=(1+wc)×(1+wc)+nu×nu;
elr:=1-wp×wp×(1+wc)/ta; eli:=-wp×wp×nu/ta;
ta:=(1-wc)×(1-wc)+nu×nu;
```

```
if ta=0 then
     begin err:=9.999₁₀9; eri:=0
     end
     else
     begin err:=1-wp×wp×(1-wc)/ta; eri:=-wp×wp×nu/ta;
     end;

e3r:=1-wp×wp/(1+nu×nu); e3i:=-wp×wp×nu (1+nu×nu);

n:=0;

writetext(30,[****wp[10s]nu[10s]wc[10s]kr[10s]ki[10s]refl[c]]);


LOOP:


comment Two-variable Newton's method used here;

diseq(elr,eli,err,eri,e3r,e3i,kbr,kbi,dbbr,dbbi);
diseq(elr,eli,err,eri,e3r,e3i,kar,kbi,dabr,dabi);

drr:=(dbbr-dabr)/(kbr-kar); dri:=(dbbi-dabi)/(kbr-kar);
dir:=-dri; dii:=drr;
ta:=drr×dii-dir×dri;
kcr:=kbr-(dii×dbbr-dir×dbbi)/ta;
 kci:=kbi-(-dri×dbbr+drr×dbbi)/ta;

if abs(kcr-kbr) < ₁₀-3 and abs(kci-kbi) < ₁₀-3 then goto OUT;

comment k determined to an accuracy of ₁₀-3;
 The number of iterations is limited to n=10;

n:=n+1; if n > 10 then
          begin writetext(30,[too*many*iterations[c]]);
          goto OUT;
          end;

 kbr:=kcr; kbi:=kci; kar:=kbr+₁₀-4;
goto LOOP;


OUT: tar:=1-kcr; tai:=-kci; tbr:=1+kcr; tbi:=kci;
ta:=tbr×tbr+tbi×tbi; tcr:=(tar×tbr+tai×tbi)/ta;
     tci:=(tai×tbr-tar×tbi)/ta;
refl:=sqrt(tcr×tcr+tci×tci);



comment Prints out ω_p/ω, ν/ω, ω_c/ω, k^r, k^i, n and R_v;

write(30,f1,wp); write(30,f1,nu); write(30,f1,wc);
write(30,f1,kcr); write(30,f1,kci); write(30,f1,refl);
write(30,format([9sndc]),n);


goto START;

FINISH: close(20); close(30);
end→
```

REFERENCE LIST

1. Laird, J.D.
"Experimental Study of Ionized Gases Produced by Shock Waves."
D.Phil. Thesis, Oxford (May, 1965).

2. Wright, J.K.
"Shock Tubes". Methuen Monographs (1961).

3. Glass, I.I. & Hall, J.G.
"Handbook of Supersonic Aerodynamics, Section 18,
Shock Tubes." N.A.V.O.R.D. Report 1488, Vol. 6 (1959).

4. Feldman, Saul.
"Hypersonic Gas Dynamic Charts for Equilibrium Air."
AVCO Research Report 40 (Jan. 1957).

5. Laird, J.D. & Heron, K.
"Shock tube gas dynamic charts, Part 1: Equilibrium Argon-free air from 3,000 to 40,000°K."
AVCO RAD-TM-64-12 (April 1964).

6. Lewis, C.H. & Burgess, E.G.
"Charts of normal shock wave properties in imperfect air."
AEDC-TDR-64-43 (March 1964).

7. Hansen, C.F.
"Approximations for the thermodynamic and transport properties of high temperature air."
NACA TN 4150 (March 1958). Succeeded by NACA TR R-50.

8. Logan Jr., J.G. & Treanor, C.E.
"Tables of thermodynamic properties of air from 3,000°K to 10,000°K at intervals of 100°K."
CAL Report No. BE-1007-A-3 (Jan. 1957).

9. Hilsenrath, J. & Klein, M.
"Tables of thermodynamic properties of air in chemical equilibrium including second virial corrections from 1,500°K to 15,000°K." AEDC-TR-65-58 (March 1965).

10. Lin, S.C., Neal, R.A. & Fyfe, W.I.
"Rate of ionization behind shock waves in air.
1. Experimental Results."
Phys. Fluids, 5, 1633 (Dec.1962).

11. Lin, S.C. & Teare, J.D.
"Rate of ionization behind shock waves in air.
2. Theoretical interpretations."
Phys. Fluids 6, 355 (March 1963).

12. Wilson, J.
"Ionisation rate of Air behind high speed shock waves."
Physics of Fluids, 9, 1913 (Oct. 1966).

13. Mirels, H.
"Laminar boundary layer behind a strong shock wave into Air."
NASA TN D-291 (Feb. 1961).

14. Mirels, H.
"Test time in low-pressure shock tubes."
Physics of Fluids, 6, 1201 (Sept. 1963).

15. Mirels, H.
"Shock tube test time limitation due to turbulent wall boundary layer." AIAA Journal, 2, 84 (Jan. 1964).

16. Mirels, H.
"Flow nonuniformity in shock tubes operating at maximum test times." Physics of Fluids, 9, 1907 (Oct. 1966).

17. Woolgar, J.A.
"The application of an electronic image converter."
D.Phil. Thesis, Oxford University (1965).

18. Schultz, D.L.
Paper in Symposium on "Some developments for temperature measurements." Inst. of Mech. Engineers (1962).

19. Dunn & Blum
"Continuous measurement of shock velocity using a microwave technique." NASA-CR- 490 (may 1960).

20. McDaniel, E.W.
"Collision phenomena in ionized gases." Wiley (1964).

21. Langmuir, I. & Mott-Smith, M.H.
"Collected works of I. Langmuir." Vol.5, Pergamon Press, Oxford.

22. Langmuir, I. & Mott-Smith, M.H.
General Electric Review, 27, pp 449, 538, 616, 762.

23. Johnson, E.O. & Malter, L.
Physics Review, 80, 58 (1950).

24. Boyd, R.L.F. & Twiddy, N.D.
Proc. Royal Society, A250, 53.

25. Su, C.H. & Lam, S.H.
"Continuum theory of spherical electrostatic probes." Physics of Fluids, 6, 1479 (Oct. 1963).

26. Cohen, I.M.
"Asymptotic theory of spherical electrostatic probes in a slightly ionised collision dominated gas." Physics of Fluids, 6, 1492 (Oct. 1963).

27. Su, C.H. & Sonin, A.A.
"Theory of the electrostatic probe in a moderately ionised gas." Physics of Fluids, 10, 124 (Jan. 1967).

28. Cozens, J.R. & von Engel, A.E.
"Theory of the double probe at high gas pressure." International Journal of Electronics, 19, 61, (July, 1965).

29. Brundin, C.L.
"The application of Langmuir probe techniques to flowing ionised gases."
University of California, Institute of Eng. Research Report No. AS-64-9.

30. Radcliffe, S.W. & Hobson, R.M.
"The interpretation of electrostatic probe responses in shock tubes."
8th Int. Conf. on Phenomena in Ionises Gases, 484 (1967).

31. Lui, J.T.C.
"Shock tube side-wall electrostatic probes."
AIAA Journal, 5, 891 (May 1957).

32. Bienkowski, G.K.
"Electrostatic sheath in a weakly ionized gas."
Physics of Fluids 10, 381 (Feb. 1967).

33. Bredfeldt, H.R., Scharfman, W.E., Guthart, H. & Morita, T.
"Boundary-layer ion density profiles as measured by electrostatic probes." AIAA Journal, 5, 91 (Jan. 1967).

34. Schlichting, H.
"Boundary layer theory". McGraw-Hill (1960).

35. Curle, N.
"The laminar boundary layer equations."
Oxford Math. Monographs, Clarendon Press (1962).

36. Dorrance, W.H.
"Viscous hypersonic flow (theory of reacting and hypersonic boundary layers)." McGraw-Hill (1962).

37. Sinnot, G., Golden, D.E., & Varney, R.N.
"Positive-ion mobilities in dry air."
Physics Review, 170, 170 (June 1968).

38. Young, R.A., Gatz, C.R., Sharpless, R.L. & Ablow, C.M.
"New Method for measuring the rates of ionic transport and loss. 1. Mobility of NO^+."
Physics Review, 138, 359 (1965).

39. Dalgano, A., McDowell, M.R.C., & Williams, A.
"The mobilities of ions in unlike gases."
Philosophical Trans. of the R.S., A250, 411 (1958).

40. Dalgano, A.
"The mobilities of ions in their parent gases."
Phil. Trans. of the R.S., A250, 426 (April 1958).

41. Aronsen, P.M. & Levine, D.
"The effects of water vapour on the electron density of shock heated Air."
US Naval Ordinance Lab. NOLTR67-79 (Jan. 1967).

42. McLaren, T.I. & Hobson, R.M.
"Measurement of ionisation and excitation cross-sections and rate constants in shock heated Argon."
8th Int. Conf. on Phenomena in Ionised Gases, 468 (1967).

43. Cobine, J.D.
"Gaseous conductors." Dover (1958).

44. Heald, M.A. & Wharton, C.B.
"Plasma diagnostics with microwaves." Wiley (1965).

45. Ginzburg, V.L.
"Propagation of Electromagnetic Waves in Plasma."
Gordon & Breach (1961)

46. Takeda, S. & Tsukishima, T.
J. Applied Physics, 35, 2548 (1964).

47. Takeda, S. & Tsukishima, T.
"Microwave reflection techniques for dense plasma diagnostics."
Nat. Bureau of Standards, TN 256 (March 10, 1965).

48. Yamanaka, C. & Nakai, S.
"Microwave measurements of shocked plasma."
J. Phys. Soc. Japan, 19, 2350 (1964).

49. Lapworth, K.C. & Townsend, J.E.G.
"Temperature and pressure studies in the reservoir of a reflected-shock hypersonic tunnel."
NPL Aero Report No. 1127 (Dec. 1964).

50. Allis, W.P., Buchsbaum, S.J. & Bers, A.
"Waves in anisotropic plasmas." MIT Press (1963).

51. Shkarofsky, I.P., Bachynski, M.P. & Johnston, T.W.
"Collision frequency associated with high temperature air and scattering cross-sections of the constituents."
Planetary & Space Science, 6, 24 (1961).

52. Bachynski, M.P., Johnston, T.W., & Shkarofsky, I.P.
"Electromagnetic properties of high temperature air ."
Proc. IRE, 48, 347 (1960).

53. Collin, R.E.
"Field theory of guided waves." McGraw-Hill (1960).

54. Hochstim, A.R.
"Electron concentration in closed form for high temperature air with additives."
Planetary & Space Science 6, 79 (1961).

55. General Radio Co.
"Operating instructions for type 900-LB precision slotted line." (1964).

56. Montgomery, C.G.
"Technique of microwave measurements."
McGraw-Hill (1947).

57. Brodwin, M.E. & Miller, D.A.
"Propagation of the Quasi-TEM mode in Ferrite-filled coaxial line."
IEEE Trans. MTT, 12, 496, (Sept. 1964).

58. Framklin, R.N.
"Reflection from an interface in a plasma-filled waveguide."
Ref. 29, Int. Conf. on the microwave behaviour of ferrimagnetics and plasmas: IEE Conf. Publication 13 (Sept 1965).

59. Franklin, R.N.
"Radio Wave propagation in a plasma."
Royal Military College of Science, Shrivenham,
Tech. Note No. RT 13 (Dec. 1961).

60 McLachlan, N.W.
"Bessel functions for engineers." Clarendon Press (1934).

61. Ratcliffe, J.A.
"The Magneto-Ionic Theory and its applications to the Ionosphere." C.U.P. (1959).

62. Gabriel, G.J. & Brodwin, M.E.
"The solution of guided waves in inhomogeneous anisotropic media by perturbation and variational methods."
IEEE Trams. on MTT, 13, 364, (May 1965).

63. Gabriel, G.J. & Brodwin, M.E.
"Distinctions between gyroelectric and gyromagnetic media in rectangular waveguide."
IEEE Trans. on MTT, 14, 292 (June 1966).

Acknowledgements.

The author firstly wishes to express his thanks to his supervisor, Dr. R.N. Franklin, for his generous help and ready advice in difficult moments.

Thanks are also due to Dr. D.L. Schultz, for much appreciated help on the organisational side of the project, and for many fruitful informal discussions.

Mr. J.M. Smith is to be thanked for his work in running the shock tube, and for his willing and skilful assistance in the design and construction of experiments.

Further gratitude is due to Dr. T.V. Jones, who, having to share a laboratory with the author, beat out with him many basic conceptions in the course of daily interaction.

Acknowledgement is also due to the staff of the Department of Engineering Science, Oxford, for much skilled assistance.

The project described in this thesis was supported by the Ministry of Technology, to which the author expresses his thanks.

To the University of Sydney Lightoller Scholarship Fund, which provided personal maintenance funds which made possible these years in Oxford, the author expresses his sincere appreciation.

Finally, my deepest thanks to Susan, for her willingness to spend a honeymoon typing and proof-reading.